DOE/MC/29257 -- 5725
(DE97005438)

Advanced Turbine Systems Program

Final Report
August 3, 1993 - August 31, 1996

Work Performed Under Contract No.: DE-AC21-93MC29257

For
U.S. Department of Energy
Office of Fossil Energy
Federal Energy Technology Center
Morgantown Site
P.O. Box 880
Morgantown, West Virginia 26507-0880

By
Allison Engine Company
P.O. Box 420
Indianapolis, Indiana 46206-0420

Disclaimer

DISCLAIMER

Portions of this document may be illegible electronic image products. Images are produced from the best available original document.

TABLE OF CONTENTS

TABLE OF CONTENTS (cont)

LIST OF ILLUSTRATIONS

LIST OF ILLUSTRATIONS (cont)

LIST OF ILLUSTRATIONS (cont)

LIST OF ILLUSTRATIONS (cont)

LIST OF ILLUSTRATIONS (cont)

LIST OF ILLUSTRATIONS (cont)

LIST OF TABLES

EXECUTIVE SUMMARY

REPORT ORGANIZATION

This executive summary provides an overview of the activities completed on each of the Statement of Work (SOW) tasks. Detailed reports on each task follow.

SUMMARY

Six tasks were approved under Modifications A007 and A008 as the Advanced Turbine Systems (ATS) extension program to the DOE contract DE-AC21-93MC29257. The six tasks include the following:

- Task 5.0 - Market Study
- Task 6.0 - GFATS Definition and Analysis
- Task 8.01 - Castcool®* Blades Fabrication Process Development
- Task 8.04 - ATS Low Emission Combustion System
- Task 8.07 - Ceramic Vane Design and Evaluation
- Task 9.0 - Program Management.

Tasks 5.0, 6.0, 8.01, 8.04, and 9.0 were initiated May 1, 1995. Task 8.07 was added to the program effective June 1, 1995.

Task 5.0 - Market Study

The objective of the market study task is to focus on distributed generation prospects for an industrial ATS, using the Allison ATS family as the primary gas turbine systems. The task got a late start because the type of study the Department of Energy (DOE) wanted to conduct needed to be clearly defined. Allison and the DOE/Morgantown Energy Technology Center (METC) jointly determined that the emerging area of power generation being emphasized by utilities and other power producers is distributed generation. Thus, the market study should concentrate on the potential of distributed generation.

Allison contacted the Electric Power Research Institute (EPRI) to find out whom they would recommend for such a study. EPRI personnel informed Allison that EPRI is conducting a comprehensive study for its member clients, and that the DOE study could dovetail with it. An informal statement of work (SOW) was generated by Allison and sent to EPRI for comments. EPRI personnel agreed that the SOW was appropriate and complete; however, they indicated that the study would cost more than the amount stated in the SOW. Allison has sent EPRI a request for proposal, and is awaiting its arrival. It appears that the EPRI contract will be let in early August. EPRI had indicated that the study would take approximately 3 months after the award. The task is expected to be complete by the end of November. At that time a final report on this task will be submitted by Allison. A detail discussion of the status of this task is presented in Section 2.

---

* Castcool is a registered trademark of Allison Engine Company.

Task 6.0 - GFATS Definition and Analysis

This task was a continuation of the task on "Gas Fired Advanced Turbine System Definition and Analysis" to explore the following specific topics: combustion section flow and heat transfer analysis; combustion section scale model rig test; study of carcass deflection from the combustor; reduced turbine cooling flow trade studies; ceramic blade track design; inlet housing loss optimization; study of mix flow LP compressor; increased rotor speed; surge protection valve study; update general arrangement drawing; effect of thin wall and coating on single crystal mechanical properties; extended oxidation testing; Castcool heat transfer effectiveness testing; thermal barrier coating of vane platforms; and design validation. This task is completed and is presented in the final form.

Key accomplishments of this task are the following:

- completion of the flow and heat transfer analysis of the combustor section and the transition to show that the proposed design would be satisfactory
- successful testing of the combustion section rig to provide useful validation information for the analytical model
- reduction of cooling flow through tighter clearances
- segmented ceramic blade track that virtually eliminated the hoop stress
- a mix flow compressor design approach requiring 50% less drive power
- results showing that an increased power turbine mechanical speed would not be cost effective
- a proposed design of a bleed valve for surge protection
- superior stress rupture capability of coated single crystal materials at 1800 and 1900°F
- useful design data on extended oxidation protection of single crystal and equiax material
- design information on flow characteristics and cooling performance of Castcool materials
- completion of design validation requirements

Details on this task are presented in Section 3.

Task 8.01 - Castcool Technology Demonstration

The Castcool blade fabrication process enabled producing good quality blades that were fully inspected. The yield showed improvements over the earlier levels in Phase 2. These blades will be tested in the ATS Phase 3 gas generator tests. All blades will be inspected after the test to verify successful engine operation.

The operational requirements for the Phase 3 test were established. A complete structural analysis of the high pressure (HP) turbine rotor, case, and static structure was accomplished.

Coating of vanes and blades was completed. Subsequent cold flow testing of blades demonstrated acceptable cooling flow levels. The coated airfoils will be evaluated as part of post-test hardware analyses.

Fabrication and acceptance of two types of film-riding face seals were completed. The seals passed all test points.

Blade tip bonding was completed during this period. Tests showed no curling of the tips. These blades will be demonstrated in the gas generator test to evaluate their durability.

Task 8.01 is completed. A detailed description of this task is presented in Section 4.

Task 8.04 - Low Emission Combustion

Various series-staged combustor configurations were evaluated. Two silo combustion systems were selected as potential candidates. One system is based on a traditional catalytic combustion concept. The other system consists of a premixer in the first stage followed by a catalyst.

Catalytica has completed feedstream contaminant testing of the two stage reactors. The results using salt and dust contaminations indicate some degradation of the catalyst may occur even at low exposure levels.

Flashback due to the ATS cycle is a concern. Extensive testing was done by modifying the standard module for the ultra-low NOx program. In this study, parametric changes were made to the velocity field, mixing efficiency, and fuel-air concentration profile. The impact of these changes was recorded in terms of flashback propensity, NOx formation, pressure drop, and nozzle wall temperature. Eight different configurations were analyzed. This testing helped in understanding the flashback phenomena.

Extensive laser Doppler anemometer (LDA) velocity measurements were made at Energy Research Consultants' atmospheric facility. These measurements were made to determine the interaction of swirling flows, velocity profiles at premixer/combustor interface, velocity profiles downstream of the module nozzle, velocity profile at the exit of the premixer, and particle size dependency of velocity measurements. The results indicated that particle size effects should be considered when interpreting velocity measurements from hardware. This testing helped in our understanding of the flashback phenomena and premixer design. The results will be used in module development for Phase 3.

This task is complete. A detailed write-up on this task is presented in Section 5.

Task 8.07 - Ceramic Vane Design and Evaluation

This task was initiated in June 1995 and is planned to continue through March 1998. Activities for this task included: thermal and mechanical stress analyses of the vane and mount designs; long-term vane life evaluations; evaluation of thermal shock tests for ceramic vanes; and design and drafting for the ceramic vanes and their mounts.

All maximum continuous power and emergency shutdown stress analyses have been completed. Stress levels and probability of survival values have been acceptable. Results show that maximum stresses occur at the trailing edge of the ceramic vane in the region of midspan. At the location of highest stress, material temperature is 1345°F. The calculated fast fracture probability of survival exceeds 99.99% for all vanes for the highest stress condition.

Although AS 800 (Allied Signal) and Sn 281 (Kyocera) are two promising ceramics for improved stress rupture lifetimes, there is currently insufficient long-term stress rupture data for

durations over 5,000 hr. Oak Ridge National Laboratories has agreed to provide long-term data for these materials at test conditions suggested by Allison.

The design and drawings for the ceramic first-stage vanes and metallic mounting hardware for retrofit into an existing Allison 501K turbine are nearly complete.

A detailed description of this task is contained in Section 6.

Task 9.0 - Program Management

The program management activity included providing direction to the team on cost and schedule, and on technical objectives of the SOW that must be met by Allison. Project management will continue through the completion of Task 5.0 - Market Study, and the transfer of Task 8.07 - Ceramic Vane Design and Evaluation to ATS Phase 3.

A detailed description of key activities under project management is provided in Section 7.

1.0 PROJECT PLAN

1.1 OBJECTIVE OF TASK

The objective of this task was to develop and document a project management plan that outlined a plan to perform Tasks 5.0, 6.0, 8.01, 8.04, 8.07, and 9.0 of the contract statement of work (SOW).

1.2 ACCOMPLISHMENTS

Allison submitted a Management Plan for this program at the start of the Phase 2 extension contract The final version of the plan incorporated DOE's comments, and was submitted on July 18, 1995.

1.3 REMAINING EFFORT

Work on Tasks 5.0, 8.07, and 9.0 will continue in accordance with DOE guidance until completion. Tasks 5.0 and 9.0 are expected to be completed by the end of November 1996. At that time, Task 8.07 will be transferred in accordance with the directions of the DOE/METC Project Manager to ATS Phase 3 and continued until completion in March 1998.

2.0 TASK 5.0 - DISTRIBUTED GENERATION MARKET STUDY

The Market Study task (Task 5.0) was defined and approved by DOE/METC late in the project. Allison subsequently generated a statement of work (SOW) to have this study conducted by an outside organization. The SOW was submitted to DOE, approved, and then sent to the Electric Power Research Institute (EPRI) in early 1996. A meeting was subsequently held at EPRI to review the scope of the study and to assess how this task might be compatible with the current EPRI study on distributed generation. The purpose of the study was to have a market study conducted on the potential application of the Allison ATS type advanced gas turbine in the distributed generation market.

EPRI reviewed the SOW and sent comments to Allison. EPRI stated that the SOW was comprehensive and the study should be conducted to include the tasks outlined. However, EPRI mentioned that the cost of the study would be $100,000 instead of the $40,000 indicated in the SOW.

A letter of request was sent by Allison to Mr. Leland Paulson, DOE/METC Project Manager, asking for his concurrence to increase the allocated cost for Task 5 from $40,000 to $100,000, without increasing the overall cost of the contract. Mr. Paulson provided the go-ahead to Allison to increase the funding for Task 5. This approval authorized Allison to adjust the cost of the tasks within the overall contract, without increasing the total contract cost to DOE/METC.

Allison subsequently sent a revised SOW to EPRI and asked EPRI if it would be interested in submitting a formal proposal. EPRI expressed interest in having this study added to a more detailed study being conducted by EPRI contractors for EPRI's members. A formal request for proposal has been sent to EPRI. The response is expected to form the basis for a formal contract with EPRI. The contract will specify that EPRI must complete the tasks outlined in the DOE/METC SOW generated by Allison, and in accordance with the funding and schedule.

A copy of the SOW sent to EPRI is presented as follows.

STATEMENT OF WORK

Introduction

Allison Engine Company (Allison) is currently under contract with the Department of Energy, Morgantown Energy Technology Center, to have a market study conducted on its Advanced Turbine Systems (ATS) configuration. The study should focus on potential applications of the Allison ATS in distributed generation.

The Electric Power Research Institute (EPRI) is conducting a comprehensive study on distributed generation for its members. This EPRI study appears to be broader in scope than the DOE-funded Allison study. The intent of the Allison requested study primarily is to utilize the work being done by the contractors for EPRI, and add the Allison statement of work to the EPRI contract as an additional task.

Objective

The objective of the distributed generation study for the Allison ATS is to determine potential markets for a 5 to 15 MW simple cycle gas turbine engine. The Allison ATS will be adaptable for installation at industrial customer sites and/or at select substations owned by electric utilities.

The specific tasks to be performed by a contractor on this study are the following:

1. From a survey of end users, determine the size range of power generation systems in terms of MW that defines "distributed generation."
2. Identify whether there is an optimum size range for gas turbines preferred by end users for distributed generation applications. This preference may vary geographically, by the type of end user, and globally.
3. Quantify the total distributed generation market niche and size (total MW) for gas turbines in the 5 to 15 MW range. Provide a market projection with time (years) for the distributed generation market. Any global projections would also be highly desirable.
4. Conduct a survey of representative end users to evaluate how well the Allison ATS gas turbines will meet their needs for their distributed generation markets. Also indicate the features these end users would like to emphasize, e.g., first cost, transportability, simple vs. combined, or other cycle modes.
5. Determine whether there are demographic and geographic regions where the Allison ATS type gas turbines could best serve the distributed generation needs. The current EPRI distributed generation study might provide inputs and guidance for this task.
6. Provide an interim and a final presentation on the results of the distributed generation study on the Allison ATS engine at a mutually agreed upon site.
7. Generate a final report on the proposed study.
8. Submit recommendations for further evaluations that would enhance understanding of the distributed generation markets.

Schedule and Cost

The study should be completed in approximately 3 months from the start of the contract. Allison will contract this study with EPRI, which in turn will select and authorize the contractor(s) currently conducting the EPRI distributed generation study.

The funding available for this study is limited to and not to exceed the sum of $100,000.

The study is expected to begin in August 1996. A final report on this task will be submitted in late November 1996.

3.0 TASK 6 - SYSTEM DEFINITION AND ANALYSIS

3.1 OBJECTIVE OF TASK

Task 6, System Definition and Analysis, was initiated in February 1994. Its purpose is to complete the conceptual design of the Gas Fired ATS (GFATS), which will be detail designed and developed in later phases of the program. Modification seven to Allison's Phase 2 contract added funding and extended the performance period for Allison to do additional analysis on selected features of the ATS engine. Scale model component testing and material specimen testing were also a part of this contract modification. This additional Task 6 work was accomplished under 15 subtasks. The work completed on each of these subtasks is discussed in this section of the report. Each of these subtask writeups will include objective, discussion of the work performed, and results.

3.2 ACCOMPLISHMENTS

3.2.1 Combustion Section Flow and Heat Transfer Analysis

Objective

To meet program emission goals, the ATS engine will include a silo-type combustor. This combustor will be centered over the top of the engine with its axis oriented 90 deg to the engine's axis. A diffuser will slow the flow exiting the compressor prior to its delivery to the combustor. A bifurcated transition duct will be located within the base of the combustor to separate its entering and exiting flow, and to direct and distribute the flow around the engine's main shafting to the turbine inlet. The flow fields internal and external to the bifurcated transition duct of the combustor are highly complex, requiring sophisticated models and analytical methods to predict them accurately. Due to the flow field complexity, it is likely that design modifications will be necessary to obtain satisfactorily uniform turbine inlet conditions.

The principal objectives of this subtask are to model the ATS combustor inlet and outlet physical flow paths, and then to apply sophisticated flow analysis procedures to predict their associated flow fields. The physical flow paths of interest include that of the diffuser and those around and through the bifurcated transition duct. Of particular interest is the flow field exiting the transition duct at the turbine inlet plane. The flow analysis results will be compared to the rig test results of subtask 6.02 (see section 3.2.2) for validation of the analytical predictions. Once validated, confidence gained in the analytical predictions will allow design changes aimed at optimizing the flow fields to be made and analyzed without having to rig test each modification for verification. The flow model thus generated will also be a key element in the subsequent heat transfer analysis as it will serve to establish wall boundary conditions.

Discussion

General

The ATS engine's diffuser and bifurcated transition duct were computationally analyzed to evaluate the aerodynamic performance of each part. The bifurcated transition duct, shown in Figure 3.2.1-1, parts a and b, turns the radial flow exiting the combustor, which is oriented at 90 deg to the engine centerline, to an axial flow that enters the turbine. The diffuser slows the flow as it exits the last compressor vane row and distributes the flow to the passage formed between the internal wall of the combustor outer casing and the external wall of the bifurcated transition duct on the flow's way up to the swirler modules mounted on the upper region of the silo combustor. Two diffuser geometries were investigated. One geometry was essentially straight axially and the other one was curved to partially turn the flow radially.

The bifurcated transition duct internal flow path and the diffuser/transition duct external flow path were decoupled and individually analyzed, with the internal flow field analysis of the transition duct being one task and the straight versus curved diffuser comparison being a separate task. Both analyses are described in the following paragraphs.

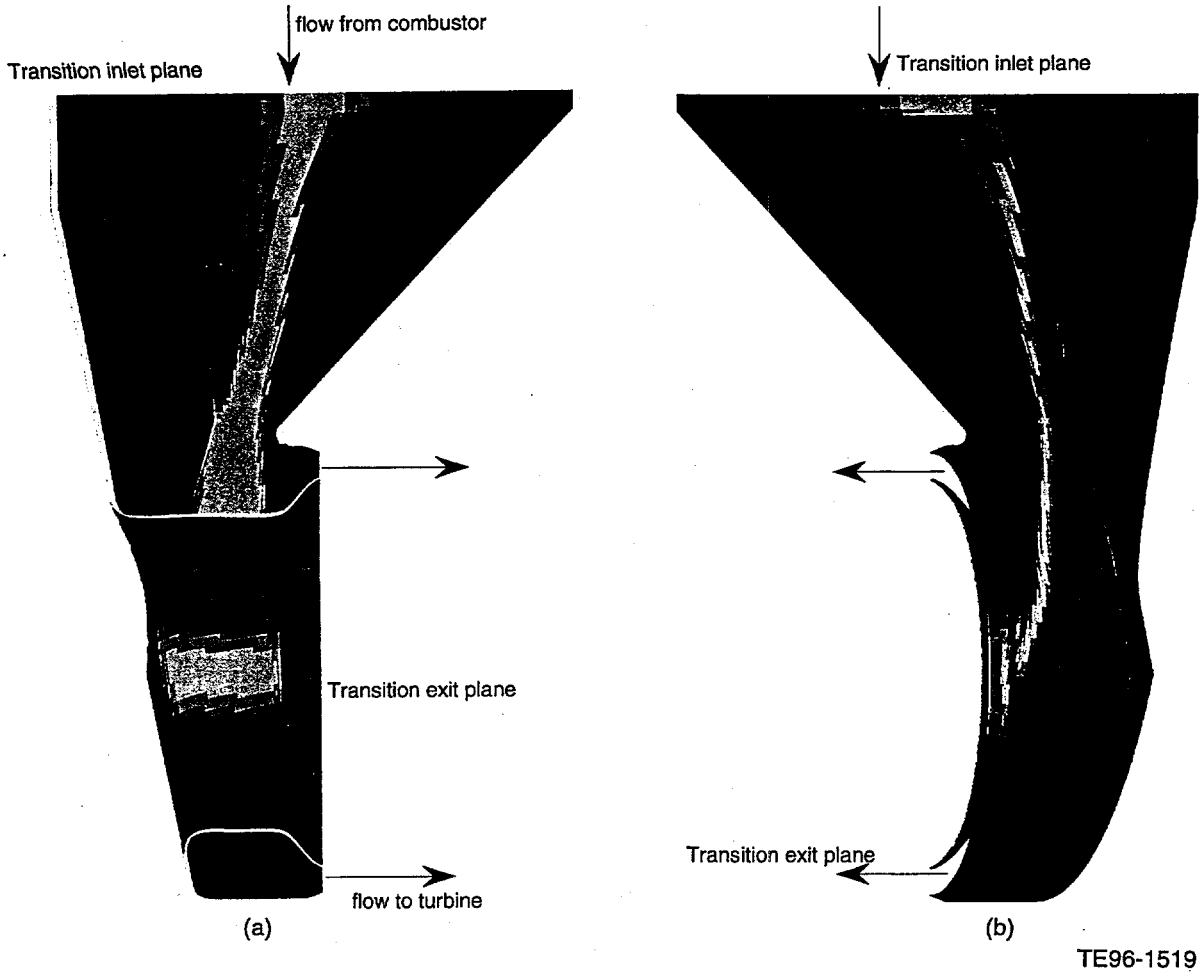

Figure 3.2.1-1. The bifurcated transition duct turns the radial flow exiting the combustor to an axial flow that enters the turbine.

ATS Bifurcated Transition Duct

The purpose of this analysis was to study the flow field within the ATS bifurcated transition duct. In particular, this included mass flow distribution heading into the turbine inlet, transition duct exit plane flow angles, and temperature mixing. The results of the computational analysis will be an integral part of the subsequent heat transfer analysis when determining cooling requirements for the system, and a part of the turbine design analysis as a guideline for designing the first stage turbine vane.

The transition duct begins as a circular cross-sectional area. This area becomes pinched in the axial direction as it leads toward the engine centerline to form the throat of the transition duct. The throat transitions into a ring-shaped duct that splits the flow symmetrically about the vertical centerline. The flow then turns 90 deg out of the ring to an axial direction where it then heads toward the turbine.

The effort of modeling the inner wall of the ATS bifurcated transition duct began by establishing a CAD surface definition of the part. The surface definition of the bifurcated transition duct

was created in ANVIL. Next, the surfaces were refined and combined in Patran to allow for easier grid generation. Once the surface definitions were properly prepared, Gridgen (a 3-D grid generation software package) was used to build a 3-D, nonorthogonal, locally structured grid within the throat and ring region of the transition duct. Locally, the blocks within the global grid were structured, yet that same structural continuity was not maintained from block to block. This allowed greater flexibility for accurately fitting grids to the geometry while yielding a grid suitable for a finite volume flow calculation. Upon completion, the grid was imported into Star-CD (licensed code of Adapco, Inc., that is an unstructured, finite volume flow solver with a user-interactive pre-/post-processor) with which the flow field was solved and analyzed.

In setting up the computational model, certain aspects of the physical flow field needed specific attention. The inlet condition was defined as a radial temperature profile (Figure 3.2.1-2), having an average temperature of 3191°R. The maximum inlet temperature of 3251°R existed in the core, while the minimum inlet temperature of 3162°R was at the wall. A plug velocity profile was used at the inlet, as this would be expected from the actual combustor flow because of the catalyst honeycomb that will flatten the velocity profile before exiting the ATS silo combustor. Walls were assigned adiabatic, no slip boundary conditions. The transition duct's exit plane in the computational model was extended for 10 in. as a constant area annulus (Figure 3.2.1-3, parts a and b). This was done to allow the flow to mix as needed before reaching the model's exit boundary. The exit boundary was modeled as a 'percentage of total mass flow' condition. In this case, 100% of the total mass flow was required to exit at the model's exit boundary plane. The system reference pressure was assigned at the transition duct exit plane. The final boundary on the model was a symmetry boundary splitting the transition duct in half along its line of symmetry. This plane is truly neither symmetric nor cyclic, yet when compared to the cyclic condition, the symmetry plane condition much more closely simulates the physics of the problem, especially when inlet swirl is near zero as it is for the ATS combustor.

ATS Diffuser/Transition Duct External Flow-Path Analysis

The purpose of analyzing the flow path through the diffuser and continuing external to the transition duct was to determine the mass distribution through the system for both diffuser configurations. By computing the mass distribution and velocity field, heat transfer analysis can be used to predict backside convective cooling effectiveness. Also of importance was knowing the mass distribution as the flow heads toward the swirler modules on the combustor. Ideally, the swirlers are to be fed uniformly.

Modeling the exterior flow path around the outside of the bifurcated transition duct required a slightly different approach than was used for the transition duct interior flow path. This model required a 3-D body fitted grid to adhere to two unattached surface definitions: one the outer wall of the transition duct and the other the inner wall of the casing. The diffuser definition, whose surface was generated separately, was attached to the combustor outer casing's inner wall surface, as shown in Figure 3.2.1-4.

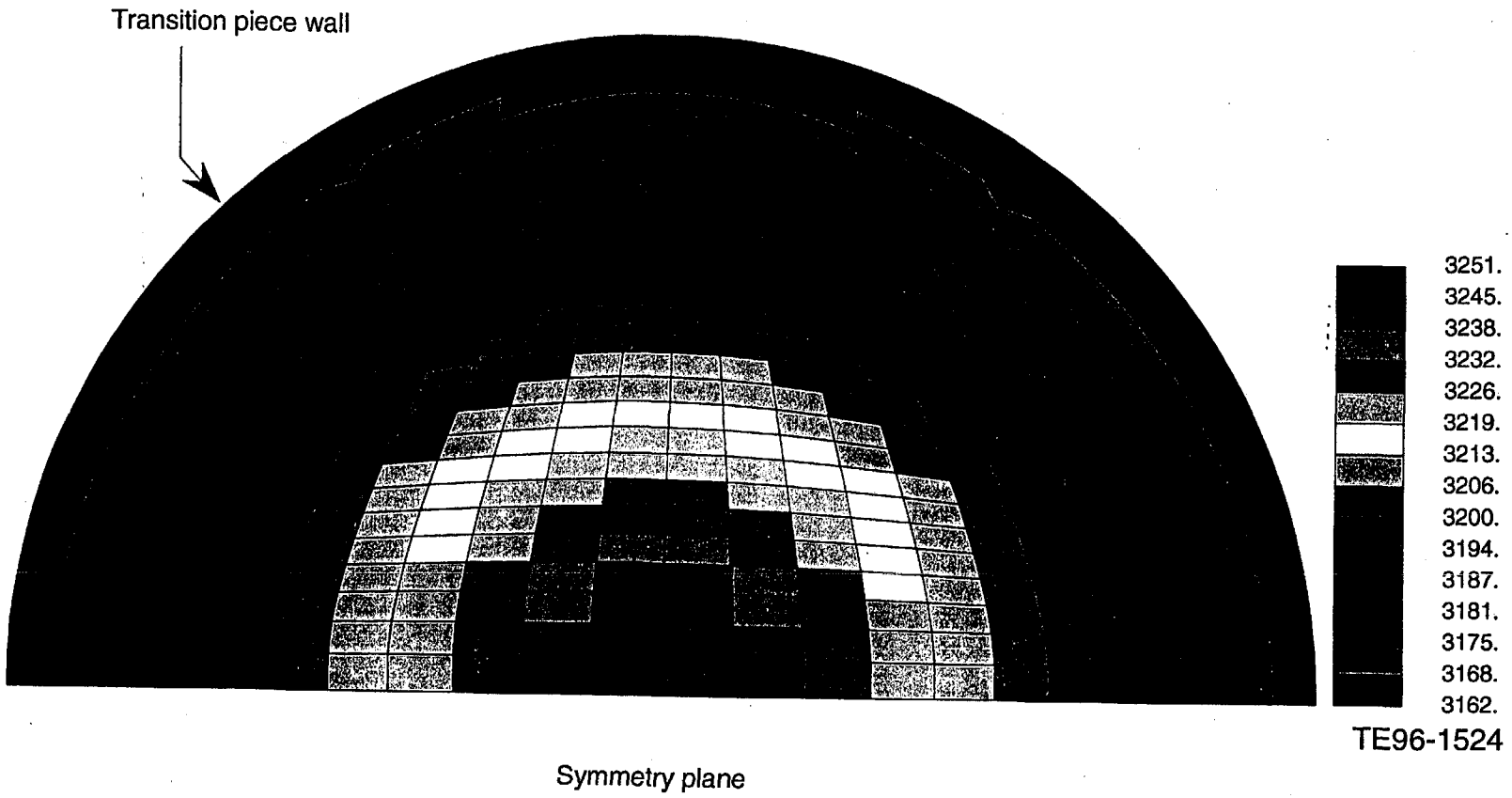

Figure 3.2.1-2. Inlet plane to bifurcated transition piece—inlet temperature profile.

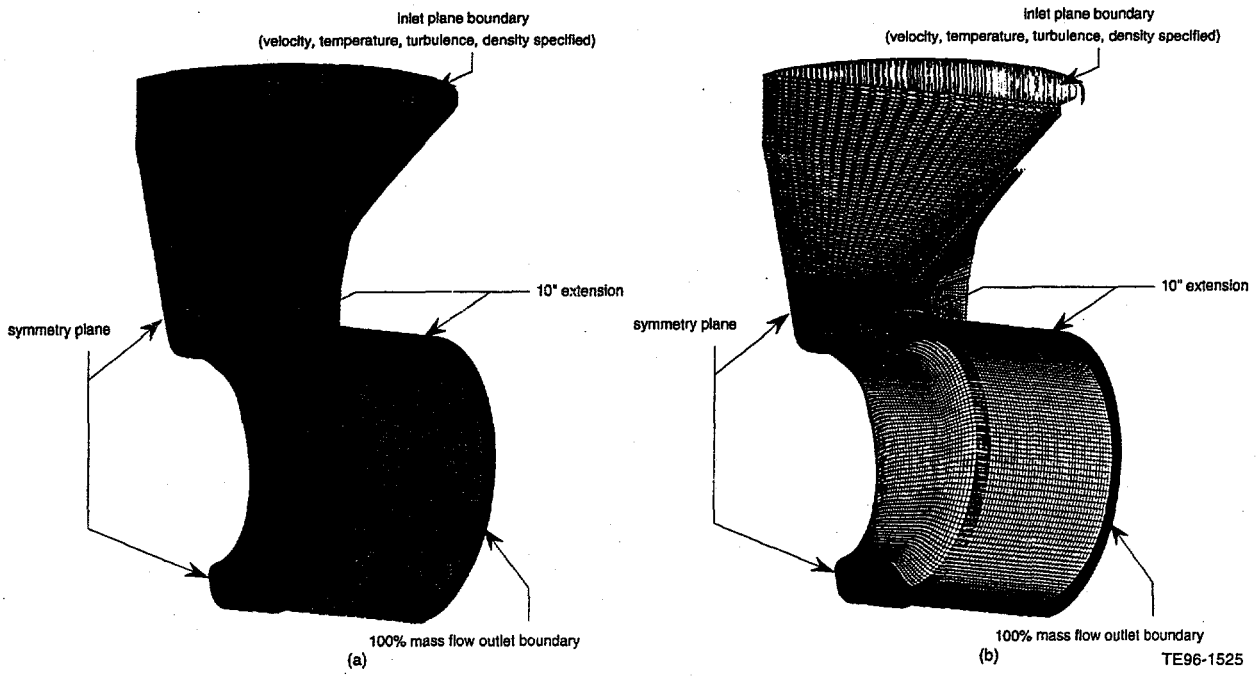

Figure 3.2.1-3. Transition piece, Phase II—temperature at liner and casing wall.

The surface definitions of the outer skin of the bifurcated transition duct and the inner skin of the casing were created in ANVIL, and then refined and combined in Patran for later grid generation. As for the diffuser geometries, surface definitions for these parts were created directly in Patran. From these new surfaces Gridgen was again used to created a 3-D multiblock grid as described previously. Once completed, the 3-D grid was imported into Star-CD for flow analysis.

In setting up the computational model, a plug velocity profile was used at the diffuser inlet. The symmetry plane of the system was modeled with a symmetry boundary condition. Walls were assigned adiabatic, no slip boundary conditions. Like the transition duct's internal flow-path exit, the flow domain exit boundary was modeled as a 'percentage of total mass flow' condition, and 100% of the total mass flow was required to exit at the transition duct's external flow-path exit boundary plane.

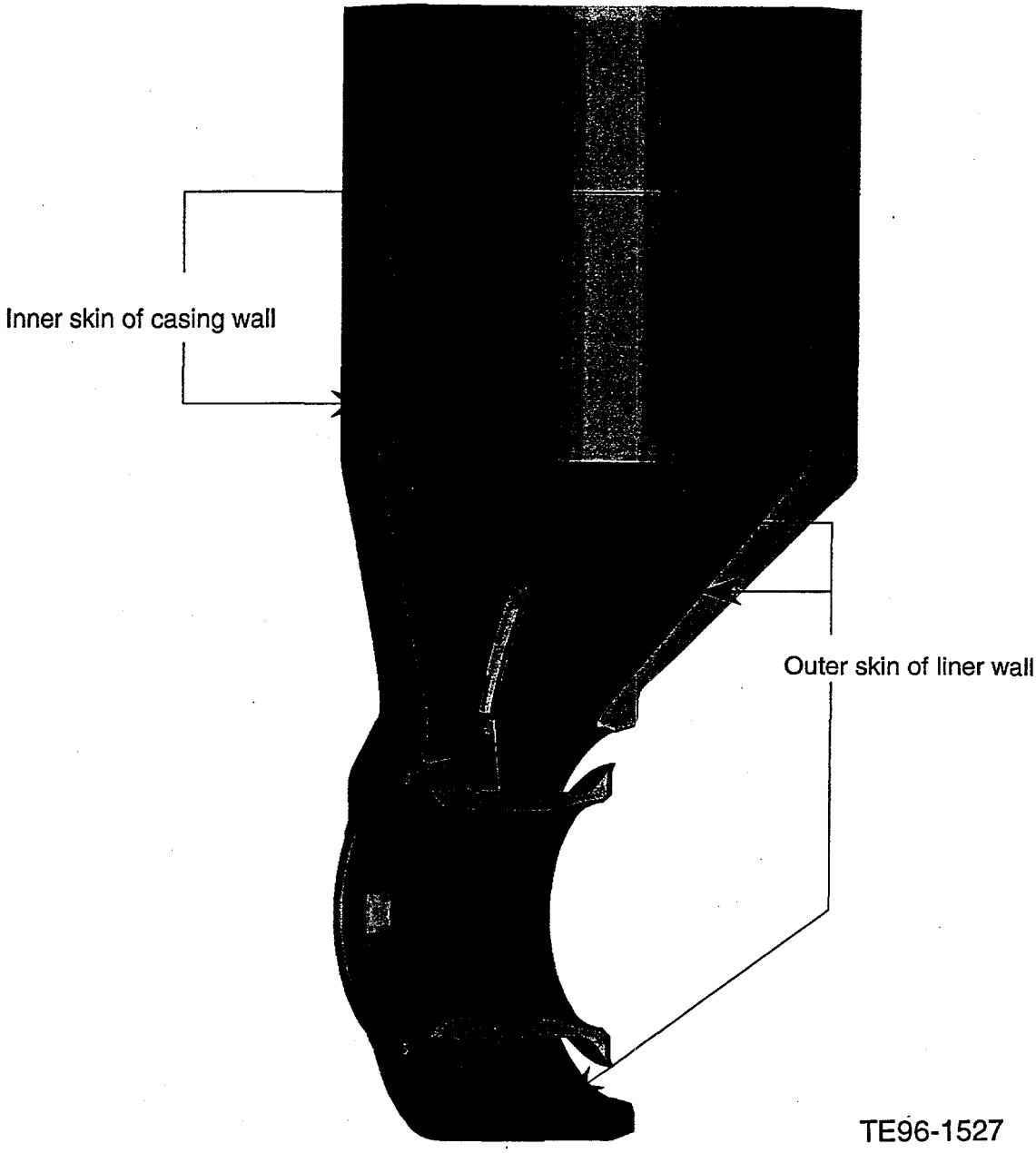

Figure 3.2.1-4. Straight diffuser (multiple colors indicate multiple blocks in grid).

Analyses

The bifurcated transition duct analysis had an input mass flow rate of 25.02 lbm/sec and a specific heat ratio of 1.3. The diffuser configuration analysis had an input mass flow rate of 24.27 lbm/sec and a specific heat ratio of 1.4. The difference between the two models was the fuel added during the combustion phase that caused the increase in mass flow and the decrease in specific heat ratio for the bifurcated transition model. The mass flow rates are half of the cycle recommended values because only half of each model was analyzed.

ATS Bifurcated Transition Duct

Initially, an exit boundary condition was placed 1 in. downstream of the transition exit plane, but because of the high flow activity in this region (from turning 90 deg), this was computationally an ill-defined boundary location. Therefore, to allow the flow to dissipate and mix after the 90-deg turn, the boundary was extended 10 in. downstream. Note that flow exit plane parameters were all taken from the physical transition exit plane, not from the 10 inch extension exit plane.

Of particular.interest in this analysis was the mass flow distribution in the ring portion of the transition duct, especially at the transition exit plane (i.e., the turbine inlet plane). Ideally, the flow should have a uniform circumferential distribution of mass flow as it exits the transition duct and enters the turbine. However, upon reviewing the results, the mass flow distribution was highly nonuniform.

Also of interest in the flow field analysis within the transition duct was swirl angle (also termed flow angle), defined as the angle between the axial component of velocity and the tangential component of velocity, measured from the axial direction. The tangential velocity component and swirl angle reach a maximum near the 90-deg mark (from top dead center). This is a negative number on the plots by definition of the selected coordinate system. Also, there is a small amount of tangentially reversed flow at the bottom of the ring where the flow reaches the symmetry plane. The symmetry also plays a role with swirl. Due to symmetry, the same maximum swirl angle magnitude will exist on the opposite side, meaning the first-stage turbine vane will see a wide range of flow angles. A uniform swirl angle throughout the transition exit plane is a more preferred turbine inlet condition.

Another point of interest in this analysis was the temperature distribution at the transition exit plane. With a radial inlet profile mixing abilities of the transition ducts should be evident by examining the temperature field at the transition exit plane. The temperature at the exit plane is fairly well mixed circumferentially with a small region of slightly cooler flow near the bottom of the ring. The larger temperature gradients appear in the radial direction. A temperature contour plot of the 3-D model, shows that the hot core gas heads down the throat of the transition duct and impinges on the top of the ring. This hot spot on the transition wall will be a main focus when considering cooling techniques for the transition duct.

ATS Diffuser/Transition Duct External Flow-Path Analysis

Both straight and curved diffuser geometries were modeled as a part of the exterior flow path. First, the straight diffuser was integrated as a part of the exterior flow path. This flow path be-

gins at the trailing edge of the compressor outlet guide vane (OGV). The flow then travels through the diffuser and is dumped into the casing cavity, with the bifurcated transition duct located in the middle of the flow field. From here the flow travels up the outside of the transition duct eventually to the top of the silo combustion can. Also of interest is the mass distribution around the silo as the flow heads toward the top of the silo; this is important from both a backside cooling aspect and swirler air supply aspect.

Straight Diffuser

The straight diffuser geometry was considered the baseline configuration. When analyzing the configuration the velocity distribution into the casing cavity was of particular interest. The flow analysis revealed that the straight diffuser tended to push mass into the casing cavity, with the discharging flow maintaining a large amount of axial momentum. This momentum carries the flow between the transition duct and the shaft housing, and also pushes some of the flow around the transition duct. A large portion of the flow reaches the turbine side of the casing cavity between the transition duct and the casing. In turn a flow starved region is formed on the compressor side of the transition duct. The corresponding low velocities in this region of low mass are visible. The low velocities regions in the silo region of the cavity pose a concern from a cooling standpoint as well as flow distribution to the combustor dome.

To address the nonuniform mass distribution around the transition duct as flow heads up the silo, a perforated ring (Figure 3.2.1-5) was installed into the straight diffuser configuration, at a distance of 24 in. from engine centerline. The ring had a uniform distribution of the ratio of open area to closed area. As shown in Figure 3.2.1-6, the flow slows down as it approaches the perforated ring and redistributes as it heads through the ring and up the silo annular cavity.

It is evident that the perforated ring does redistribute the flow, yet a wide range of exit velocity magnitude still exists. A more uniform mass distribution is preferred for supplying flow evenly to the lean premix modules. The mass distribution was improved by using a perforated ring with nonuniform holes. The curved diffuser discussion addresses this improvement.

Curved Diffuser

The curved diffuser geometry was designed to turn the flow radially outward to improve the feed to the silo. The analysis of the curved diffuser configuration focused on mass distribution into the system. Similar to the straight geometry, the curved diffuser discharged flow into the casing cavity with large amounts of axial momentum, which drove a portion of the flow to the turbine side of the silo cavity. Additionally, the flow had enough radial momentum to push some of the flow to the side region of the silo cavity, as shown in Figure 3.2.1-7. However, a region of low velocity flow still existed in the front of the silo cavity as in Figure 3.2.1-8, which shows the normal velocity component at the exit plane.

To improve this velocity distribution, a perforated ring was modeled in the flow field around the transition duct at the same location as was in the straight diffuser configuration. As shown in Figure 3.2.1-9, this perforated ring was designed to aggressively redistribute mass to the low mass regions. This was accomplished by allowing more open area in the low mass region and reducing the open area in the high mass region (turbine side of silo). The perforated ring improved the distribution along the sides of the siloas well as the uniformity of the flow at the exit plane.

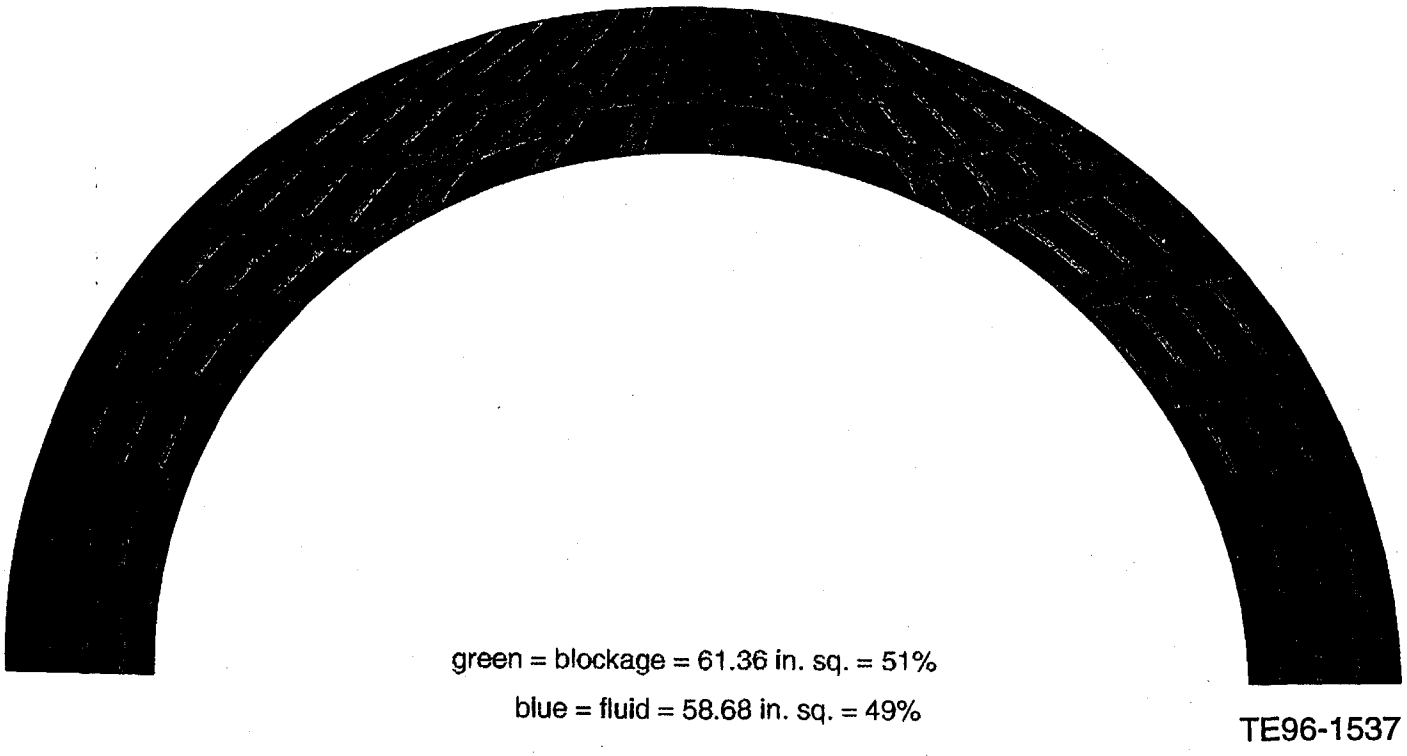

Figure 3.2.1-5. Exterior flow of ATS transition piece: straight diffuser with perforated plate.

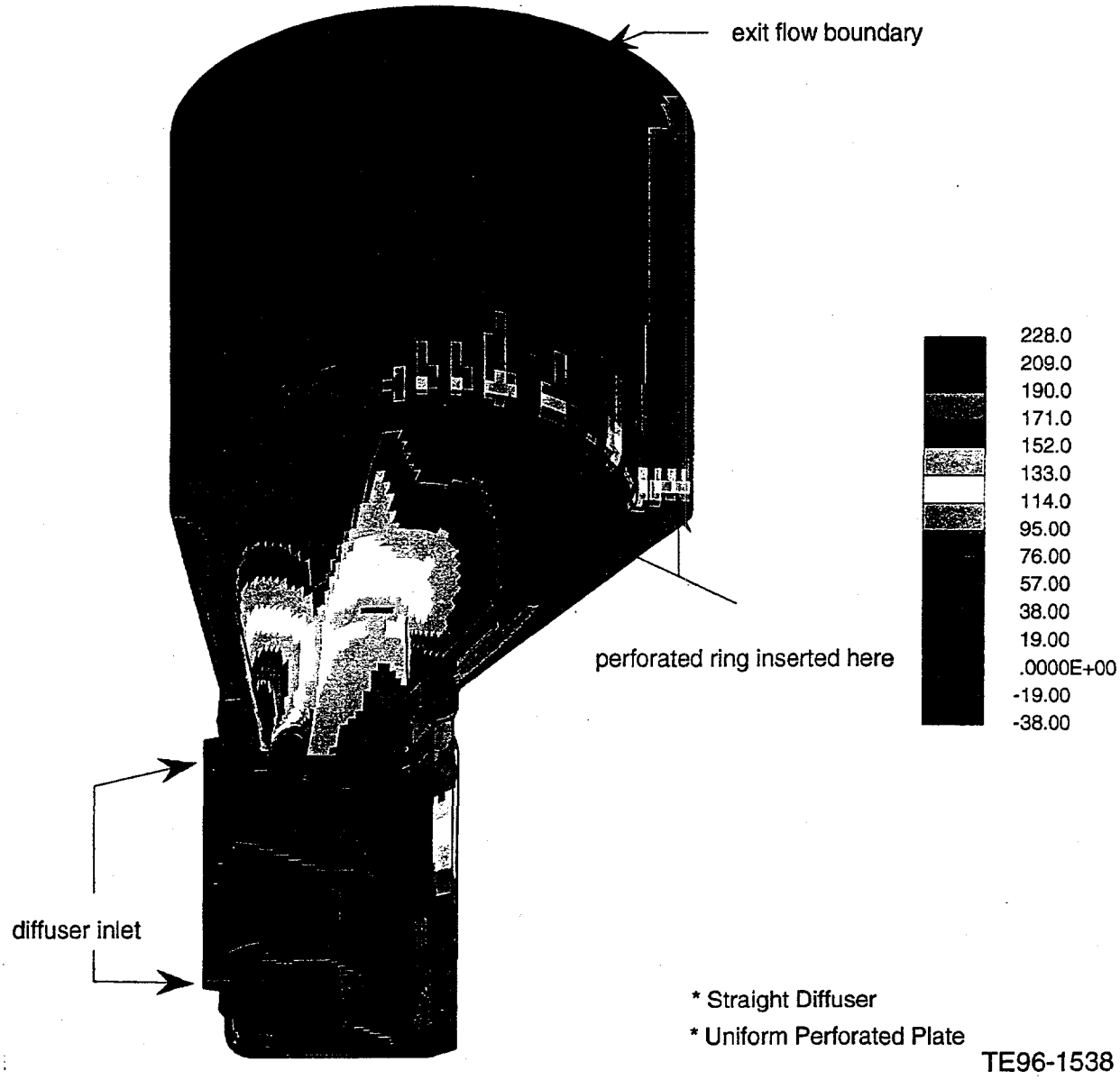

Figure 3.2.1-6. Flow into casing cavity and around silo combustor.

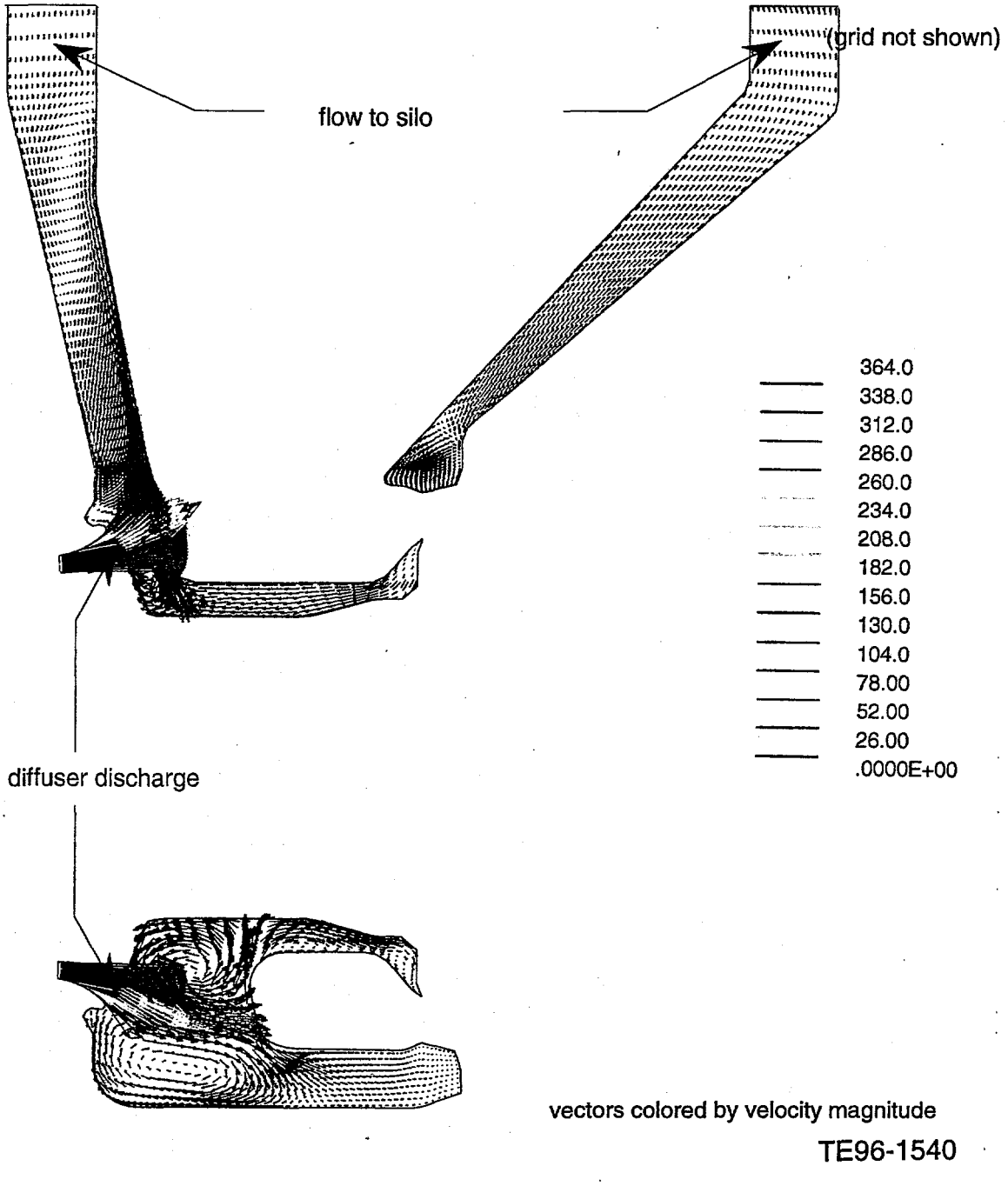

Figure 3.2.1-7. Curved diffuser geometry: velocity vector plot at symmetry plane.

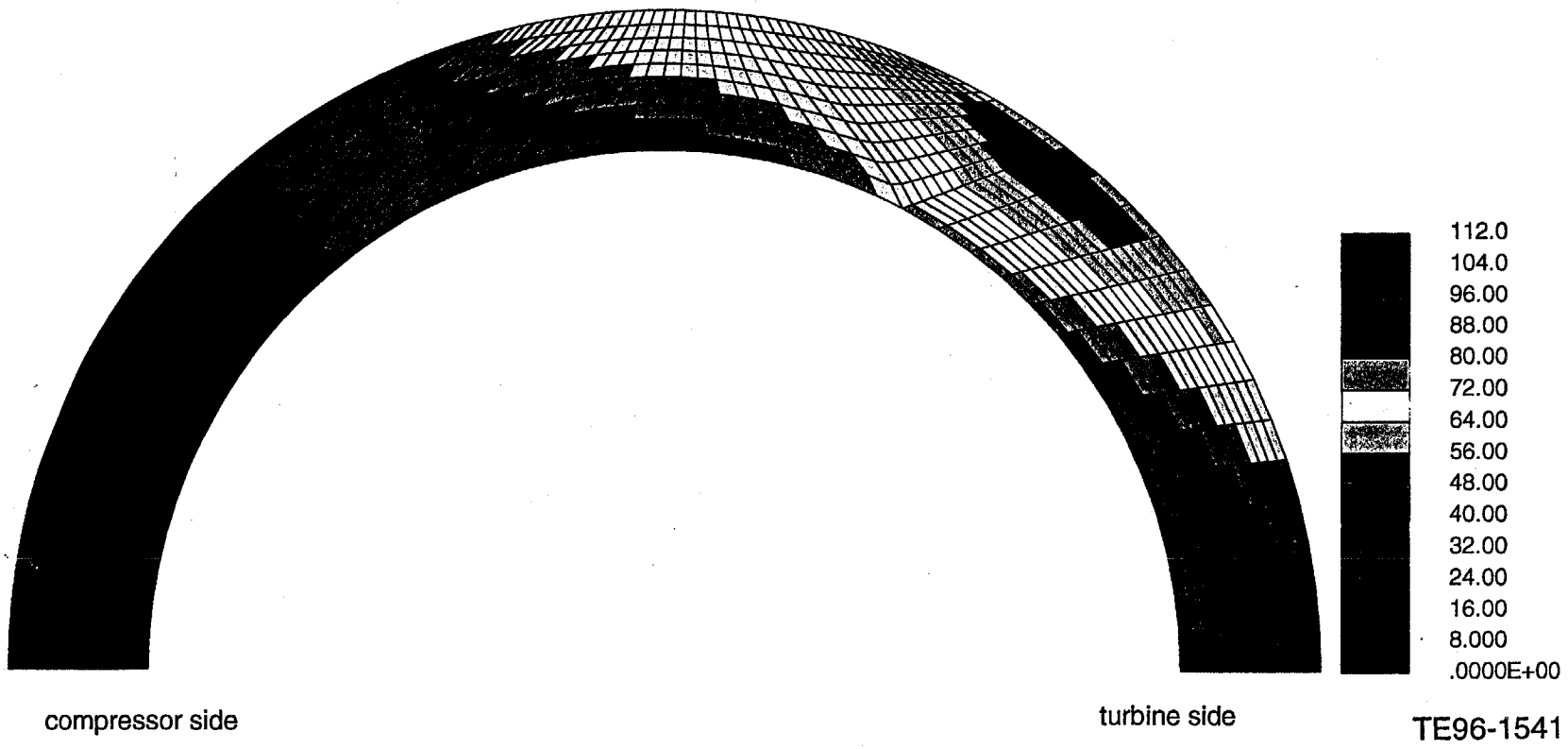

Figure 3.2.1-8. Curved diffuser geometry: exit boundary velocity plot.

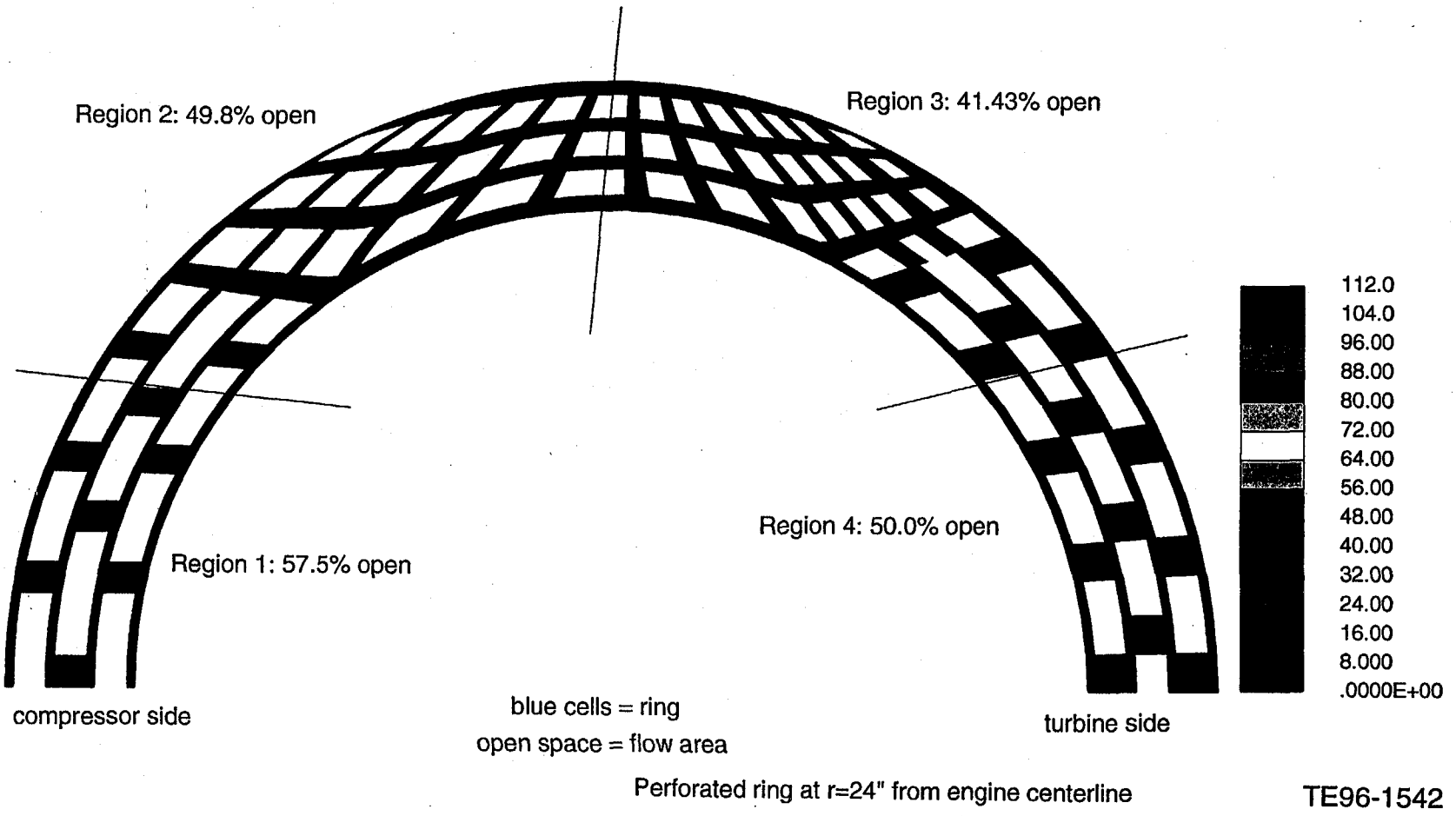

Figure 3.2.1-9. Nonuniform perforated plate in curved diffuser geometry.

Results

ATS Bifurcated Transition Duct

Although the system pressure drop calculated in the analysis for the bifurcated transition duct was low, other performance characteristics were less than satisfactory. The relatively large radial temperature gradients and the large swirl angle range of the flow into the turbine were undesirable flow features of this design. However, the highly nonuniform mass flow distribution at the transition exit plane was the single largest factor in deciding to develop another transition duct design that would deliver improved performance, especially improved flow distribution. A scroll configuration combustor-to-turbine transition duct in place of the bifurcated transition duct will be designed and analyzed in Phase 3A of the program. Due to the unsatisfactory performance results of the bifurcated transition duct and the need for significant transition duct configuration changes, the detailed heat transfer analysis was not conducted at this time.

ATS Diffuser/Transition Duct External Flow-Path Analysis

Upon reviewing the results of both the straight and curved diffuser computational models, it appears the curved diffuser is a slightly better design from a flow distribution standpoint. Additionally, both diffusers required the aid of a perforated ring to help distribute the flow around the transition duct in the silo cavity. The nonuniform design modeled in the curved diffuser configuration distributed the flow better than did the uniform design in the straight diffuser configuration; however, a slight pressure loss penalty was paid (0.07 increase for straight diffuser, 0.12 increase for curved diffuser).

3.2.2 Combustion Section - Scale Model Rig Test

Objective

Subtask 6.01 analyzed the flow characteristics from the exit plane of the HP compressor through the combustion system to the inlet plane of the HP turbine. This flow path is a very complex shape, particularly from the diffuser exit around the transition duct to the combustor inlet, and through the transition duct to the inlet to the turbine. The objective of this subtask is to verify the predicted flow field by conducting a half size scale model test and comparing the test results to the predicted values.

Discussion

Introduction

The ATS engine proposed by Allison incorporates a single silo-type combustor oriented at 90 deg to the engine centerline as shown in Figure 3.2.2-1. A half size fully instrumented model of this system from the inlet plane of the diffuser, through a simulated combustor and transition duct (Figure 3.2.2-2), to the inlet plane of the high pressure (HP) turbine, was built and tested at Allison. Two diffuser configurations, a straight and a curved version, were built and tested as a part of this program.

The model incorporated total pressure (P_t) and static pressure (P_s) instrumentation along the flow path and a full 360-deg rotating turbine inlet plane survey mechanism. The survey mechanism housed two 3-hole prism probes capable of radially traversing across the flow path. This exit instrumentation provides adequate information to determine exit Mach number and flow angle. The assembled test hardware is shown in Figure 3.2.2-3, and the instrumentation locations are shown schematically in Figure 3.2.2-4.

Facility

The airflow test of the ATS combustion system was conducted in the Allison Aerodynamic Research Facility. This is a state-of-the-art multipurpose facility used for full and scaled model testing of engine inlets, exhaust nozzles, and combustion liners. The facility consists of a continuous in-draft vacuum leg system capable of flowing air at the rate of 2 lbm/sec. Mass flow through the test article is measured with vortex shedding flow meters that have been qualified by a secondary standard to within 1.5% accuracy. The facility includes a fully integrated PC controlled system providing rapid set point control and data acquisition with on-line analysis displaying key variables, system losses, and surface pressure plots in real time. The primary data acquisition system consisted of an IBM 466DX/T computer recording and converting signal voltages relayed by a HP 3497A data acquisition control unit and a HP3456A digital voltmeter. This primary system acquired all pressures, temperatures, and flow rates needed to evaluate the test article's aerodynamic performance.

Instrumentation

The test rig was heavily instrumented at the turbine inlet plane (see Figure 3.2.2-2) to furnish sufficient information on the swirl angle circumferential variation of the air entering the turbine

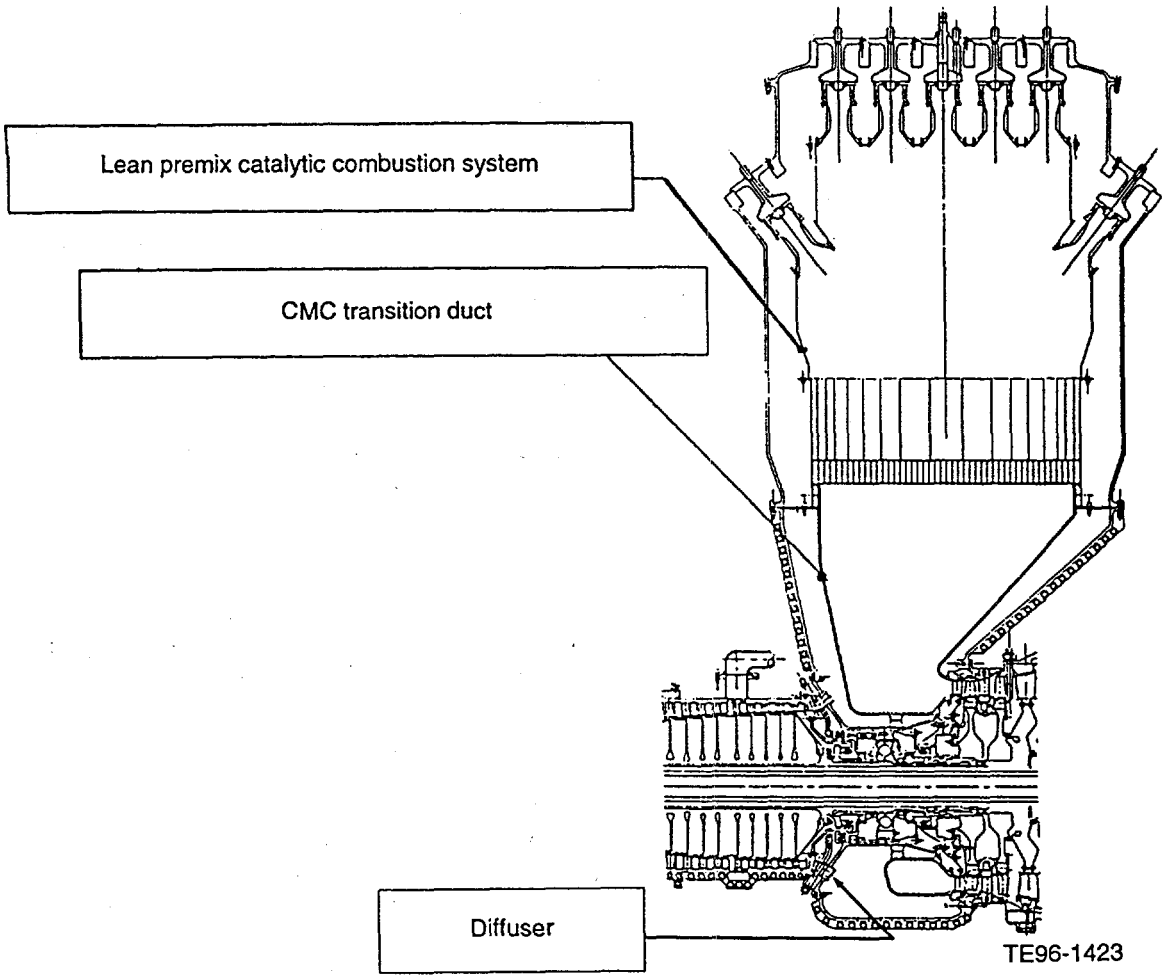

Figure 3.2.2-1. ATS engine combustion system.

to make a valid comparison to the predicted swirl angle variation determined under Subtask 6.01.

Three circumferentially placed pairs of two and three element equal area total pressure rakes were installed at the diffuser inlet along with three each hub and tip static pressure taps to characterize the rig inlet conditions. Due to the relatively small inlet passage height the inlet P_t profile was obtained by using a two and a three element rake to span the passage height. The two and three element rakes were located 20-deg apart with the static pressure tap between each pair.

To measure the diffuser exit parameters, three circumferentially placed three element total pressure rakes and three each hub and tip static pressure taps were installed in the exit planes of each of the two test diffusers. The information from these P_t rakes and P_s taps provides the data necessary to calculate the mass averaged total pressure at the exit of the diffuser. Subsequently, the diffuser total pressure loss can be determined by comparing the diffuser inlet and exit pressures. The installation of the diffuser exit total pressure rakes is shown in Figure 3.2.2-5.

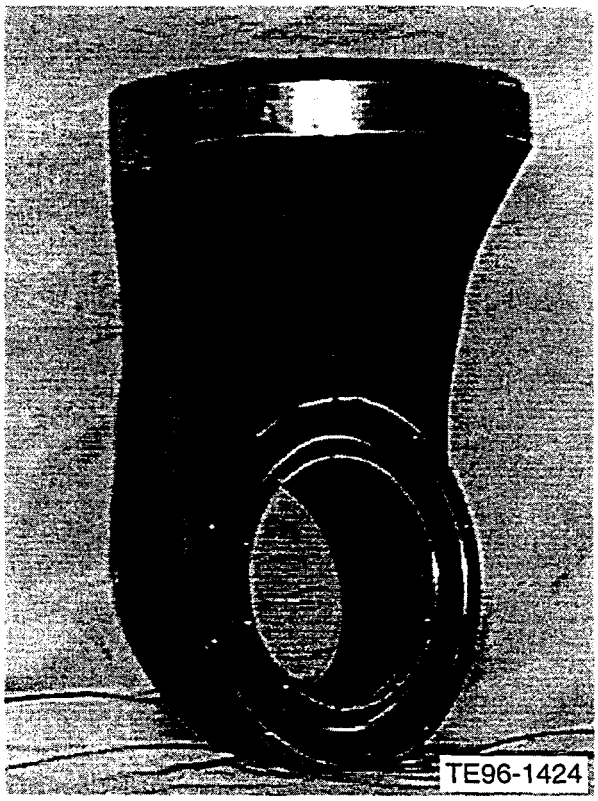

Figure 3.2.2-2. A half size fully instrumented model from the inlet plane of the diffuser, through a simulated combustor and transition duct.

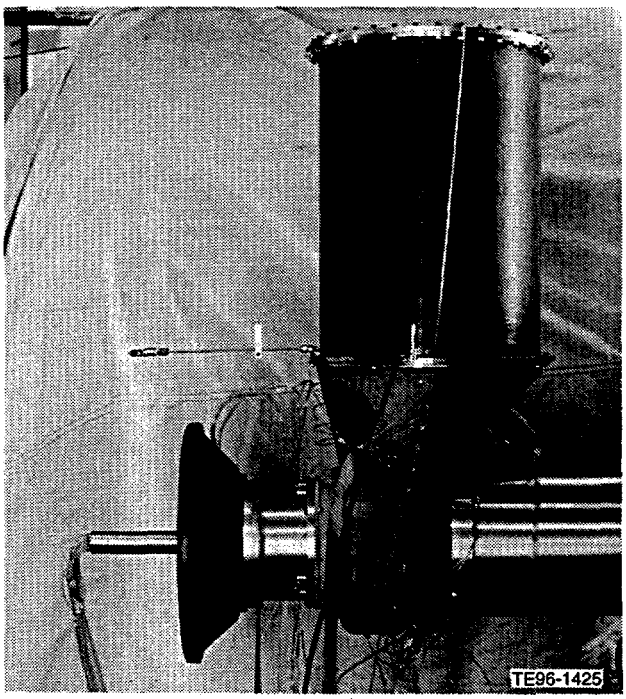

Figure 3.2.2-3. Assembled test hardware.

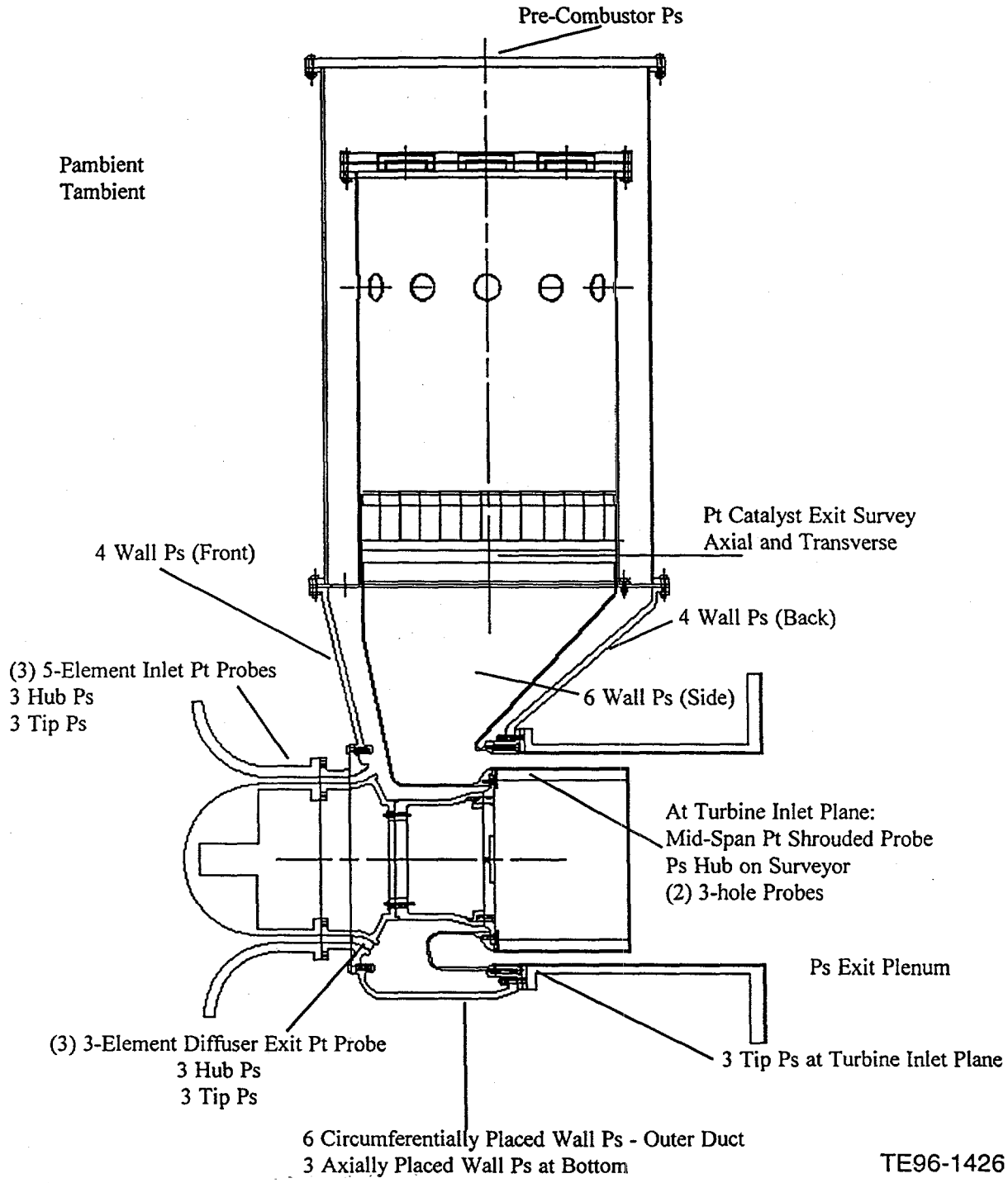

Figure 3.2.2-4. Instrumentation locations.

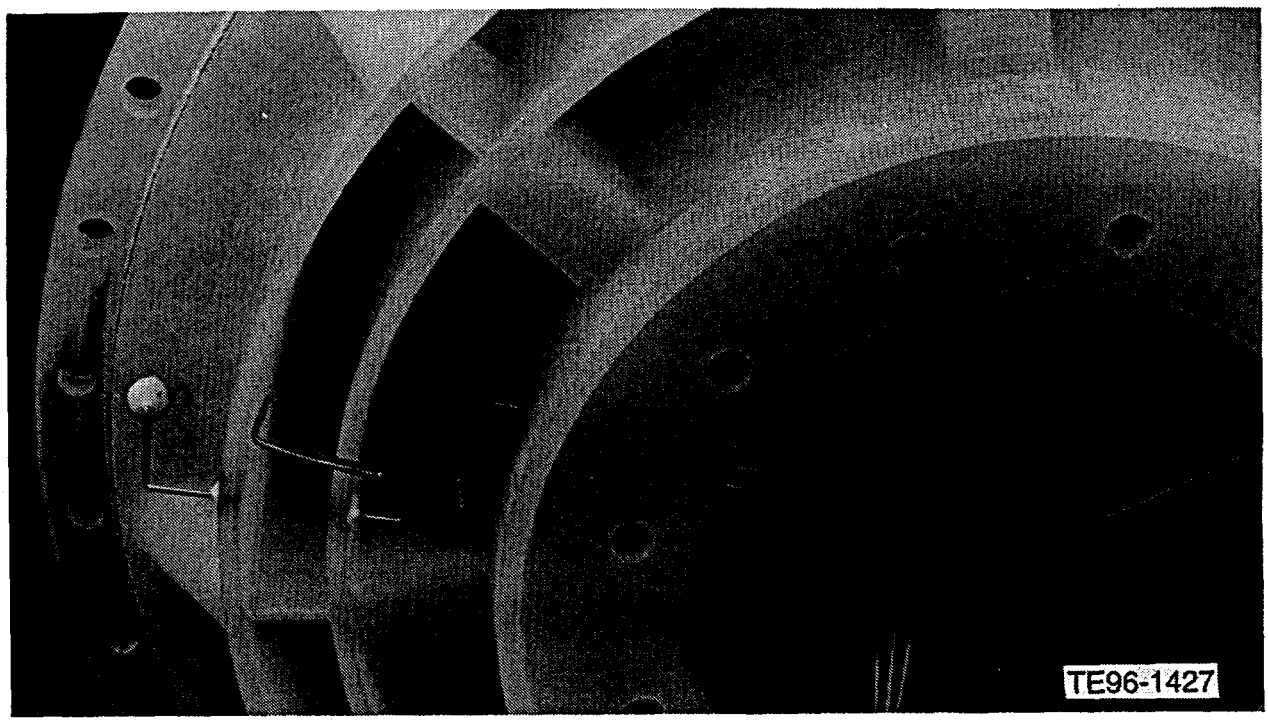

Figure 3.2.2-5. Diffuser exit instrumentation.

Static pressure taps were also installed along the front, back, and both side walls of the outer combustor casing. This information was used to determine the pressure distribution of the air feeding the combustion liner.

Provisions were also made for a manual total pressure survey at the exit plane of the simulated catalyst. This survey consisted of measuring the pressure at 1 in. intervals across the diameter of the flow path. This information was used to determine the uniformity of the flow field entering the transition duct. This survey was conducted along two axes: one parallel to the engine centerline and one at 90 deg to the engine centerline.

At the rig exit, which corresponds to the turbine inlet plane, a 360-deg circumferential survey was performed. The inner flow path housed a mechanism that performed a circumferential and radial survey using two 3-hole probes located 180-deg apart. This mechanism is shown in Figure 3.2.2-6. Due to the predicted ±36-deg flow angle at the turbine inlet plane, one 3-hole probe was oriented at +18 deg and the second probe was oriented at -18 deg. Each 3-hole probe was then calibrated to ±18 deg and, therefore, would cover the entire predicted range of flow angles. The calibration information was then entered into the data reduction program for determination of the correct total pressure and flow angle. Located 90 deg from the two 3-hole probes was a shrouded total pressure probe that was radially fixed at midspan. Located 45 deg from the total pressure probes was a wall static pressure tap. This hub static pressure measurement was used in conjunction with the three outer wall static pressure measurements to provide mass averaged values at the plane of the turbine inlet.

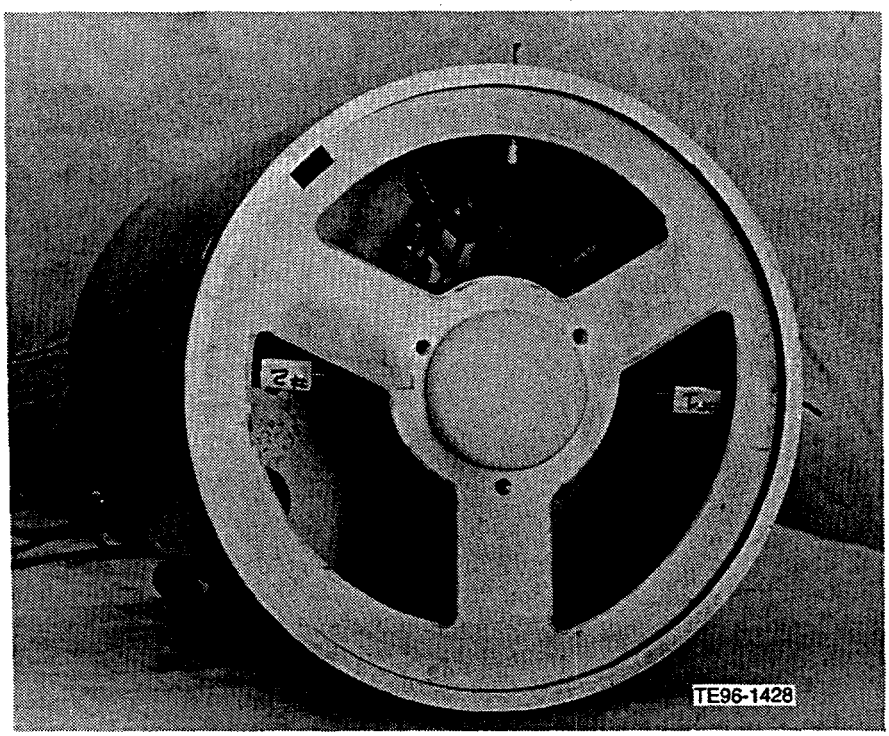

Figure 3.2.2-6. Exit survey mechanism.

Rig Parameters

As previously stated, and shown in Figure 3.2.2-2, the rig used for this flow simulation represents the engine flow path through the diffuser and combustion system to the HP turbine entry plane. Two configurations of dump diffusers were tested. The air exiting the diffuser entered a cavity that directed the air up through a perforated plate into the annulus between the combustor and the outer combustion case (Figure 3.2.2-7). The air was then turned 180 deg prior to entering the combustor through seven swirlers simulating the pressure drop of the lean premix modules.

Inside the combustion chamber was a catalyst supplied by Catalytica. The catalyst consisted of a winding of corrugated metal wound around a core insert and an outer stainless steel casing as shown in Figure 3.2.2-8. This assembly was installed in the combustor and supported on metal rods welded to the inside of the combustor. A flow evaluation was performed across the catalyst to determine its pressure drop characteristics.

Inlet Conditions

The inlet to the diffuser consisted of a simple circular arc inlet bell and bullnose contracting section followed by a 5-in. constant area section that held the flow path screen/trip. This inlet configuration generated a flat diffuser inlet total pressure profile.

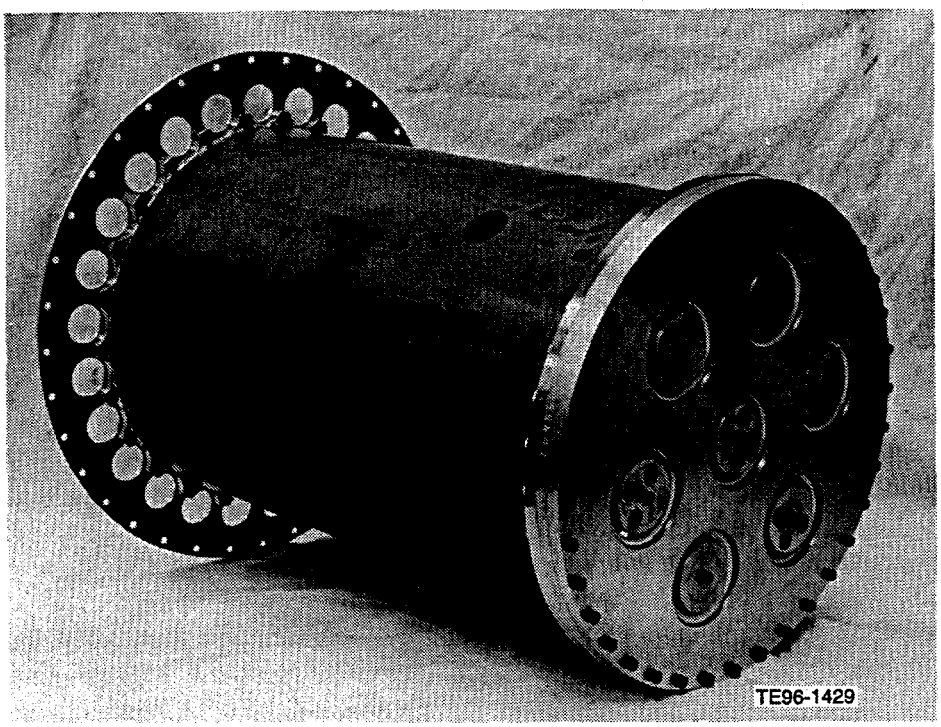

Figure 3.2.2-7. Combustion section configuration.

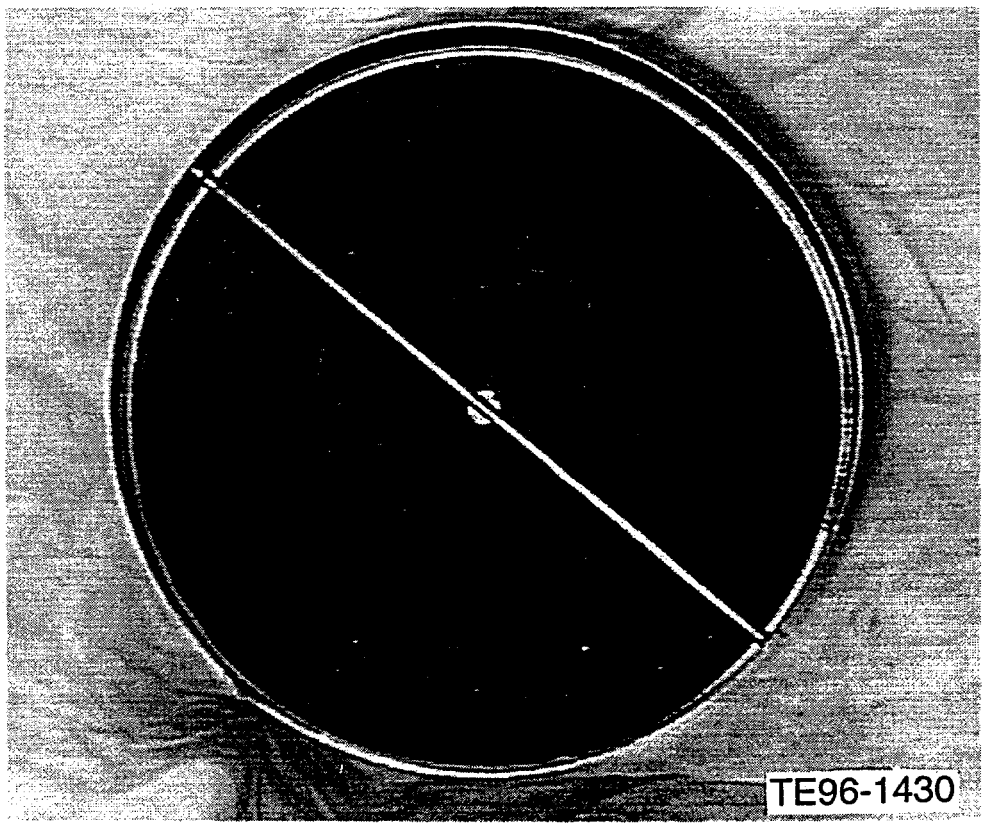

Total Pressure Loss

During this investigation the primary parameter used to evaluate prediffuser performance was the system total pressure loss. The pressure drop curves are as predicted, showing increasing loss with increased flow. Note that, when setting the flow condition to a Mach similar condition at the turbine inlet, the Mach number at the diffuser inlet will be higher in the scaled rig than in the actual engine. Therefore, the pressure losses are significantly higher than will exist in the engine.

To determine the actual rig pressure drop, the individual pressure losses of the various portions of the system must be taken into account. First, the loss from the diffuser inlet to the diffuser exit plane is determined from the compressor exit Mach number, or diffuser inlet Mach number. The flow losses from the diffuser exit along the outside of the combustor and into the combustion chamber itself are then taken into account. These are also based on the compressor exit Mach number. Since there is no measurement plane upstream of the catalyst, a loss value from the diffuser exit plane to a point downstream of the catalyst is obtained. The pressure drop across the catalyst, which was previously measured, is then subtracted. This gives the loss from the diffuser inlet to the entrance to the catalyst. Modeling the losses for the remainder of the system based on the turbine inlet Mach number, a value for the drop across the catalyst is added to the loss figure. Finally, adding the loss from downstream of the catalyst to the turbine inlet plane gives the overall system pressure loss. This correction was also performed for the off-design high and low flow points. The results of this correction show that the curved diffuser actually is higher in loss at design conditions than the straight diffuser when corrected for Mach number ranges for each component.

Diffuser Performance

During this investigation three three-element total pressure rakes were used to record the profile at the exit plane of the diffuser. Also, hub and tip static pressure taps were located 10 deg from the P_t rakes at the diffuser exit.

Another measure of diffuser performance is the static pressure recovery factor C_p. C_p is an indicator of the diffuser's ability to diffuse the airflow.

Turbine Inlet Parameters

Extensive measurements were obtained at the turbine inlet plane as discussed in the instrumentation section of this report. The two circumferentially and radially traversing 3-hole probes, the circumferentially traversing hub P_s and P_t shrouded probe, and the tip P_s taps provided detailed information on the flow field at this measurement plane. This information was used to calculate and plot the flow angle, Mach number, and mass flow distribution circumferentially around the turbine inlet plane. The plots showing this information include the analytical results from the work discussed in section 3.1 of this report. Due to the plenum formed in the combustion chamber of the rig and the presence of the catalyst, the flow field differences between the straight and curved diffusers were eliminated prior to entering the transition duct. Therefore, the following plots will present the straight diffuser data for the three radial survey points of 32%, 52%, and 71% span.

The measured value and the analytical model curves were normalized using their respective maximum P_s pressures. This plot demonstrates excellent correlation between measured and analytical results. The characteristics of the pressure profile along with the pressure levels are in good agreement. The high static pressure at the 180-deg position, where the split flow fields come back together, indicates a reduced velocity at the bottom center of the turbine inlet flow field. The flow at 0 deg shows a 2.5% lower static pressure, which indicates a higher velocity flow field at the top of the turbine inlet plane. This was also predicted by the analytical model. The lower static pressure on the hub at 0 deg also corresponds with the tip static pressure reading at this flow point. The 0-deg tip static pressure correspondingly shows that the velocity is higher than that at 120 deg and at 240 deg by 1%.

In the data reduction for the following plots, the calibrated range of measurement for the two 3-hole probes had to be considered. The turbine inlet flow angle, Mach number, and mass flow were dependent on accurate readings for the total pressure and the left and right side ports for both probes. To determine when acceptable data for each 3-hole probe was obtained, a plot of the corrected total pressure was compared to the shrouded total pressure probe data. A corrected total pressure was determined from the data collected during the calibration of the 3-hole probe. Due to incidence angle effects on the center port of the 3-hole probe, as the flow angle increased, there was a loss in the total pressure of the center point. This value was corrected during data acquisition to give a corrected total pressure based on the flow angle of both 3-hole probes. Comparison of the two corrected total pressure curves at midspan versus the data from the shrouded total pressure probe, which is more insensitive to incidence angle, revealed which of the 3-hole probe readings to use at each circumferential position.

After determining the valid region for each 3-hole probe, a plot of the turbine inlet flow angle for the midspan location could be made. Excellent correlation is obtained along the top half of the unit from 270 deg up to 0 deg and around to 80 deg. The measured values and the model show a shift in the correlation along the lower half of the rig primarily where the two flow fields interact at 180 deg. The shift of the measured data reveals that the actual flow field is not perfectly symmetric. This is driven by the geometry of the hardware. Although the average flow angle at the turbine inlet plane is near 0 deg, the variation in flow angle is very severe.

Calculation of the turbine inlet Mach number was performed with the point wise total pressure and a linearly interpolated static pressure from the circumferentially measured hub static pressure and the average tip static pressure.

Finally, the point wise normalized mass flow rate was calculated at the turbine inlet plane. The correlation of normalized mass flow is good along the upper half of the flow field, with the characteristic curve of the analytical model following the measured data. The portion of the flow field between 120 deg and 240 deg is the region where the measured flow field differs from the model. This is a region of three-dimensional highly turbulent flow where the split flow fields merge together.

Correlation is excellent between the measured and predicted angles, both in the characteristic curve shape and the flow magnitude. The characteristic near the 180-deg location at 32% span shows the increase and decrease in flow angle. The amplitude of these excursions is more pronounced in the rig than was predicted. Again, this is due to the three-dimensional highly turbulent flow field where the split flow field merges together.

The Mach numbers at the 32% span locations more closely match the predicted values than at the 71% span locations. The large circumferential variation in Mach number is more prevalent close to the hub wall. When traversing outward from the inner wall, the circumferential Mach number variation tends to become less than predicted for the 32%, 52%, and 71% span plots.

As in the Mach number plots, the measured mass flow at the 32% span location matches the predicted value quite well. Scatter occurring near the 180 deg, as shown in many of the plots, is the result of the highly active flow field where the split flow comes together. This results in an area of low mass flow and low Mach number as was predicted. The 71% location plot shows that measured flow values follow the predicted curves in the upper half of the flow field but tend to flatten in the lower portion of the flow field. This occurs at a slightly higher level than predicted.

Results

Two major conclusions can be drawn from the work done under this subtask. The first conclusion is that the results of the scale model flow test agree very well with the predictions discussed in section 3.2.1 of this report. The circumferential and radial variations in turbine inlet swirl angle and mass flow distribution were in such good agreement that a high degree of confidence now exists in the computer modeling tools that were used for the complicated flow field that was analyzed.

The second conclusion resulting from this work is that the initial concept for the shape of the transition duct produces unsatisfactory exit flow characteristics. Both the analysis and the test results indicate that a significantly more uniform flow distribution and much less swirl angle variation will be required for the engine. The further development of the transition duct shape will take place under Phase 3A of the ATS program. This work will rely heavily on the relatively low cost analytical approach, at least initially, because of the good correlation demonstrated under this subtask. The configuration that Allison plans to evaluate initially in Phase 3A is a scroll type transition duct. This concept has been used successfully on several small engines that have been developed by Allison for future automotive applications.

3.2.3 Study of Carcass Deflection from Silo Combustor

Objective

The silo-type combustor may have the potential for causing nonuniform axial thermal growth of the outer combustion case between its front and rear splitlines, effectively bowing the engine carcass. If this should occur, the resulting radial misalignment of the overhung high pressure (HP) turbine rotor relative to the turbine case introduces the potential for additional rub with an associated reduction in engine efficiency. This subtask was created to study the possibility of nonuniform axial thermal growth of the outer combustion case.

Discussion

Maintaining minimum clearances between rotating and stationary flow-path parts throughout the operating envelope is critical for maximizing gas turbine engine efficiency. If excessive distortion exists due to the nonuniform axial growth of the outer combustor, additional HP turbine flow-path seal rub (blade tip and vane segment inner diameter) toward one side could occur since it is overhung as opposed to straddle mounted. The additional rub would result in increased overall diametral clearance, which thereby reduces engine efficiency. The temperature data generated in subtask 3.2.1 were to be used to predict the thermal growth of the outer combustion case used with the silo combustor. If excessive distortion was found, potential geometry changes to minimize distortion were to be identified and evaluated.

Results

Due to the timing of the completion of subtask 3.2.1, subtask priorities, and resource limitations, the analysis to be performed in this subtask was not completed. The thermal growth characteristics of the outer combustion case will be determined as part of the Phase 3A design activity associated with the combustion system of the engine.

3.2.4 Reduced Turbine Cooling Flow Trade Studies

Objective

To achieve the ATS design goal for engine thermal efficiency, additional cooling air economies need to be made. With conservative estimates of seal clearance, a model of the preliminary design configuration shows an excess consumption of cooling air. A trade study is needed to focus on the most productive areas for added conservation of air. Cooling air reduction will be evaluated by identifying reduction schemes for specific areas, assessing the maximum feasible reduction, and estimating the effect on manufacturing cost, risk, and complexity.

Discussion

The chargeable cooling air requirement for the ATS engine was 10.70% of the total 59.3 lb/sec mass flow as described in the Final Technical Report, EDR 17144. However, further investigation of the Secondary Flow Report, TDR AX-0003-039, shows that the total chargeable cooling air used for the cycle was 13.59% or 2.89% more than that used in the performance cycle. The primary effort for this subtask is to identify where cooling air can feasibly be reduced by 2.89% of engine mass flow. Table 3.2.4-I shows the chargeable flow for the ATS cycle as defined by secondary flow. Note that the nonchargeable flow has not been included since this will not affect the engine performance using current performance analysis methods.

Table 3.2.4-I.
Original secondary flow cooling flow budget.

Chargeable flow	Compressor discharge (%)	9th stage compressor (%)
1V inlet		0.51
1V-1B	1.62	0.36
1B	4.28	0.08
1B-2V	0.92	0.28
2V	2.30	0
2V-2B	1.06	0.31
2B	0.73	0.12
2B-3V	0.26	0.12
3V-3B	0	0.22
3B-4V	0	0.09
4V-4B	0	0.18
4B-exit	0	0.09
Overboard leakage	0.13	
Subtotal	11.30	2.29
	Total	13.59

The primary effort for this task was spent investigating the clearances used to establish the secondary flow cooling budget and determining how they could then be reduced. Table 3.2.4-II shows the areas identified for reduced clearances.

Table 3.2.4-II shows that a reduction of 2.63% chargeable cooling flow would be possible by using slightly more aggressive seal clearances. This would effectively offset the 2.89% delta between the performance analysis and the secondary flow numbers, thereby obtaining the desired performance.

Labyrinth Seals

Flow management in the turbine will involve many types of seals, but one of the most critical is the use of labyrinth seals to channel the desired flow to the appropriate cavity. One of the reliable and cost-effective methods to date has been a labyrinth seal design using a rotating knife along with a stationary honeycomb seal. In addition, this approach permits excellent rub tolerance to compensate for transient operation while permitting an effective seal. However, compared to other design approaches such as brush seals, the leakage rate is relatively high. Because of the cost and low experience level, brush seals will not be employed extensively in the turbine; consequently, the question is whether the seal clearance reductions noted in Table 3.2.4-II are feasible. The desired operation of a labyrinth seal is to have it run effectively line to line or just touching the honeycomb surface to cut a minor seal track. Experience has shown

Table 3.2.4-II.
Potential reductions in secondary flow.

Description	Baseline		Reduction		Delta
	% flow	Clearance/gaps	% flow	Clearance	% reduction
Nonchargeable	0.56	0.0024	0.0	N/A	0.56
1st vane inlet					
HPT chargeable (CDT)					
Stg 1, preswirler outer lab	1.59	0.010	0.79	0.005	0.80
1st blade platform lkge	0.41	0.0005	0.21	0	0.20
Stg 2 preswirler outer lab	0.92	0.010	0.46	0.005	0.46
2nd blade platform lkge	0.20	0.0005	0.10	0	0.10
2nd wheel aft lab	0.48	0.007	0.34	0.005	0.14
LPT chargeable (stg 9, comp)					
1-2 labyrinth seal	0.34	0.015	0.11	0.005	0.23
2-3 labyrinth seal	0.27	0.015	0.09	0.005	0.18
3-4 labyrinth seal	0.21	0.015	0.07	0.005	0.14
Case cooling	0.38	N/A	0	N/A	0.38
			Total chargeable		2.63

that this can be done, but it involves a number of test runs to set the continuous running clearance while still minimizing the amount of seal interference during transients.

The clearance at the first-stage blade preswirl outer labyrinth seal was reduced from 0.010 in. radial clearance to 0.005 in. This reduction accounts for 0.80% and should be achievable with testing. Similar changes were also made at the second-stage preswirl and aft wheel cavities. In the low pressure turbine (LPT), a reduction was made from 0.015 to 0.005 in. These numbers should also be achievable with testing to optimize the cold build settings. Although none of the reductions are large by themselves, the sum of each individual seal accomplishes a sizable reduction.

Platform Clearances

Another area of leakage in the turbine that results in wasted cooling air is platform leakage across the first- and second-stage blades. This leakage results from end gaps that exist between the individual blade platforms. The typical bladed wheel will require that the blade platforms be assembled as tightly as possible so that during hot running operation the lowest possible leakage will be present. This leakage results from wheel growth at hot running conditions, which causes gaps to open up between blade platforms. Table 3.2.4-II shows that running end gaps of 0.0005 in. were used to calculate the original leakage flows. A reduction of 0.3% between the first and second blade is possible if the gap is set to be 0. The installation of seal strips at the platform ends will significantly reduce leakage and permit the blades to be assembled cold while sealing off leakage flow during hot operation. In spite of the seal strips, achieving zero leakage will be extremely difficult in practice. However, due to the small amount of leakage flow originally accounted for (i.e., 0.3%), it could be possible to reduce this number during engine testing.

Results

The cooling flow budget used in the ATS performance calculations was 10.70%, while the secondary flow budget was 13.59%, as shown in Table 3.2.4-I. This resulted in a cooling deficit of 2.89%. Review of the secondary flow input data showed that the leakage flow could be reduced by 2.63% using tighter clearances, which are judged to be feasible. This would offset the 2.89% deficit, but would not further increase the performance as outlined in the proposal for ATS. The stated reduction in cooling flow was accomplished by reducing the running clearance of honeycomb labyrinth type seals along with some reduction in the blade platform leakage. The honeycomb labyrinth seals will likely remain the seal of choice due to their low cost, reliability, and rub tolerance. Selection of other sealing methods such as brush seals is possible, but the experience base is lower, which increases the long-term risk. Therefore, the recommendation will be to reduce leakage flow using the clearances as defined in Table 3.2.4-II along with standard honeycomb labyrinth seals.

3.2.5 Ceramic Blade Track Design

Objective

The objective of this subtask is to evaluate the use of a one-piece, continuous ceramic blade track for use on the first and second stages of the HP turbine. The effort was initiated to reduce the cooling air requirements (up to by 1.3%) needed for metallic blade tracks, thereby increasing the overall thermal efficiency of the engine.

Additional benefits from using a continuous ceramic blade track for this application include minimization of the leak paths present in the turbine gas path by reducing turbine blade running clearances, reducing hardware requirements by implementing a continuous ring instead of a segmented ring, and increasing blade track life at operating temperatures by using a more durable material than metal. Evaluation of the continuous ceramic blade track concept was a step-wise process, initiating as an HP layout drawing and finishing with stress analysis using finite element modeling and stress analysis software.

Discussion

A continuous ceramic blade track for the HP turbine was proposed in an effort to reduce the cooling flow needed for a typical metallic blade track. Four geometry variations (two attachment schemes and two blade track ring designs) were examined to quantify thermal and mounting imposed stresses to the blade track rings.

The differences between the blade track designs were in the mounting of the blade tracks (radially located pins or tabbed retaining ring) and the blade track ring geometry (a solid ring or one with 16 evenly spaced rectangular pockets on the outer diameter). The two different mounting schemes and two ring designs were explored in an effort to reduce the stresses experienced by the ceramic material. On both mounting schemes, brush seals were employed to provide radial location of the ceramic blade track by means of a "soft mount" design, which minimizes point stresses applied to the blade track (see Figure 3.2.5-1).

The ceramic material properties used in the analysis were based on a silicon carbide fiber reinforced alumina (SiC_f/Al_2O_3) made by DuPont Lanxide Composites, Inc. For the life requirement of 16,000 hr, DuPont Lanxide representatives recommended maximum temperature and tensile stress levels as 2200°F and 5 ksi, respectively.

Steady-state maximum power condition thermal stress analyses were completed for all four blade track variations. Thermal analysis was based on the ATS cycle (W_{eng} = 59.123 lbm/sec) with inlet cooling flow temperatures of 1017°F. The gas path conditions used at the blade track are given in Table 3.2.5-I.

The thermal stress analyses generated isotherm maps of the ceramic ring's cross section. With the baseline cooling flow as a percentage of engine flow as in Figure 3.2.5-2, the maximum temperature values were 2500°F for both the pocketed and solid ring designs. Additional cooling flow was added (1.3%) until maximum material temperatures were reduced to 2200°F (see Figures 3.2.5-3 through 3.2.5-6).

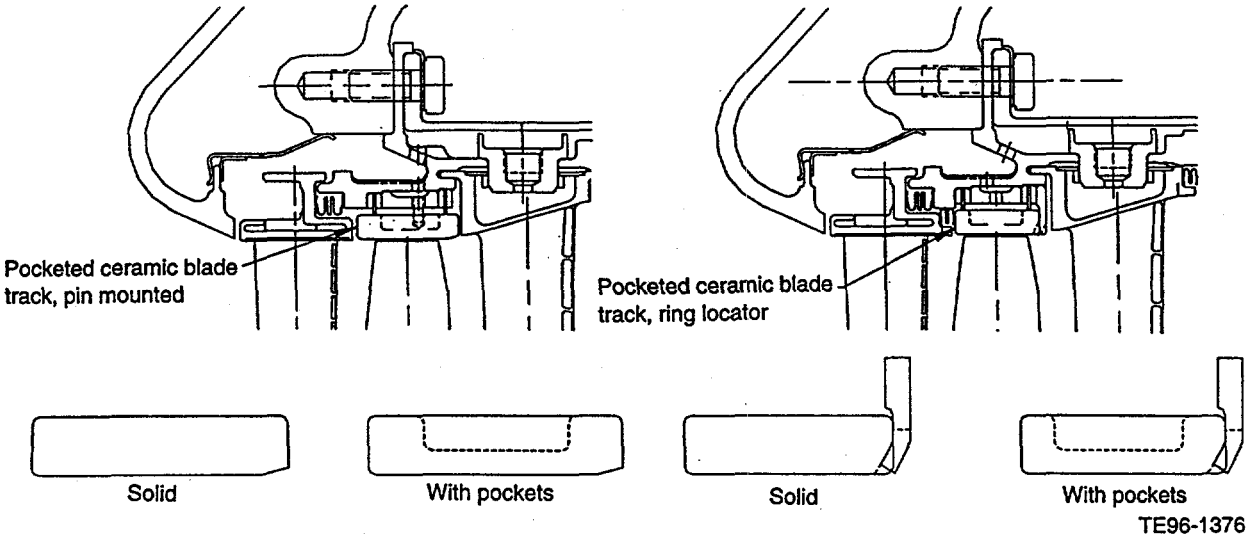

Figure 3.2.5-1. Engine cross section showing ceramic blade track designs.

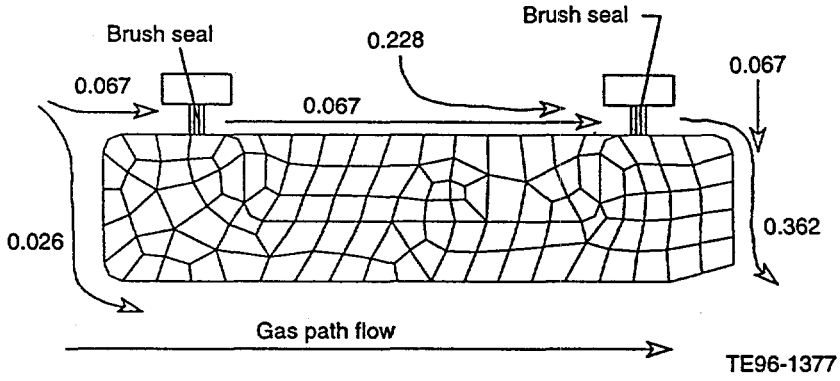

Figure 3.2.5-2. Ceramic blade track cooling flow based on W_{eng} = 59.123 lbm/sec engine flow.

Table 3.2.5-I.
HP rotor tip inlet and exit conditions for ATS cycle.

	Inlet	Exit
Tt (°F)	2564	2231
Pt (psi)	368.5	195.2
Ps (psi)	291.4	188.9

These analyses considered only internal thermal stresses and did not consider any stresses imposed by the mounting arrangements. As was predicted, maximum tensile stress occurred in the tangential (hoop) direction on the continuous blade track. Both the solid and pocketed models of the continuous ceramic blade track generated 40 ksi maximum tensile stress levels, which are eight times the acceptable level (Table 3.2.5-II).

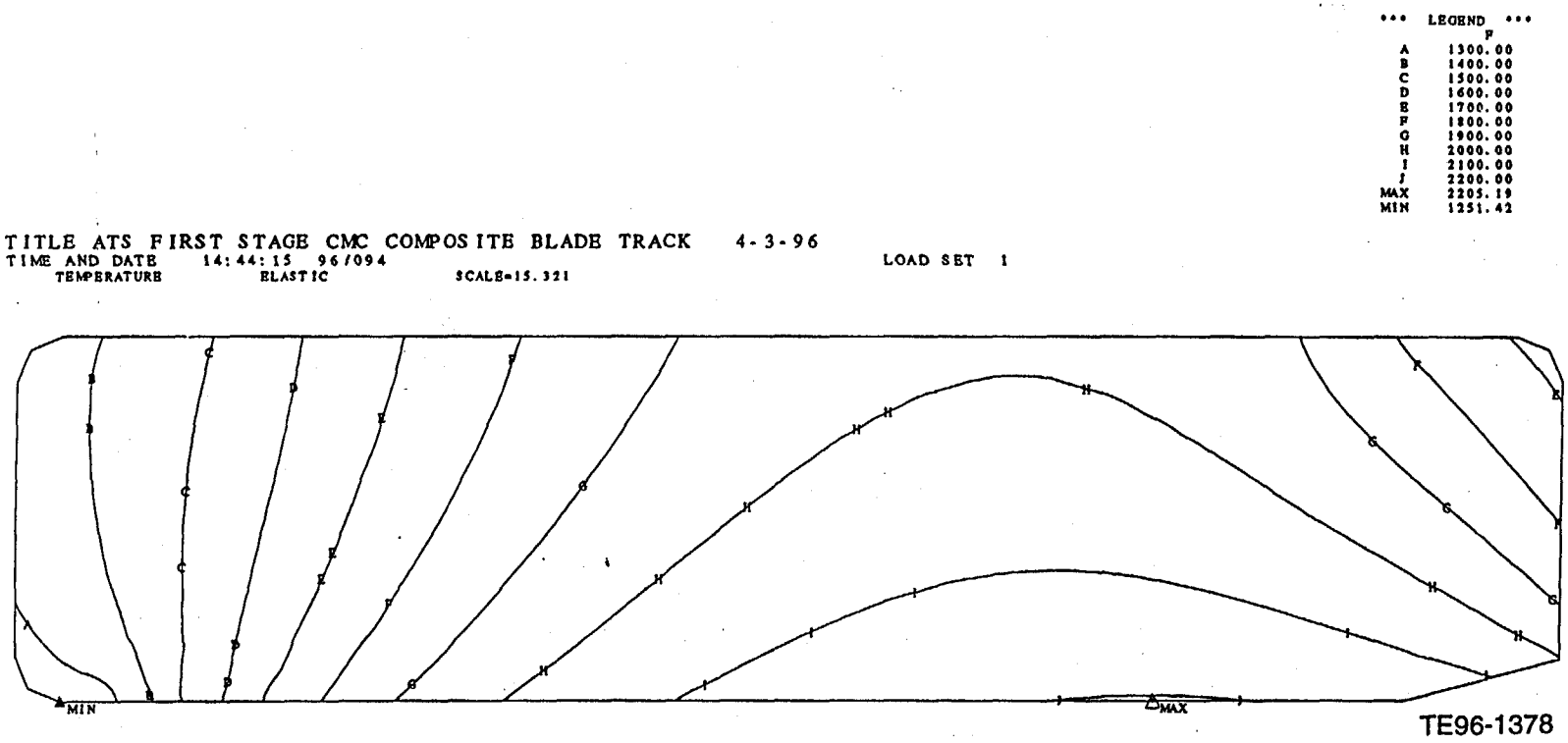

Figure 3.2.5-3. Thermal analysis results, solid ceramic blade track.

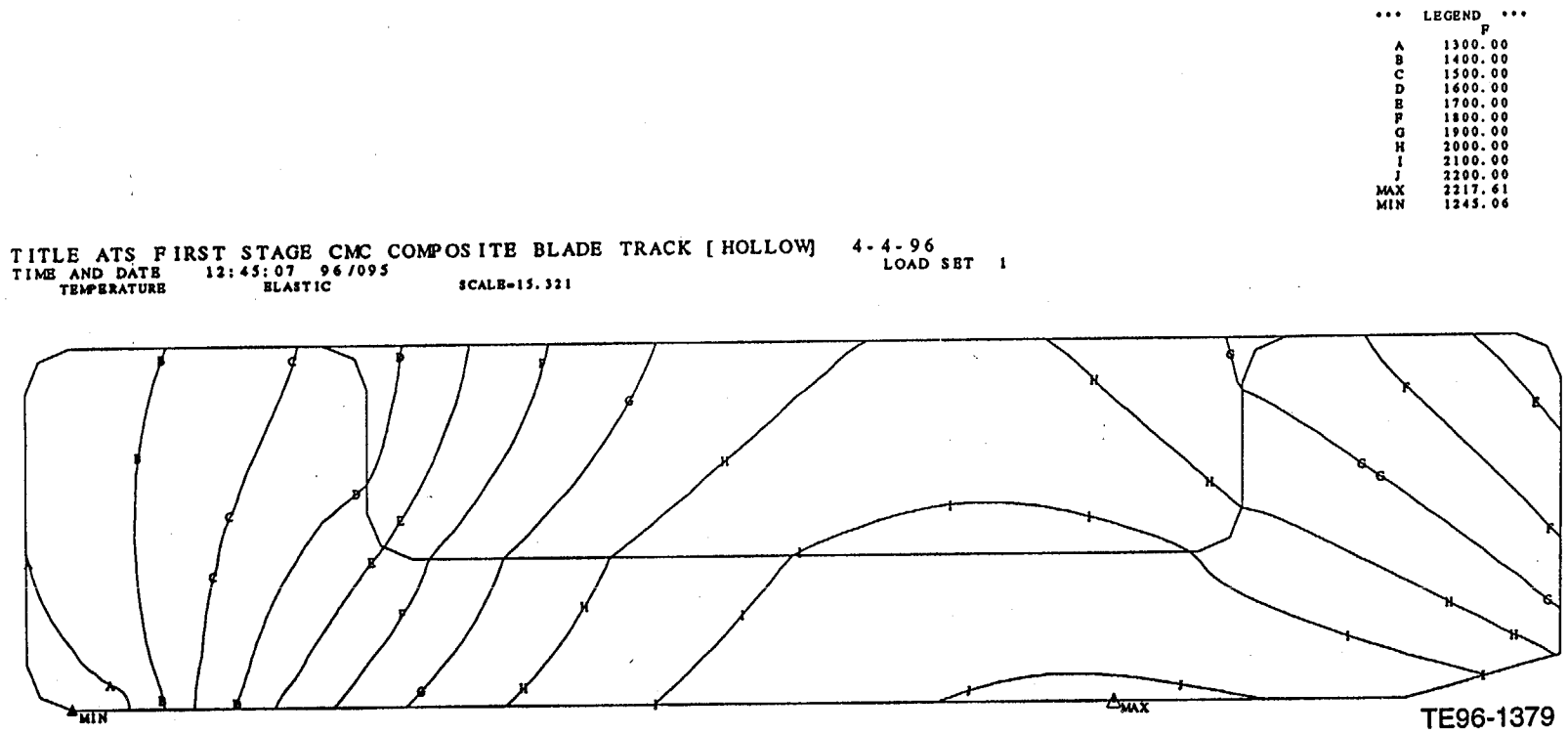

Figure 3.2.5-4. Thermal analysis results, pocketed ceramic blade track.

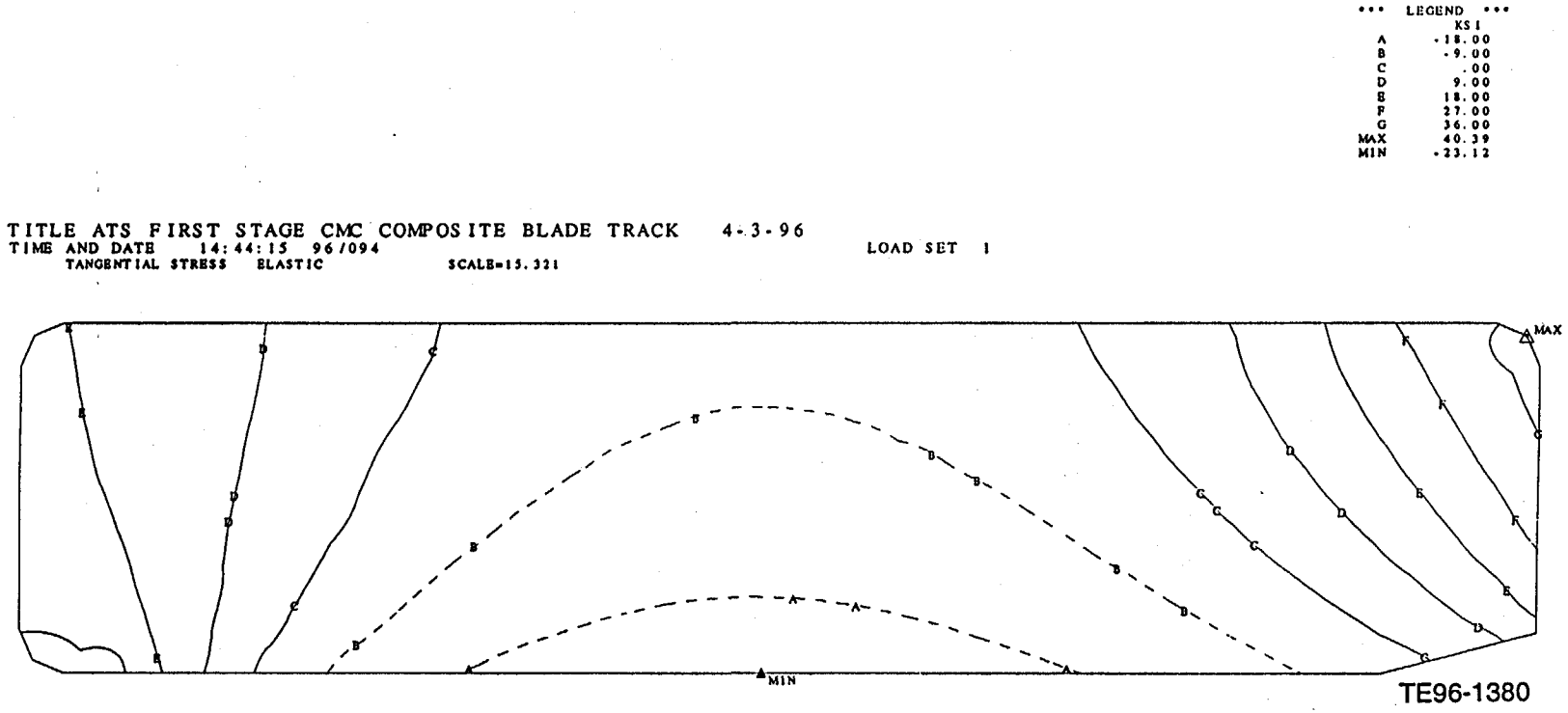

Figure 3.2.5-5. Stress analysis results, solid ceramic blade track.

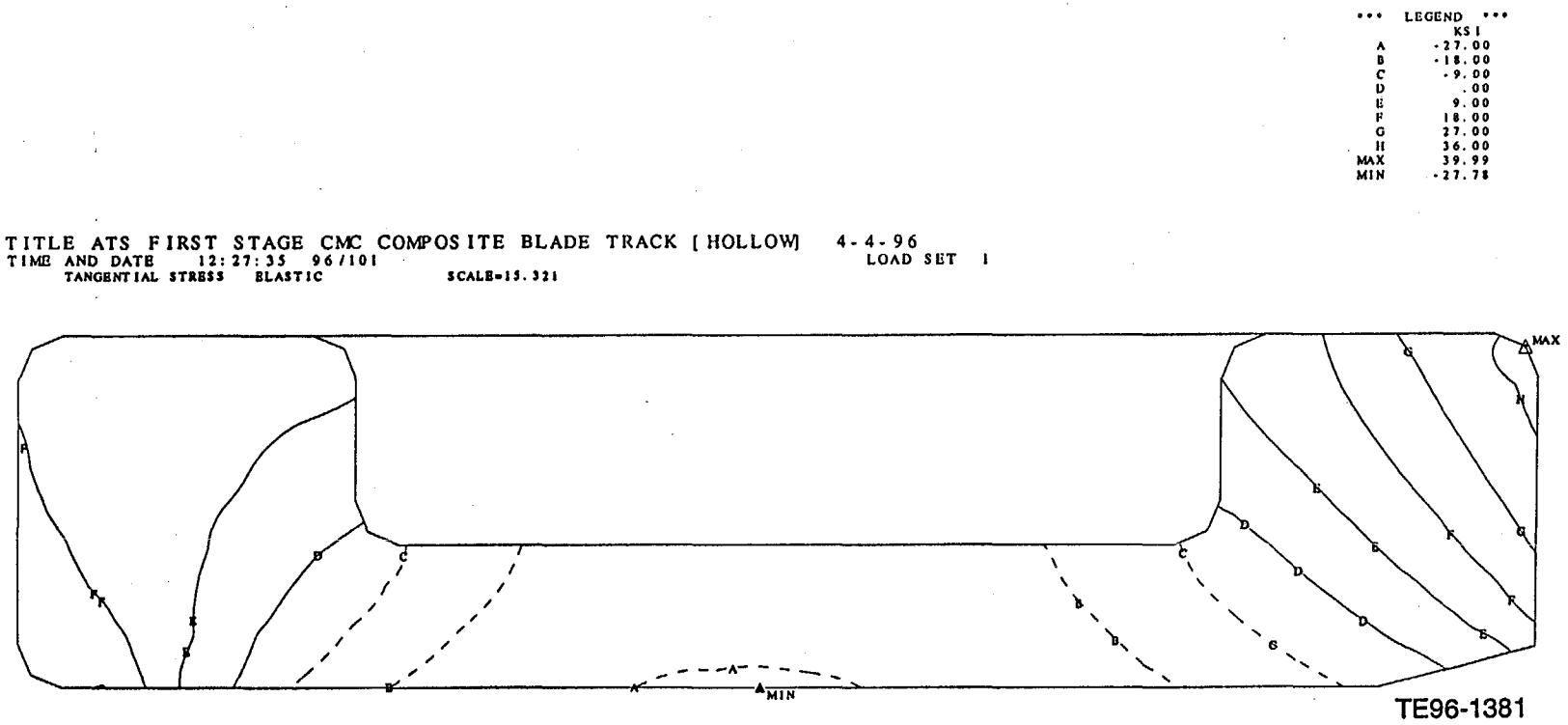

Figure 3.2.5-6. Stress analysis results, pocketed ceramic blade track.

Table 3.2.5-II.
Ceramic blade track max tensile stress

Configuration	Max tensile stress* (ksi)	Comments
Continuous solid ring	40.49	Tangential stress
Continuous pocketed ring	39.99	Tangential stress
Segmented solid ring	1.82	Radial stress
Segmented pocketed ring	2.24	Axial stress

*The solid and pocketed versions of the ceramic blade tracks experienced virtually the same stress levels for both the continuous and segmented versions, indicating that there is little advantage to adding the pocketing as stress relief features.

The addition of the 16 stress relief pockets to the continuous blade track model did not significantly reduce the maximum calculated tensile stress level. However, sectioning the continuous blade track into six equal segments reduced the stress levels dramatically. The maximum tensile stress dropped to 2.24 ksi, which is well under the maximum allowable for 16,000 hr of life.

It is clear that a continuous ceramic blade track is not feasible given the operating conditions of the ATS engine. Stress levels created solely from the thermal transients in the engine flow path would cause premature failure of this design within a short time of operation. However, segmenting the blade track to eliminate the highest stress (hoop) appears to have promise for this application.

Currently, all effort has ceased on the continuous ceramic blade track design, though a segmented ceramic design is being considered for use in the ATS engine. Development of mounting and intersegment sealing technologies will be needed prior to incorporation of ceramic blade tracks in the ATS engine design.

Results

Thermal and stress analysis was conducted on the two proposed continuous ceramic blade track designs that used two attachment schemes. Steady-state, maximum power operating condition was used to complete the analysis on all four design variations. The results indicate that maximum tensile (hoop) stresses generated from internal thermal gradients in the continuous blade tracks are eight times higher (40 ksi) than the maximum tensile stress acceptable for 16,000 hr of life (2 to 5 ksi).

Segmenting the continuous ceramic blade track into six sections virtually eliminated the hoop stress, reducing the maximum tensile stress experienced by the individual ceramic blade track segments to the 2 to 5 ksi range. Further work on a design incorporating a continuous ceramic blade track was abandoned, and efforts are now under way to develop a segmented ceramic blade track design.

3.2.6 Inlet Housing Loss Optimization

Objective

Minimizing inlet housing aerodynamic flow-path pressure losses is one contributing factor in providing the best possible cycle efficiency. This subtask was created to define the optimum aerodynamic flow path for the ATS inlet housing, which consists of the inner and outer flow-path surfaces and the support struts.

Discussion

The ATS engine incorporates a radial inlet housing. A radial inlet housing is better suited than an axial inlet housing for cold end (front) drive industrial engines such as the ATS since the output drive shaft length can be shortened. The original plan for this subtask was to develop methodology and an analytical model to define the optimum aerodynamic flow path for the radial inlet. However, the timing of the execution of this subtask ended up coinciding with a derivative engine program of another Allison industrial engine, for which a similar radial inlet was needed in a shorter timeframe. Thus, the methodology for defining a low loss radial inlet housing was developed for the other Allison industrial engine. This subtask directly benefited since the same methodology was directly applicable to the ATS radial inlet.

As a result of the significant reduction in workscope for this subtask, it was redirected, with the agreement of the COR, to aim at optimizing the inlet plenum flow path upstream of the inlet housing. The goal was to reduce engine performance losses by reducing inlet distortion. Sophisticated analytical flow analysis was judged to be unfeasible due to concerns about obtaining accurate results at such low Mach numbers, availability of resources for performing such an analysis, and timeliness of the analysis. Scale model testing was identified as being the most attractive analysis method based on expected accuracy of the results. After receiving estimates from the research lab for scale model work, it has become apparent that the effort would not be within the available resources and schedule of this subtask. Also, such a scale model program is not cost effective in light of the relatively small potential performance payoff.

Results

Radial inlet housing flow-path aerodynamic optimization specific to the ATS engine was not performed during the Phase 2 add-on program. The applicable methodology was developed for another concurrent Allison industrial program. As a result of the reduced workscope, inlet plenum flow-path aerodynamic optimization was investigated. Neither scale model testing nor sophisticated analytical modeling were determined to be suitable, due to cost effectiveness in light of the relatively small potential performance payoff, and accuracy of the results, respectively.

As a result of the Phase 3A engine reconfiguration with a free power turbine and hot end drive, a radial inlet housing is no longer planned for Allison's ATS engine.

3.2.7 Study of Mixed Flow LP Compressor

Objective

This study arose out of discussions about technologies that could be incorporated in Allison's ATS program to reduce engine life cycle costs. The LP (low pressure) compressor for the ATS engine is currently planned to be a two-stage axial flow design, as shown in Figure 3.2.7-1. A significant engine cost reduction could potentially be achieved as a result of reduced parts count by using a single stage LP compressor instead. However, efficiently achieving the required pressure ratio of 1.74 in a single stage axial flow design is not feasible. An acceptable single stage solution may be found in a mixed flow design, which combines axial and centrifugal compressor characteristics. This subtask was created to investigate the viability of the mixed flow design approach from both an aerodynamic and cost perspective.

Discussion

An extensive aerodynamic design and analysis effort was performed on the mixed flow single stage LP compressor concept. This is reported in detail here, and includes both the rotor and stator at the design point. Included as well is an assessment of its power modulation capability compared to an all axial design. Following the report sections addressing aerodynamics, the preliminary cost analysis is discussed.

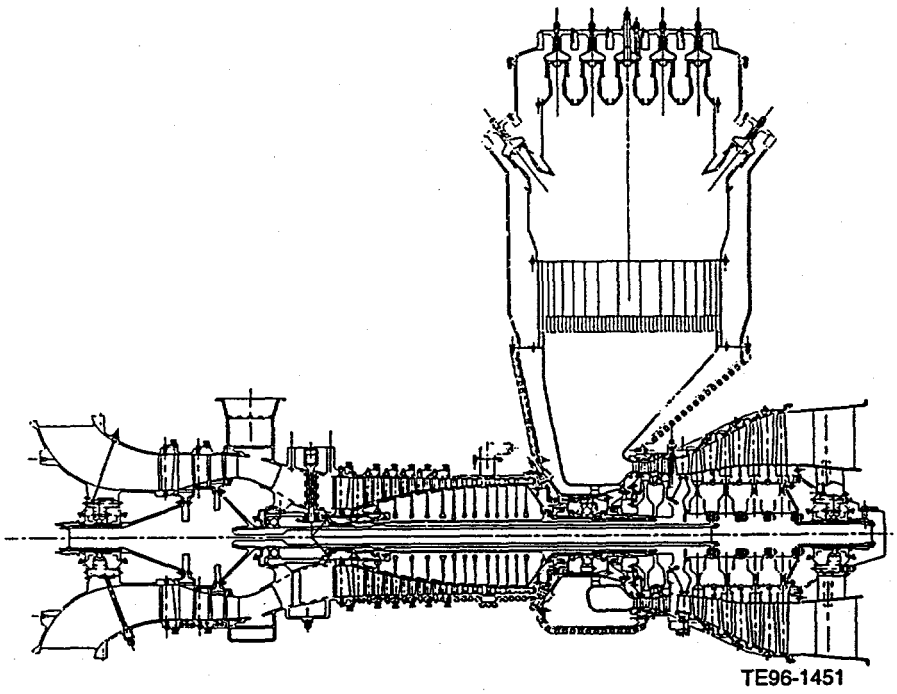

Figure 3.2.7-1. Preliminary cross section of Allison's proposed ATS industrial gas turbine.

Introduction

The technical feasibility of using a mixed flow compressor in this application was evaluated through a series of aerodynamic design iterations. After developing the required techniques, the rotor and stator were aerodynamically designed using a combination of modified axial and centrifugal compressor design tools. The resulting design was analyzed using advanced three-dimensional (3-D) viscous flow techniques for assessment and verification. This process was repeated with the goal of optimizing the mixed flow design and determining how much, if any, design point performance loss was predicted compared to the two-stage axial flow design. Any LP compressor performance loss would result in increased fuel usage and reduced output power. The plan was to weigh these potential negatives against the anticipated positive engine cost savings resulting from the reduced parts count, so that a prediction could be made as to which design would be more cost effective overall from the operator's perspective.

The single-stage mixed flow compressor flow path shown in Figure 3.2.7-2 was designed as a possible replacement for a conventional two-stage axial LP for the ATS engine. The design point for the ATS LP compressor is given in Table 3.2.7-I. The potential life cycle savings are strongly driven by the efficiency level obtained by the mixed flow LP compressor. The results of the following study show that the mixed flow LP compressor should have a comparable performance level to the two-stage axial design, but with a 3-in. length increase.

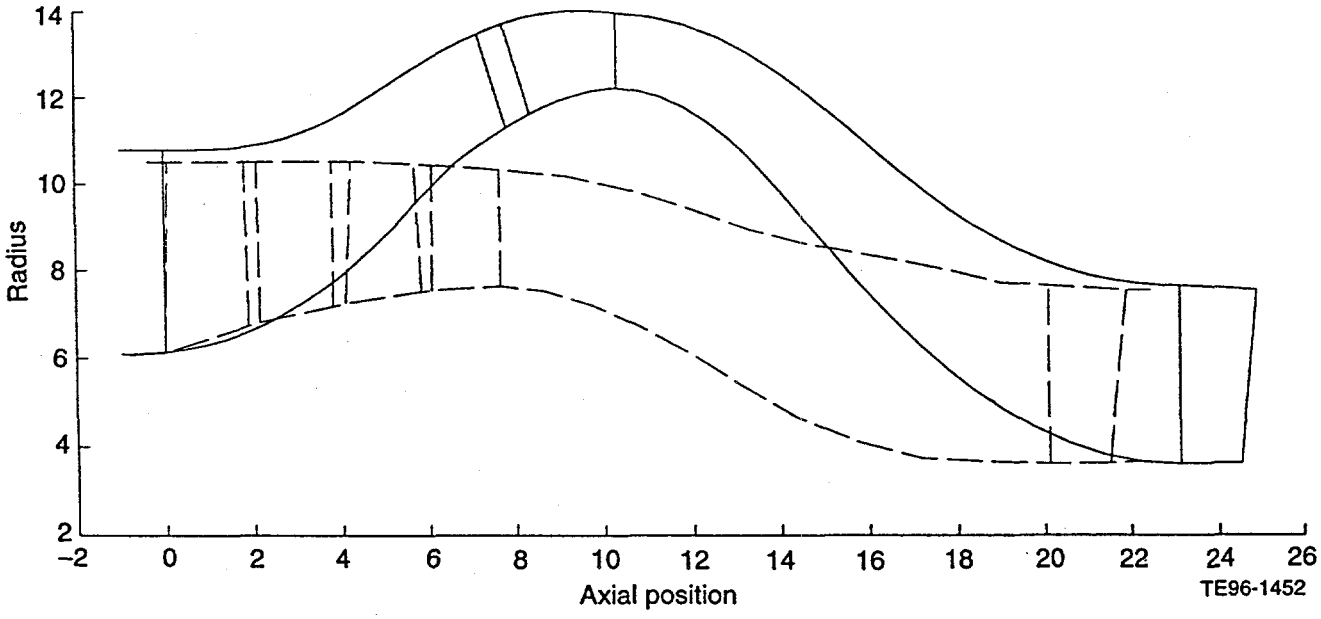

Figure 3.2.7-2. Comparison of mixed flow versus two-stage axial boost compressors for ATS engine: solid line = mixed flow; dashed line = two-stage axial.

Table 3.2.7-I.
ATS LP compressor design goals.

Wac (lbm/sec)	60.0
R_c (T-T)	1.74
η_c (T-T)	89.2
rpm	10,836

Previous Research

A literature search revealed that limited research and testing of mixed flow compressors has been done since the 1950s and that mixed flow machines have not been significantly developed for production in the gas turbine industry. Dussourd gives an extensive bibliography of the mixed flow work done in the 1950s. The efficiency of these early machines was hampered by some of the same issues confronting early centrifugal compressor designers: (1) limited experimental data base, (2) radial blade elements, (3) limited computational/analysis capability, and (4) problems with diffuser design. Computational advancements in the 1970s revolutionized the compressor design process through the development of streamline curvature codes for the inviscid analysis of arbitrary airfoil elements with flow-path curvature. These advancements, along with the use of backswept impellers, propelled centrifugal compressor technology to the point where it is now competitive with axial machines for applications with smaller flow (power) requirements where axial compressor efficiency suffers from high endwall boundary layer and tip clearance losses at small blade heights.

Streamline curvature techniques were used to design several mixed flow compressors starting in the late 1970s. Table 3.2.7-II presents some of the relevant test data for machines with pressure ratios of 3.0 or higher. An important observation is that even though the stage efficiencies are not impressive, the rotor efficiencies are respectable with measured values in the 91 to 92% range. This implies that significant losses are generated in these stators due to operating at the high Mach number (0.8 or above) and high swirl (60 deg or above) associated with the flow exiting these rotors. The stator design problems for these mixed flow compressors are similar to those encountered in centrifugal compressors; it is very difficult to efficiently diffuse the flow exiting a high pressure ratio mixed flow or centrifugal rotor. Both of the 3:1 mixed flow machines in Table 3.2.7-II used tandem stator arrangement that were not very efficient. The 7:1 compressor used a single high diffusion stator that had even worse performance.

Table 3.2.7-II.
Mixed flow compressor experimental data.

Configuration	Wac (lbm/sec)	$(R_c)_{imp}$	$U_{t,cor}$ (ft/sec)	$\eta_{c,imp}$ (T-T)	$\eta_{c,stg}$ (T-T)
Garrett	20.2	3.5	1,800	~92%	~86%
Williams	6.4	3.0	1,400	~91	~84
BMW/Rolls	5.5	7.5	~2,000	~91	~72

Comparison of Mixed Flow and Centrifugal Compressors

As shown in Figure 3.2.7-3, the main distinguishing feature of a mixed flow compressor is that the flow exits the rotor at some angle between axial and radial. Mixed flow rotors are similar to centrifugals because they can achieve high pressure ratios by pushing the air (against the centrifugal force field) to a higher exit radius. This centrifugal component of pressure rise is efficient, in theory, because it is achieved without flow diffusion. In practice, both centrifugal and mixed flow machines diffuse the relative flow to achieve even higher pressure ratios. A common feature of both types of machines is the significant meridional flow-path curvature through the rotor passage. Centrifugal impellers have large curvatures over the entire blade length while mixed flow impellers tend to have less flow-path curvature because of the increased rotor length. The large shroud curvatures in centrifugal impellers are believed to be a major loss generation region and the probable source of the low momentum "wake" flow typically observed. It is possible that mixed flow machines can achieve higher rotor efficiencies than equivalent centrifugal machines because of the reduced (or even reversed) shroud curvatures. This potential efficiency gain may be offset by the increased profile and tip clearance losses associated with the increased length of the mixed flow rotor.

Figure 3.2.7-3 compares a mixed flow and centrifugal compressor stage designed for the same duty. This figure shows that the most significant difference is in the diffusing system with the mixed flow design giving a 37% frontal area reduction over a centrifugal design using a radial vaned diffuser. The mixed flow stage length and weight are higher than the centrifugal stage. Thus for the same duty, the stator diffusion requirements for mixed flow and centrifugal stages are similar even though the design techniques are different. As mentioned earlier, both stator systems will have problems efficiently diffusing the high Mach number, high swirl flow exiting a high pressure ratio mixed flow or centrifugal rotor.

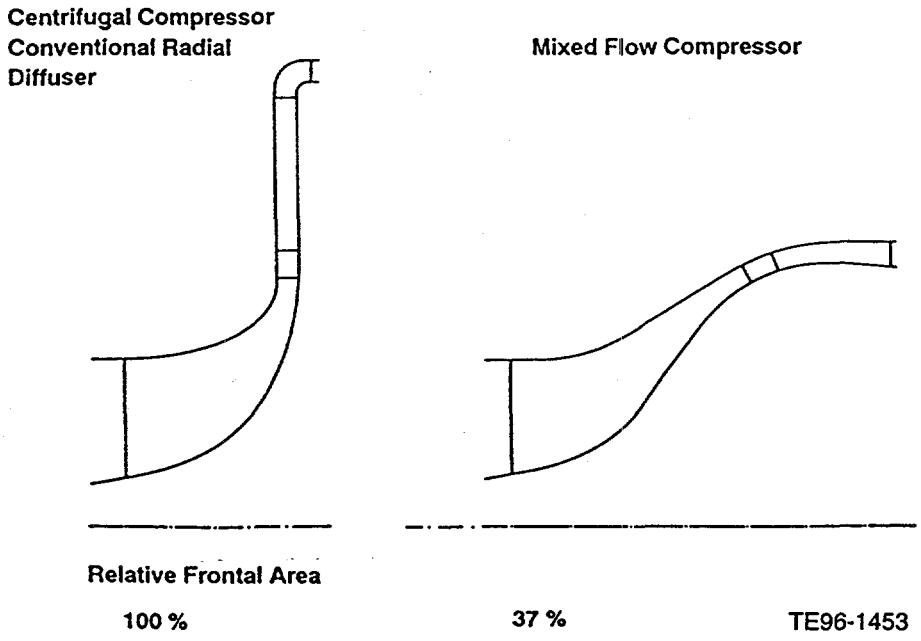

Figure 3.2.7-3. Comparison of centrifugal versus mixed-flow compressor stages for similar duty.

Applications

Mixed flow compressors have historically been considered in applications where minimizing the compressor diameter is of critical importance, such as for turbofan or turbojet powered missiles. Compared to centrifugal designs, the cost of the increased compressor weight and length must not outweigh the benefits of its reduced frontal area. Compared to axial designs, the lower part count and reduced manufacturing costs of a mixed flow stage must outweigh a typically lower compressor efficiency (not lower at low flow rates), slightly higher frontal area, and increased weight. In spite of these potential payoffs, the mixed flow compressor has not been adopted because of the higher risk due to a lack of previous development.

A unique application, which is proposed in this report, is to use a mixed flow compressor as an LP stage for an industrial gas turbine. The reduced manufacturing and maintenance costs of a single-stage mixed flow compressor must outweigh any increase in operating costs due to a potentially lower compressor efficiency compared to a multistage axial design. Multistage axial LP compressors are typically used to supercharge industrial gas turbines to increase power output. Multistage axials are usually chosen over centrifugal and mixed flow types because of superior efficiencies at higher flow rates. This is based on the premise that mixed flow and centrifugal compressors have low efficiencies even at low pressure ratios. It seems possible that a highly efficient mixed flow compressor can be designed to provide the modest 1.74 LP pressure ratio required by the ATS engine cycle (see Table 3.2.7-I). Remember that a significant amount of the loss generated in a high pressure ratio mixed flow or centrifugal compressor stage occurs as the stator diffuses the high Mach number, high swirl flow exiting the rotor. For a low pressure ratio stage, the mixed flow or centrifugal rotor exit flow will have much lower Mach number and swirl levels, which implies a more efficient stator design. It seems feasible that a mixed flow stage can be designed to meet the LP requirements of the ATS engine with efficiency levels comparable to a conventional multistage axial compressor. The additional weight of the mixed flow compressor is not an issue for industrial engine applications.

The mixed flow approach was selected over a centrifugal for this application because it is believed to have an efficiency advantage. The mixed flow stage also has an advantage in the downstream ducting of the air to the HP compressor.

Design Methodology

New methods and procedures were developed for the design of the mixed flow compressor stage. The resulting methods are a combination of axial and centrifugal design tools that were modified as necessary. The initial design effort was hampered by the lack of an experimental data base and appropriate design rules for mixed flow compressors. Advanced 3-D viscous flow codes were used extensively to assess and verify the effects of design changes on compressor performance.

Rotor Design Procedure

The following general procedure was developed to design mixed flow rotors:

1. Set velocity triangles and areas using a mean-line design/analysis program.
2. Design the arbitrary blade mean-line shapes and the hub and shroud flow-path contours using the centrifugal impeller design code (axisymmetric throughflow).

3. Analyze the rotor design using 3-D viscous flow codes.
4. Interrogate the computational fluid dynamics (CFD) results.
5. Redesign the rotor based on 3-D viscous flow analysis

Stator Design Procedure

The following general procedure was developed to design stators for mixed flow compressors that are more closely related to axial type than radial type diffusers:

1. Lay out the stator flow path.
2. Design the stator vane geometry (Note: geometry is specified along conical endwalls since the code used does not have intravane stations).
3. Assess flow-path curvature effects on the axisymmetric flowfield using the streamline curvature code.
4. Redesign the stator flow path and vane geometry.
5. Analyze the stator design using 3-D viscous flow codes.
6. Interrogate the computational fluid dyanmics (CFD) results.
7. Redesign stator based on 3-D viscous flow analysis.

Preliminary Design

This section describes the preliminary design of the mixed flow stage. The goal is to design an efficient single-stage mixed flow compressor to replace a conventional two-stage axial LP for the ATS cycle. A design objective was established to meet the flow, pressure ratio, and efficiency goals stated in Table 3.2.7-I using the specified speed of 10,836 rpm. This approach allows a "back to back" comparison of the two compressor types at the same cycle point. Another design objective was to constrain the mixed flow stage length, including the ducting to the HP compressor, to fit within the current ATS configuration. The goal was to have minimal impact on the current placement of the LP rotor bearings and support structure.

Selection of Inlet Specific Flow

To reduce rotor tip losses, the inlet specific flow (flow per unit area) of the mixed flow rotor was selected to minimize the relative tip Mach number. The inlet hub radius is limited by the LP rotor bearing structure, thus setting the hub radius to the same value used for the first rotor of the two-stage axial. The inlet flow conditions are given in Table 3.2.7-III along with the resulting rotor inlet geometry.

Table 3.2.7-III.
Mixed flow rotor inlet conditions.

Wa (lbm/sec)	59.3
P_{T1} (psia)	14.51
T_{T1} (°R)	518.7
Speed (rpm)	10,836
R_{hub} (in.)	6.123
R_{tip} (in.)	10.778
Spec. flow (lbm/sec/ft^2)	35.0
$M_{R1,tip}$	1.05

Various values of the inlet specific flow were chosen and the corresponding inlet areas and tip radii were calculated assuming uniform inlet flow hub to tip. Using the inlet specific flow to estimate the axial Mach number and the rpm and tip radius to get the tangential Mach number, the resulting relative tip Mach number was calculated. A design specific flow of 35.0 lbm/sec/ft^2 was selected because it minimized the value of $M_{R1,tip}$ to 1.05.

Mean-Line Parametric Study

Method—A parametric study was performed because of the lack of previous experience selecting the mean-line design velocity diagrams for a mixed flow stage. The proper selection of velocity diagrams is very important because they determine the overall rotor and stator diffusion levels. Experience shows that problems arising due to poorly chosen velocity triangles cannot be easily rectified during the detailed design. A mean-line design program was developed to study a wide range of possible conditions that satisfy the overall stage performance. This analysis should allow the selection of parameters that achieve the overall design goals in an optimum manner.

The analysis is simply a solution of Euler's turbine equation along with conservation of mass. The overall design parameters of mass flow (Wa), pressure ratio ($R_{c,stg}$), stage and rotor efficiency ($\eta_{c,stg}$ and $\eta_{c,r}$) and rpm are specified along with other variables related to the rotor exit area. The rotor velocity diagram can be completed once two independent exit flow properties are specified. The flow properties of meridional velocity (V_{m2}) and relative flow angle (β_2) were chosen as the two parameters because of their relation to the rotor exit height (h_2) and backsweep (related by deviation angle), respectively. These parameters were varied over the following range:

400 ft/sec < (V_{m2}) < 600 ft/sec
45 deg < β_2 < 60 deg

There are other valid independent parameters, for example the exit blade speed, but the actual choice does not affect the generality of the results. For this study, flow properties instead of rotor geometry were purposely chosen as independent parameters because the rotor geometry is only valid for a given rpm. The parametric results presented as follows in terms of flow properties are valid even if a different rpm is selected.

This analysis is also used to estimate the stator blade loading by specifying the stage exit velocity diagrams. Once the stage exit Mach number and flow angle are specified, then the mean-line stator diffusion factor can be estimated. This was very useful for trade studies on the effects of rotor geometry on the stator loading. The parametric study was performed using the assumptions given in Table 3.2.7-IV for the mean-line rotor and stator design parameters.

Results—The results of the analysis are presented in Figures 3.2.7-4 through 3.2.7-11. The results of each independent parameter variation, namely β_2 (related to backsweep) and V_{m2} (related to exit blade height), are discussed separately.

Table 3.2.7-IV.
Preliminary design goals for parametric study.

Rotor:

Wa (lbm/sec) =59.3	$Rc_{,stg}$ = 1.74
$\eta_{c,stg}$ = 89.2	$\eta_{c,r}$ = 92.5
P_{T1}(psia) = 14.51	T_{T1}(°R) = 518.7
Speed (rpm) = 10,836	α_1 (deg) = 0.0
No. blades = 16	
TE thickness (in.) = 0.035	
Aero blockage = 0.95	

Stator:

M_3 = 0.5
α_3 (deg) = 0.0
Solidity, σ= 1.5

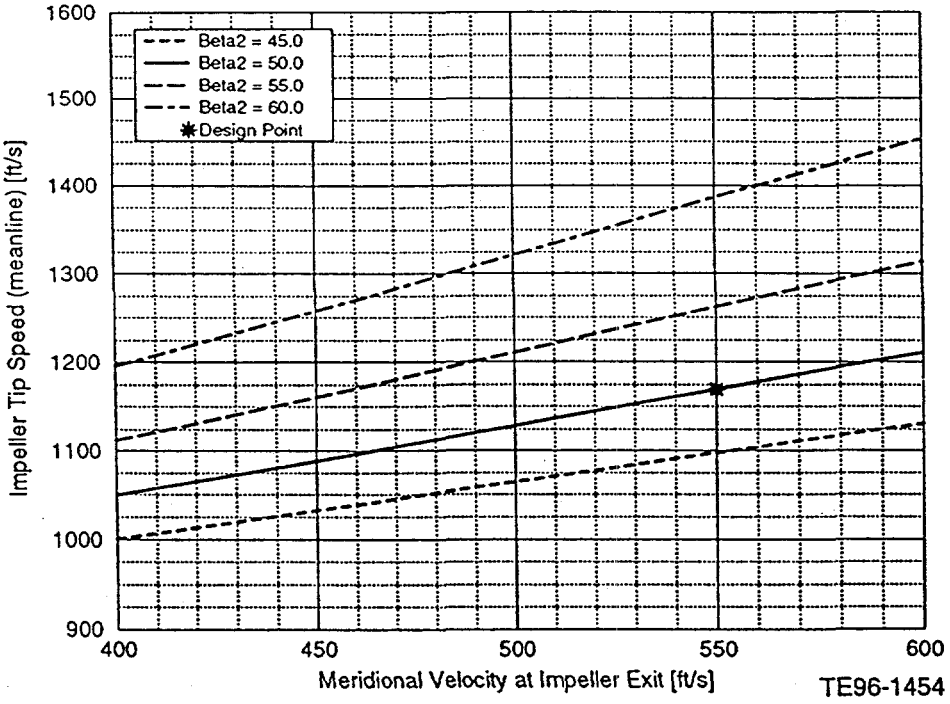

Figure 3.2.7-4. Parametric dependence of (mean line) rotor exit blade speed on V_{m2} and β_2 for design conditions: Wa = 59.3 lbm/sec, $R_{c,stg}$ = 1.74, $\eta_{c,r}$ = 92.5, rpm = 10,836.

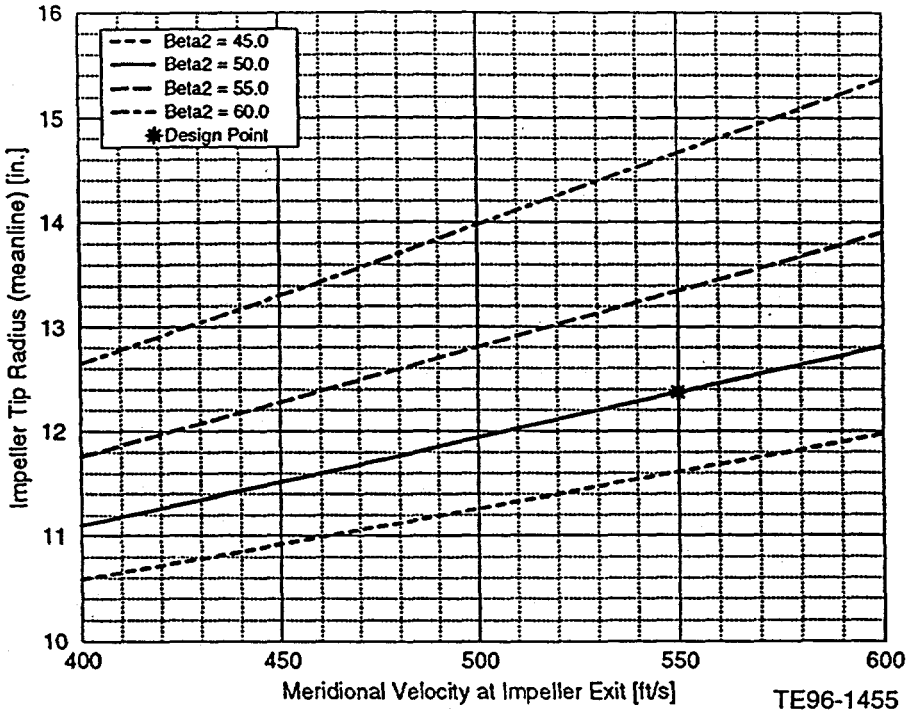

Figure 3.2.7-5. Parametric dependence of (mean line) rotor exit tip radius on V_{m2} and β_2 for design conditions: Wa = 59.3 lbm/sec, $R_{c,stg}$ = 1.74, $\eta_{c,r}$ = 92.5, rpm = 10,836.

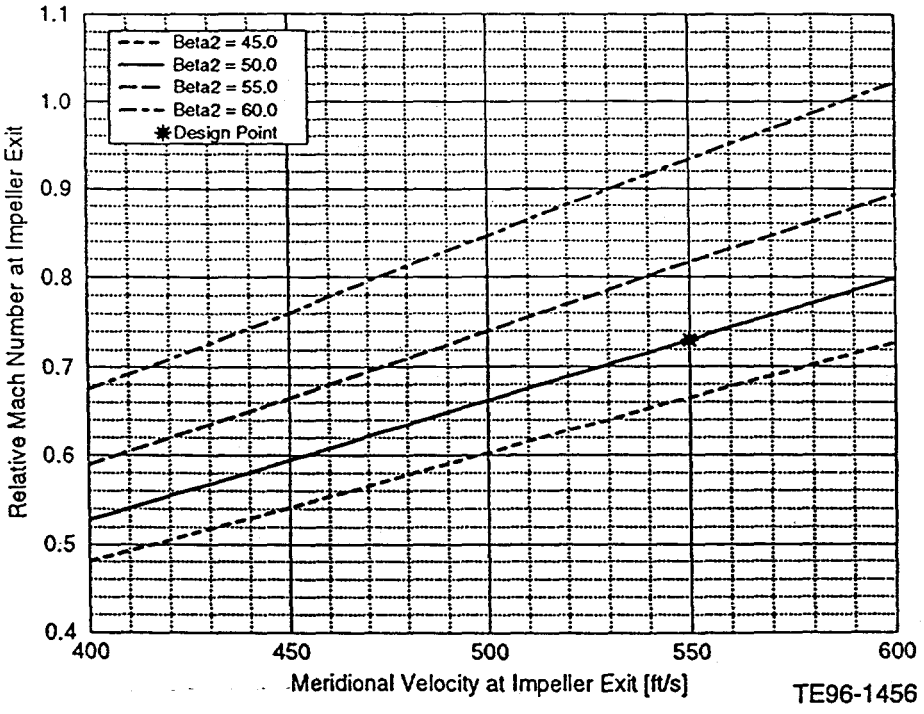

Figure 3.2.7-6. Parametric dependence of (mean line) rotor exit relative Mach number on V_{m2} and β_2 for design conditions: Wa = 59.3 lbm/sec, $R_{c,stg}$ = 1.74, $\eta_{c,r}$ = 92.5, rpm = 10,836.

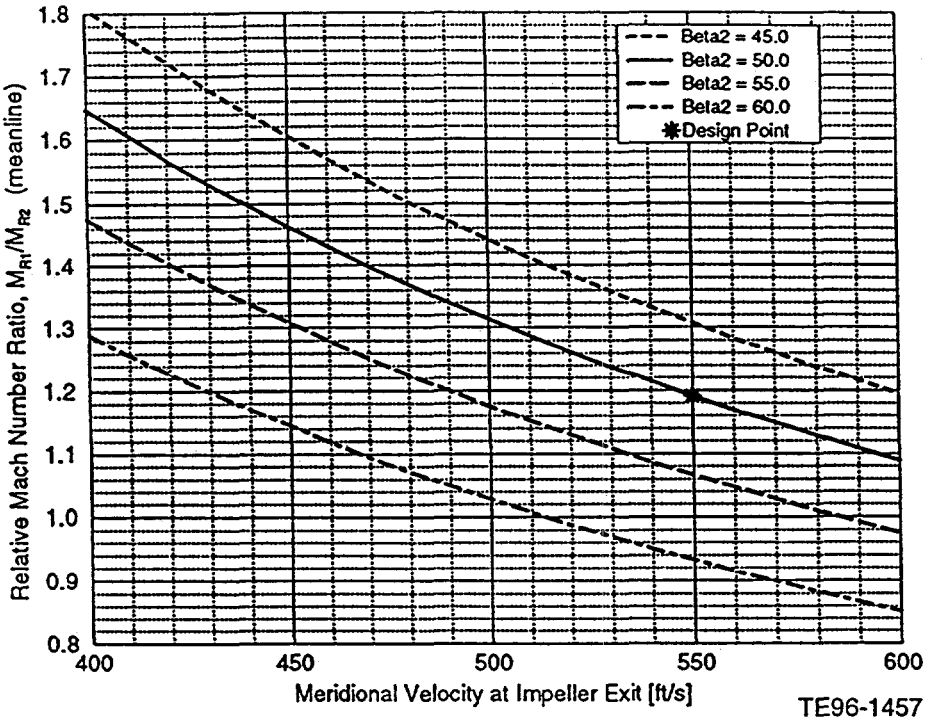

Figure 3.2.7-7. Parametric dependence of (mean line) rotor relative Mach number ratio on V_{m2} and β_2 for design conditions: Wa = 59.3 lbm/sec, $R_{c,stg}$ = 1.74, $\eta_{c,r}$ = 92.5, rpm = 10,836.

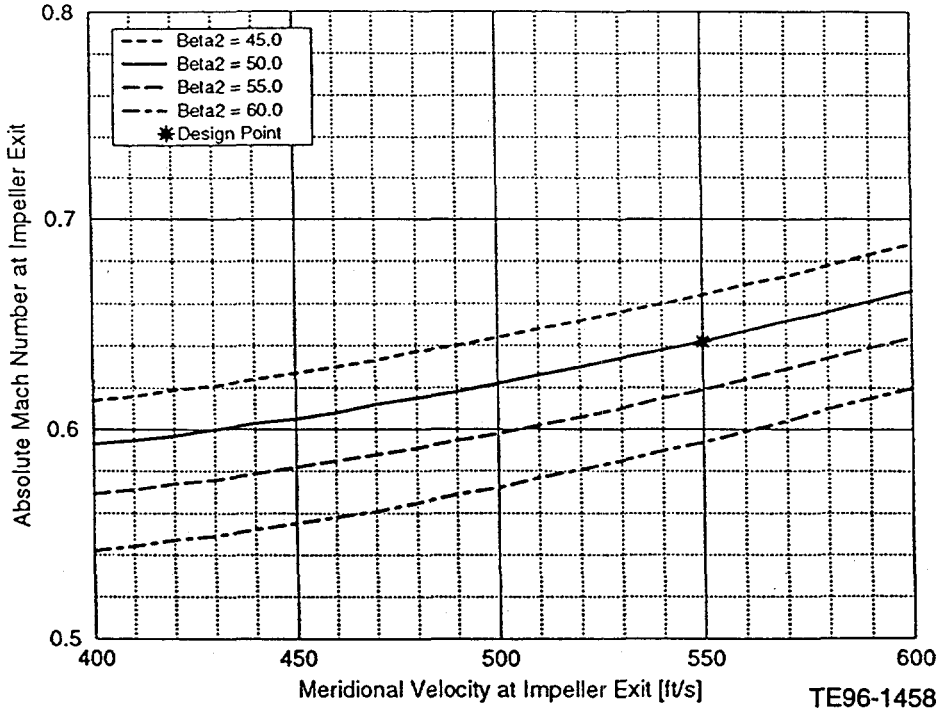

Figure 3.2.7-8. Parametric dependence of (mean line) rotor exit absolute Mach number on V_{m2} and β_2 for design conditions: Wa = 59.3 lbm/sec, $R_{c,stg}$ = 1.74, $\eta_{c,r}$ = 92.5, rpm = 10,836.

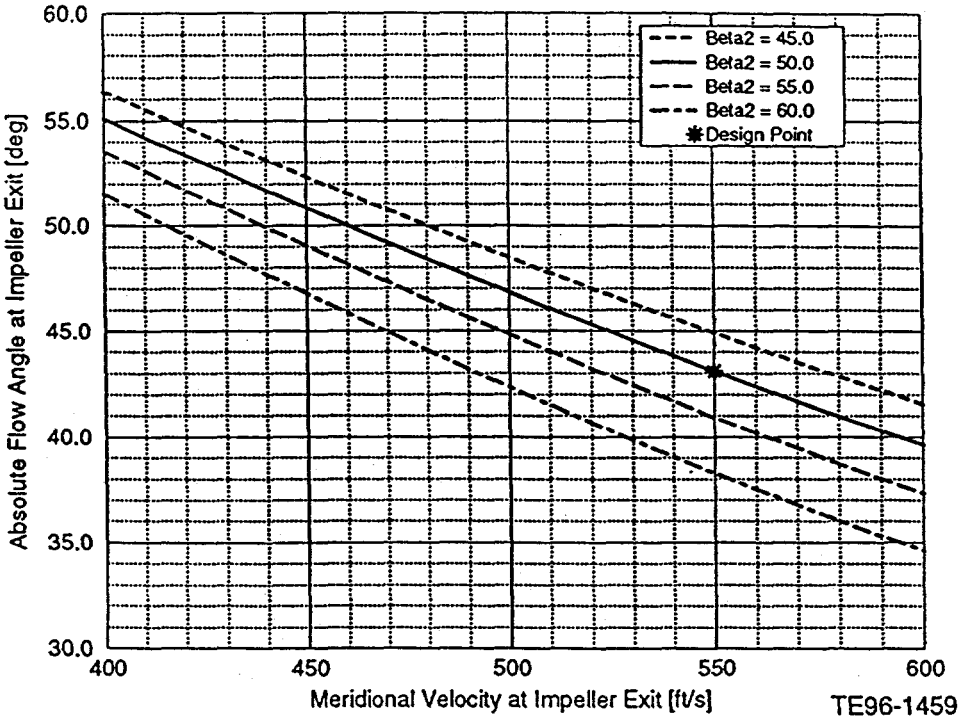

Figure 3.2.7-9. Parametric dependence of (mean line) rotor exit absolute flow angle on V_{m2} and β_2 for design conditions: Wa = 59.3 lbm/sec, $R_{c,stg}$ = 1.74, $\eta_{c,r}$ = 92.5, rpm = 10,836.

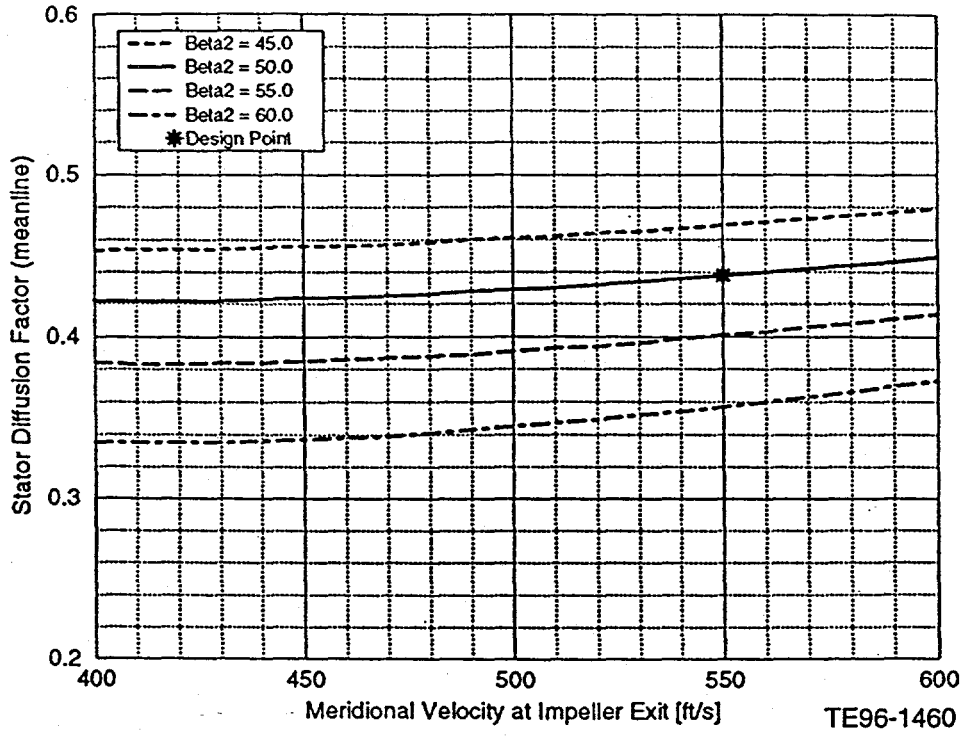

Figure 3.2.7-10. Parametric dependence of (mean line) stator diffusion factor on V_{m2} and β_2 for design conditions: Wa = 59.3 lbm/sec, $R_{c,stg}$ = 1.74, $\eta_{c,r}$ = 92.5, rpm = 10,836.

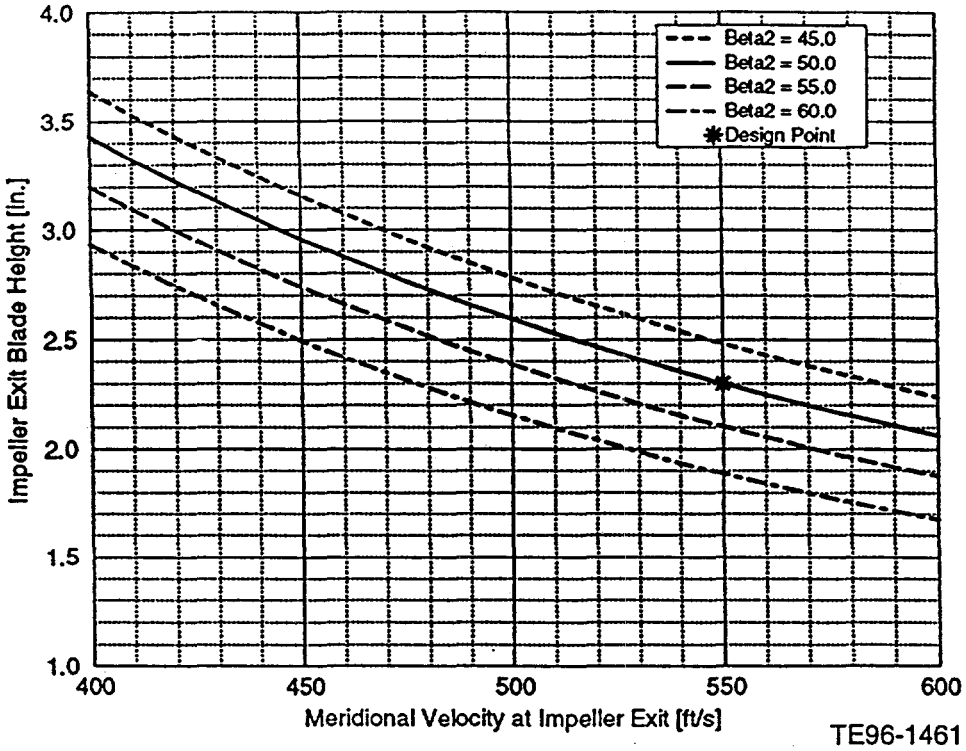

Figure 3.2.7-11. Parametric dependence of rotor exit blade height on V_{m2} and β_2 for design conditions: Wa = 59.3 lbm/sec, $R_{c,stg}$ = 1.74, $\eta_{C,R}$ = 92.5, rpm = 10,836.

Effect of Rotor Backsweep—The dependence of the mean-line rotor exit blade speed (U_2) on the rotor exit relative flow angle is shown in Figure 3.2.7-4. The maximum β_2 was limited to 60 deg because beyond this angle there is negative flow turning in the rotor. This figure shows that increasing the rotor backsweep, at a constant V_{m2}, causes an increase in U_2 to make up for the reduced turning. Higher values of blade speed increase rotor stress, but because of the low rotor pressure ratio, the values of U_2 in Figure 3.2.7-4 should not cause stress problems. The main disadvantage of an increased U_2 is the corresponding increase in the rotor diameter and length. Figure 3.2.7-5 gives the rotor exit mean-line radius, R_2, for the rpm of 10,836. A layout of the ATS flow path shows that rotor size restrictions will limit the maximum allowable U_2. It should be mentioned that increasing the rotor rpm will relax this constraint, but that was not allowed in this study.

Figure 3.2.7-6 shows that increasing the rotor backsweep tends to increase the rotor exit relative Mach number, M_{R2}. Increasing M_{R2} means that less rotor flow diffusion is required and thus the tendency to separate or create losses is reduced. The mean-line relative Mach number ratio, M_{R1}/M_{R2}, is plotted in Figure 3.2.7-7 as a gage of rotor diffusion. The diffusion levels are within reasonable levels, and it is interesting that for high β_2 and high V_{m2} the rotor becomes completely unloaded with no streamwise diffusion or turning of the relative flow.

The effect of rotor backsweep on stator loading is illustrated in Figures 3.2.7-8 through 3.2.7-10. Figure 3.2.7-8 shows that the rotor exit absolute Mach number, M_2, into the stator decreases as backsweep is increased. Figure 3.2.7-9 shows that the rotor exit absolute flow angle, α_2, also decreases as backsweep is increased. Both of these effects tend to reduce the overall stator aerodynamic loading as shown in the diffusion factor plot in Figure 3.2.7-10. The stator D factor is calculated using the assumed stage exit conditions given in Table 3.2.7-IV. It is only an

approximate measure of diffusion since it does not account for the three-dimensional effects of flow-path turning on stator surface loading. It is still a useful gage of stator loading and Figure 3.2.7-10 shows that the main benefit of increased stator backsweep is a reduction in stator loading. The D factors in this figure are within acceptable limits and indicate that a conventional axial type stator design should be feasible for the ATS design point.

In summary, a large value of rotor backsweep has a favorable effect on both the rotor and stator aerodynamic loadings. Its main drawback is that it increases the required rotor tip speed which negatively impacts the rotor diameter, length, and stress. The geometric constraints of the ATS application will restrict the maximum value chosen for the rotor backsweep.

Effect of Rotor Exit Blade Height—Figure 3.2.7-4 shows the dependence of rotor exit blade speed, U_2, on the exit meridional velocity, V_{m2}, which is directly related to the rotor exit blade height through mass flow continuity. This figure shows that for a constant β_2, increasing V_{m2} (i.e., decreasing blade height, h_2) tends to increase the required rotor tip speed and tip radius (see Figure 3.2.7-5). Figure 3.2.7-6 shows that increasing V_{m2} tends to increase the exit relative Mach number, which reduces rotor diffusion levels (see Figure 3.2.7-7) and Figure 3.2.7-8 shows that the absolute Mach number, M_2, also increases, which tends to increase stator loading. Figure 3.2.7-9 shows however that the rotor exit absolute swirl is reduced as V_{m2} is increased, which tends to counteract the effect of an elevated M_2 on stator loading. This point is illustrated in Figure 3.2.7-10 where the stator D factor is shown to be a weak function of V_{m2}.

In summary, the selection of rotor exit meridional velocity (i.e., rotor exit blade height) does not strongly impact overall stator aerodynamic loading, although it does impact the stator inlet Mach number and turning. Rotor diffusion levels are reduced as rotor exit blade height is decreased, but this is not a critical issue for this application.

Selection of Mean-Line Design Velocity Diagrams—The mean-line design conditions selected for the ATS mixed flow LP compressor are given in Table 3.2.7-V. The difficulty of selecting a single design velocity diagram is apparent considering that all of the curves in Figures 3.2.7-4 through 3.2.7-11 are theoretically valid solutions. The final design conditions were selected because they were felt to be the best compromise between the overall stage performance and the geometric constraints of this application.

The following constraints determined the final selection of the rotor exit velocity diagrams. First, the ATS engine flow path was used to estimate the maximum rotor exit radius that resulted in a mixed flow stage, including the ducting to the HP compressor, still within the length constraints of the engine. Secondly, the decision was made to reduce the risk by limiting stator mean line turning to values less than about 45 deg (independent of D factor) because this is

Table 3.2.7-V.
Final rotor exit (mean-line) velocity diagram.

β_2 (deg)	= 50.0	α_2 (deg)	= 43.1
V_{m2} (ft/sec)	= 550	h_2 (in.)	= 2.30
U_2 (ft/sec)	= 1,170	r_2 (in.)	= 12.371
M_{R2}	= 0.73	M_2	= 0.64

outside of Allison's design data base. These constraints led to the selection of the design conditions given in Table 3.2.7-V and shown in Figures 3.2.7-4 through 3.2.7-11.

Rotor Design

This section presents the design and analysis of the mixed flow rotor for the ATS application. This was not intended to be a detailed design for production purposes, but rather an in-depth aerodynamic study of the mixed flow concept to assess its potential as a high efficiency LP compressor. The mixed flow rotor was designed to be manufactured using the same processes as for centrifugal impellers. Mean-line angles and thickness distributions are defined along the blade hub and tip with the rest of the blade surface being constructed by connecting the hub and tip definitions via straight line segments. This approach reduces manufacturing costs, without any compromise in performance or design freedom, by allowing the use of an inexpensive milling process for blade production.

The mixed flow rotor was primarily designed using an Allison impeller design program. The goal was to design a rotor that delivers the desired mean-line exit conditions given in Table 3.2.7-5 with the highest possible efficiency. A 3-D viscous analysis of the final blade is performed to assess its performance. Specifically, this analysis allows a more rigorous assessment of the choke margin, losses, deviation, and blockage assumptions made during the design process.

Rotor Design/Analysis

The axisymmetric throughflow impeller design program was used to analyze several proposed blade mean-line shapes and flow-path contours. Several design iterations were performed before the rotor configuration presented as follows was selected for further development.

Input Parameters—The design program analysis requires the input of the following parameters which have a strong impact on rotor performance: adiabatic efficiency ($\eta_{c,r}$), aerodynamic blockage, and slip factor (i.e., deviation). There were no known correlations for these parameters for mixed flow rotors. For centrifugal designs these parameters are usually scaled from test data for similar impellers. The values assumed for this rotor were:

$\eta_{c,r}$ = 92.5 %
Blockage = 0.94
Slip factor = 0.965

The rotor adiabatic efficiency was based on an assumed rotor polytropic efficiency of 93%. Based on Allison centrifugal impeller data, this is a conservative estimate. The blockage and slip factor estimates were based on published mixed flow rotor test data and a developed data match model. If these assumptions are found to be significantly incorrect by either test data or a viscous analysis, then a rotor redesign will be required to meet the design goals.

Figure 3.2.7-12 shows that the losses associated with a 92.5% mean-line efficiency are assumed to be equally distributed over all the streamlines for the rotor design. The streamwise distribution of relative total pressure loss is assumed to vary quadratically as given in Figure 3.2.7-13. Figure 3.2.7-14 shows that the aerodynamic blockage is assumed to vary linearly to the trailing edge value of 0.94.

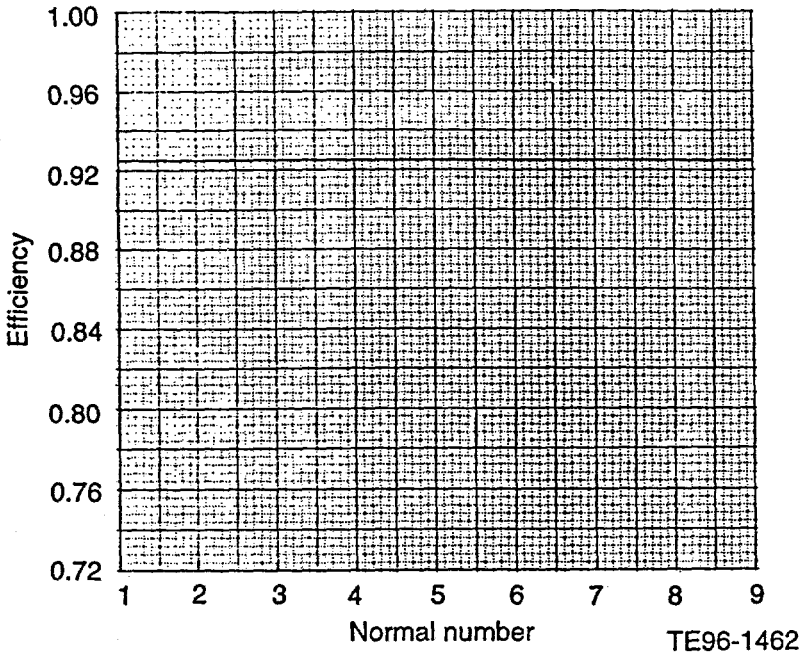

Figure 3.2.7-12. Assumed adiabatic efficiency for each streamline at exit for rotor design.

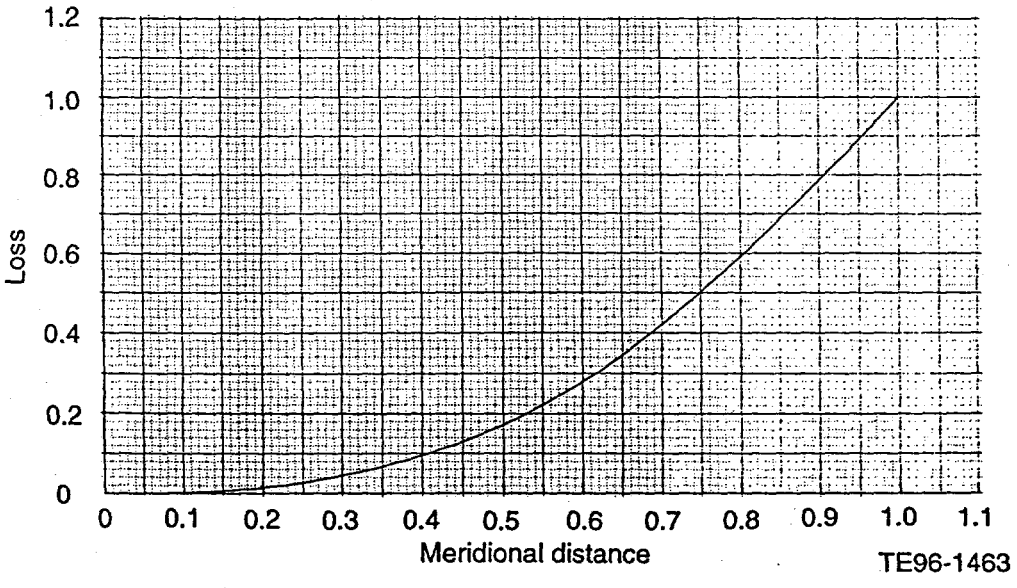

Figure 3.2.7-13. Assumed streamwise distribution of loss for rotor design.

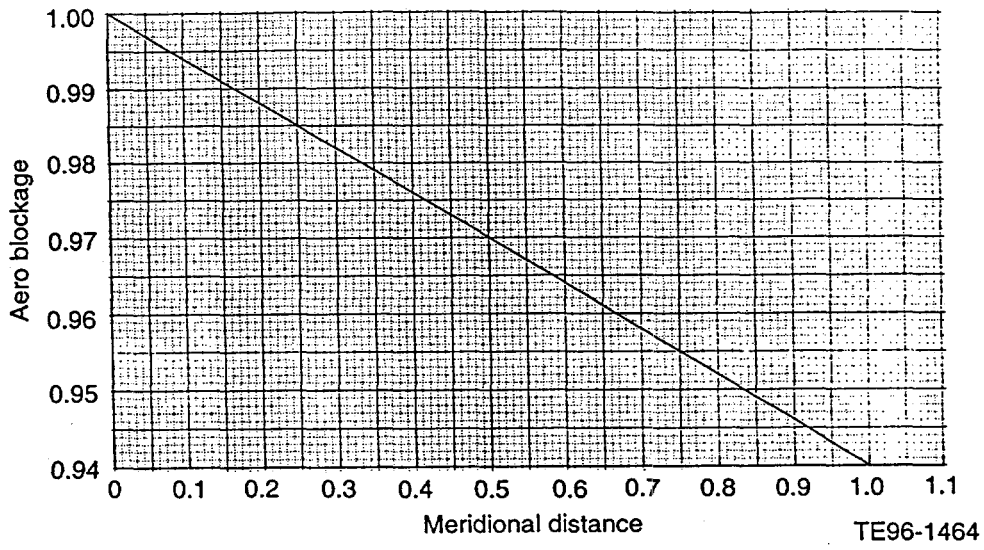

Figure 3.2.7-14. Assumed streamwise distribution of aerodynamic blockage for rotor design.

Mechanical Design Features—The final rotor configuration has 16 nonsplittered blades. The hub and shroud normal blade thickness distributions given in Figure 3.2.7-15 were scaled from an Allison centrifugal impeller design (IGT 404 engine). These thickness distributions have not been verified by a stress or dynamics analysis, and it is possible that a rotor redesign would be needed for mechanical reasons. This is not a critical aerodynamic issue because the rotor flow field is not very sensitive to blade blockage. An interesting feature of the thickness distributions in Figure 3.2.7-15 is that the trailing edge thicknesses are kept to a minimum. This is different than for a centrifugal impeller where trailing edge thickness is less important because of the presence of a large "wake" region.

Flow Path/Blade Geometry Definition—The main features to be specified by the design program analysis are the hub and shroud flow-path contours and the blade mean-line (now meaning camber line instead of mean streamline) angles. The iterative nature of the rotor design is apparent when one considers that the effects of flow area, flow-path curvature, and blade-to-blade turning all combine to set the flow field. The shroud contour design was particularly emphasized because of centrifugal experience showing its strong impact on the flow field. Shroud curvature plays an important role in establishing the pressure field for streamlines near the rotor tip. For a "typical" centrifugal impeller, the flow near the shroud rapidly decelerates as it begins to cross the maximum curvature point (the "knee"). For most impellers this rapid diffusion around the knee creates a large low momentum region, which is typically referred to as the "wake" flow. This is a high loss region that also generates significant mixing downstream of the rotor. The mixed flow rotor's lower shroud curvature should reduce the losses associated with this flow region.

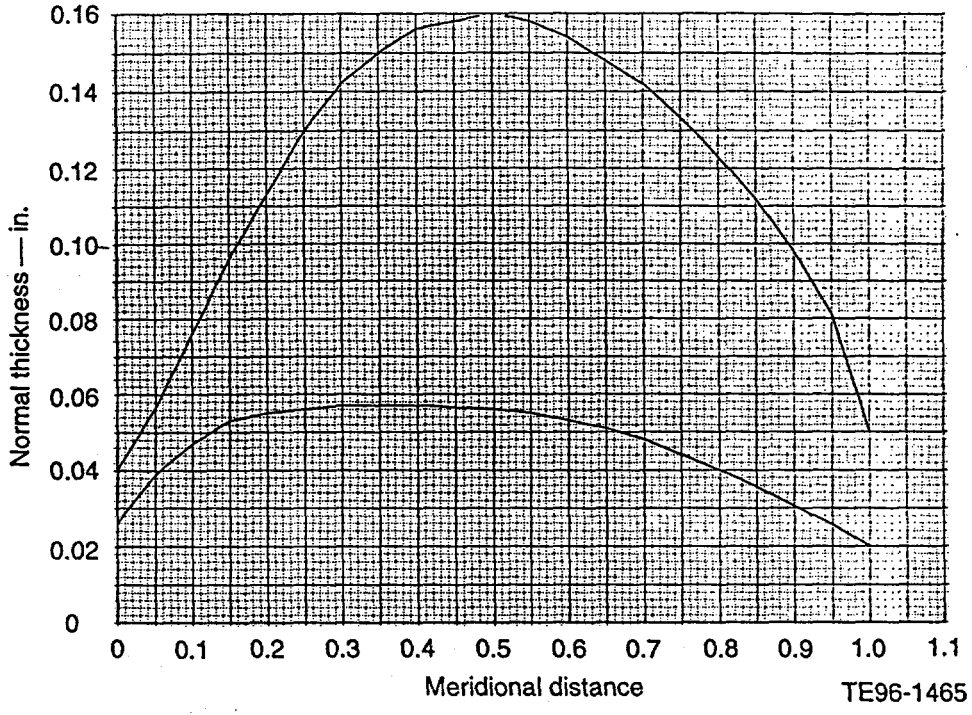

Figure 3.2.7-15. Rotor hub and shroud normal blade thickness distributions.

Several flow-path iterations along with several blade angle distributions were attempted before the hub and shroud contours shown in Figure 3.2.7-16 were selected. The corresponding hub and shroud curvature distributions are given in Figure 3.2.7-17. The flow path was layed out to meet the rotor exit radius and blade height determined from the analysis of Preliminary Design section. A design goal of 30 deg or less for the rotor exit ramp angle was established to facilitate the use of an axial type stator design. The hub flow path was set by smoothly varying the curvature from the inlet to the exit, using reverse flow-path curvature near the exit to achieve an exit ramp angle near 30 deg. The shroud contour was designed to minimize the curvature at the inlet to avoid accelerating the high Mach number flow near the tip before the blade passage has had the opportunity to diffuse the flow. The curvature begins near 35% meridional distance and reverse shroud curvature was also used to minimize the exit ramp angle.

The final hub and shroud blade mean-line angle distributions are given in Figure 3.2.7-18. An attempt was made to set the inlet and exit blade angles to meet incidence and exit total temperature goals. The reason that the mean exit blade angle is low compared to the design goal of 50-deg exit flow angle (not including deviation) will be discussed later. The intrablade mean-line angle distributions were then iteratively set to give a desirable internal rotor flow field. The mean-line angle distribution, through its effect on flow area, was a significant driver on the streamwise flow diffusion. The rate of change of the blade mean-line angle (i.e., the curvature in the blade-to-blade plane) was also used to influence blade loading.

Predicted Flow Field—The resulting flow field, as predicted by the design program code, is presented in Figures 3.2.7-19 through 3.2.7-26. The blade-to-blade relative Mach number distributions for the shroud, mean, and hub streamlines are presented in Figure 3.2.7-19. The corresponding relative velocity distributions are given in Figure 3.2.7-20. The midpitch velocity

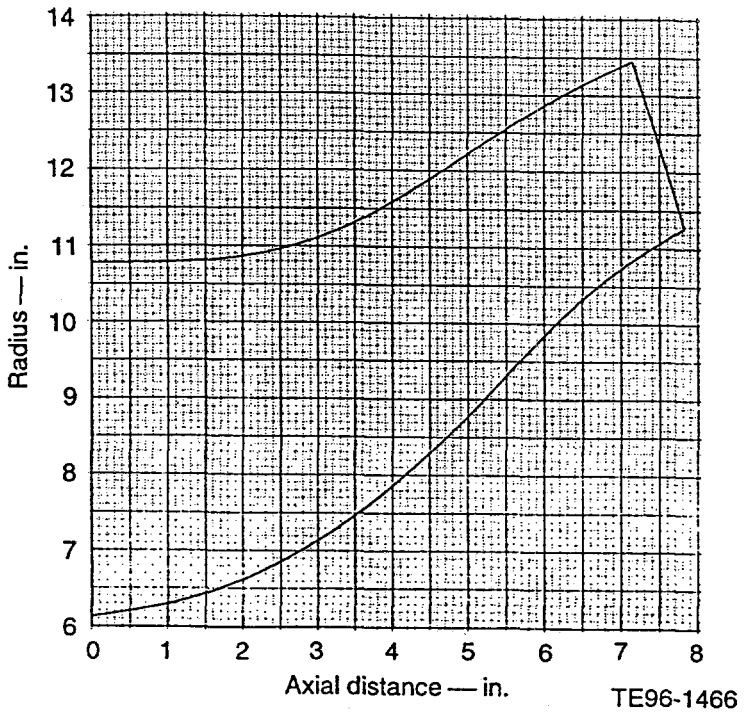

Figure 3.2.7-16. Final rotor flow path.

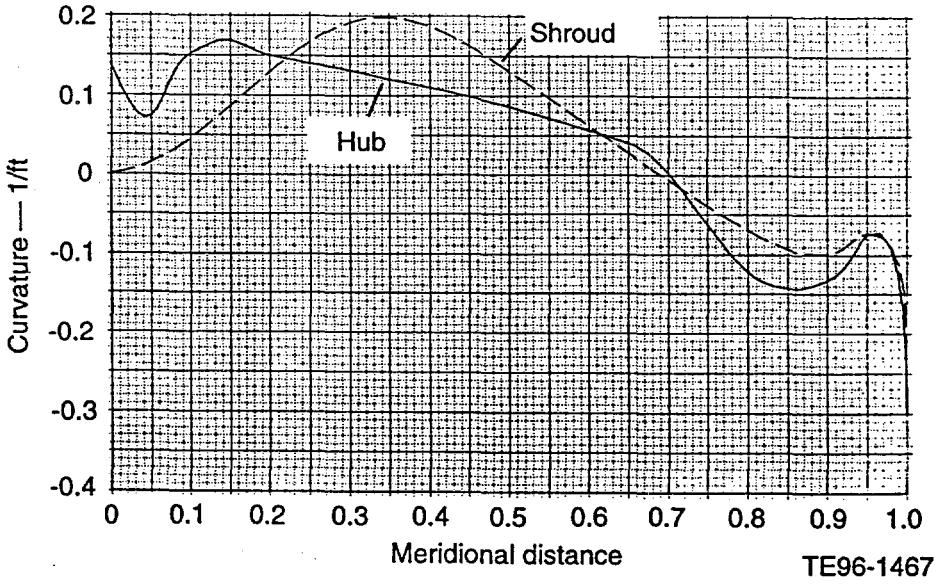

Figure 3.2.7-17. Rotor hub and shroud flow-path curvature distributions.

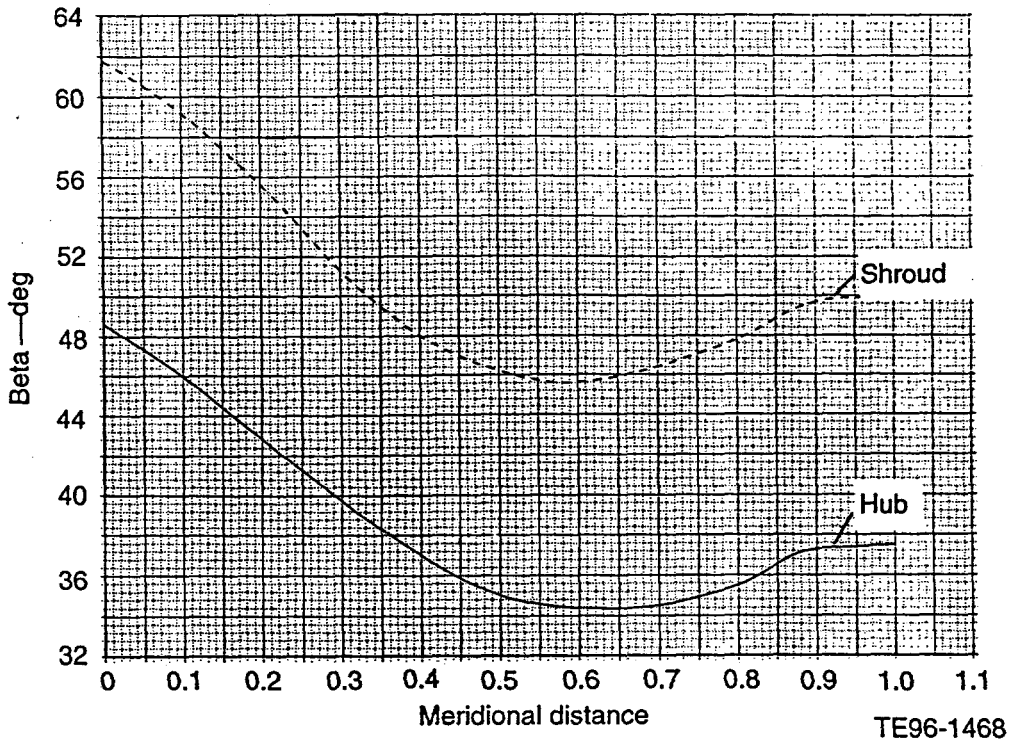

Figure 3.2.7-18. Rotor hub and shroud blade mean line angle distributions.

distributions as predicted by the axisymmetric calculation are shown as the center curve in each figure with the suction and pressure surface velocities being estimated using an approximate method. The difference between suction and pressure surface profiles is used to assess blade loading. The relative Mach number distribution for the shroud streamline is presented in Figure 3.2.7-20a. The midpitch distribution shows an almost linear diffusion from the inlet relative Mach number of 1.06 to 0.67 at the exit. The low shroud curvature in the inlet region was used to avoid flow acceleration to higher Mach numbers. The blade loading is fairly low over the entire blade length. The mean streamline Mach number distribution in Figure 3.2.7-20b shows a relatively low diffusion of the streamwise flow and that the blade loading is also not high. The hub streamsurface, shown in Figure 3.2.7-20c, exhibits weak diffusion up to 40% meridional distance before being accelerated toward the exit. This behavior is caused by the hub surface curvature. The blade loading is also kept low.

The blade loading coefficient is plotted in Figure 3.2.7-21 as an additional gage of aerodynamic loading for the hub, mean, and shroud streamlines. The blade loading coefficient is defined as the pressure difference across the blade divided by the local dynamic head. A rule of thumb used in centrifugal impeller design is to keep this parameter below a value of 0.8 to avoid high secondary flow and tip clearance losses. Based on this criterion this blade is lightly loaded.

The midpitch relative velocity magnitude and meridional velocity distributions through the rotor are illustrated in Figures 3.2.7-22 and 3.2.7-23, respectively. The relative velocity magnitude for the hub, mean, and shroud streamlines in Figure 3.2.7-22 is the same information as in Figure 3.2.7-20 but in a more convenient format. The mild diffusion of the midpitch flow is observed. Figure 3.2.7-23 shows the effect of reverse hub and shroud flow-path curvature on the meridional velocity distribution near the rotor trailing edge. The hub meridional velocity is

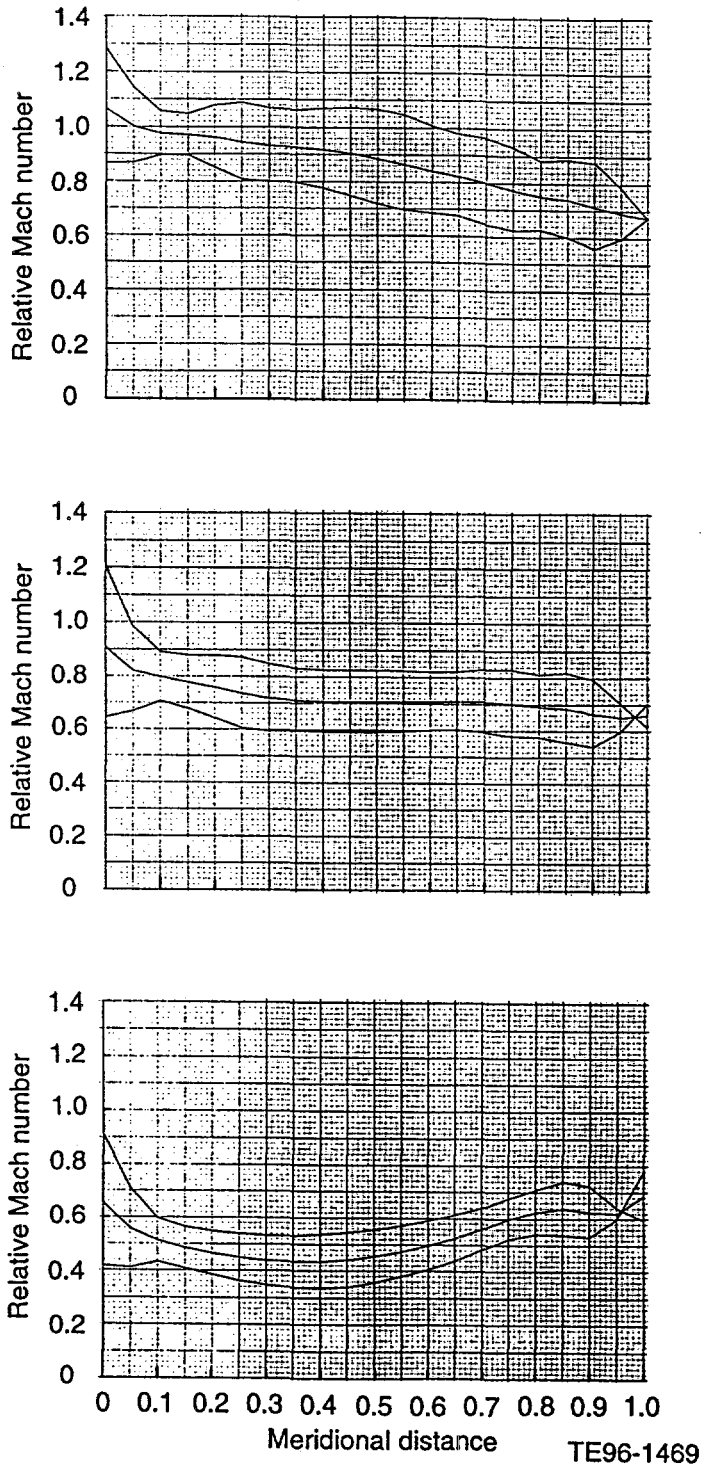

Figure 3.2.7-19. Streamline curvature prediction of rotor blade-to-blade relative Mach number distributions: (a) shroud, (b) mean, and (c) hub streamlines.

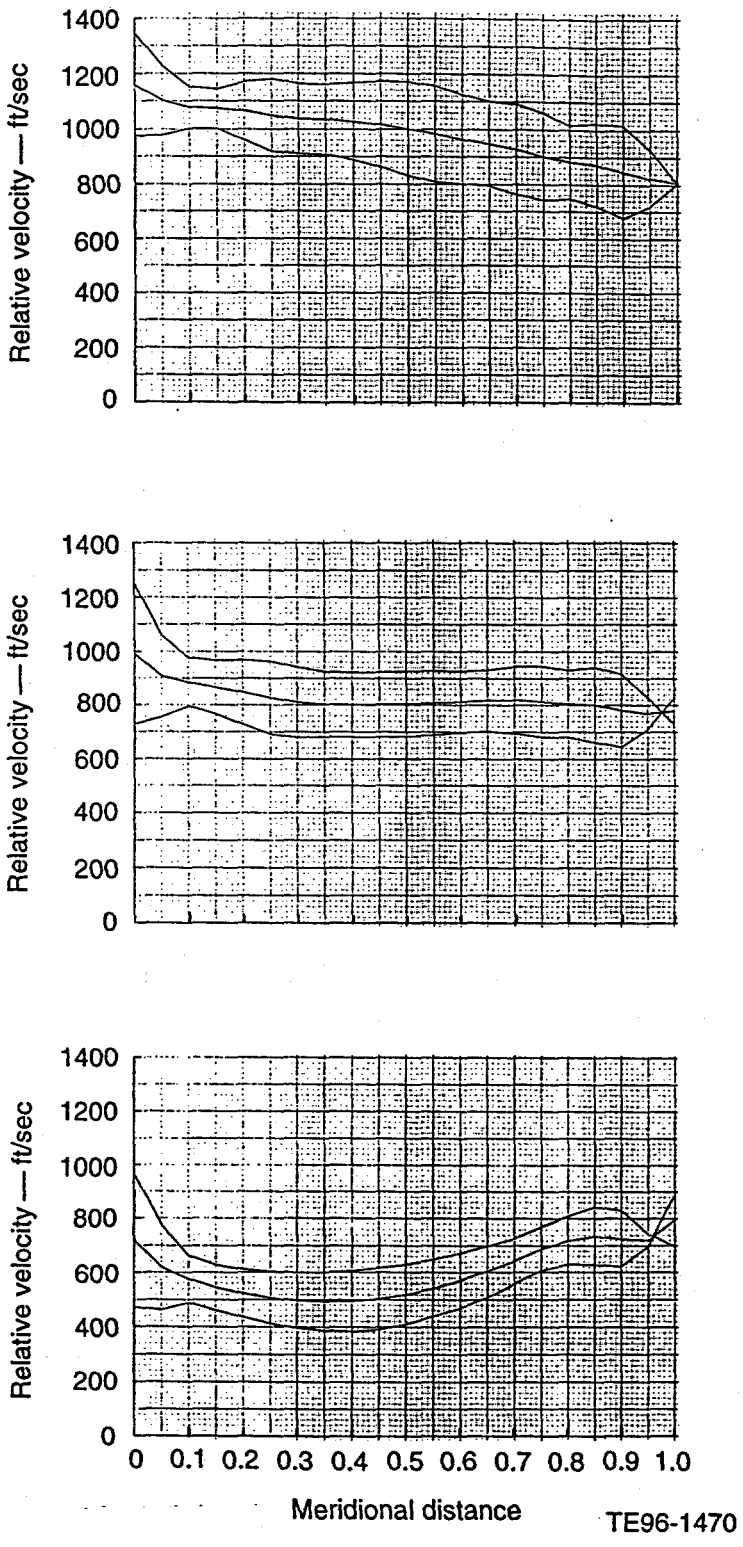

Figure 3.2.7-20. Streamline curvature prediction of rotor blade-to-blade relative velocity distributions: (a) shroud, (b) mean, and (c) hub streamlines.

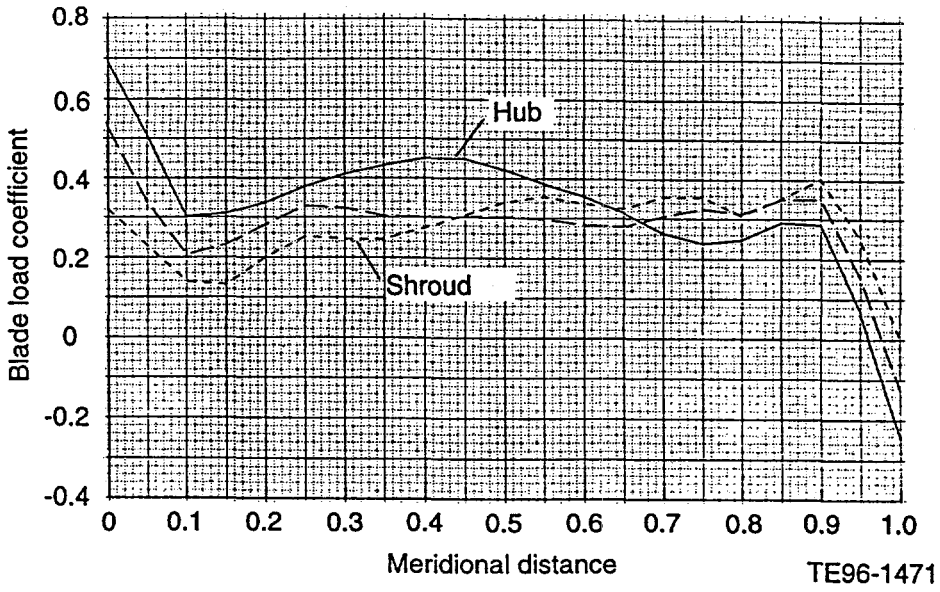

Figure 3.2.7-21. Streamline curvature prediction of rotor blade load coefficient distributions.

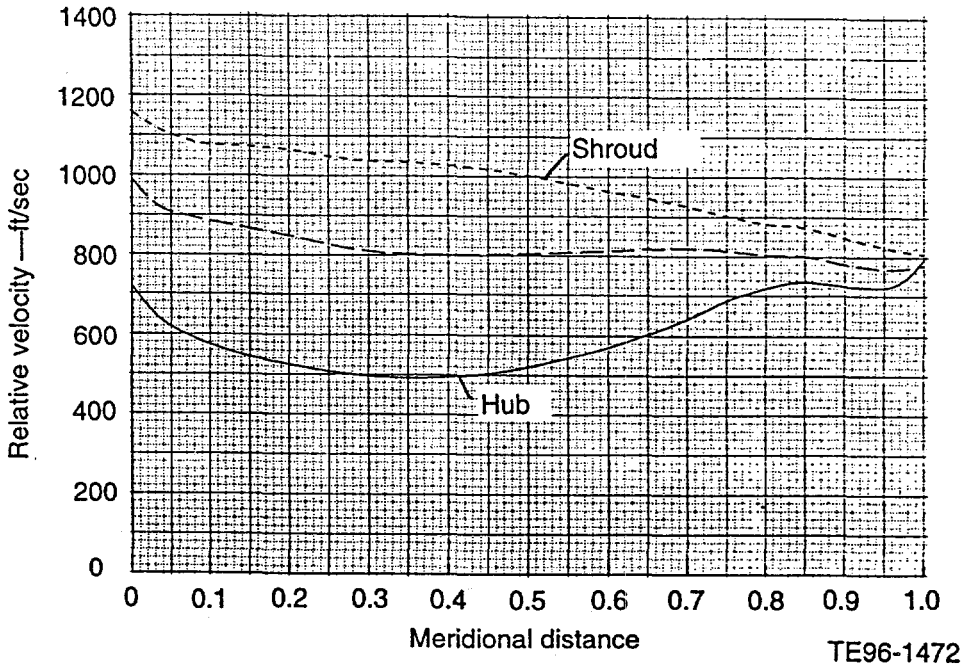

Figure 3.2.7-22. Streamline curvature prediction of rotor midpitch relative velocity magnitude.

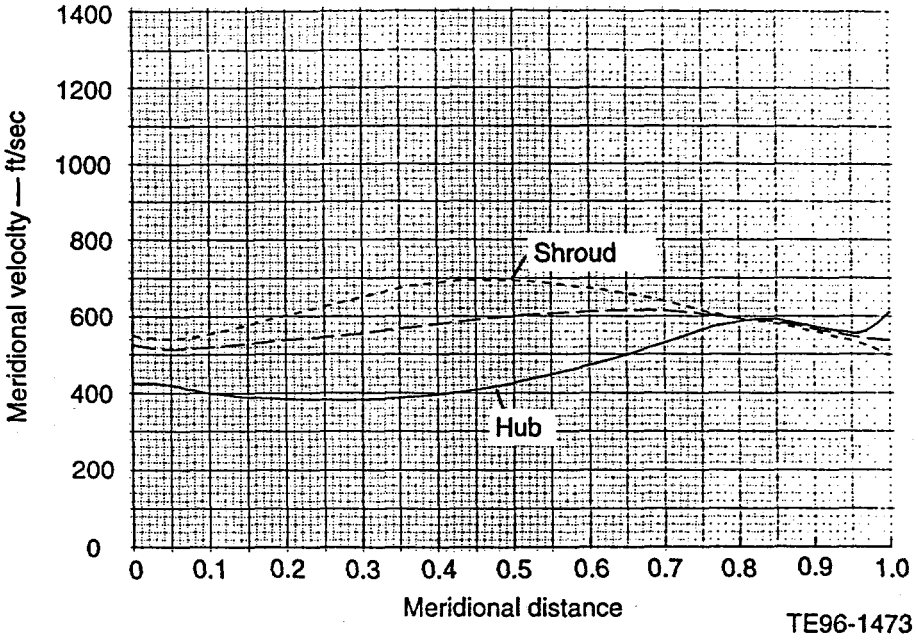

Figure 3.2.7-23. Streamline curvature prediction of rotor midpitch meridional velocity.

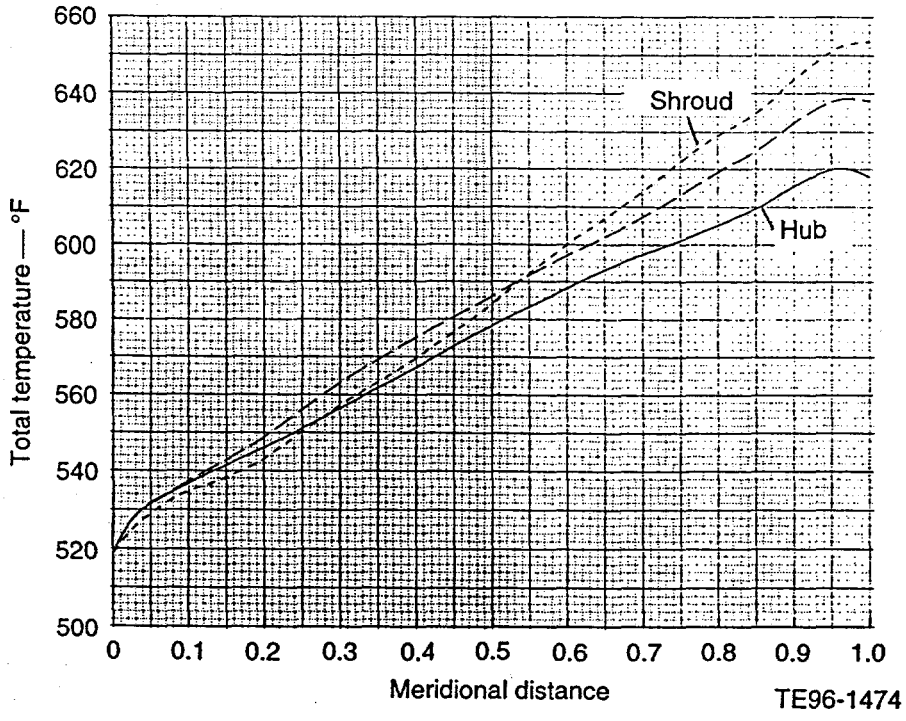

Figure 3.2.7-24. Streamline curvature prediction of rotor (absolute) total temperature distribution.

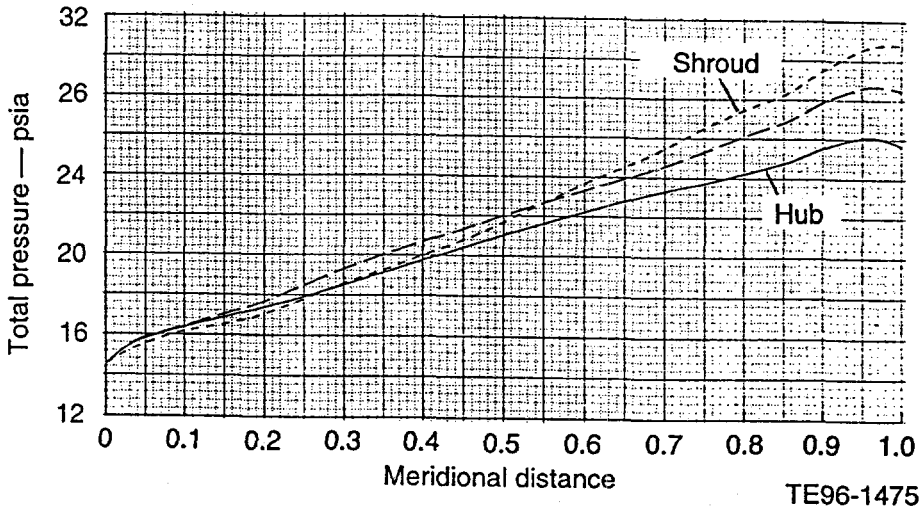

Figure 3.2.7-25. Streamline curvature prediction of rotor (absolute) total pressure distribution.

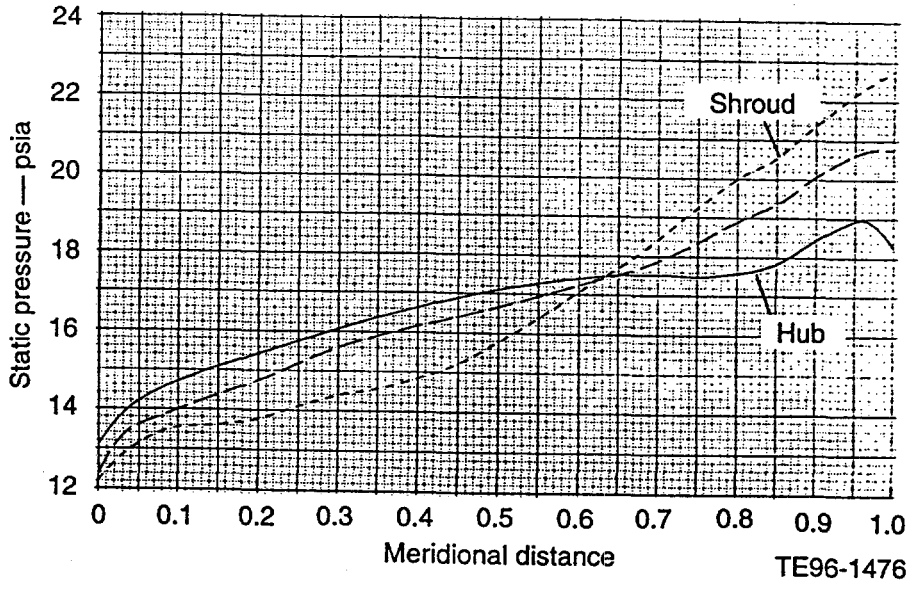

Figure 3.2.7-26. Streamline curvature prediction of rotor static pressure distribution.

observed to be higher than the shroud and the mean streamline value is near the design goal value of 550 ft/sec.

The aerothermodynamic flow properties of total temperature, total pressure, and static pressure are illustrated in Figures 3.2.7-24, 3.2.7-25, and 3.2.7-26, respectively. Figure 3.2.7-24 shows a shroud strong total temperature distribution with a mean exit temperature of 638°R, which is higher than the design goal of 619°R. This high exit total temperature is caused by a general overturning of the flow due to the lower than desired exit relative flow angle. Several attempts were made to fix this problem by redesigning the rotor mean-line angles with more backsweep at the exit. As the exit blade angles were increased, the mean-line angles near the trailing edge also were increased, which resulted in massive blade unloading. It was soon realized that the only viable solution was to totally redesign the hub and shroud flow-path contours to give more meridional area near the trailing edge. Since the exit total temperature is strongly dependent on the assumed slip factor (deviation), the decision was made to use the current design and analyze it with the viscous code. If the viscous analysis also predicts a high exit total temperature, then a rotor redesign will be required to meet the design objectives. The total pressure distribution in Figure 3.2.7-25 also shows a mean exit pressure higher than the design goal of 25.8 psia. This is caused by the higher than design exit total temperature. Figure 3.2.7-26 shows some of the unique features of the rotor's static pressure field. Near the rotor exit the combined effects of reverse flow-path curvature and the swirling flow cause the shroud static pressure to have higher values than the hub. This pressure field is unique to the mixed flow rotor, but the exit spanwise profile is qualitatively similar to that of an axial compressor.

3-D Viscous Analysis

Two 3-D viscous analysis codes were used to assess the rotor performance. Considering that limited mixed flow data exists, the use of advanced CFD codes should reduce the time and cost associated with compressor development. Overall performance, inlet and exit circumferentially averaged profiles, and detailed internal flow features were examined. The viscous flow results were promising with regard to the efficiency potential of this machine.

Code Validation—Due to limited experience with centrifugal type rotors, some effort was expended validating the two analysis codes for these types of machines. Previous experience has shown these codes to be useful tools for the prediction of axial compressor performance. The main conclusions from the code validation effort were the following:

1. Centrifugal impeller predictions are made difficult by the presence of large low momentum or separated flow regions (the so-called "wake") in the rotor passage.
2. The first code (code 1) does better when these large low momentum flow regions are present.
3. The second code (code 2) does better for "clean" axial type flow fields.

These results indicate that both codes should be used to analyze the mixed flow rotor since each has advantages depending on the type of flow field exhibited by the mixed flow rotor.

Grid Generation—The centrifugal compressor aero design group's preprocessing program was used to generate the grid shown in Figure 3.2.7-27. This code was modified to allow the specification of the hub and shroud contours for the grid downstream of the rotor trailing edge. The

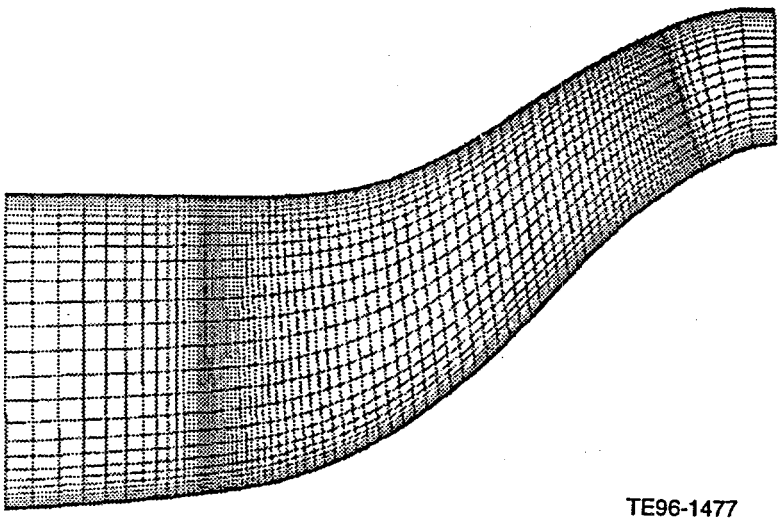

Figure 3.2.7-27. Meridional view of H-type grid used for 3-D viscous calculations.

previous version of the code assumed radial rotor exit flow. The final mesh has 118,437 total grid points with 97 points in the axial, 37 points in the radial, and 33 points in the pitchwise directions. Five radial grid points were used in the tip clearance gap (0.010 in.) which was modeled using code 1's "pinched" blade tip method. The final grid file was converted into a code 2 compatible format. Code 2 input and boundary condition files also were created. The solutions were obtained using parallel versions of both codes on the 64 processor NCube parallel computer. The grid was subdivided for 32 processor computation, so that 2 operating points (i.e., back pressures) could be run simultaneously. Convergence for code 2 was determined by monitoring the overall performance parameters of inlet and exit mass flow, pressure ratio, and efficiency.

Overall Performance—Figures 3.2.7-28 and 3.2.7-29 present the overall rotor performance predictions at 100% speed for both codes. Figure 3.2.7-28 gives the pressure ratio versus flow characteristics (speedlines) with the rotor design point shown for comparison. Code 2 predicts a rotor pressure ratio that is too high by over 10% at the design flow with code 1 predicting an even higher pressure ratio. The high pressure ratio is caused by two effects: (1) flow overturning due to low rotor backsweep (i.e., predicted deviation is similar to that assumed for design), and (2) the predicted rotor efficiency is higher than assumed during the design. If this rotor is selected for further development this flow overturning should be corrected by adding 2 deg to 3 deg more backsweep. The codes also predict that the rotor chokes between 5 to 6% above the design flow and thus has sufficient flow capacity. The surge point for centrifugal type machines however cannot be accurately predicted with these codes. All that can be deduced is that the flow at surge is most likely lower than the last stable operating points shown in this figure.

Figure 3.2.7-29 gives the predicted adiabatic efficiency versus flow characteristics. The efficiency was calculated at two grid points downstream of the trailing edge taking into account specific heat variations. Both codes predict high rotor efficiency levels with code 2 peak efficiency over 96%, while code 1 predicts almost 98%. The centrifugal code validation effort indicated that code 1 tends to provide an upper bracket on the measured impeller efficiency. For axial compressors, the code 2 tends to overpredict efficiency by approximately 2%. If it is

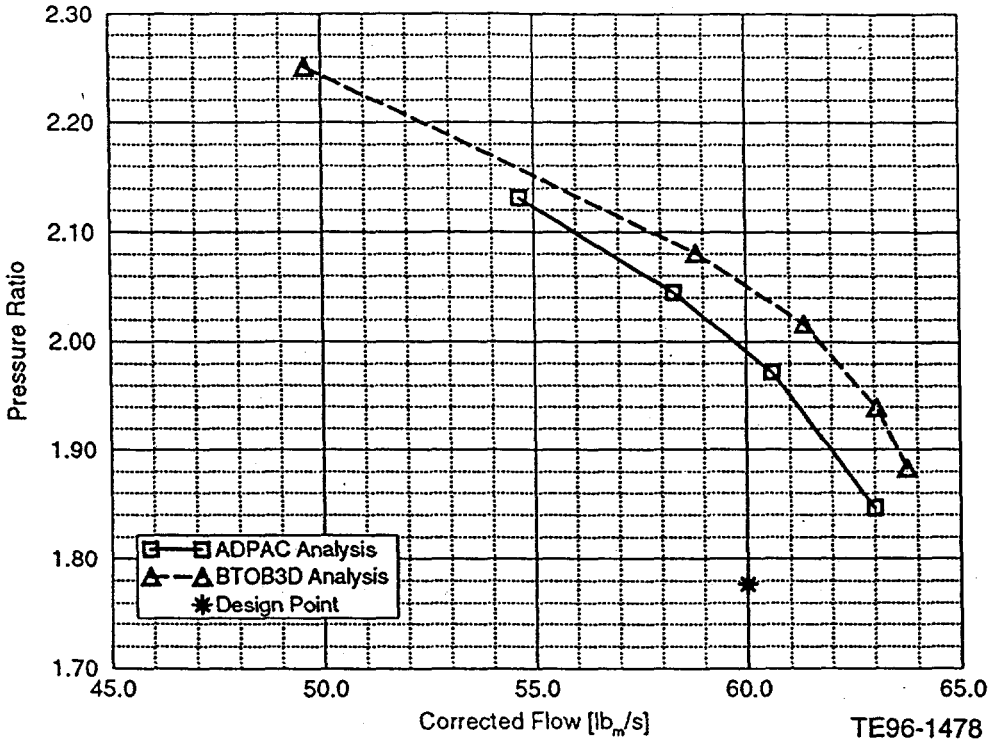

Figure 3.2.7-28. Predicted rotor pressure ratio versus corrected flow characteristic at 100% speed.

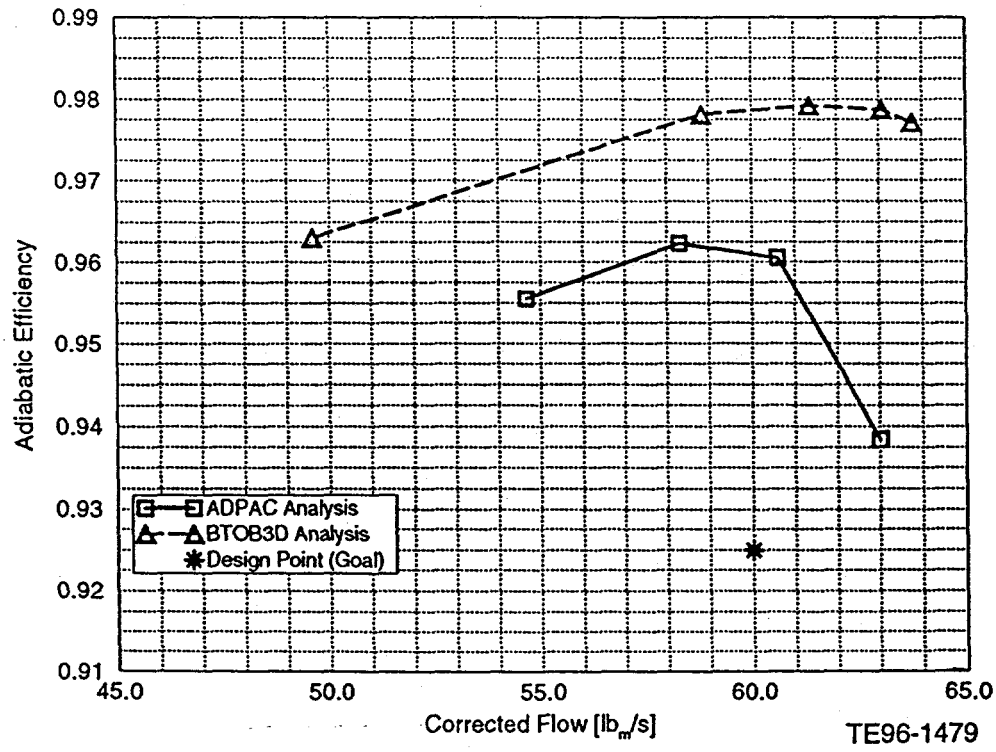

Figure 3.2.7-29. Predicted rotor adiabatic efficiency versus corrected flow characteristic at 100% speed.

assumed that the type of flow field the mixed flow rotor more closely resembles, axial versus centrifugal, is not known, then the analysis brackets the "real" efficiency between 94 and 98%. Although this is a wide efficiency range, this analysis indicates that the mixed flow rotor should meet or exceed its design goal of 92.5%.

Inlet and Exit Radial Profiles—Rotor inlet and exit circumferentially averaged flow properties are presented in Figures 3.2.7-30 through 3.2.7-38 for the code 2 solution closest to the design mass flow. Figure 3.2.7-30 shows the predicted absolute total pressure at the rotor exit. Also shown is the mean-line design intent and the design program (streamline curvature) predicted total pressures at hub, mean, and shroud. The code 2 analysis predicts a general overpumping of the flow with a tip strong profile that is qualitatively similar to the design program analysis. A fall off in total pressure is predicted on the outer 15% of the blade span. The spanwise total temperature profile given in Figure 3.2.7-31 also shows a general overturning of the flow compared to the design intent. The total temperature profile is tip strong especially on the outer 15 to 20% of the span which was not captured by the design program analysis. Figure 3.2.7-32 gives the spanwise adiabatic efficiency distribution, which was calculated from the exit total pressure and temperature profiles assuming constant specific heats. The rotor efficiency is high over most of the span except on the outer 20% of the blade. The source of this high loss region will be discussed in the detailed performance section. The predicted static pressure profile is given in Figure 3.2.7-33. As expected it shows a tip strong static pressure distribution different than for most centrifugal impellers.

The inlet and exit meridional velocity profiles are given in Figure 3.2.7-34. The prediction shows a hub strong profile with the midspan value close to the design intent of 550 ft/sec. This implies that the 6% blockage assumption used during the rotor design is reasonable. The code

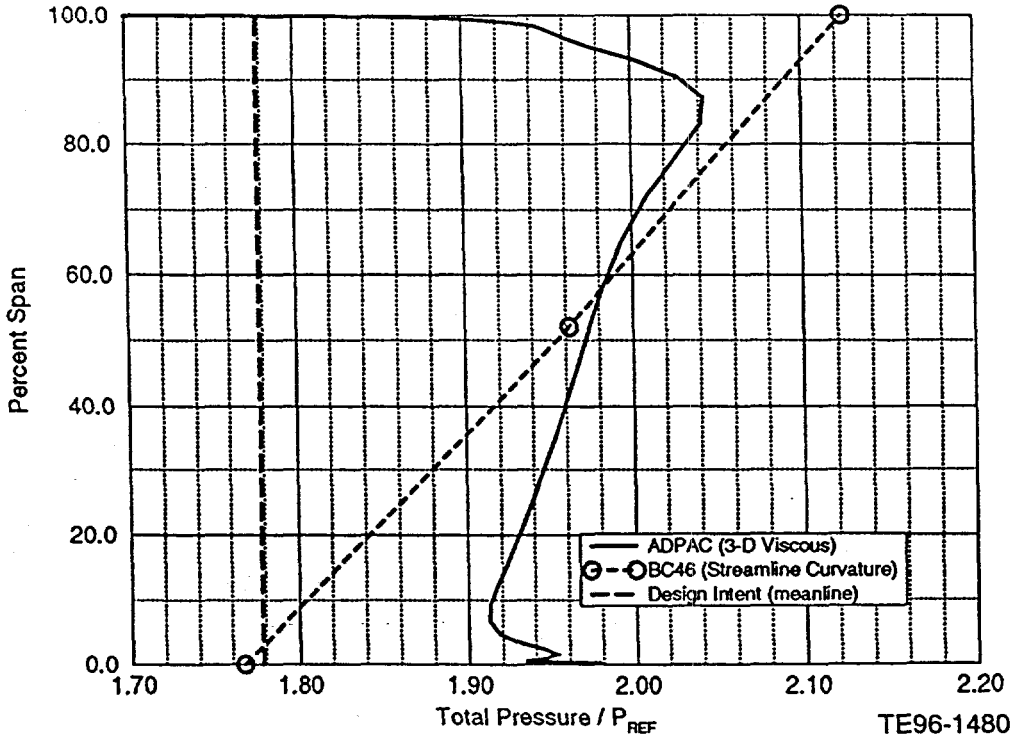

Figure 3.2.7-30. Predicted rotor exit total pressure profiles at design flow.

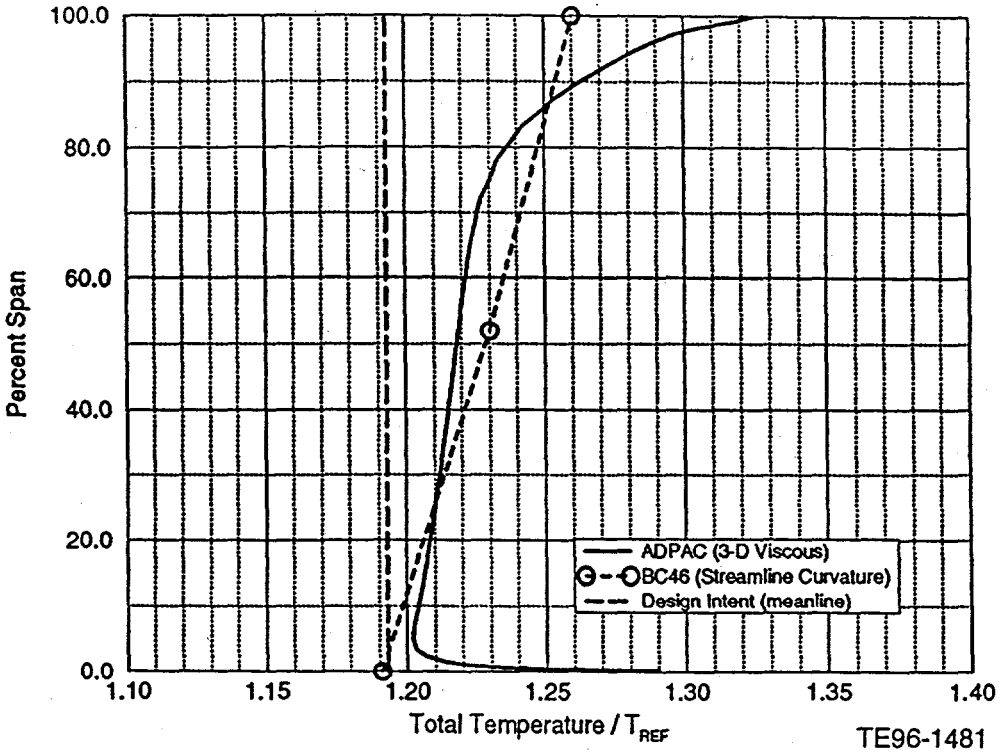

Figure 3.2.7-31. Predicted rotor exit total temperature profiles at design flow.

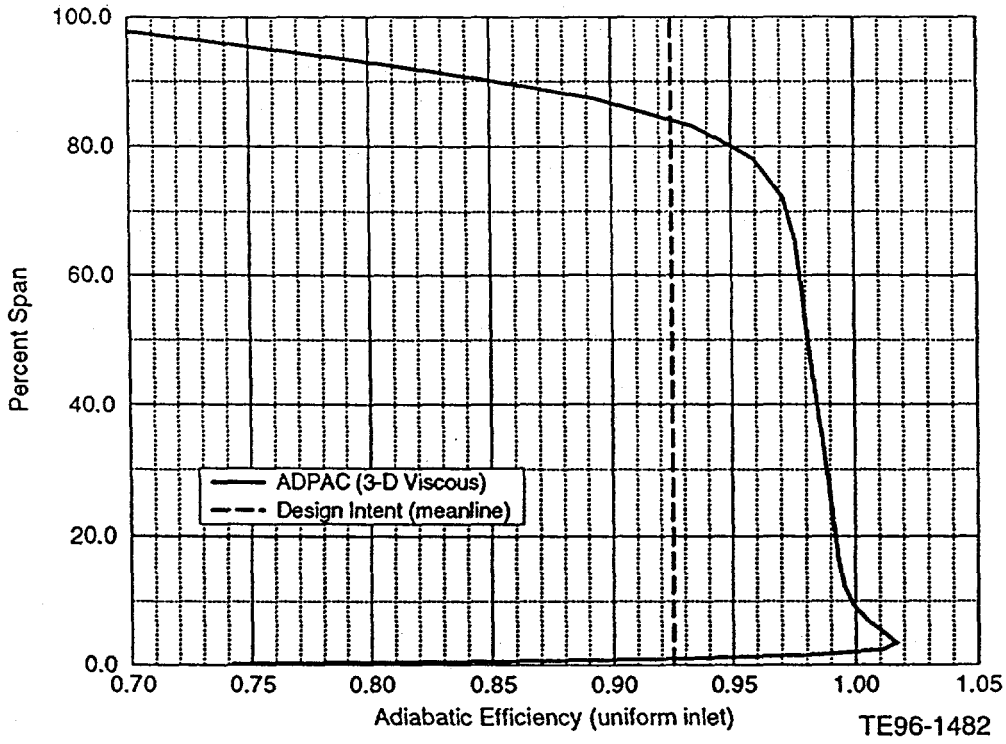

Figure 3.2.7-32. Predicted rotor exit efficiency profiles at design flow.

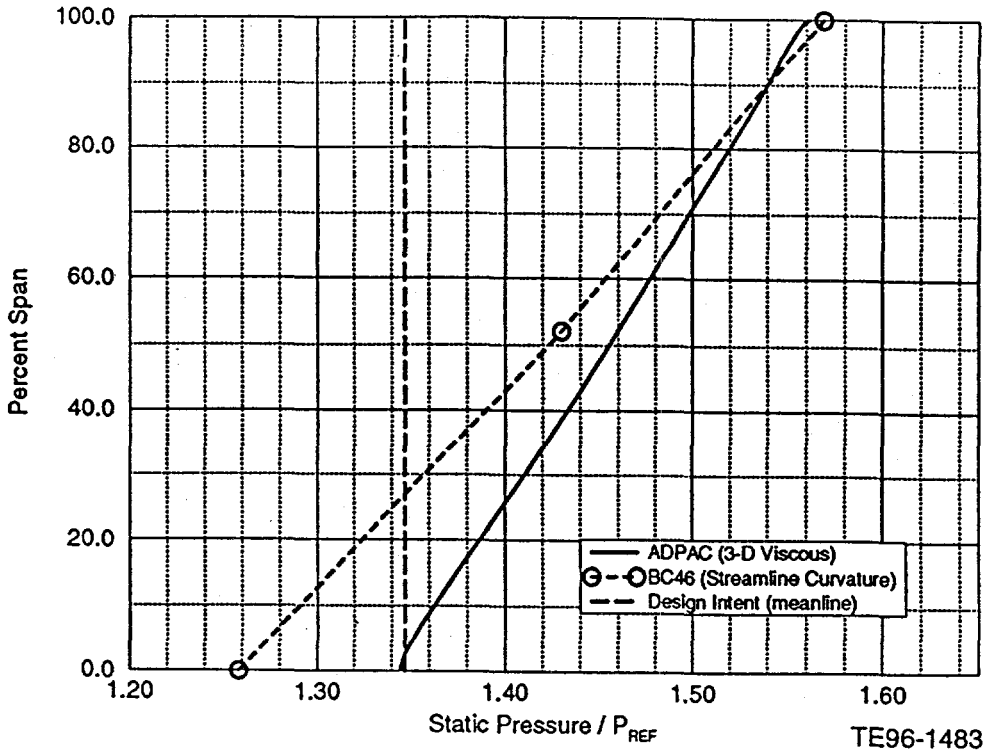

Figure 3.2.7-33. Predicted rotor exit static pressure profiles at design flow.

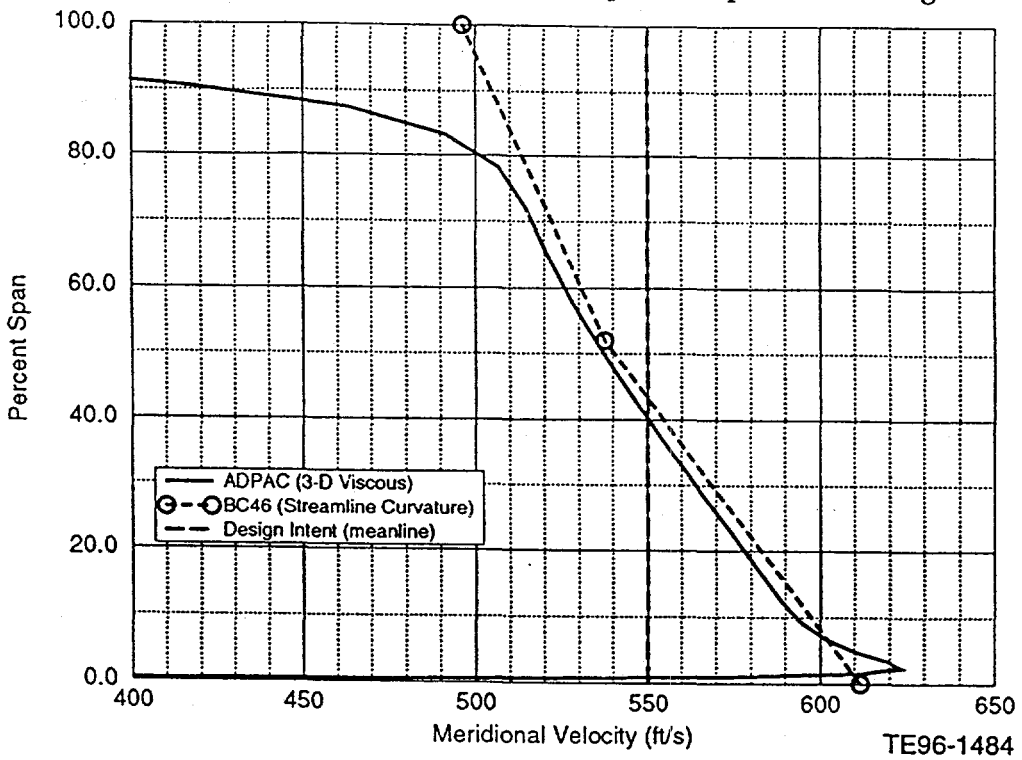

Figure 3.2.7-34. Predicted rotor meridional velocity profiles at design flow.

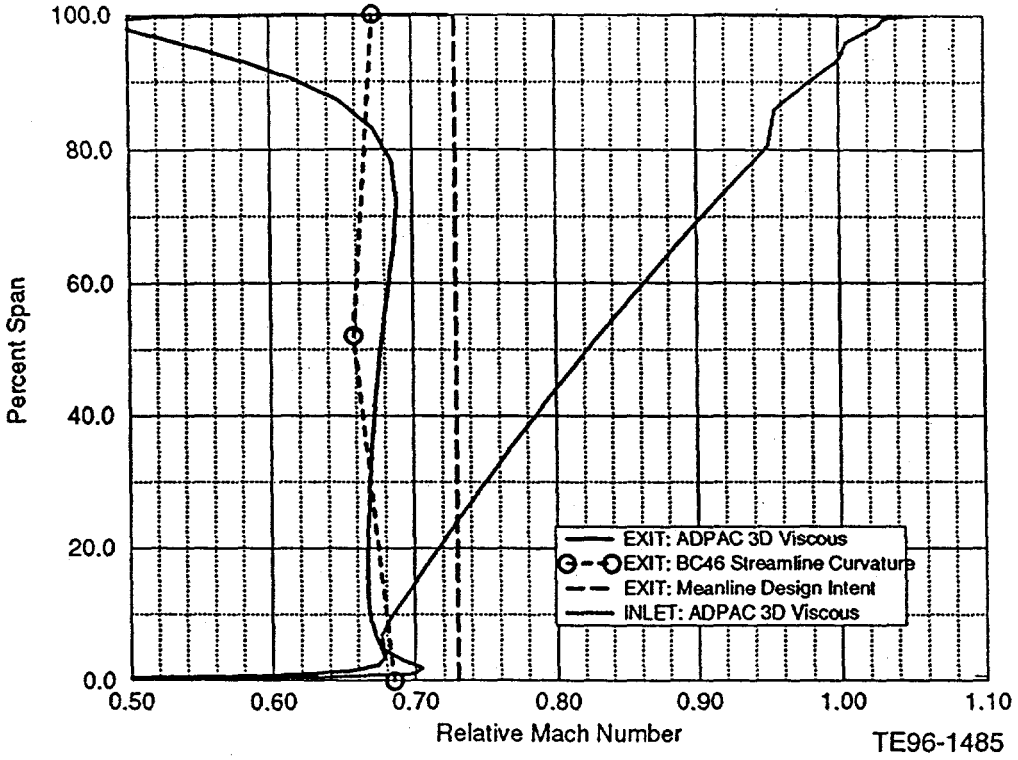

Figure 3.2.7-35. Predicted rotor relative Mach number profiles at design flow.

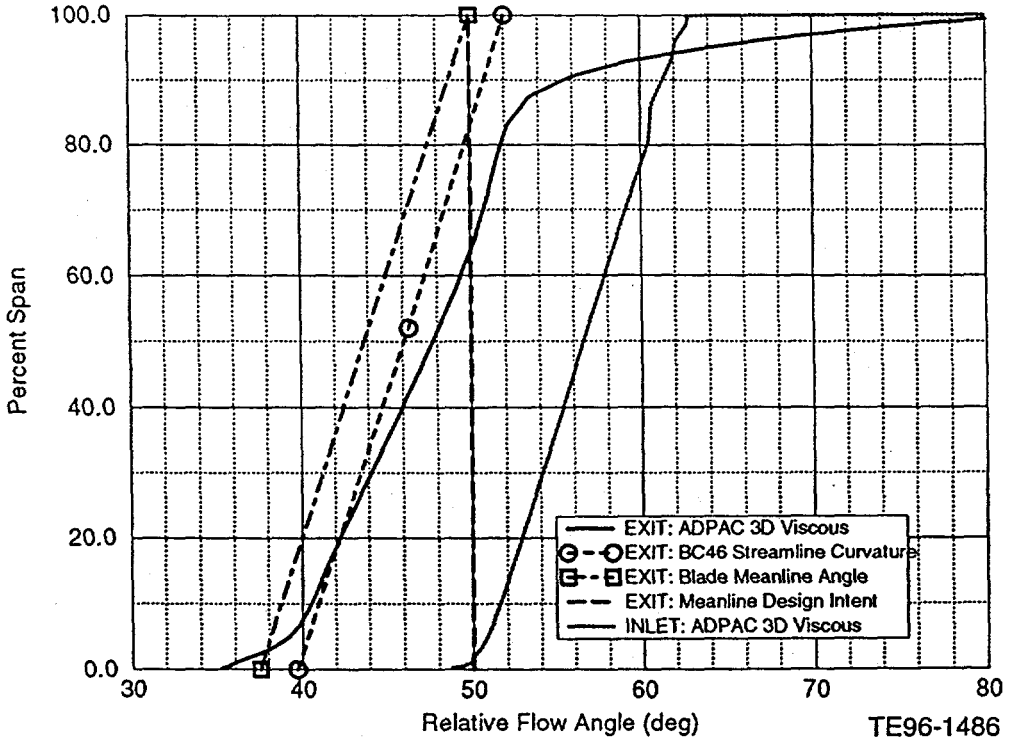

Figure 3.2.7-36. Predicted rotor relative flow angle profiles at design flow.

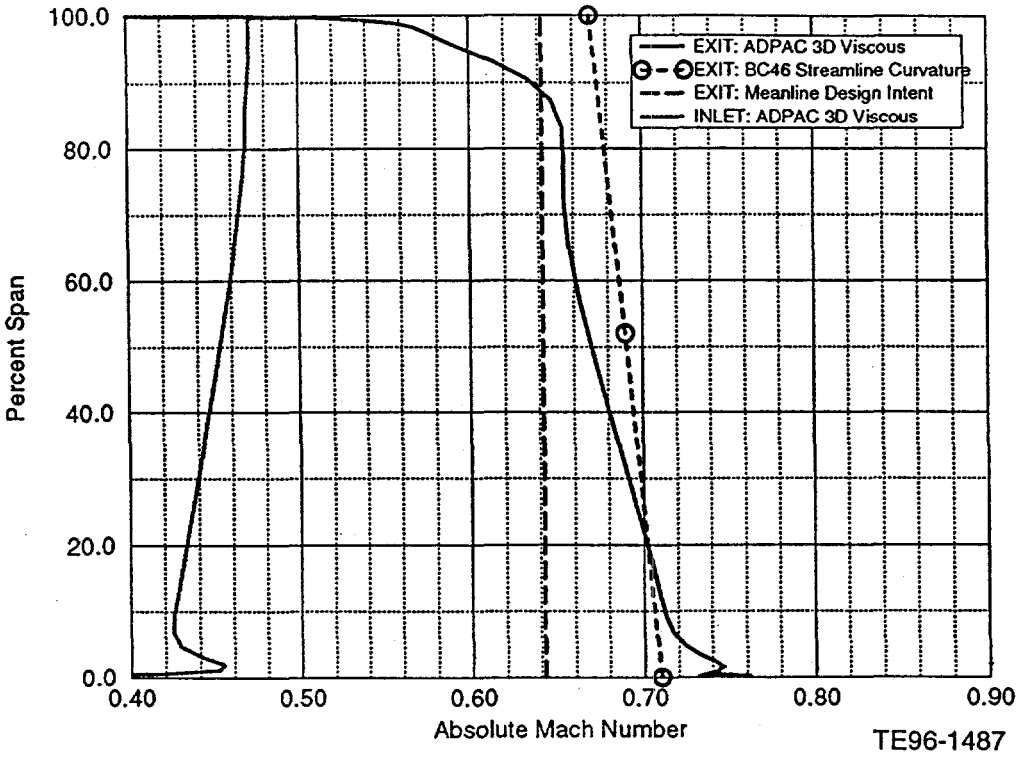

Figure 3.2.7-37. Predicted rotor absolute Mach number profiles at design flow.

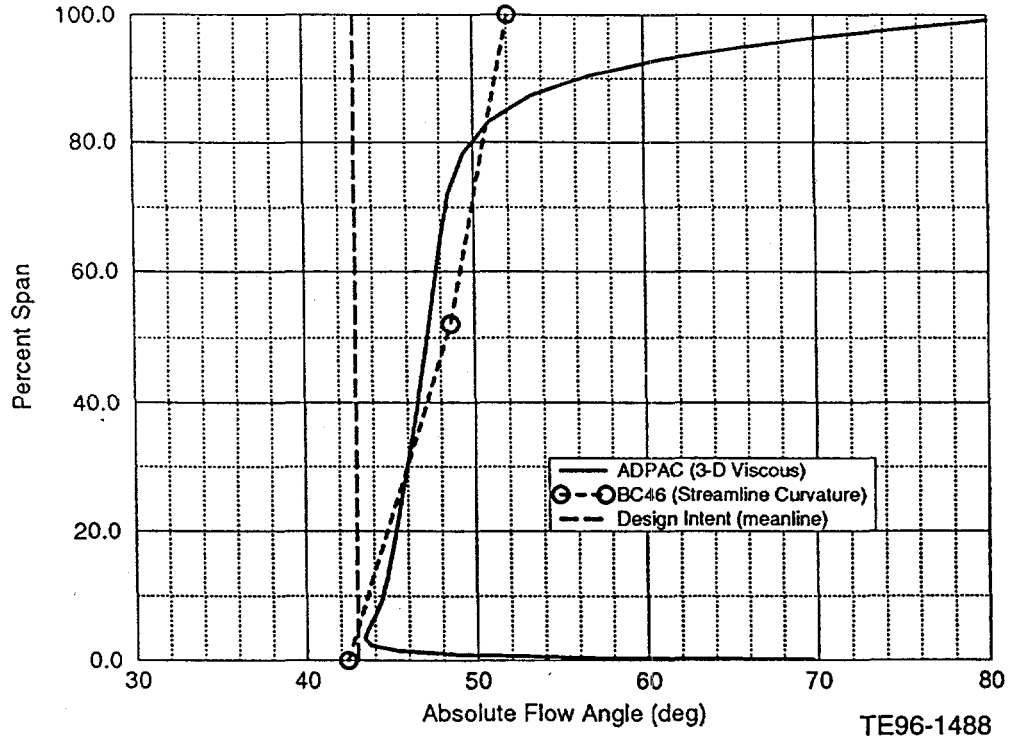

Figure 3.2.7-38. Predicted rotor exit absolute flow angle profiles at design flow.

predicts a strong velocity deficit on the outer 20% span. Figure 3.2.7-35 gives the predicted inlet and exit relative Mach number, which shows that the exit relative profile is fairly uniform and slightly lower than the design value of 0.73. Exit Mach number also falls off near the outer 20% span. A comparison of the inlet and exit profiles shows that most of the flow diffusion is done near the rotor tip. Figure 3.2.7-36 gives the inlet and exit relative flow angle distributions with the mean-line design intent and rotor exit blade angles shown for reference. The first observation is that the rotor design intent of 50 deg is not achieved. The flow follows the exit blade angle fairly well, with about 2-deg deviation near the hub and 4-deg near the tip, but the relative angle is below the design intent by about 2 deg. Therefore, the deviation (slip factor) assumed for the rotor design was close to being correct and this low relative angle causes the high exit total temperature, which was also predicted by the design program. This rotor should be redesigned with more exit backsweep to correct this problem. Another observation from this figure is that only 9 to 10 deg of turning is done over most of the span, except on the outer 15% where the flow bends toward tangential.

Figures 3.2.7-37 and 3.2.7-38 present profiles of the absolute flow properties that impact the stator loading requirements. Figure 3.2.7-37 shows that the exit absolute Mach number levels are slightly higher than design intent. The exit profile shape is as expected, except for the deficit on the outer 10 to 15% span. These slightly high Mach number levels were caused by the low exit relative flow angle. Figure 3.2.7-38 shows that the exit absolute flow angles are also higher than the design intent. The flow angles on the outer 15% span were especially troubling considering that the stator must remove the swirl from this flow. Any future redesign should clean up the rotor tip flow field to avoid problems in the downstream stator. It should be mentioned here that for the stator design effort it was assumed that a rotor redesign will be done to reduce the exit flow problem near the shroud.

Detailed Performance—The detailed internal flow features predicted by code 2 are presented in this section. Figures 3.2.7-39 through 3.2.7-41 show the circumferentially averaged flow field through the rotor. Figures 3.2.7-39 and 3.2.7-40 show the static pressure and relative Mach number fields, respectively. The relative Mach number plot is especially interesting because low momentum flow is observed near the shroud (recall the rotor exit profiles). As discussed earlier, the diffusion of the tip flow as it crosses the knee in the shroud causes a rapid growth in the boundary layer. A test case was also run with zero tip clearance to verify that the low momentum flow was not caused by the tip clearance vortex. This flow region is responsible for most of the loss generated within the passage and causes the undesirable rotor exit flow conditions near the shroud. Possible design fixes would include reducing the maximum shroud curvature near the knee by putting more curvature near the inlet. The flow passage area also could be redesigned to reduce the diffusion near the shroud downstream of the knee.

Blade-to-blade relative Mach number contour plots are presented in Figure 3.2.7-41 for grid lines near 93, 50, and 7% span. Notable features are the absence of loss producing passage shocks and separated flow regions. However, at 93% span the low momentum region is observed at midpitch near the rotor exit. Figure 3.2.7-42 gives the surface isentropic Mach number distribution for the same grid locations. It is interesting to note that the 3-D viscous analysis gives blade loadings very similar to the design distributions from the streamline curvature design program analysis (see Figure 3.2.7-19).

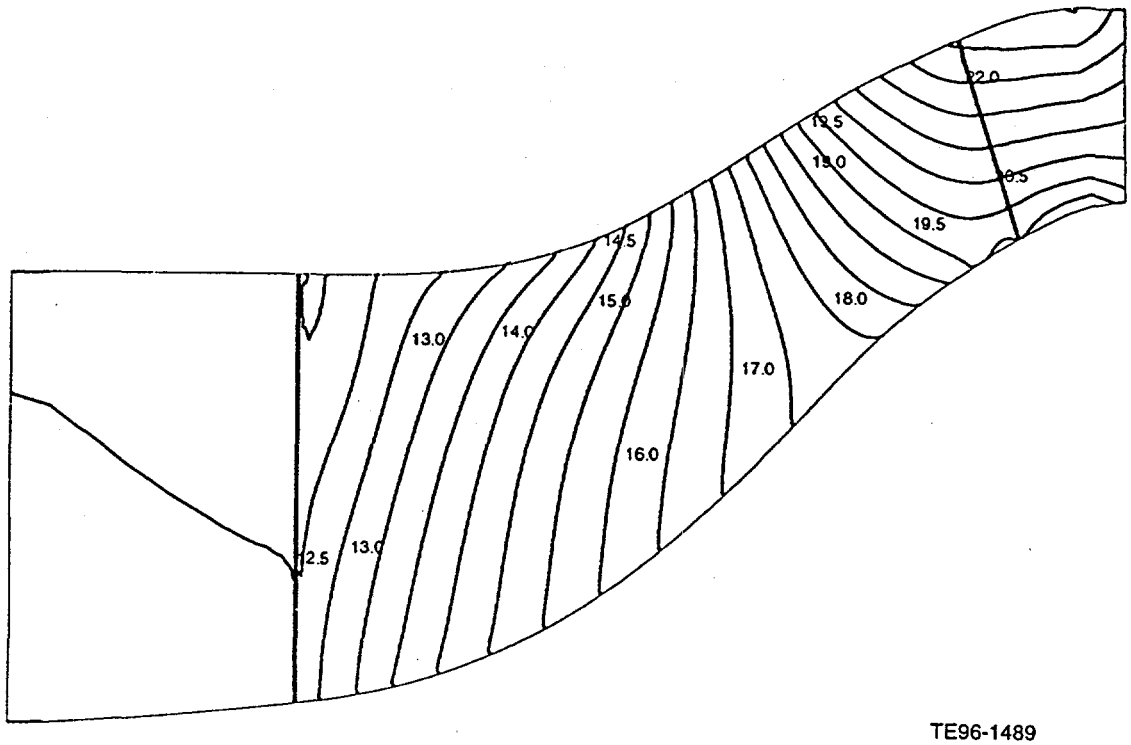

Figure 3.2.7-39. Circumferentially averaged rotor static pressure for ADPAC solution near design flow.

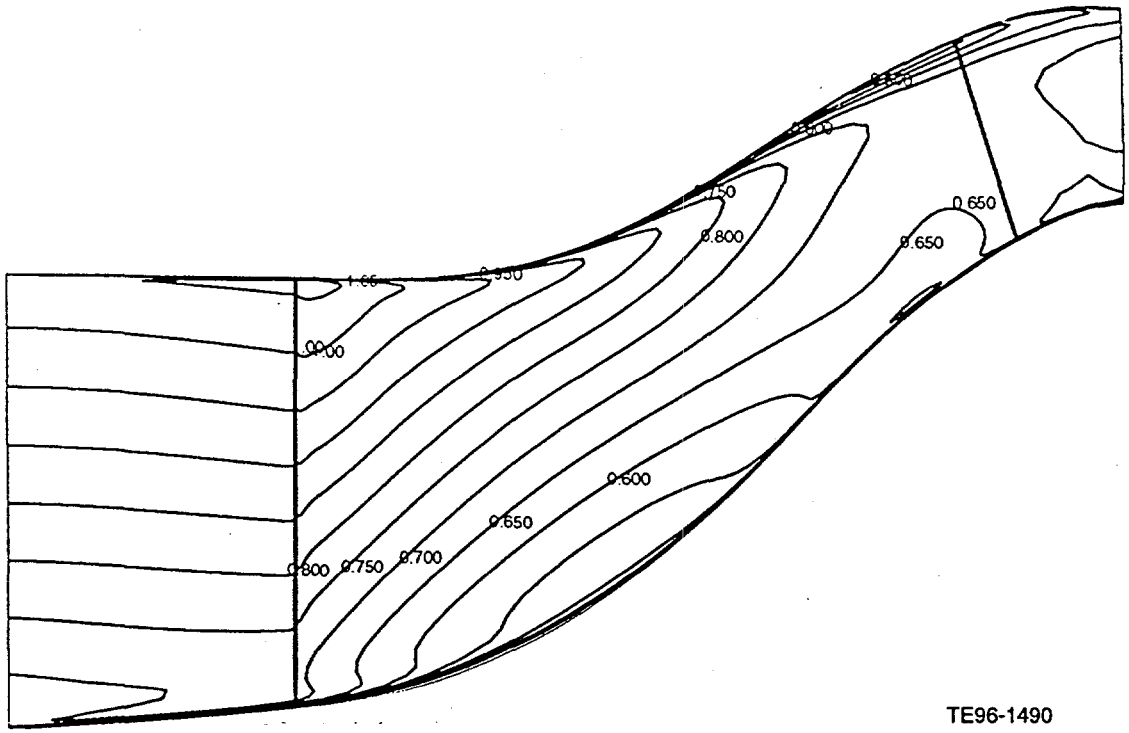

Figure 3.2.7-40. Circumferentially averaged rotor relative Mach number for ADPAC solution near design flow.

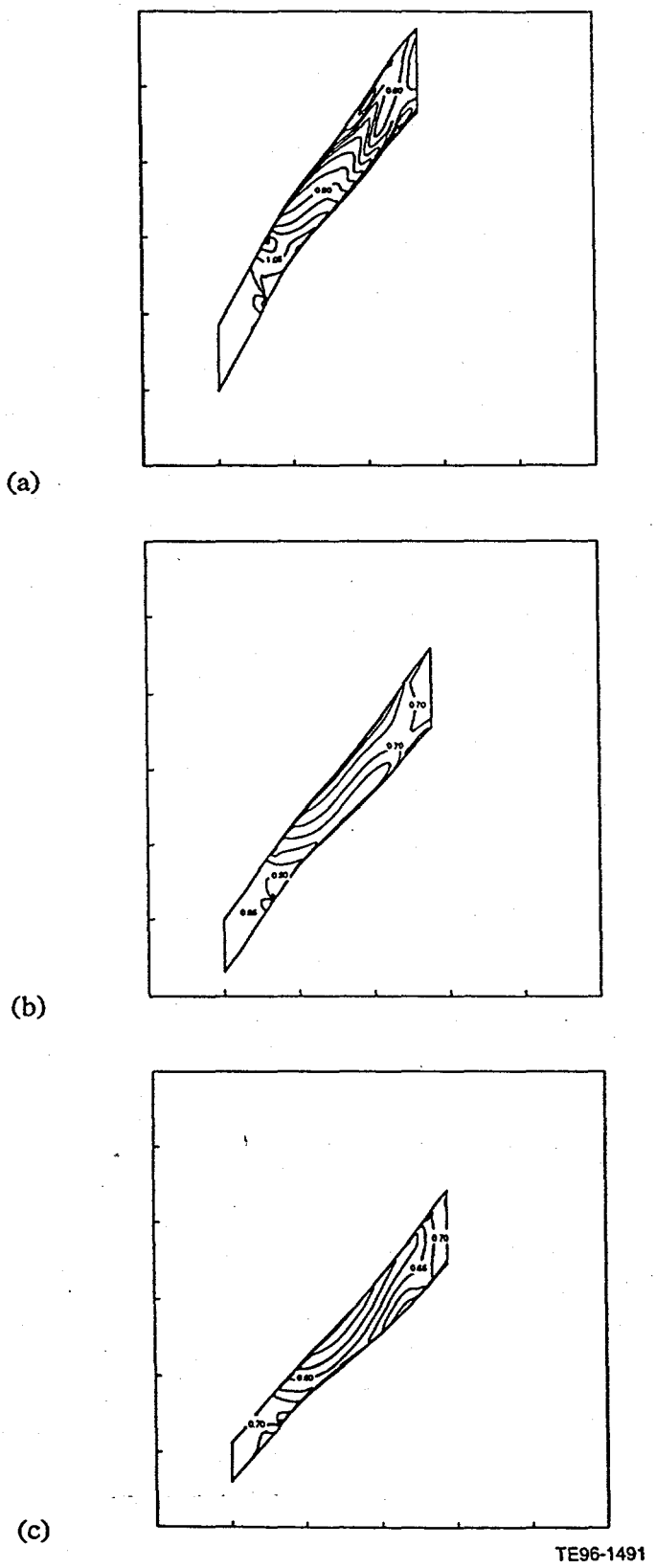

Figure 3.2.7-41. ADPAC prediction of rotor blade-to-blade relative Mach number (contour increment = 0.05) near design flow: (a) 93% span (j = 25), (b) 50% span (j = 17), (c) 7% span (j = 9).

(a)

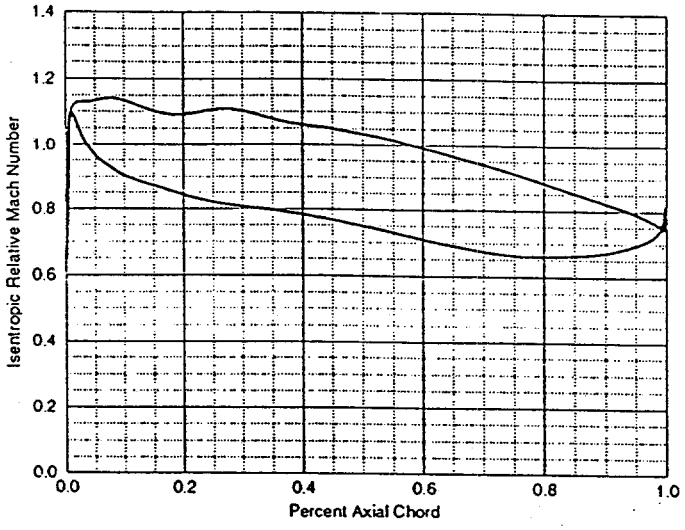

(b)

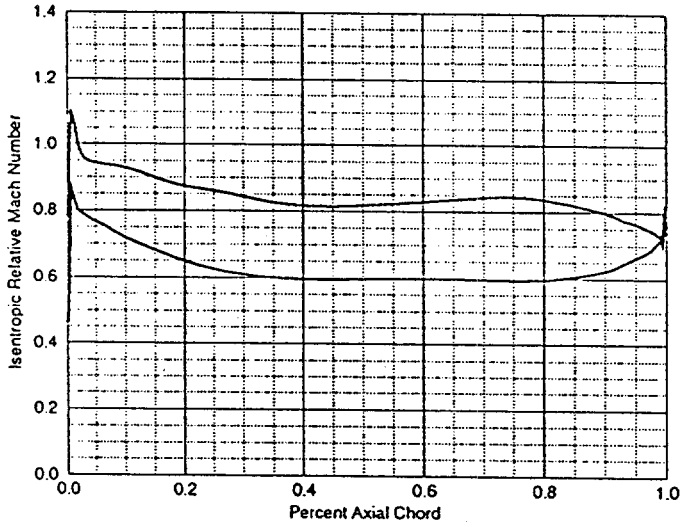

(c)

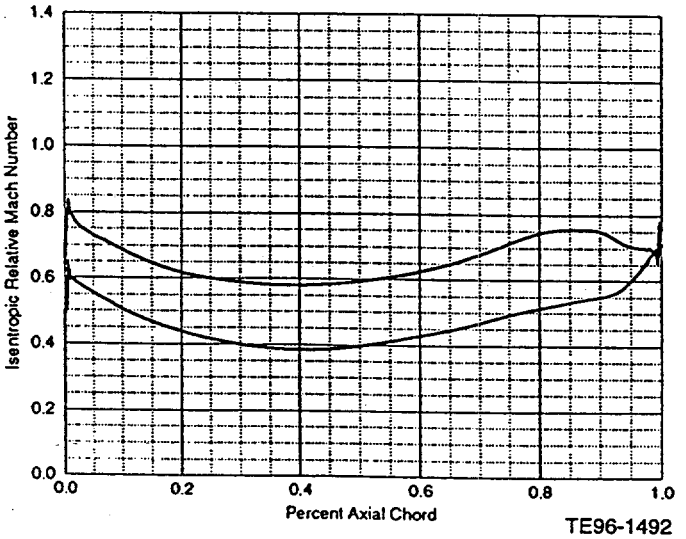

TE96-1492

Figure 3.2.7-42. ADPAC prediction of rotor isentropic Mach number distributions at design flow: (a) 93% span (j = 25), (b) 50% span (j = 17), (c) 1% span (j = 9).

Power/Flow Modulation Analysis

An analysis was developed to estimate the power/flow modulation capability of the mixed flow LP stage. The ability of the LP compressor to run efficiently at part power is important if the industrial engine is required to operate for extended periods at part load. The problem is that the HP compressor accepts less flow as the engine is throttled to part power. This tends to push the LP compressor toward stall, since it operates at constant speed, unless variable geometry stators are used to reset the rotor inlet flow angles. The conventional two-stage axial LP compressor for the ATS engine was designed with two rows of variable stators for this reason. A concern for the mixed flow stage is how effectively it can run at part power with only one row of variable vanes. To effectively reduce the amount of power required to drive the compressor, the flow and temperature rise must be decreased without drastically reducing its efficiency. A concern for the mixed flow stage is how well it can terminate temperature rise, compared to an axial stage, because of the radius change across the rotor. This issue was addressed using the analysis presented as follows.

The following procedure was developed to assess the theoretical (ideal) ability of the mixed flow rotor to operate at part power settings with a variable IGV. First, a mean-line model of the mixed flow stage at its design point was developed using an aero program for centrifugal compressors. To model each part power operating condition, the mass flow was reduced while holding rpm constant and the mean-line model was adjusted as follows:

1. The IGV angle was reset until the design incidence angle was achieved at the rotor tip. This assured sufficient surge margin at this part power condition.
2. The rotor static pressure rise coefficient was adjusted until the rotor exit blockage was held constant at its design point value. This assured reasonable Mach numbers at the rotor exit.

It is important to understand that this is an ideal analysis because the changes in loss across the IGV, rotor, and stator are not modeled. This analysis reflects the LP compressor's ideal power modulation capability. In reality, as the IGV is closed off, the losses will get higher, which increases the compressor power requirements. The only reliable way to assess the "true" power modulation capability is to experimentally measure it. Therefore, these results are only valid for IGV settings where massive flow separations and losses are avoided.

The results of this analysis are presented in Figures 3.2.7-43 through 3.2.7-45. Figures 3.2.7-43 and 3.2.7-44 show the LP compressor flow and horsepower modulation, respectively. The results are plotted versus IGV reset, which is expressed as a percentage of the most closed position. From previous experience, the most closed IGV was assumed to occur at a reset angle of 60 deg since the IGV is ineffective beyond this due to flow separation. The results show that the LP compressor inlet flow is less than 60% of the design point value for the most closed IGV. More importantly, Figure 3.2.7-44 shows that the ideal power required to drive the compressor is 40% of the design point value at the most closed IGV position. Figure 3.2.7-45 presents the mixed flow analytical results compared to test data for an Allison three-stage axial compressor. The mixed flow compressor's ideal power modulation curve compares favorably with the measured curve for the three-stage axial. This implies that the radius increase across this mixed flow rotor does not drastically reduce its power modulation capability compared to an all axial design. This conclusion is, of course, dependent on the radius increase across a particular

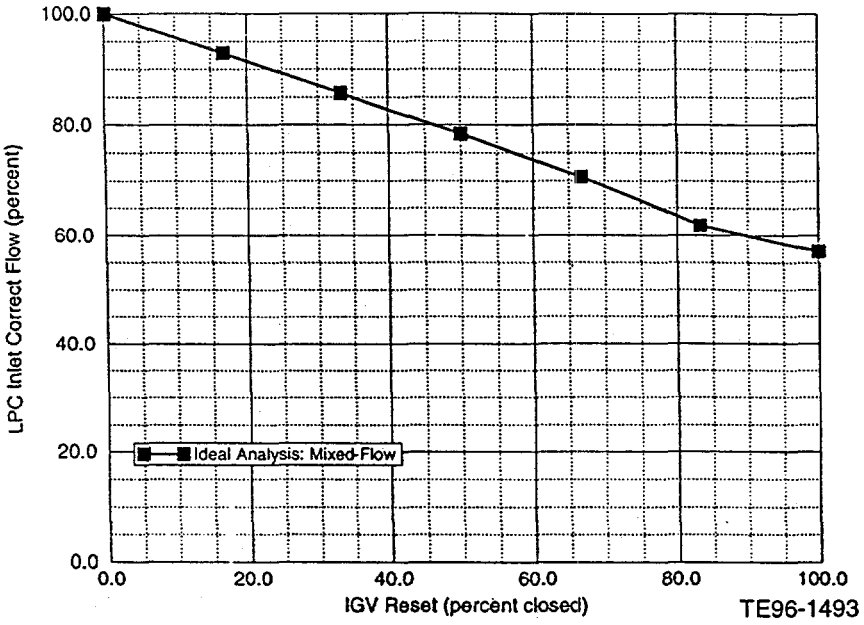

Figure 3.2.7-43. Analytical (creare) prediction of mixed-flow compressor inlet flow modulation versus IGV setting angle.

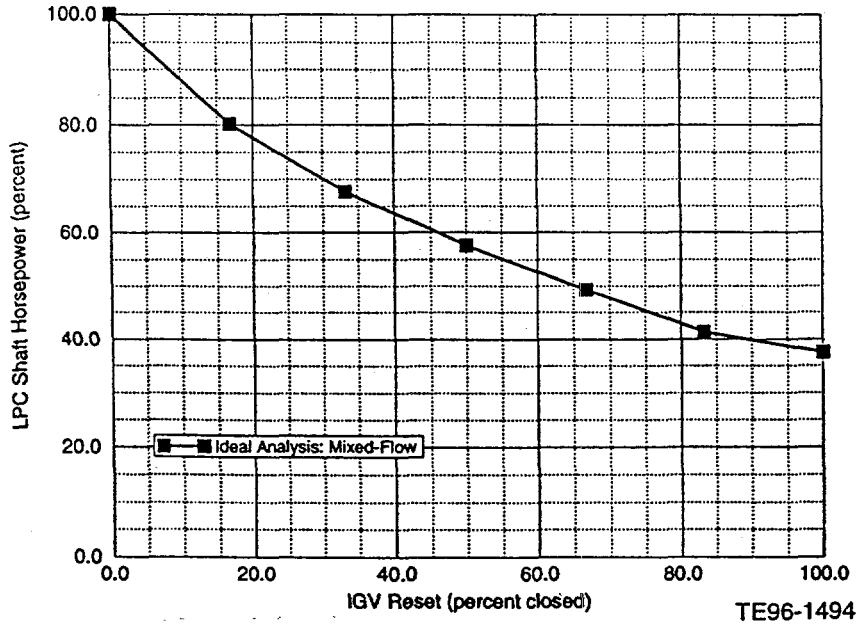

Figure 3.2.7-44. Analytical (creare) prediction of mixed-flow compressor power modulation versus IGV setting angle.

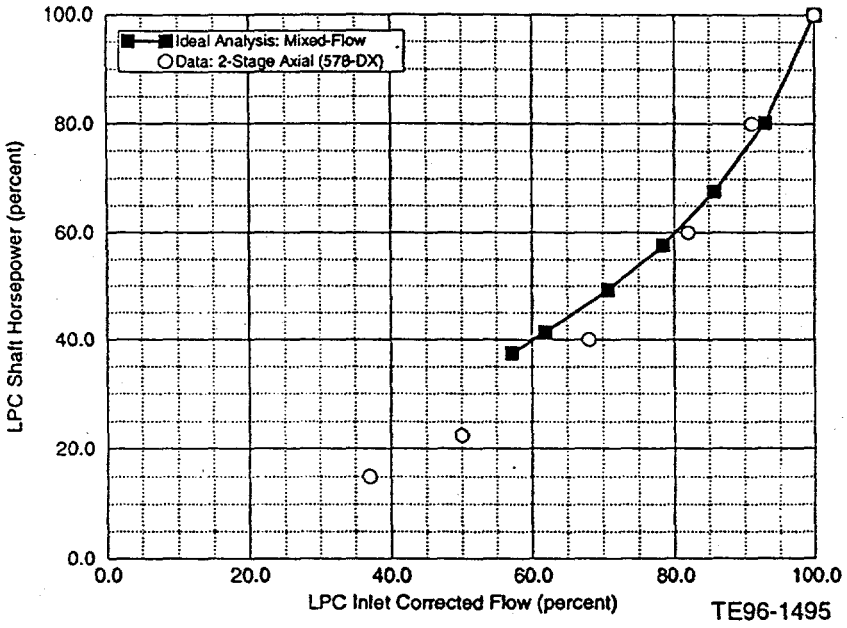

Figure 3.2.7-45. Comparison of mixed-flow and axial compressor power modulation capabilities.

mixed flow rotor. This effect will become more important for higher pressure ratio machines with larger radius increases through the rotor.

Conclusions/Recommendations

A mixed flow rotor was designed that was predicted by a 3-D viscous analysis to exceed the 92.5% rotor efficiency goal. The rotor was shown to have sufficient flow capacity but overturned the flow. An ideal analysis also was performed that indicated that the mixed flow rotor with a variable IGV could modulate the LP compressor's power below 50% of its design value.

If this mixed flow rotor design is chosen for the ATS cycle given in Table 3.2.7-I, it is recommended that the following steps be taken before the blade design is finalized for testing:

1. Redesign the rotor with 2 to 3 deg more backsweep to correct the overpumping problem.
2. Redesign the rotor shroud, as discussed in the Detailed Performance section, to reduce the rotor tip losses and to produce more favorable exit profiles for the downstream stator.
3. Perform a stress/dynamics analysis to determine if the blade thicknesses must be increased.

Stator Design

This section presents the stator design and analysis for the ATS mixed flow compressor stage. An axial type stator design with significant flow-path curvature was chosen to facilitate the turning of the rotor exit flow back into the HP compressor (see Figure 3.2.7-2). The overall sta-

tor design goals were to remove all of the rotor exit swirl and diffuse it to a Mach number of 0.5 with a loss coefficient less than 0.068 (1.9% of stator inlet total pressure). This should provide a design that efficiently ducts the flow from the mixed flow LP rotor exit to the inlet of the HP compressor.

A major objective of this study was to develop design rules for stators with significant flow-path curvature and to gain a better understanding of the 3-D flow effects. Code 2 for viscous flow was used extensively to analyze proposed stators and proved to be a valuable tool by revealing design problems caused by excessive flow-path turning that were not revealed by traditional analysis techniques.

Stator Design

Early Design Iterations—The first step in the design was to specify the flow-path midspan contour from the rotor exit to stator exit. This is an important step because it determines the amount of meridional turning through the stator which sets the strength of the flow-path curvature effects. It is desirable to maximize the amount of stator flow-path turning since it reduces the length of the downstream duct. However, too much flow-path curvature must be avoided because it adversely affects stator hub diffusion levels. In the absence of previous experience early stator flow-path designs had approximately 50 deg of meridional turning as shown in Figure 3.2.7-46. Also shown in this figure is the final stator configuration which has only about 30 deg of flow-path turning.

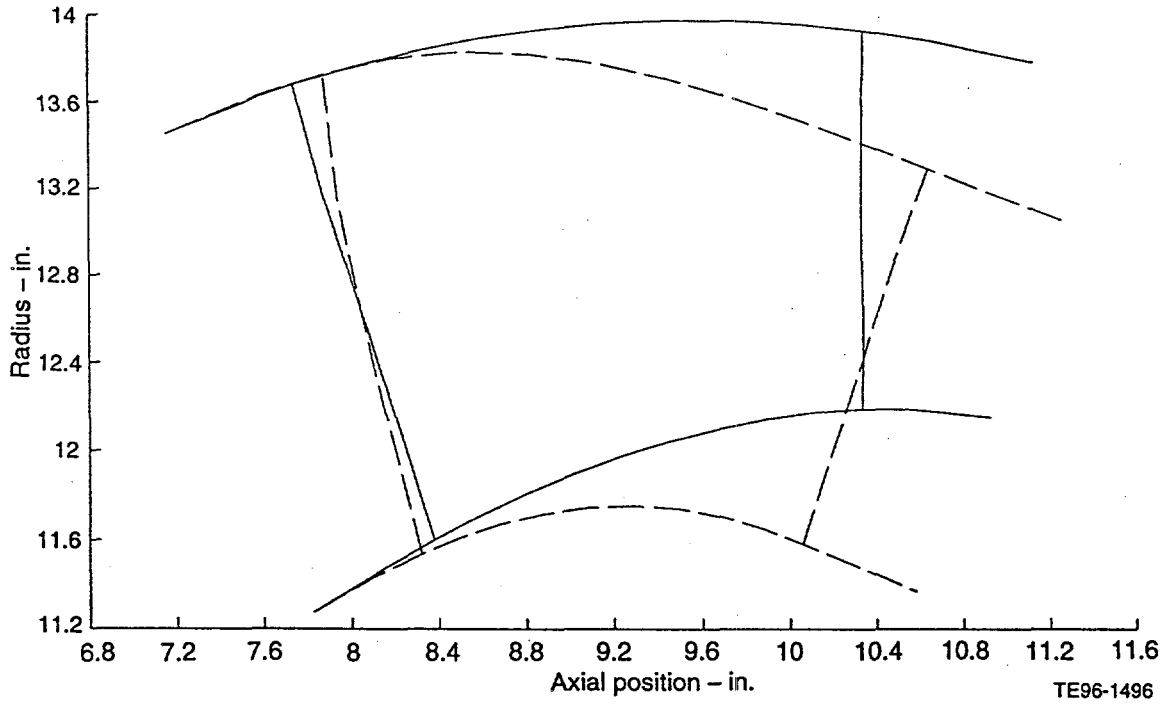

Figure 3.2.7-46. Comparison of stator flow-path configurations for mixed-flow stage: solid line = final flow path with 30-deg turning, dashed line = early flow path with 50-deg turning.

The early stator configurations that had 50 deg of flow-path turning were not successful designs. Code 2 3-D viscous predictions for these configurations showed large suction surface separations on the lower 30% span. The flow separation was caused by the adverse effects of flow-path curvature on the vane surface loading near the hub (the two-dimensional D factor was less than 0.35 for some of these designs). Many attempts were made to correct the hub separation problem by redesigning the stator geometry while leaving the overall flow-path turning through the stator unchanged. The following stator design modifications were attempted:

1. Increase solidity by increasing chord and number of vanes.
2. Recontour hub flow path to move the maximum curvature toward the trailing edge while holding the overall flow-path turning at 50 deg.
3. Redesign stator hub sections (lower 50% span) with arbitrary mean-line angles to reduce the rate of diffusion through the passage.
4. Redesign stator hub sections (lower 50% span) with reduced turning to allow 10 deg of swirl at the stator hub exit.
5. Close stator exit area by 5% to reduce overall streamwise diffusion while leaving the overall flow-path turning at 50 deg.

The code 2 predictions for these modified stator designs still showed vane surface separation near the hub. It became apparent that the overall flow-path turning would have to be reduced to 30 deg through the stator as shown in Figure 3.2.7-46. This was an unavoidable design compromise that resulted in increasing the curvature of the downstream duct and extending the length of the LP compression system by 3 in. (see Figure 3.2.7-2).

Final Design Configuration—This section presents the design details of the final stator configuration. The hub and shroud contours were specified based on meridional flow area considerations. The vane geometry was designed using an Allison axial compressor design program code and the axisymmetric flow field was analyzed using the a streamline curvature code. The stator geometry was designed with zero exit swirl for the inlet conditions shown in Figure 3.2.7-47. These conditions were obtained by scaling the rotor exit profiles predicted by code 2 to give stator inlet conditions for a rotor design that satisfies the rotor design goals specified in the Rotor Design section. The code 2 rotor exit profiles also were modified to reflect a rotor redesign with a cleaned up shroud flow field (see the Inlet and Exit Radial Profiles section). The axial compressor design program model was set up using an IGV to introduce the stator inlet swirl instead of modeling the mixed flow rotor. An attempt was made to generate the desired stator inlet conditions in the design code by modeling the mixed flow rotor with conical endwalls, but this was unsuccessful because of the inability to accurately capture flow-path curvature effects near the rotor trailing edge.

The profiles given in Figure 3.2.7-47 show that the stator was designed for a shroud inlet Mach number of 0.58 and flow angle of 54 deg. The shroud flow turning was higher than typically acceptable for conventional axial stator designs, but the low streamwise diffusion and favorable effects of flow-path curvature reduce the vane surface loading such that this amount of turning was not a problem. The main area of concern was the hub with an inlet Mach number of 0.69 and flow angle of 39 deg. Near the hub the flow-path curvature tends to increase the suction surface adverse pressure gradient, which means that less turning will be possible than for a conventional stator with straight endwalls.

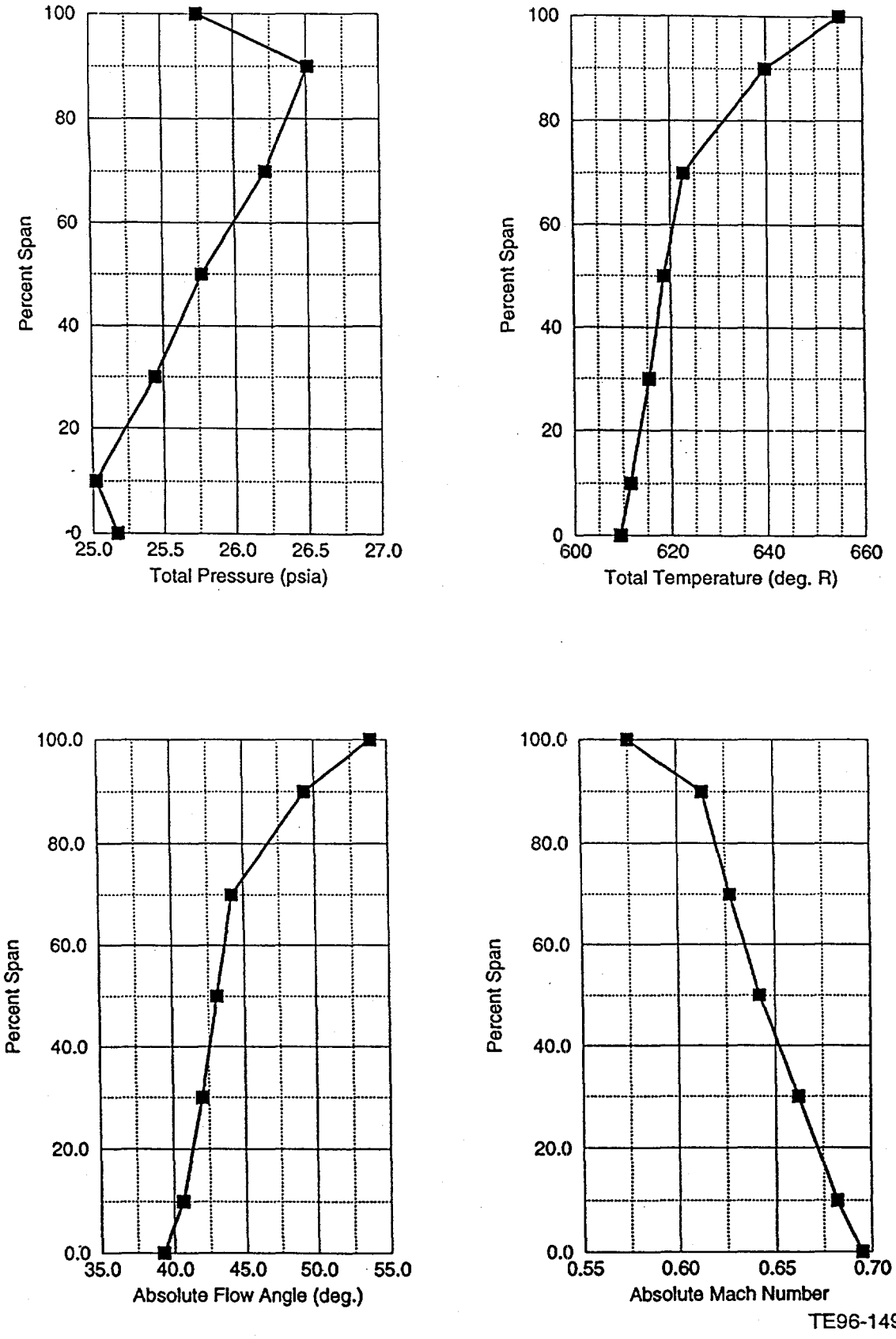

Figure 3.2.7-47. Inlet conditions for stator design (scaled rotor exit profiles from ADPAC analysis).

As a starting point, the stator geometry was generated using analytic double circular arc (DCA) surface definitions on circular arc mean lines. A design incidence of -1 deg was chosen for all vane sections and a 2-D deviation rule was used to set the exit mean-line angles for zero exit swirl. The viscous code was used to predict the three-dimensional effects on the exit flow angle which was then used to correct the deviation rule for subsequent design iterations. The chord length and number of vanes (59) was selected to give a mean-line solidity of about 1.8, as shown in Figure 3.2.7-48. The vane thickness/chord was originally set at 5% at the hub and 3% at the shroud. Thicker vanes may be needed for dynamic stress reasons. Leading edge and trailing edge radii of 0.010 in. were used.

Streamline Curvature Code Analysis

The results of an axisymmetric streamline curvature code analysis of the final stator configuration is given in Figures 3.2.7-49 through 3.2.7-53. The flow path, which has roughly 30 deg of flow-path turning, is shown in Figure 3.2.7-49. The maximum curvature levels for the hub and shroud were approximately 0.3 (1/ft) and 0.2 (1/ft), respectively. The predicted Mach number and static pressure fields are given in Figures 3.2.7-50 and 3.2.7-51, respectively. It is important to remember that these are axisymmetric averages that give no indication of the maximum or minimum values on the vane surface. Figure 3.2.7-50 shows that the overall Mach number levels are generally higher near the hub than the shroud. The hub streamline experiences an acceleration to a Mach number of 0.73 as it enters the passage and then diffuses to a value of 0.60 near the exit. The hub diffusion for this stator was much lower than previous stator configurations with 50 deg of flow-path turning. The shroud streamline sees a flow deceleration on the forward 60% of the vane and a slight acceleration on the rear portion of the vane. The exit

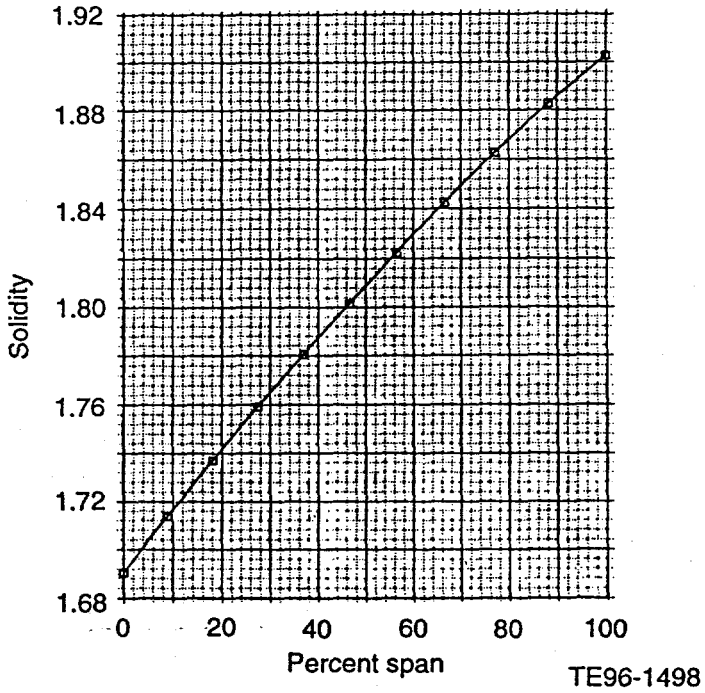

Figure 3.2.7-48. Solidity distribution versus span for final stator configuration.

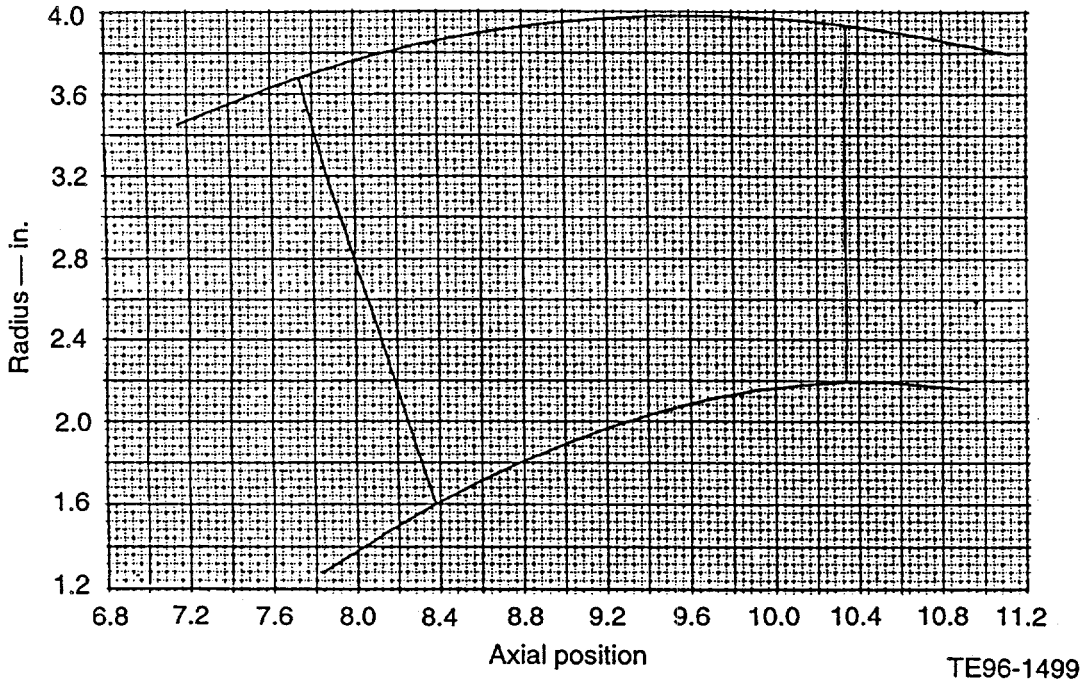

Figure 3.2.7-49. Final stator flow path for streamline curvature analysis (UDO300).

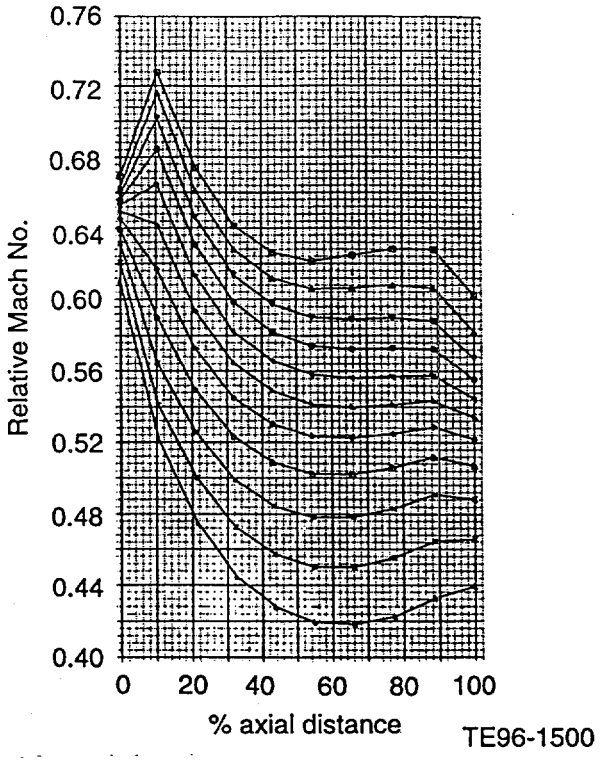

Figure 3.2.7-50. Streamline curvature prediction of stator axisymmetric Mach number distribution.

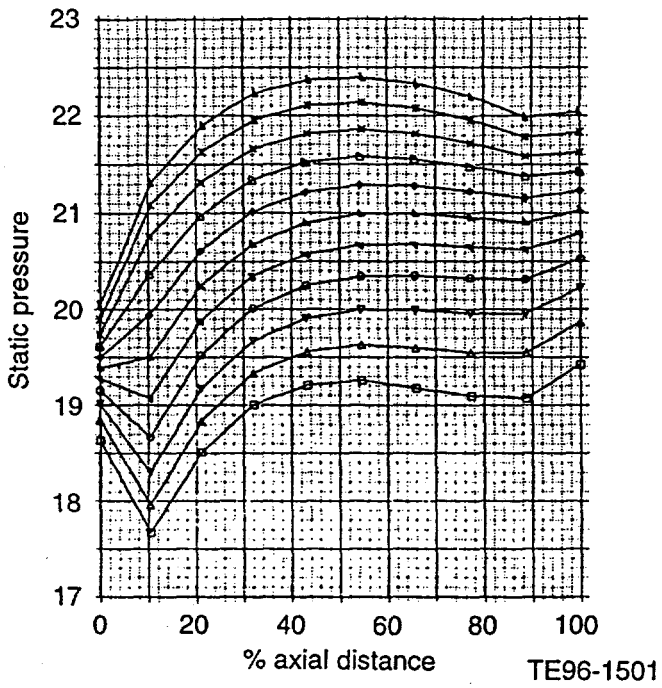

Figure 3.2.7-51. Streamline curvature prediction of stator axisymmetric static pressure distribution.

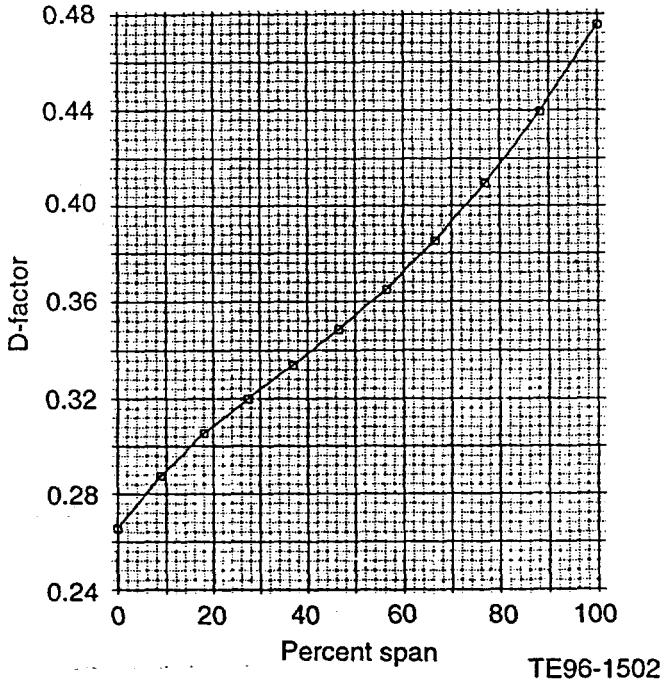

Figure 3.2.7-52. Streamline curvature prediction of stator diffusion factor (based on two-dimensional cascade definition) versus span.

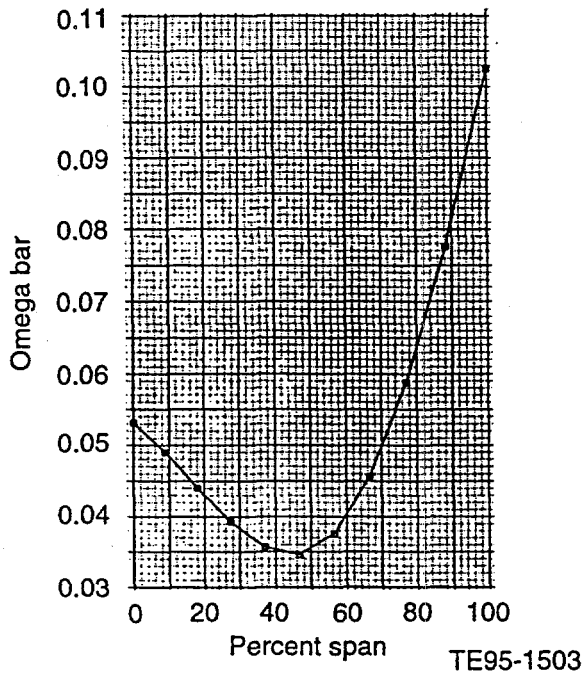

Figure 3.2.7-53. Streamline curvature prediction of stator loss-coefficient versus span (based on empirical correlation versus D factor - loss set 64).

Mach number profile is hub strong with a midspan value of 0.535 which is higher than the design goal of 0.50. The static pressure field in Figure 3.2.7-51 shows similar trends. It is interesting that the flow-path curvature causes a shroud strong exit static pressure profile even though the flow swirl has been removed.

Figure 3.2.7-52 gives the traditional gage of vane loading, the diffusion factor, versus span. The D factor is only given here as a rough gage of the actual diffusion level since it only accounts for the 2-D effects of streamwise diffusion and vane element turning. The effects of meridional flow-path curvature on the suction surface diffusion is not captured by this parameter. As alluded to earlier, flow-path curvature tends to increase the effective D factor near the hub and decrease it near the shroud. The main limitation of the axisymmetric code analysis is its inability to predict the effects of flow-path curvature on the peak suction surface velocities. A more advanced streamline curvature code with coupled throughflow and vane-to-vane calculations could be used to capture these effects. During this stator design, viscous code 2 was used to evaluate the 3-D flow diffusion levels. Figure 3.2.7-53 gives an estimate of the stator loss coefficient (omega-bar) based on an empirical D factor (2-D) correlation. If the effects of flow-path curvature on vane surface loading are considered, the hub loss will tend to be higher and the shroud loss lower than shown in Figure 3.2.7-53. An important observation is that the average stator loss coefficient based on this correlation meets the design goal of 0.068. The 3-D viscous analysis also was used to estimate the loss for this design.

3-D Viscous Code Analysis

The grid used for the viscous flow analysis, shown in Figure 3.2.7-54, was generated using an Allison grid generation code. The final mesh had a total of 194,000 grid points. The solutions were obtained using parallel versions of code 2 on the 64 processor NCube computer. A range of solutions with various back pressures were run until the correct mass flow was achieved. Solution convergence was determined by monitoring the inlet and exit mass flow and total pressure loss.

The code 2 results were used to assess the stator overall performance. The analysis predicted an overall loss of 0.6% of the stator inlet total pressure, which corresponded to a loss coefficient of 0.026. It is not known how accurately code 2 can predict stator loss since the code has not been rigorously validated against stator test data. However, it is apparent that even if the actual loss magnitude is twice the predicted value, this stator still meets the design goal loss coefficient of 0.068.

The circumferentially averaged radial profiles are presented in Figures 3.2.7-55 through 3.2.7-59. The stator inlet and exit absolute flow angle profiles are shown in Figure 3.2.7-55. Recall that the stator inlet flow angle boundary condition was set to match the scaled code 2 rotor exit conditions. The exit flow angle profile shows that most of the swirl was removed, even though this stator was designed with a delta deviation table derived from a previous stator design configuration. Some overturning is observed near the endwalls, due to secondary flows, which could be accounted for in future designs using endbends. The difference between the inlet and exit profiles shows that more flow turning is done near the shroud than the hub and that the midspan turning is 43 deg. Recall that the shroud is able to do more turning due the favorable effects of flow-path curvature. It is also noteworthy that no large separated flow regions were observed.

Figure 3.2.7-56 gives the stator inlet and exit Mach number profiles. The inlet profile matches the goal hub and shroud values from the scaled code 2 rotor exit profiles relatively well. However, the inlet profile shape is flatter than desired, which causes the midspan inlet Mach number to be low. The reason for this discrepancy is that code 2 boundary conditions are

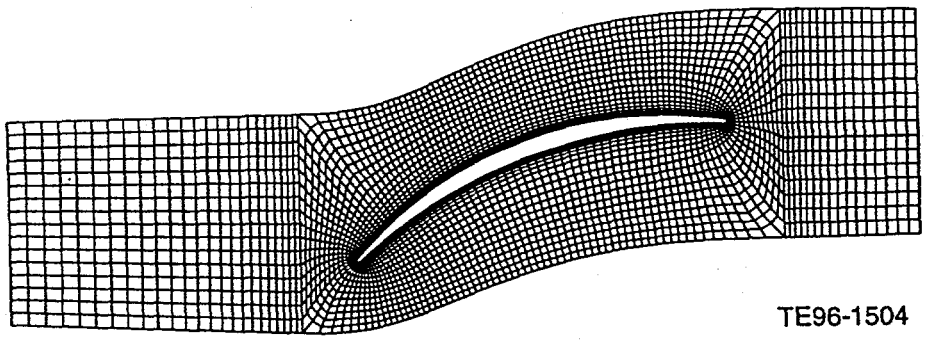

Figure 3.2.7-54. Stator mesh system used for viscous flow analysis.

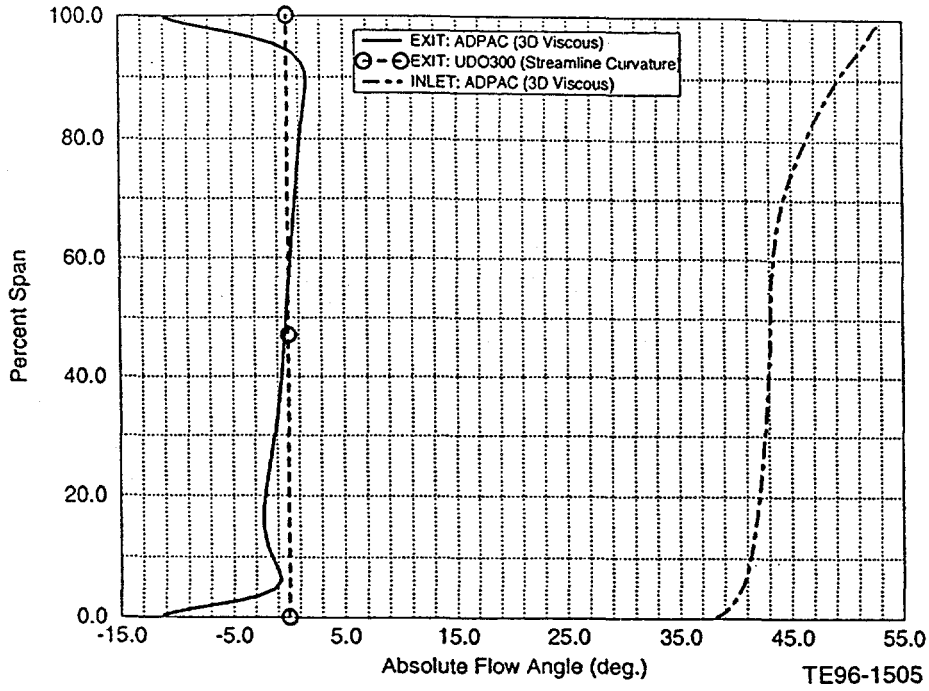

Figure 3.2.7-55. Predicted stator absolute flow angle profiles at design flow.

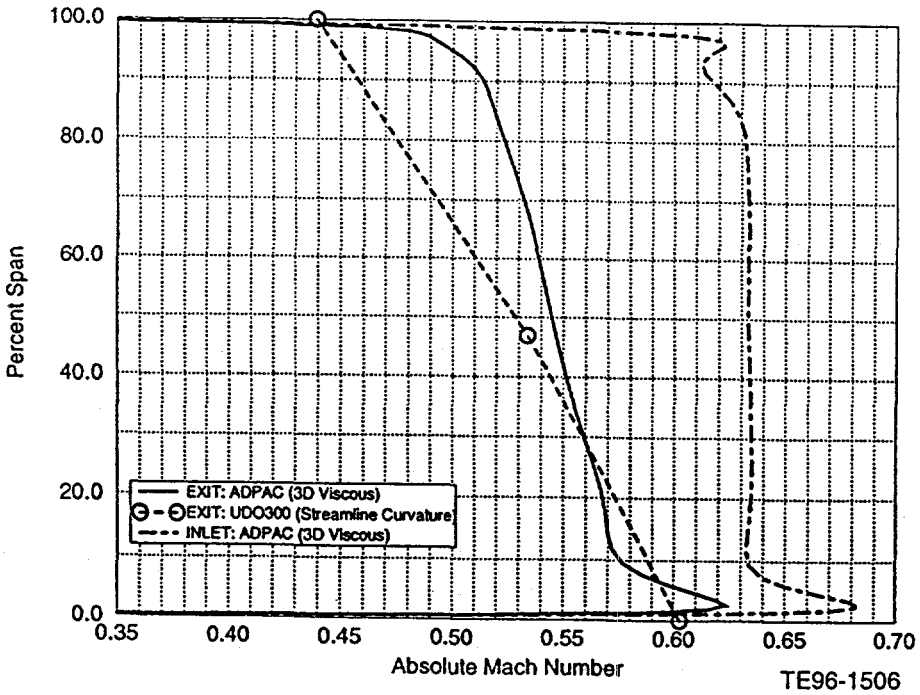

Figure 3.2.7-56. Predicted stator absolute Mach number profiles at design flow.

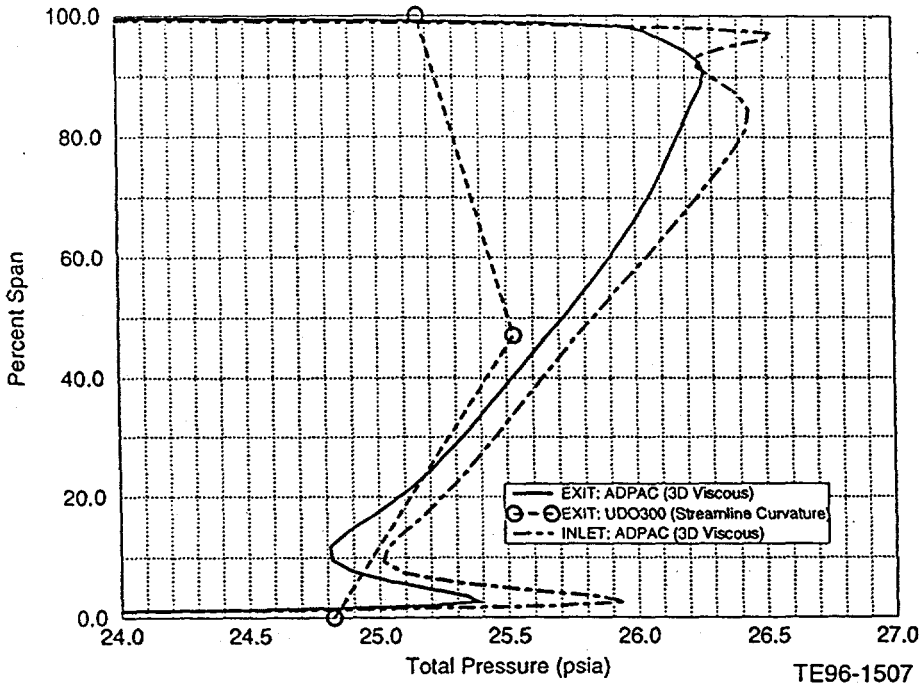

Figure 3.2.7-57. Predicted stator total pressure profiles at design flow.

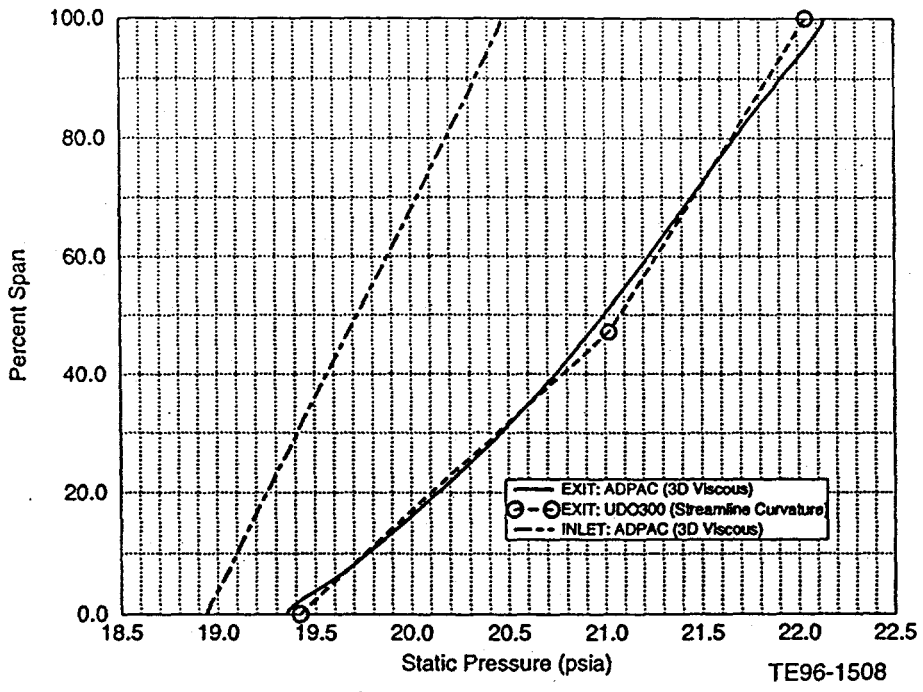

Figure 3.2.7-58. Predicted stator static pressure profiles at design flow.

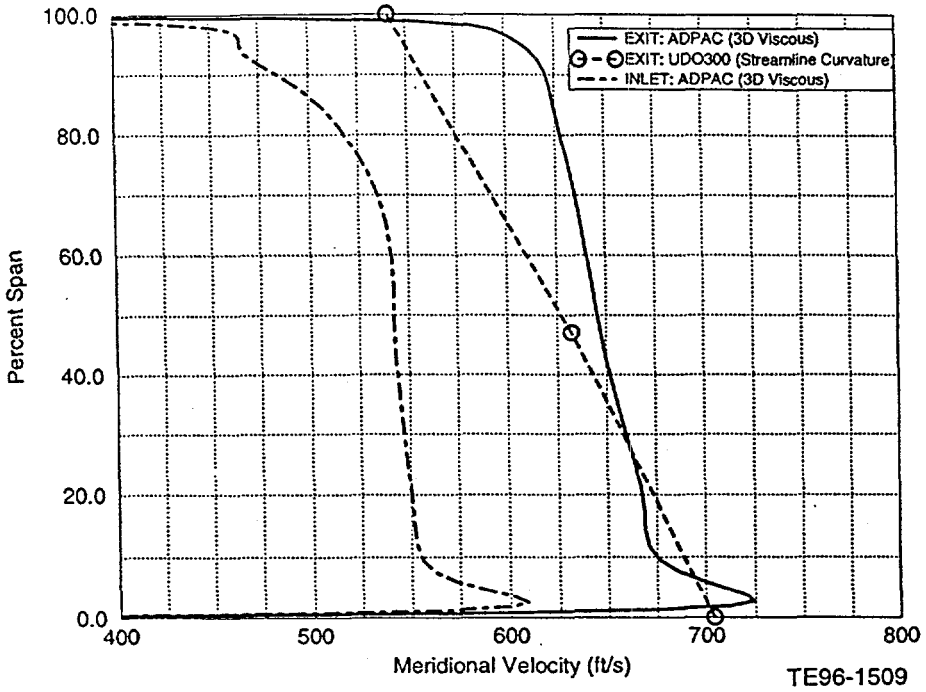

Figure 3.2.7-59. Predicted stator meridional velocity profiles at design flow.

formulated to set the inlet total pressure, total temperature, and flow angle profiles, and the hub exit static pressure. The inlet Mach number profile then "falls out" from the static pressure field, which is strongly influenced by flow-path curvature upstream of the leading edge. This discrepancy in the inlet Mach number profile was caused by inaccurate modeling of the streamline curvature effects upstream of the rotor trailing edge. A stator mesh was generated with a grid that extended upstream of the rotor trailing edge using a fictitious flow-path definition. A better way to model the stator flow field would be to couple the rotor and stator solutions via a mixing plane boundary condition. The discrepancy in the inlet Mach number profile is small enough that the current results are still meaningful. The exit Mach number profile in Figure 3.2.7-56 shows that the streamwise diffusion near the hub is lower than the shroud and that the overall streamwise diffusion across the vane is low. The hub strong exit Mach number profile should be useful for negotiating the curvature of the downstream duct.

The inlet and exit total pressure profiles are given in Figure 3.2.7-57. The interesting features from this figure are that the total pressure loss is evenly distributed over the span and that the predicted loss magnitude is low. Figure 3.2.7-58 gives the inlet and exit static pressure profiles. As expected from the other flow properties, more static pressure rise is done near the shroud than the hub. Figure 3.2.7-59 shows the inlet and exit meridional velocity profiles. This figure is interesting because it shows that the meridional velocity is actually being accelerated through the vane, even though the total velocity is diffused by removing the swirl from the flow.

The surface isentropic Mach number distributions are given in Figure 3.2.7-60 for grid lines near 10, 50, and 90% span. This is an important figure because it gives information related to the effect of flow-path curvature on vane surface diffusion which is used to assess the possibility of vane boundary layer separation. Recall that the streamline curvature code analysis only

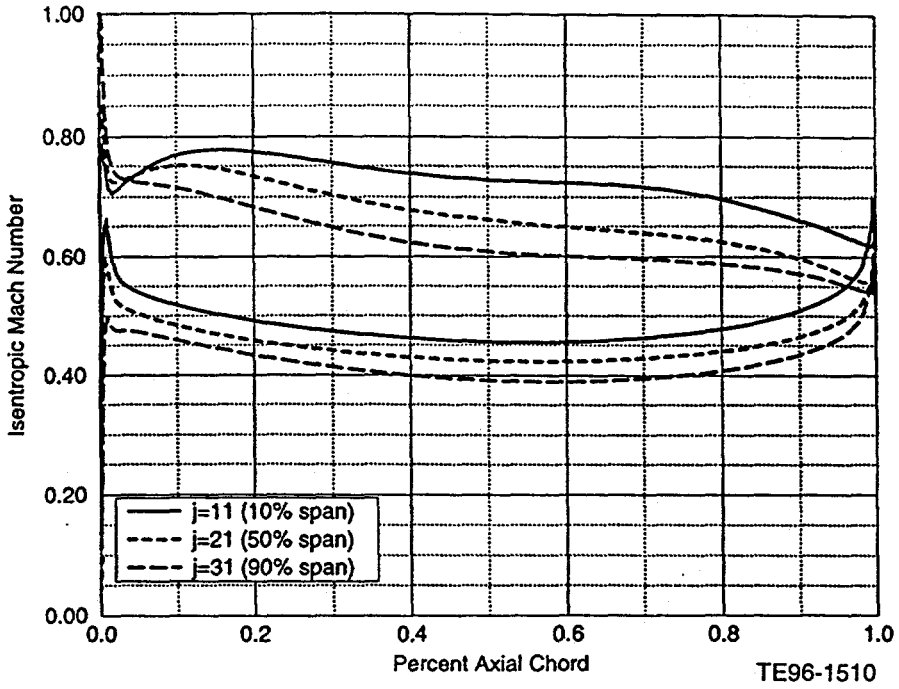

Figure 3.2.7-60. ADPAC prediction of stator isentropic Mach number distributions at design flow: (a) 90% span (j = 31), (b) 50% span (j = 21), (c) 10% span (j = 11).

gives the axisymmetric average diffusion through the passage. The streamline near the hub shows a mild deceleration from a peak Mach number of 0.78 to a value of 0.62 near the trailing edge. This implies that the suction surface boundary layer for streamlines near the hub should not separate or generate excess loss. The streamline near the tip is very interesting because the favorable effect of the flow-path curvature is apparent. The code 2 analysis shows that the suction surface flow sees little deceleration, although the stator is turning the flow 53 deg and diffusing the streamwise Mach number from 0.62 to 0.51 (a two-dimensional D factor of 0.48). The code 2 analysis clearly shows that the main effect of flow-path turning is to noticeably relieve vane loading near the shroud and increase it near the hub. These effects should be considered when choosing the spanwise stator velocity diagrams. The use of traditional 2-D cascade type load parameters and design rules may lead to stator designs that do not perform as intended.

Conclusions/Recommendations

A stator was designed for the mixed flow compressor stage that was predicted by a 3-D viscous analysis to meet, or exceed, its loss coefficient goal of 0.07 (1.9% of stator inlet total pressure). This implies that the mixed flow LP compressor will meet the ATS stage efficiency design goal of 89.2%. The analysis also predicted that the stator would efficiently remove the rotor exit swirl and provide a reasonable exit Mach number for the downstream duct. The resulting stator had 30 deg of flow-path turning to reduce the stage length. The final mixed flow configuration, including the ducting to the HP compressor, was 3 in. longer than the proposed two-stage axial design. An analysis of the downstream duct was performed using the Allison axial compressor design program which indicated that flow separation should not occur.

If this mixed flow stage design is chosen for the ATS cycle given in Table 3.2.7-I, it is recommended that the following issues be addressed before the stator design is finalized for fabrication:

1. Perform a dynamic stress analysis to determine if the stator thicknesses must be increased.
2. Run a coupled rotor/stator 3-D viscous analysis to verify stator inlet conditions. Reset stator inlet angles accordingly.
3. Analyze off-design stator performance using the 3-D viscous code to assess the choke and stall flow range.

Cost Analysis

A preliminary cost analysis of the customer's internal rate of return was performed for various assumed levels of reduced LP compressor efficiency. The associated increased cost of additional fuel usage and reduced output power was weighed against the estimated reduced initial engine procurement cost resulting from the lower recurring cost of the mixed flow design (less parts). Based on a 20-year period, for the ATS engine application the cost analysis showed that when the mixed flow design was assumed to be 1% less efficient than the two-stage axial flow design goal, an approximate break-even condition resulted. However, this was before factoring in significant nonrecurring costs associated with the mixed flow design, including extensive rig testing and the procurement of necessary manufacturing equipment.

Extensive rig testing would be required due to the unique and untested nature of the ATS mixed flow LP compressor. The rig testing would be used to thoroughly map its aerodynamic performance characteristics and to verify it mechanically from stress and dynamic standpoints. This testing would require rig adaptive hardware specifically designed for testing the mixed flow design. The rig testing associated with the two-stage axial design would be far less extensive and need relatively little unique rig adaptive hardware due to its aerodynamic and mechanical similarity to other thoroughly tested axial compressors.

Allison has historically machined the compressor wheels, both axial and centrifugal, used in its engines. Due to the overall size of the ATS mixed flow LP compressor rotor, it would not be possible to machine one on existing equipment at Allison. The cost of procuring the required machine for manufacturing the mixed flow rotor has been estimated as high.

Results

A single-stage mixed flow LP compressor (rotor and stator) was aerodynamically designed specifically for the ATS engine application as part of this subtask. Advanced 3-D viscous flow analysis of the mixed flow design predicted comparable performance to the goals of the two-stage axial flow design at the ATS engine design point. Due to the mixed flow rotor's radial exit flow component and the stator's associated turning requirement, a 3 in. flow-path length increase compared to the two-stage axial design is needed to satisfactorily duct the air to the HP compressor inlet. An off-design point operation 'ideal' analysis was also performed. It indicated that a variable IGV could successfully be used with the mixed flow rotor to modulate the LP compressor down at least to operating conditions requiring 50% less drive power than at design point.

This modern, high efficiency single-stage mixed flow design is essentially a new technology. Therefore, extensive rig testing with significant nonrecurring costs would be necessary to prove the design before it could be released. Significant nonrecurring costs associated with procuring necessary manufacturing equipment would also be incurred. Risk of falling short of the predicted performance must be considered in program planning as well. These factors combine to make the mixed flow approach unattractive at this time for the ATS application from an economic and technical risk perspective. This is true in spite of its favorable recurring costs and the extensive design and 3-D viscous flow analysis effort that indicated it would have comparable performance to the goals of the two-stage axial flow design at the ATS engine design point.

3.2.8 Increased LP Rotor Speed

Objective

The original objective of this task was to improve engine efficiency by increasing component efficiency. The principal idea was that increasing the speed of the LP turbine would increase its efficiency. Based on preliminary studies by the Turbine Aerodynamics and the Structural Mechanics groups, no significant efficiency improvement was identified for any reasonable increase in the LP rotor speed. The objective was then redirected to analyze reducing the LP turbine from four to three stages as a means of lowering engine cost.

Discussion

Turbine efficiency was the primary design concern that led to the selection of a moderately loaded, high efficiency, four-stage power turbine for the ATS engine. This turbine was close-coupled to a derivative of Allison's AE 301X HP turbine. This portion of the Phase 2 Add-on technical effort involved two design trade studies. The first study assessed the aerodynamic and mechanical trade-offs associated with increased power turbine mechanical speed. The second evaluated the impact of reduced power turbine stage count on performance, which would have the added benefit of reduced cost. The results of these two studies are presented in the following paragraphs.

PT Mechanical Speed Study

The rotational speed of the four-stage baseline power turbine was consistent with an exit Mach number of 0.35 and an exit AN^2 number of 6. The diffuser loss will be directly proportional to the exit Mach number, and exit AN^2 is a factor used to determine the acceptability of blade to wheel attachment stresses. Both of these values are compatible with current industrial engine design practices using conventional turbine materials.

Sensitivity of the baseline power turbine's efficiency to increased rotational speed was to be determined in this study. Increased mechanical speed results in reduced stage loading due to a reduction in the work required to turn the air. Speed was incrementally increased and the change in power turbine efficiency was calculated using Allison's design point efficiency prediction code. This computer code is an extension of the work of Ainley & Mathieson. The results of this study are shown in Figure 3.2.8-1. Data from the plot indicate increasing power turbine speed 10% will provide an efficiency gain of only 0.3 %, with a corresponding exit AN^2 of approximately 7.3. This value of AN^2 imposes an unacceptable mechanical risk when using conventional turbine materials. Preliminary investigation showed that the potential cost of developing and testing advanced materials for this purpose was not justified considering the small gain in efficiency that was predicted.

PT Stage Count Study

The definition of the optimum ATS power turbine must consider both initial acquisition costs and thermodynamic efficiency, and how these parameters affect the overall cost effectiveness of the power generation system. The acquisition cost of an axial flow turbine is essentially

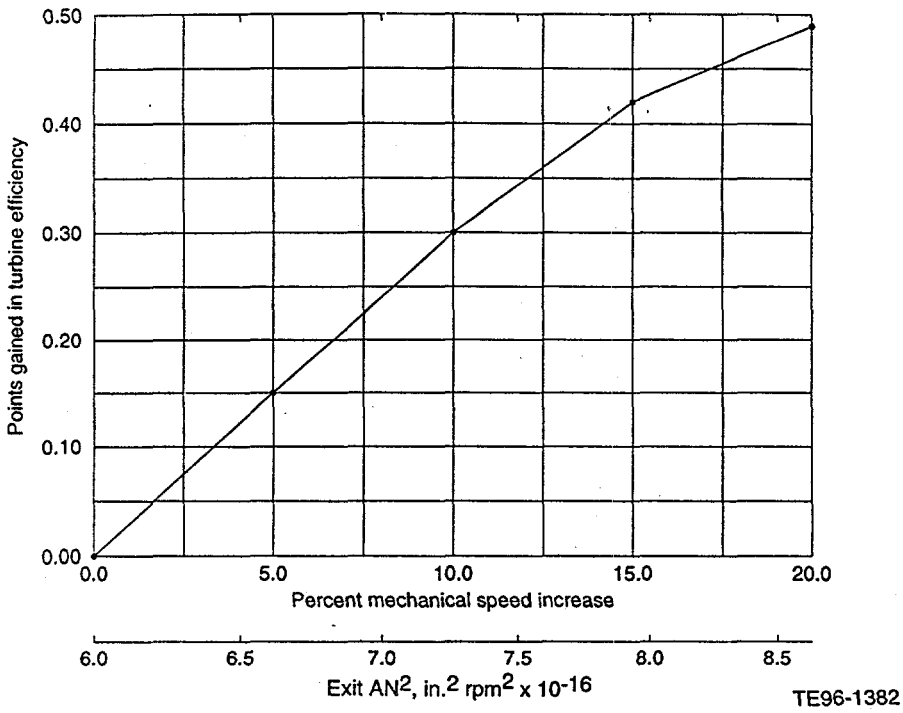

Figure 3.2.8-1. ATS power turbine—sensitivity of baseline efficiency to increase in speed.

proportional to stage count. However, for a well-designed turbine, reducing stage count characteristically lowers component performance.

The purpose of this trade study was to quantify the loss in power turbine performance associated with reducing the stage count from four (the baseline turbine) to three stages. A three-stage power turbine was designed with comparable loadings, reactions, work split, exit Mach number, swirl, and AN^2 levels to that of its four-stage counterpart. To achieve these loadings, the turbine was moved radially outward and an interturbine duct was required between the HP and power turbine as shown in the flow-path comparison of Figure 3.2.8-2.

The average stage loadings for the three stages are similar to those of the four stages as shown in Figure 3.2.8-3. Generally, a four-stage turbine would be more efficient than a three-stage turbine due to the reduced amount of turning per stage. This results in lower stage loading and a corresponding efficiency increase.

The duct was designed to have minimum loss using diffuser duct loss correlations based on the work of Sovaran & Klomp. Duct pressure loss (delta P_t/P_t) was estimated at 0.5%, which equates to a power turbine efficiency loss of 0.2%. In addition, the three-stage power turbine itself was predicted to have 0.5% lower efficiency than the baseline four-stage machine. The total effective penalty in utilizing a three-stage power turbine, including the inter turbine duct, is 0.7% in efficiency.

As a part of this study, an Allison AE 3012 HP turbine, a turbine with a 25% higher corrected airflow, was matched to the new three-stage ATS power turbine. The AE 3012 is another model being developed in the Allison AE family of engines. This resulted in net increases in overall

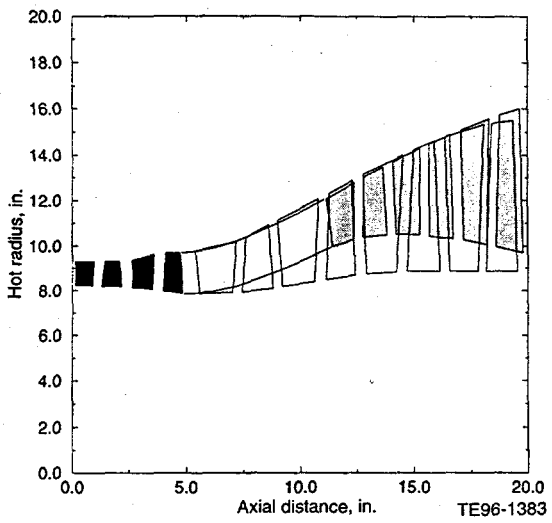

Figure 3.2.8-2. Candidate ATS three-stage power turbine flow path compared to baseline.

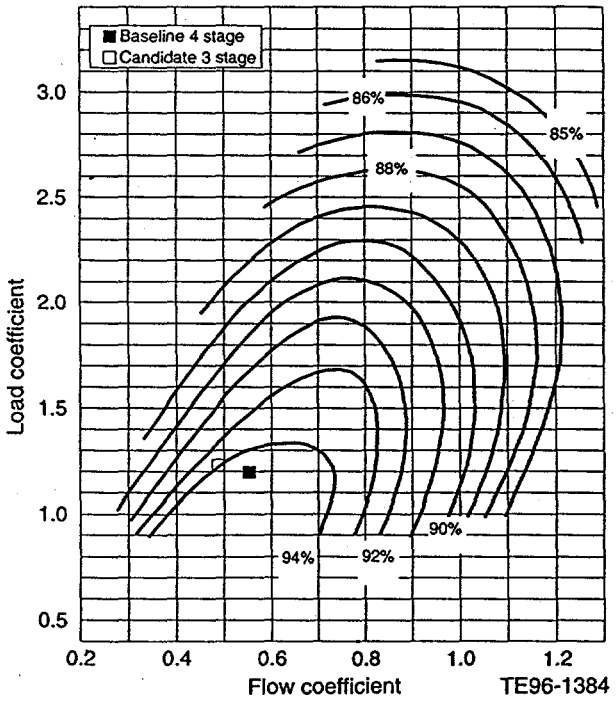

Figure 3.2.8-3. Efficiency correlation for zero tip losses—ATS three-stage power turbine maintains baseline flow-path load coefficient.

engine efficiency and horsepower of 0.1% and 0.2%, respectively. Combining these increases with an approximate $50,000 hardware cost reduction yields an increase in IRR from 22.8% to 23.125% (+ 0.315%).

Results

In summary, increasing the power turbine mechanical speed is not deemed to be cost effective. Switching to a larger diameter three-stage power turbine configuration with the previous AE 300X based HP turbine results in an overall component efficiency loss of 0.7% when compared to the four-stage close-coupled machine. However, this configuration results in an approximate $50,000 reduction in cost. Using the AE 3012 HP turbine gives an overall engine efficiency and horsepower increase and results in a higher internal rate of return for the customer. This configuration will be pursued under Phase 3A of the ATS program.

3.2.9 Surge Protection Valve Study

Objective

To meet the ultra-low emissions goals of the program, the ATS engine has a silo combustor sized for a relatively large volume of high pressure and temperature air. Due to the large volume, it is felt that there may be an increased risk of severe engine damage if a surge should occur. This subtask was created to investigate the need for surge protection, and also to investigate the control and mechanical systems required.

Discussion

Compressor surges, while infrequent, may occur in industrial gas turbine engines due to potential causes such as inlet blockage, engine mishandling, and fuel scheduling problems. In the event of a violent surge, severe damage to the compressor flow-path hardware can occur from the pressure pulses (mechanical deflections) and airfoil heating (thermal growth and rub, or melting). A preliminary study was conducted to determine if surge protection was necessary.

During surge and stall, blade heating takes place. This may result from a very small net flow occurring during some parts of the stall process, with the compressor churning a large amount of energy into the small amount of flow. The ATS combustor is approximately 10 times larger than that of a compact system not designed for low emissions. The relatively large volume of combustor air carries the hazard of blade melting during the stall process, preliminarily establishing the need for surge protection. It is estimated that a 4-in. diameter bleed valve downstream of the compressor exit would reduce the combustor pressure by one half in approximately 0.1 sec after stall. Allowing for a 0.1 sec actuation delay, the compressor should recover within 0.5 sec. Since it is believed that compressor blade melting in stagnation takes several seconds to occur, such a valve should be adequate protection.

During the study another concern surfaced relative to the large combustor volume and the associated amount of stored energy. The concern was for the potential of an overspeed in the event of an electrical generator load loss. A preliminary study was conducted to determine if overspeed protection was necessary.

Generator inertia is the dominant output shaft term in an overspeed. With a normal size combustor and typical generator, the energy stored in the combustor volume is equivalent to approximately a 4% speed increase. This value rises to approximately 30% for the ATS silo combustor. Other factors affect the speed increase, such as amount of fuel flow injected after load loss based on control system response time, and the duration of combustion continuation based on the nature of the combustor's flow field. In common combustors the flame is suppressed by the rotating stall cell, whereas in the ATS engine combustion is expected to continue and contribute to extra overspeed. Generators are typically designed with a 25% overspeed margin and the ATS engine would therefore require pressure relief in addition to rapid fuel flow reduction. For the ATS output shaft, the initial acceleration rate is estimated to be about 35%/sec. Since this is relatively slow due to the generator's high inertia, the bleed valve would quickly suppress the acceleration.

An initial study of the mechanical systems and control requirements was performed. Mechanically, it has been determined that one valve can be doubly useful by providing protection from either event (surge or overspeed). The valve needs to be located downstream of the compressor exit to prevent the induction of hot combustion air into the compressor. The valve would be located on the combustor outer case and vent to the engine exhaust. Due to its exposure to combustor inlet air, it will need to have relatively high temperature and pressure capability for a mechanical valve.

Modern engine digital electronic controls have more than sufficient memory and computing power available for any calculations, schedules, or algorithms required for the ATS engine. Spare digital and analog inputs and outputs exist on the digital controls. For surge protection, the valve could be triggered by a differential pressure transducer signaling the large negative rate of change in pressure associated with surge. For overspeed protection, it would be appropriate to trigger the bleed valve to open with an output power based signal. A signal should also be provided that indicates that the engine is no longer connected to the grid. The bleed valve could either be an open/close or modulated type. A modulated valve would require a feedback signal to the control. The control would already be integrated with the engine compressor variable geometry system, so compressor airflow could also be modulated. For both protections provided, it would be appropriate to link the valve's actuation to fuel flow reduction or cancellation, depending on other system considerations such as the need to keep the engine operating for process steam.

Results

The need for surge protection—and in the electrical generating application, overspeed protection—from the large volume of high energy gas in the ATS silo combustor has been preliminarily identified. Both protections can be provided by a single bleed valve mounted on the combustor outer case and vented to the exhaust. The high temperatures involved present challenges, as specialized valving would be required. General control system requirements have been identified and are believed to be achievable.

3.2.10 Update Design Sketches

Objective

Several of the design studies that were planned for the Phase 2 Extension may result in changes to the basic engine configuration. This subtask provides for the revision of the General Arrangement drawing that was developed in Phase 2 of the program.

Discussion

Two of the subtasks had the potential to lead to major changes in the ATS engine configuration: 6.07 - Study of Mixed Flow Compressor and 6.08 - Increased LP Rotor Speed. The mixed flow compressor, which would replace the two-stage LP compressor with a single-stage compressor, was unattractive on the basis of cost effectiveness. As a result, it was dropped from consideration and no drawing revision was required.

The subtask to evaluate the potential for improving LP turbine efficiency by increasing rotor speed was also shown to have an adverse effect on life cycle cost. The increased part costs resulting from the material changes required to increase speed outweighed the cost savings associated with the increased efficiency. This subtask was then redirected, with the agreement of the COR, to determine the cost effectiveness of reducing the number of stages in the LP turbine. This study showed that a significant improvement could result from such a change. As this reconfiguration was explored further, it was determined that even greater benefits in the areas of cost, efficiency, and power could be made if more extensive changes were made to the engine. It was decided that the effort to define these changes would exceed the scope of this subtask. Therefore, the further development of the revised configuration was incorporated into Phase 3A of the program, thereby obviating the need to revise the engine General Arrangement drawing.

Results

No revisions to the engine General Arrangement drawing were identified during the Phase 2 Extension portion of the ATS program.

3.2.11 Effect of Thin Walls and Coatings on Single Crystal Mechanical Properties

Objective

Mechanical property testing of single crystal alloys has previously focused on cast-to-size specimens with thicker walls than walls of current cooled blades. Thin walls and protective coatings are known to have adverse effects on a material's mechanical properties. To quantify these effects on ATS mechanical components (primarily turbine blades and vanes), thin wall specimens with prospective coatings were tested.

The focus was on the selection of protective coating materials, and the effects these coatings have on mechanical properties of thin wall configurations of CMSX-4 single crystal alloys subjected to an elevated temperature environment. To quantify the effects on ATS components, a particularly thin sheet-type specimen was used for conducting creep-rupture testing under isothermal laboratory conditions.

Discussion

Three types of oxidation/environmental protection coatings (Allison electrophoretic [AEP] Pt-Al, conventional Pt-Al, NiCoCrAlY coating) for CMSX-4 single crystal alloys were selected for ATS component application. Figure 3.2.11-1 shows three of the coated samples after testing. Figure 3.2.11-2 shows the comparison plots of rupture stress as a function of rupture life under an imposed stress-oxidation environmental condition. The evidence from this figure indicates that, at the equivalent stresses and the specimen geometric configuration, the short time rupture life for the NiCoCrAlY overlay coating is superior to the short time rupture life of the conventional Pt-Al coating. Note that this analysis does not take into account the volume and density of the coating for centrifugal loads.

From the results shown in Figure 3.2.11-2, preliminary Larson-Miller plots were created for the NiCoCrAlY coated and Pt-Al coated samples (Figures 3.2.11-3 and 3.2.11-4). Larson-Miller curves incorporate stress-rupture strength, time, and temperature into a single presentation that can be used directly for mechanical design. The figures display the data gathered to date, with the long-time data points in the 400-hr range.

To fully quantify the effects of the prospective coatings on ATS components, and to better identify the rupture life characteristics of each coating, it is necessary to conduct the creep-rupture tests at the higher test temperatures over a longer test time. The influence of the protection system superalloy interdiffusion on the test results can be fully understood after the continued testing. To use the extrapolation methodology based on the Larson-Miller plot to predict creep rupture life over 10,000 hr, data are needed to 1,000 hr or more.

Note that a substantial amount of time under this Phase 2 Add-on task was spent obtaining the single crystal alloy specimens with acceptable microstructure alignment. Delays obtaining specimens caused the testing start dates to be delayed, resulting in the need to continue testing beyond the contractual end for ATS Phase 2 Add-on.

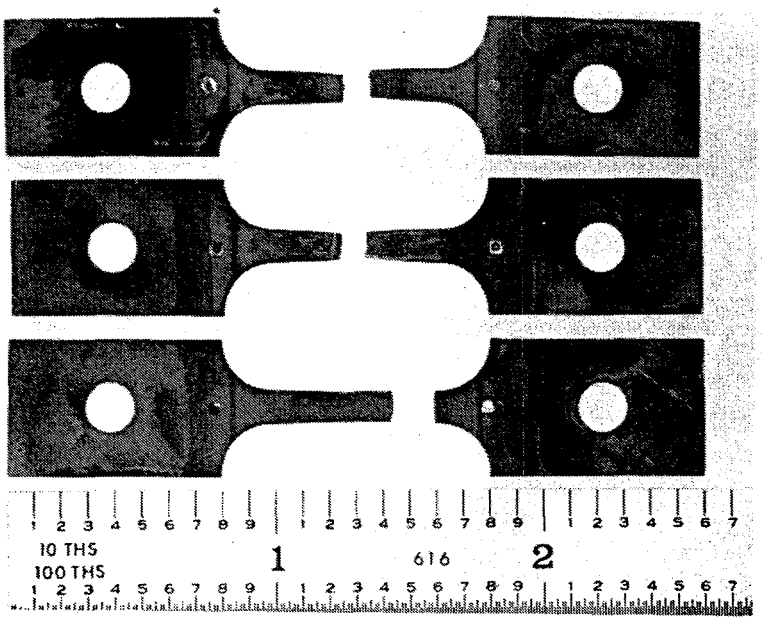

Figure 3.2.11-1. Coated single crystal specimens after testing.

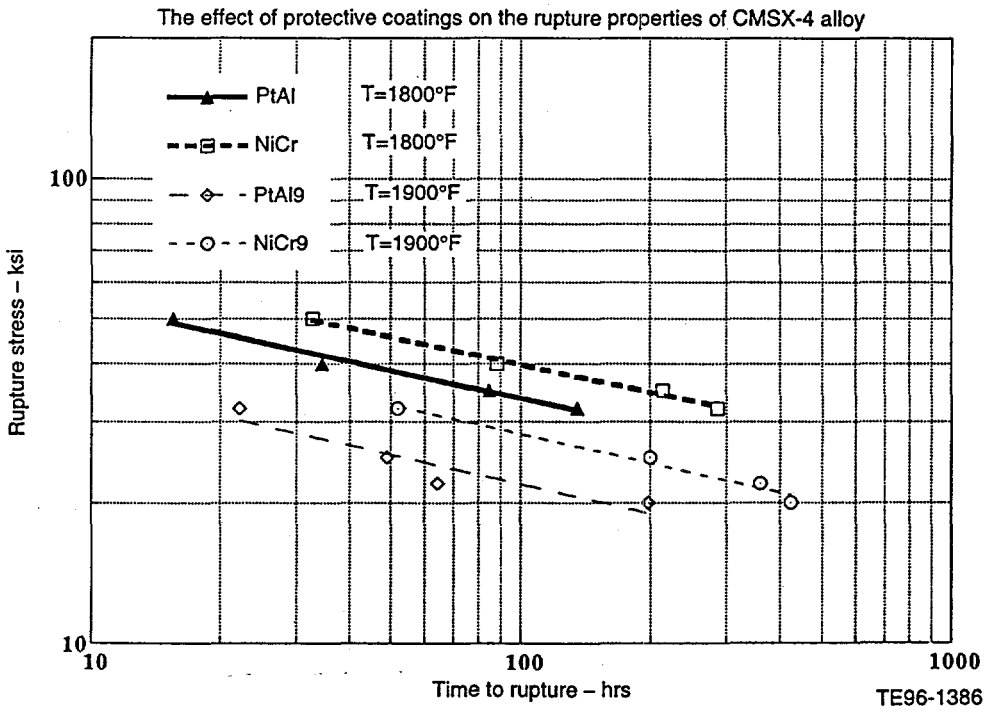

Figure 3.2.11-2. Rupture stress versus rupture life for NiCoCrAlY and conventional Pt-Al coatings.

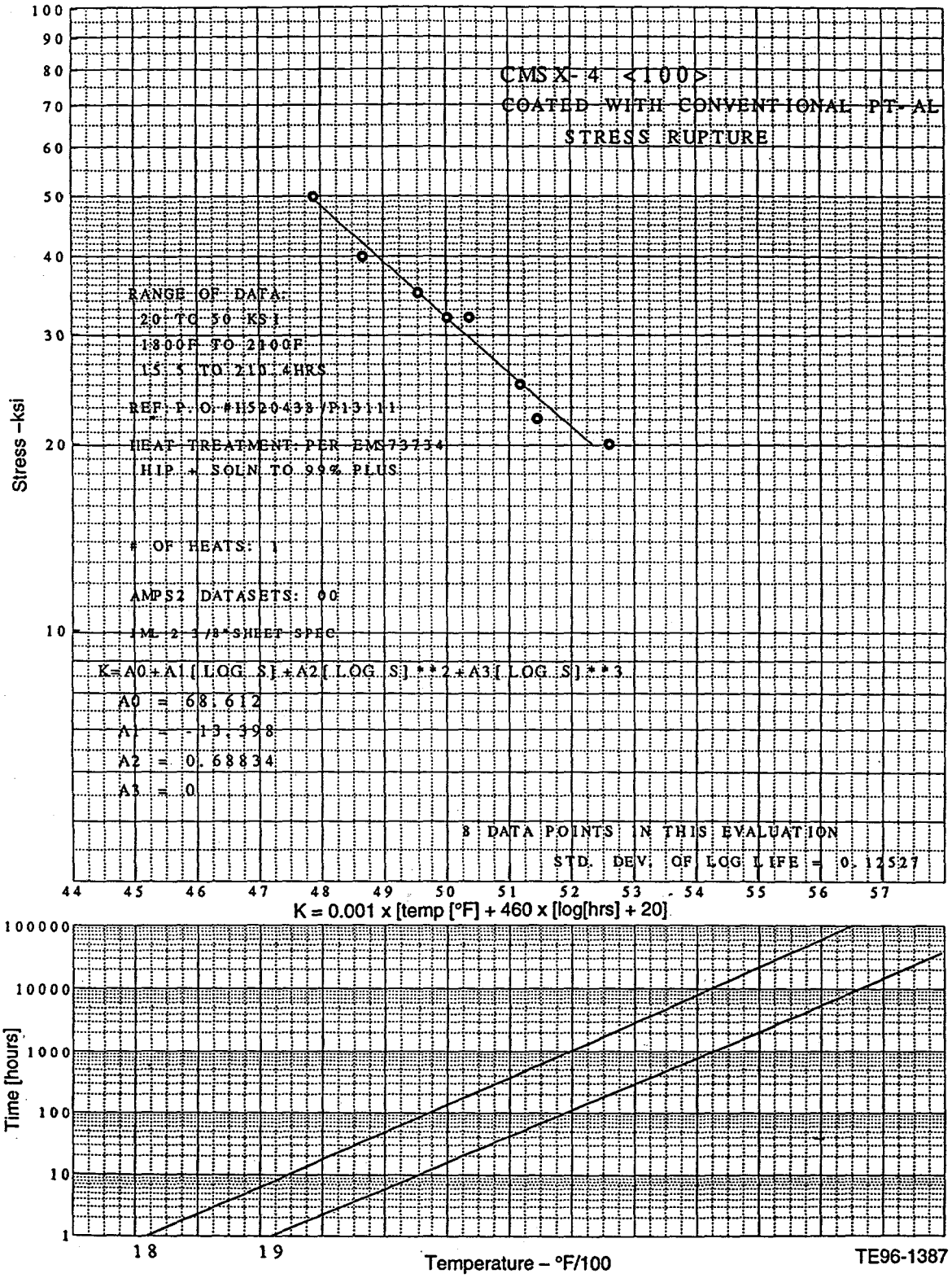

Figure 3.2.11-3. Larson-Miller curve for conventional Pt-Al coated single crystal specimens.

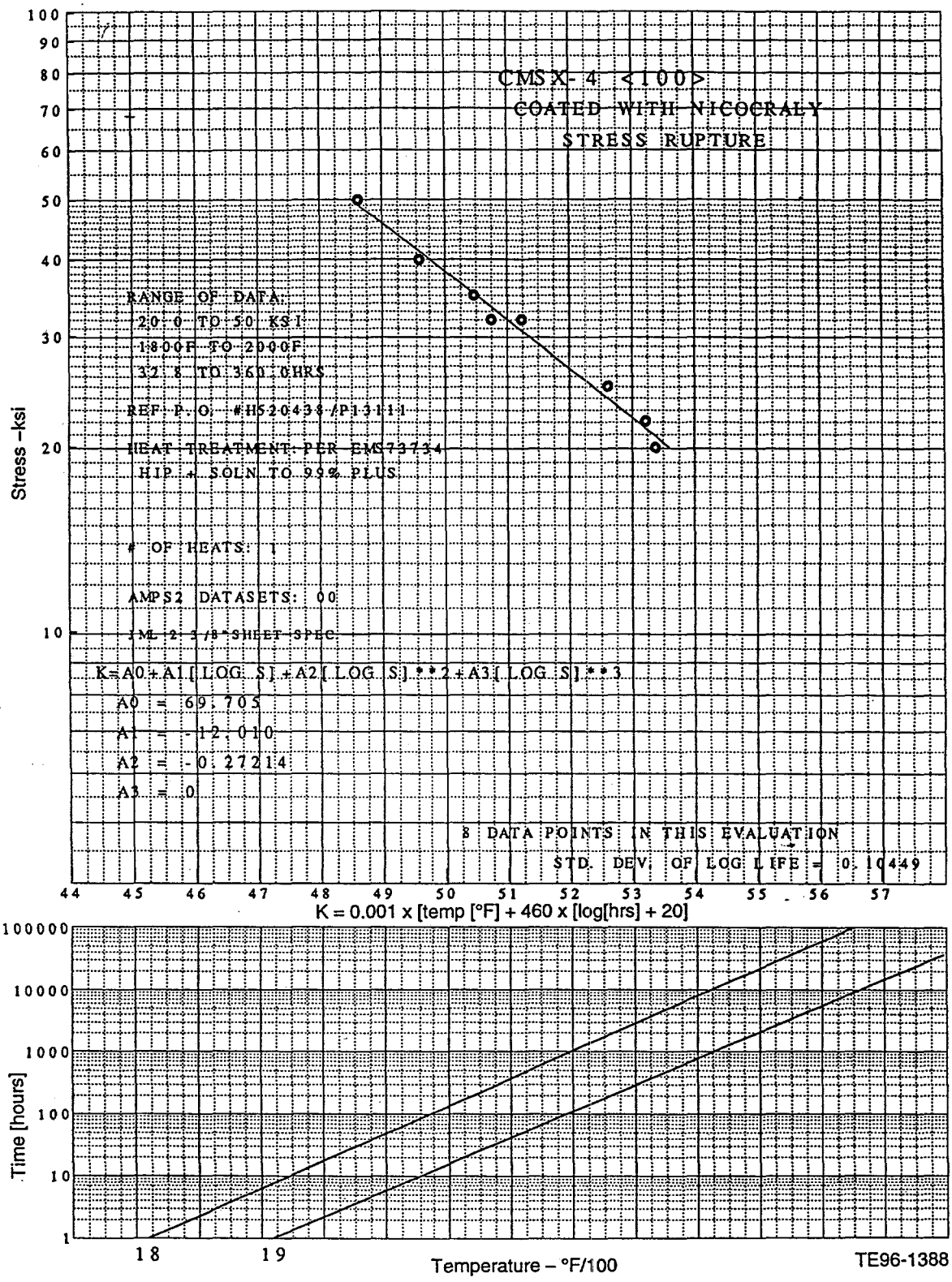

Figure 3.2.11-4. Larson-Miller curve for NiCoCrAlY coated single crystal specimens.

Therefore, this ATS Phase 2 Add-on task will be completed under ATS Phase 3A. The remainder of the 100 test specimens created under Phase 2 Add-on will be tested to failure, and Larson-Miller curves will be created incorporating the additional data gathered during Phase 3A.

Results

Sixteen samples (eight NiCoCrAlY coated and eight conventional Pt-Al coated) have been tested to failure to date. At both 1800°F and 1900°F, the NiCoCrAlY-coated samples exhibited superior stress rupture capability, requiring twice the time to rupture as the conventional Pt-Al coated samples. The test results presented here are considered preliminary, since data points are limited to less than 400 hr. Figure 3.2.11-1 shows the effect of protective coatings on the rupture properties of CMSX-4 single crystal alloys as a function of test temperatures.

Additional testing is needed to complete the study, since data points in the 400-hr range are not sufficiently long to be useful for mechanical component design for ATS. The ATS demonstrator is scheduled to run 8,000 hr, so data points in the 1,000-hr range are needed for reasonable extrapolations to the 10,000-hr range. Larson-Miller curves can then be created from the data, which will be used directly for design. Therefore, this ATS Phase 2 Add-on task will be completed under ATS Phase 3A.

3.2.12 Extended Oxidation

Objective

Dynamic oxidation testing conducted during the Phase 2 effort collected data through 5000 hr of testing at 1900°F metal temperature. In the first phase of testing, specific alloy and coating combinations showed some excellent long-term oxidation life results. Many of the candidate samples exhibited positive weight gain after 5000 hr of cyclic high temperature exposure. Although the existing 5000 hr data base is very useful, additional test time would enhance the results further by quantifying the weight loss characteristics of the alloys which presently show positive weight gain. This subtask is intended to continue testing until the weight loss characteristics are completely defined

Discussion

Background

In Phase 2 Allison initiated dynamic oxidation and hot corrosion tests. The hot corrosion test was reported in its entirety in the Final Topical Report, EDR 17144. The oxidation test was extended for the purpose of determining the long time oxidation behavior of ATS candidate alloys and coatings. Previous Allison experience consisted of relatively short oxidation tests that ranged between 500 and 1000 hr. In the original Phase 2 effort, a total of 5000 hr was accumulated and the Phase 2A Add-on effort extended the data base to 8000 hr.

As noted in the objective, the selected temperature was 1038°C (1900°F). This temperature represents a peak expected temperature in a Lamilloy airfoil, although experience shows that a 1900°F metal temperature is higher than the temperature needed to attain a 16,000 hr first vane life or 30,000 hr first-stage blade life.

The alloys selected for testing consisted of third generation single crystal (SC) and directionally solidified (DS) alloys from Cannon-Muskegon and conventionally cast (CC) alloys from various sources. The SC and DS alloys are designated CMSX-4 and CM186LC. These alloys contain significant amounts of rhenium (Re), which has been shown to partition to the gamma phase of the alloy. Re inhibits diffusion and alters the high temperature creep mechanism. The test matrix was expanded to include a more exotic alloy (CMSX-4 + lanthanum [La]) and some conventionally cast alloys (Mar-M247, IN 738, and X-40). These alloys expand the scope of the data base for materials required for cooler stages of the turbine such as the low pressure turbine (LPT). The composition of all alloys tested is listed in Table 3.2.12-I. The alloys are all aluminum-oxide (alumina) formers, except for IN 738 and X-40, which are chrome-oxide (chromia) formers.

The coatings tested include a NiCoCrAlY overlay, a platinum aluminide comprised of Pt-Si-Al, and a simple aluminide comprised of Al-Cr-Mn; the high Al content of the coatings promotes alumina formation. The NiCoCrAlY was applied by electron beam physical vapor deposition (EB-PVD) while the aluminide coatings were applied by Allison's electrophoretic process (AEP). The coatings were heat treated at temperatures that correspond to the primary age temperature for the substrate. These coatings were selected to provide a rational number

Table 3.2.12-I.
Nominal alloy compositions for specimen testing.

Alloy	Al	Cr	Ti	Co	Mo	Ta	W	Re	Hf	Zr	Ni
IN 738	3.45	16.0	3.45	8.5	1.75	1.75	2.6	--	--	0.055	Bal
Mar M247	5.5	8.4	1.05	10.0	0.65	3.05	10.0	--	1.4	0.055	Bal
CMSX-4	5.6	6.5	1.0	9.65	0.6	6.5	6.4	2.95	0.95	<0.0075	Bal
CM186LC	5.75	6.25	0.7	9.25	0.5	3.5	8.5	2.95	1.5	0.007	Bal
X-40	--	25.5	--	Bal	--	--	7.5	--	--	--	10.5

of material combinations to test in the burner rig since it accommodates only 12 0.218-in. diameter specimens at a time.

Since many of the bare alloys were removed much earlier than the coated versions, this left open slots for investigation of some other alloys such as X-40 and IN 738. A short-hand method was devised for simplicity in tracking, plotting the data, and taking photographs of the specimens. The expanded test matrix with the materials tested is shown in Table 3.2.12-II along with the designated nomenclature. The letter designates the coating, the first digit the substrate, and the final digit the sample number; the sample numbers start at zero.

Test Procedure

Single crystal and DS oversize bars were cast from low phosphor and sulfur (<2 ppm) heats of CMSX-4 and CM186LC. These materials were cast at Allison's Single Crystal Operations (SCO). The CC test bars were cast in Allison's pilot foundry. Test specimens 0.218 in. in diameter were machined from the bars. The bars coated with NiCoCrAlY were prepared by the Chromalloy, Orangeburg (CMSX-4) or Middletown (X-40) facility. Bars coated with AEP aluminides were coated by Allison's Advanced Coatings Group in a laboratory setup. Materials were coated per standard Allison processing specifications.

The samples were tested in a burner rig manufactured by Becon Corp. and shown in Figure 3.2.12-1. The Becon burner consists of a modular combustor, which closely models the flow, mixing, and combustion chemistry of many industrial combustors. The JP-5 fuel used for this test was introduced into the front of the combustor and the combustion was stabilized by a strong swirl recirculation zone. The hot combustion gases are cooled by dilution by secondary air located in the back of the combustor. The samples rotate at 600 rpm and cycle through a 60-minute dwell time in the flame followed by a 5-minute cold air blast. Samples were removed after they had experienced a minimum 20 mg/cm^2 of mass reduction. This loss in mass correlates to approximately 50 μm (0.002 in.) of surface loss, which is analogous to a typical coating thickness.

Table 3.2.12-II.
Samples tested for the ATS program in hot corrosion and dynamic oxidation.

Sample	Test	Alloy	Coating type	Coating material	Longest exposure time in DO
B1X	HC/DO	CMSX-4	None	None	5600
N1X	HC/DO	CMSX-4	Overlay	NiCoCrAlY	8000
P1X	HC/DO	CMSX-4	Diffusion	AEP PtAl	8000
S1X	HC/DO	CMSX-4	Diffusion	AEP aluminide	8000
B2X	HC	CM186LC	None	None	--
N2X	HC	CM186LC	Overlay	NiCoCrAlY	--
P2X	HC/DO	CM186LC	Diffusion	AEP PtAl	8000
S2X	HC/DO	CM186LC	Diffusion	AEP aluminide	8000
B5X	DO	CMSX-4La	None	None	3000
P5X	DO	CMSX-4La	Diffusion	AEP PtAl	3000
S5X	DO	CMSX-4La	Diffusion	AEP aluminide	3000
N31	Do	CMSX-3	Overlay	ED CoNiCrAlY	2500
B8X	DO	IN 738	None	None	545
N8X	DO	IN 738	Overlay	NiCoCrAlY	3000
P8X	DO	IN 738	Diffusion	AEP PtAl	3000
B41	DO	X-40	None	None	145
S41	DO	X-40	Diffusion	AEP aluminide	115
S42	DO	X-40	Diffusion	AEP aluminide + Si	115
B71	DO	Mar M247	None	None	1290
P7X	DO	Mar M247	Diffusion	Conv PtAl	

B = bare, N = NiCoCrAlY, P = PtAl, S = simple aluminide
The first digit identifies the substrate alloy and the second identifies the specimen number starting with 0.

The data gathered consisted of visual observations and macrophotographs, weight changes, and microscopic examination at the end of the test. The microscopic examination included measurement of coating features including the coating thickness, beta phase thickness, and interaction depth.

Baseline Coating Composition

The baseline coating compositions were determined using the scanning electron microscope and semi-quantitative X-ray energy dispersion spectroscopy (XEDA). The typical coating compositions are shown in Figure 3.2.12-2 for the two diffused coatings on both CMSX-4 and CM186LC alloys and the NiCoCrAlY coating. In addition, the compositions are listed in Tables 3.2.12-III through 3.2.12-VII.

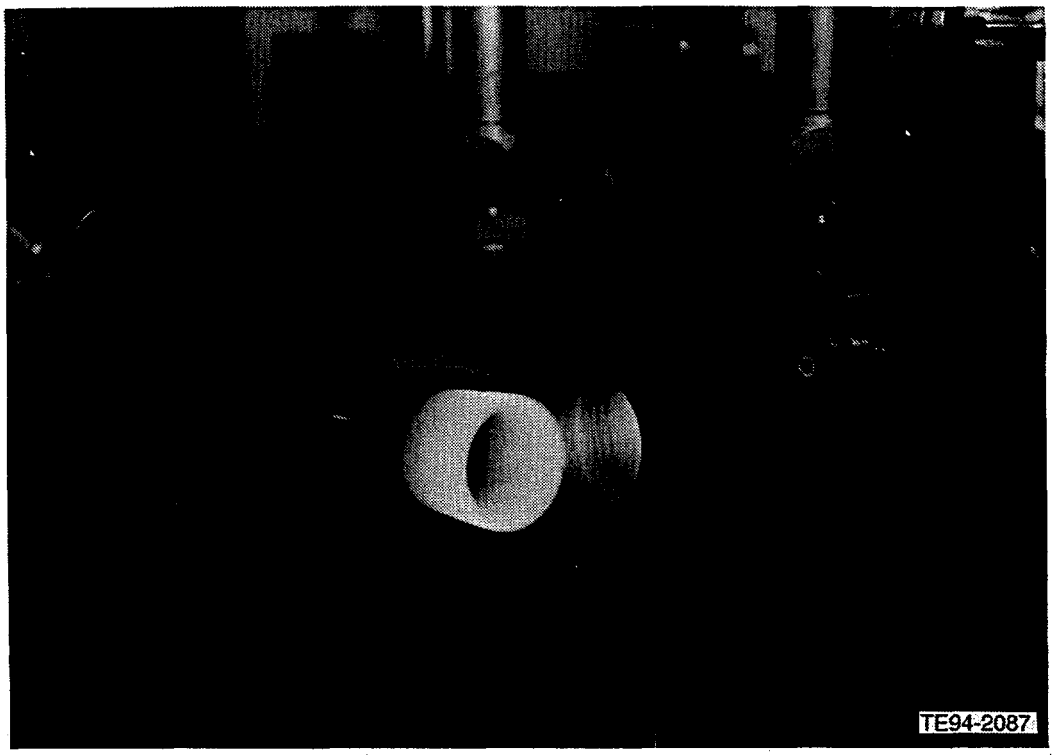

Figure 3.2.12-1. The samples are directly exposed to the flame during burner rig testing.

Table 3.2.12-III.
NiCoCrAlY coating.

Position	Al	Si	W	Pt	Mo	Ti	Cr	Mn	Co	Ni	Y-L
0	10.49	N/A	1.33	N/A	N/A	0.00	15.48	N/A	24.27	48.22	0.00
10	11.65	N/A	0.00	N/A	N/A	0.00	14.21	N/A	23.06	49.83	0.00
20	10.39	N/A	1.05	N/A	N/A	0.02	15.38	N/A	24.19	48.13	0.00
30	9.85	N/A	1.41	N/A	N/A	0.04	15.73	N/A	23.33	48.80	0.00
40	10.32	N/A	2.12	N/A	N/A	0.08	14.39	N/A	22.34	50.05	0.00
50	10.20	N/A	2.23	N/A	N/A	0.04	15.16	N/A	22.08	49.38	0.17

CMSX-4 and CM186LC Data 0-5000 Hr

Macrophotographs of the pins tested in the original Phase 2 effort are presented in 3.2.12-3. The time increments are 500 hr for the first two pictures, Figure 3.2.12-3, parts a and b, and 1000 hr for Figure 3.2.12-3, parts c through f. These figures can be used to compare to the most recent data for the test. The pins depicted are the ones that were extended the additional time. Sample B10 exhibited spallation after 1000 hr as is clearly shown by the change in oxide coloration for the section of the sample exposed to the flame. The other five samples shown do not exhibit signs of distress for up to 4000 hr. At this point there is a small penetration visible on sample S20. Sample S10 exhibits a small amount of surface discoloration after 5000 hr.

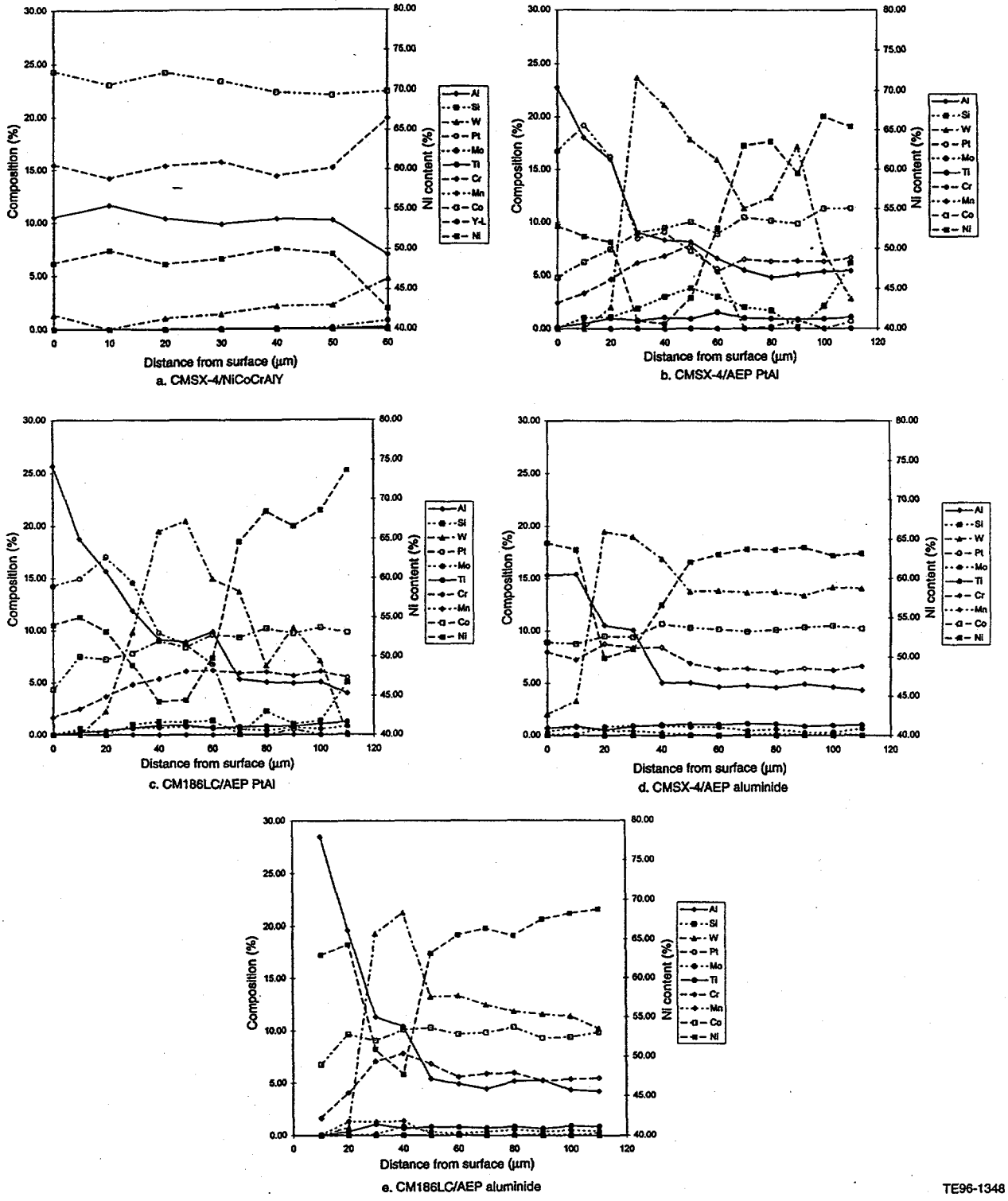

Figure 3.2.12-2. The coating composition profiles for aluminide coatings reveal higher Al content than the NiCoCrAlY overlay. Minor differences in the surface Al content of the diffused aluminide coatings exist between the two substrate alloys with CM186LC consistently being slightly higher: (a) CMSX-4/NiCoCrAlY, (b) CMSX-4/Pt-Al, (c) CM186LC/Pt-Al, (d) CMSX-4/aluminide, and (e) CM186LC/aluminide.

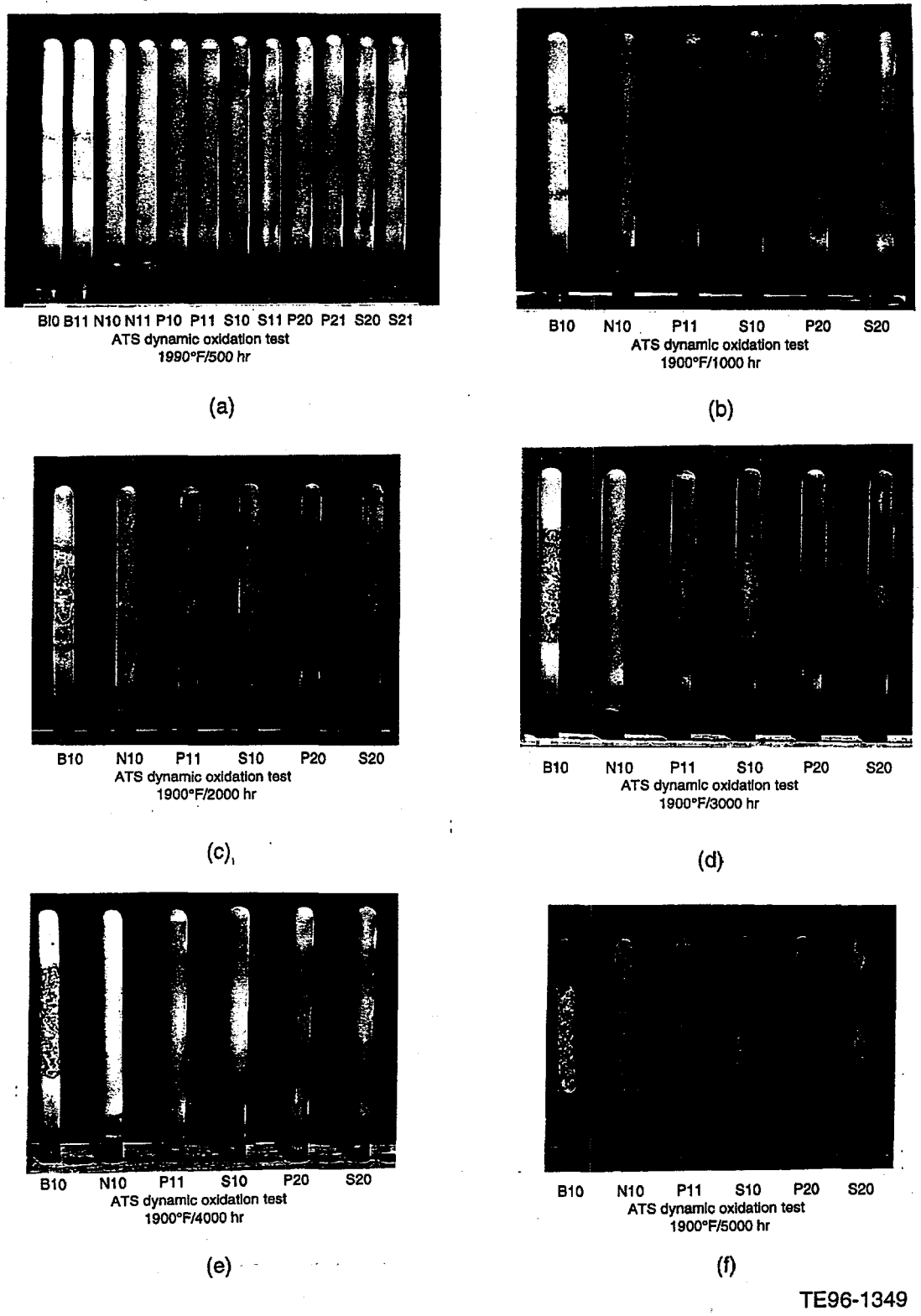

Figure 3.2.12-3. Macrophotographs of the pin surface from the start of the test to 5000 hr reveal little distress for up to 4000 hr on the coated samples. The bare pin exhibited distress after only 1000 hr.

Table 3.2.12-IV.
CMSX-4/AEP PtAl.

Position	Al	Si	W	Pt	Mo	Ti	Cr	Mn	Co	Ni
0	22.78	0.08	0.00	16.75	N/M	0.15	2.42	N/A	4.81	52.86
10	18.03	1.01	0.00	19.18	N/M	0.47	3.31	N/A	6.23	51.55
20	15.96	1.10	2.00	16.20	N/M	0.99	4.66	N/A	7.47	50.86
30	9.03	1.86	23.68	8.46	N/M	0.77	6.13	N/A	8.99	40.97
40	8.35	3.01	21.12	9.08	N/M	1.06	6.81	N/A	9.46	40.63
50	8.14	3.80	17.84	7.27	N/M	0.92	7.81	N/A	9.99	43.82
60	6.58	2.99	15.91	5.56	N/M	1.54	5.32	N/A	8.90	52.59
70	5.45	1.97	11.27	0.00	N/M	0.99	6.47	N/A	10.42	62.97
80	4.80	1.67	12.30	0.15	N/M	0.93	6.28	N/A	10.12	63.52
90	5.06	0.12	17.15	0.77	N/M	0.86	6.30	N/A	9.84	59.47
100	5.35	2.10	7.13	0.00	N/M	0.92	6.27	N/A	11.27	66.72
110	5.38	6.12	2.76	0.67	N/M	1.08	6.60	N/A	11.27	65.42

Table 3.2.12-V.
CMSX-4/AEP aluminide.

Position	Al	Si	W	Pt	Mo	Ti	Cr	Mn	Co	Ni
0	15.34	N/A	2.01	N/A	0.12	0.70	8.00	0.38	8.92	64.53
10	15.40	N/A	3.30	N/A	0.05	0.86	7.25	0.74	8.75	63.65
20	10.53	N/A	19.47	N/A	0.84	0.54	8.77	0.44	9.49	49.93
30	10.07	N/A	18.97	N/A	0.92	0.83	8.38	0.41	9.41	51.01
40	5.08	N/A	16.90	N/A	0.93	1.03	8.44	0.27	10.69	56.66
50	5.05	N/A	13.75	N/A	0.80	1.05	6.89	0.06	10.28	62.12
60	4.67	N/A	13.85	N/A	0.80	1.06	6.35	0.00	10.17	63.09
70	4.76	N/A	13.66	N/A	0.42	1.12	6.36	0.06	9.92	63.71
80	4.60	N/A	13.73	N/A	0.59	1.09	6.06	0.18	10.09	63.66
90	4.90	N/A	13.37	N/A	0.24	0.86	6.39	0.00	10.32	63.92
100	4.64	N/A	14.17	N/A	0.31	0.96	6.23	0.22	10.49	62.97
110	4.33	N/A	14.05	N/A	0.62	0.99	6.59	0.00	10.21	63.22

CMSX-4 and CM186LC Data 5000-8000 Hr

Macrophotographs of the samples showing the surface condition from 5000 to 8000 hr are shown in Figure 3.2.12-4. These photos show the growth of the damaged areas on sample S10 and S20 and very little surface degradation on samples N10, P11, and P20. The red discoloration at the top and bottom of the pins is due to iron oxide (rust) contaminates in the fuel and cooling air.

Table 3.2.12-VI.
CM186LC/AEP PtAl.

Position	Al	Si	W	Pt	Mo	Ti	Cr	Mn	Co	Ni
0	25.69	0.00	0.00	14.25	0.00	0.00	1.66	N/A	4.37	54.02
10	18.73	0.58	0.00	14.95	0.43	0.21	2.47	N/A	7.50	55.02
20	15.69	0.00	2.27	17.05	0.32	0.41	3.69	N/A	7.27	53.23
30	11.89	0.98	9.81	14.55	0.62	0.66	4.81	N/A	7.79	48.88
40	9.14	1.27	19.46	9.76	0.71	0.91	5.36	N/A	9.00	44.29
50	8.87	1.20	20.45	8.65	0.77	0.92	6.07	N/A	8.34	44.45
60	9.86	1.38	14.92	6.77	0.74	0.64	6.18	N/A	9.60	49.84
70	5.30	0.00	13.67	0.00	0.51	0.75	5.88	N/A	9.30	64.58
80	5.04	2.26	6.63	0.00	0.42	0.83	6.03	N/A	10.18	68.49
90	4.91	1.03	10.22	0.51	0.69	0.79	5.61	N/A	9.67	66.56
100	5.05	1.33	7.09	0.00	0.55	1.06	6.06	N/A	10.26	68.60
110	3.95	5.03	0.00	0.07	0.82	1.22	5.46	N/A	9.77	73.67

Table 3.2.12-VII.
CM186LC/AEP aluminide.

Position	Al	Si	W	Pt	Mo	Ti	Cr	Mn	Co	Ni
0	49.56	N/A	0.75	N/A	0.59	0.05	5.25	0.02	3.50	40.27
10	28.46	N/A	0.00	N/A	0.07	0.00	1.64	0.09	6.74	62.98
20	19.59	N/A	0.77	N/A	0.00	0.35	4.05	1.31	9.62	64.30
30	11.28	N/A	19.30	N/A	0.12	1.07	7.03	1.28	9.03	50.90
40	10.37	N/A	21.25	N/A	0.86	0.65	7.75	1.34	10.06	47.71
50	5.38	N/A	13.23	N/A	0.34	0.81	6.78	0.07	10.25	63.15
60	4.88	N/A	13.32	N/A	0.18	0.77	5.54	0.12	9.65	65.54
70	4.43	N/A	12.43	N/A	0.37	0.73	5.86	0.00	9.79	66.39
80	5.14	N/A	11.78	N/A	0.54	0.83	5.93	0.00	10.30	65.47
90	5.24	N/A	11.53	N/A	0.39	0.67	5.20	0.17	9.28	67.52
100	4.34	N/A	11.35	N/A	0.49	0.91	5.34	0.00	9.35	68.23
110	4.21	N/A	10.18	N/A	0.41	0.87	5.45	0.27	9.83	68.78

CMSX-4 + La 0-3000 Hr

Macrophotographs of the CMSX-4 + La pins are shown in Figure 3.2.12-5 for times up to 3000 hr. There was no degradation evident for any of these pins after 3000 hr. This is in comparison to the bare conventional CMSX-4 that showed onset of attack after 1000 hr. The improved oxidation resistance can likely be traced to the addition of lanthanum, which has been shown to improve oxide adherence by combining with sulfur thus preventing it from segregating at the oxide/substrate interface and weakening the bond which in turn leads to premature failure of the coating. The addition of lanthanum is of interest for ATS because it is more controllable than yttrium and has essentially the same benefit for oxidation resistance.

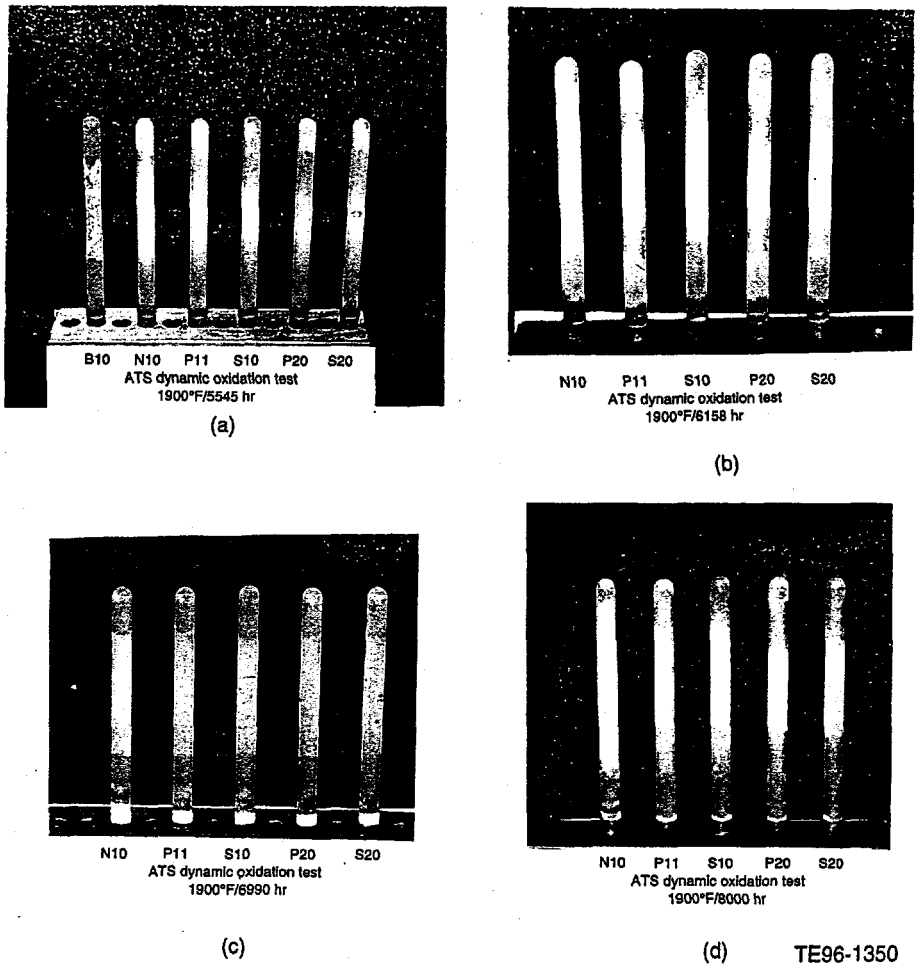

Figure 3.2.12-4. Exposure for an additional 3000 hr reveals increased damage to the simple aluminide coatings on both CMSX-4 and CM186LC.

IN 738

The surface condition of the IN 738 samples is shown in Figure 3.2.12-6. The bare sample (B81) shows a significant amount of degradation after 245 hr. There is a noticeable reduction in the diameter after 545 hr (hourglass shape). No distress is apparent after 3000 hr for the PtAl or NiCoCrAlY coated samples. A simple aluminide coated sample exposed for 1300 hr also shows no distress.

X-40

Figure 3.2.12-7 shows the surface condition of the bare and coated X-40. A dark oxide is evident on the bare sample (B41). The oxide was loosely adherent and readily flaked off during weighing. A large section of the aluminide coating spalled from the conventional aluminide coating after 105 hr. The silicon modified aluminide coated sample is still intact after 150 hr, although there is a band of discoloration in the hottest section of the pin.

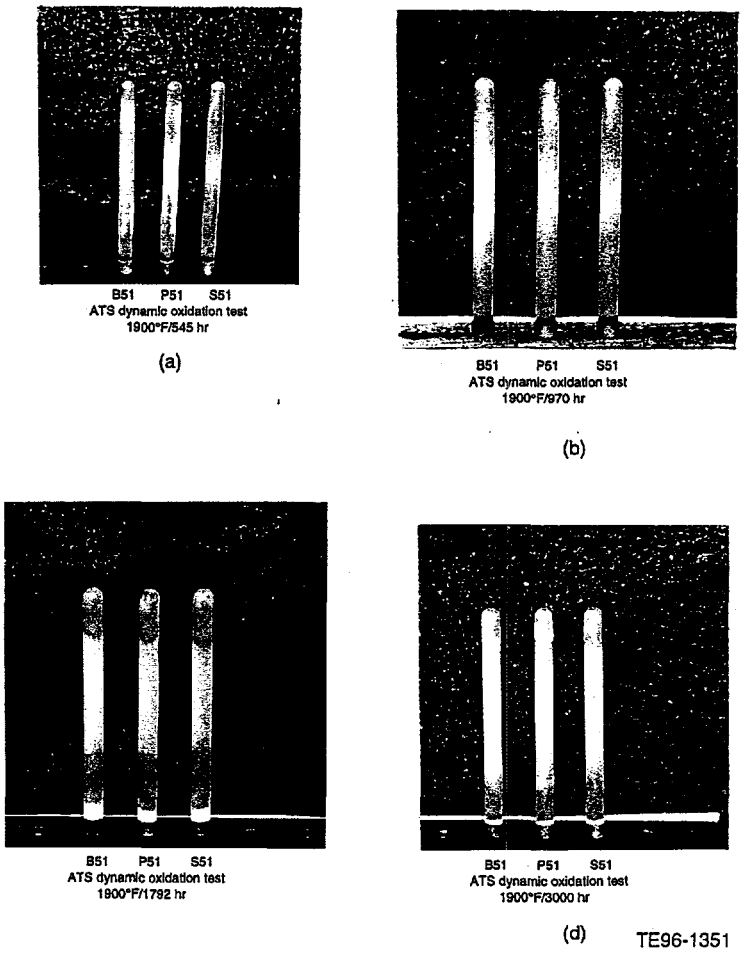

Figure 3.2.12-5. The surface of bare and diffusion coated CMSX-4 + La shows no sign of distress after 3000 hr.

Comparison

Figure 3.2.12-8 shows the post-test surface condition for the NiCoCrAlY coated CMSX-3, IN 738, and CMSX-4 samples. There is no evidence of gross coating degradation. Figure 3.2.12-9 shows the surface condition of the AEP Pt-Al coatings on the four base metals. These samples do not show any coating distress either. Figure 3.2.12-10 shows the AEP simple aluminide coatings on CMSX-4, CM186LC, and CMSX-4+La. The two pins that were exposed for 8000 hr show localized and general material loss, as described previously.

Figure 3.2.12-11 shows the surface condition of the bare alloys after the times indicated. There is general distress on all of the pins tested after these exposures except for the Lanthanum doped CMSX-4. A conventional chemistry CMSX-4 exposed for 3000 hr exhibiting generalized distress was shown in Figure 3.2.12-3, part d.

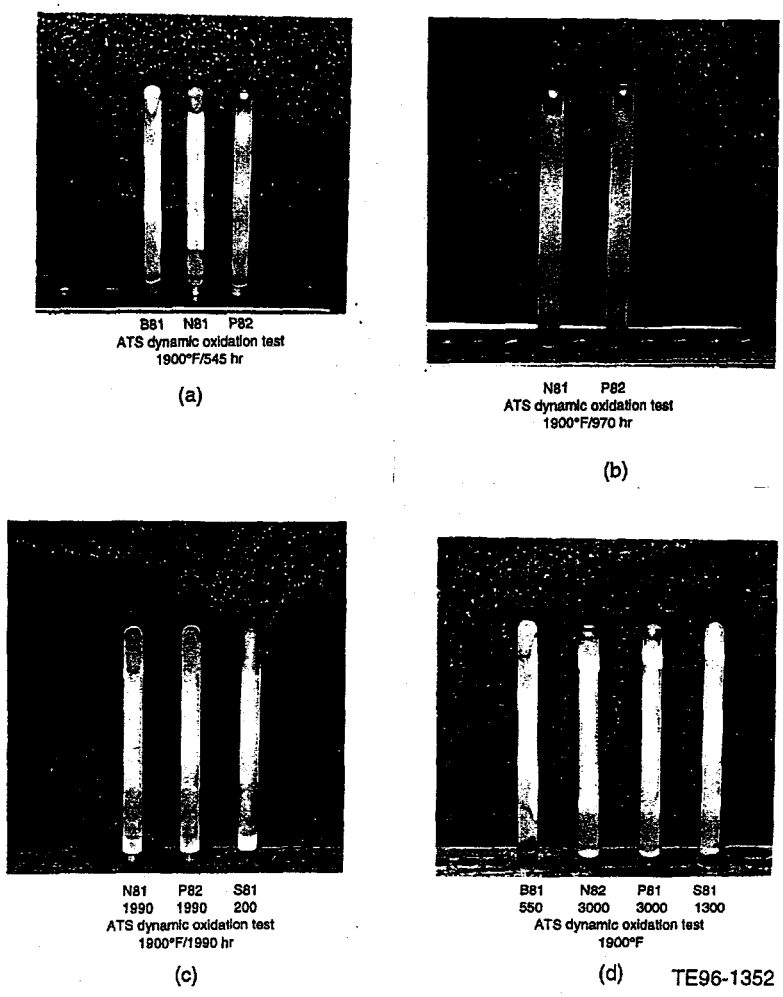

Figure 3.2.12-6. The surface of coated IN 738 samples shows no damage after 3000 hr exposure. There was significant surface recession after only 245 hr for the bare sample.

Gravimetric Data

The gravimetric (i.e., oxidation weight change) curves for the 8000 hr test samples are shown in Figure 3.2.12-12. These samples show a similar trend to that observed after 5000 hr. The bare sample continued to spall and was removed from the test after 5600 hr. This was done so that another coating substrate combination could be evaluated. All of the samples began to lose mass after as few as 100 (B10 - Bare CMSX-4) or as many as 5900 hr (P20 - CM198LC/AEP PtAl) as shown in the maximum weight column of Table 3.2.12-VIII. The "crossover" point is also indicated in this table. This point has been termed the breakaway point by some and provides an easily identified mass change with which to compare coatings and substrates. Other indicators for the coating life are provided in Table 3.2.12-VIII. The life relative to bare CMSX-4 is listed.

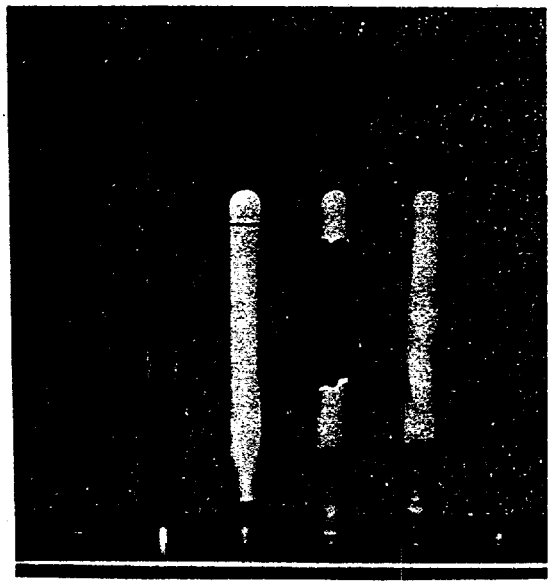

Figure 3.2.12-7. Simple aluminide coated X-40 spalls after relatively short thermal exposure.

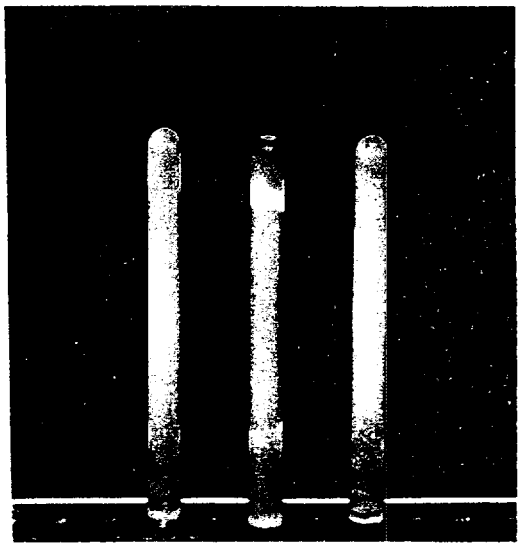

Figure 3.2.12-8. NiCoCrAlY coated samples show little distress.

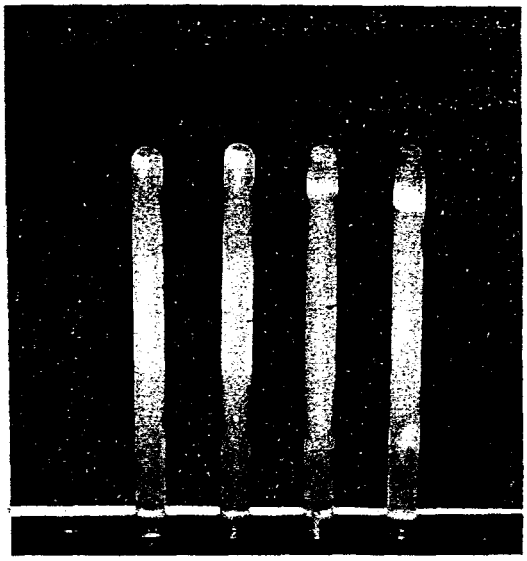

Figure 3.2.12-9. Pt-Al samples show no signs of distress on the surface after testing to 8000 hr.

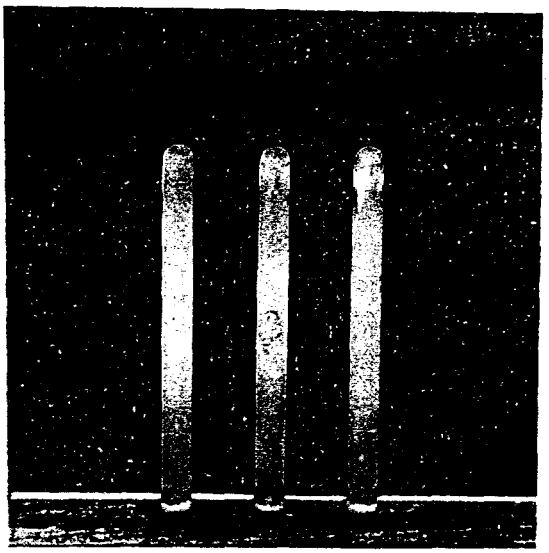

Figure 3.2.12-10. General metal recession is visible on the simple aluminide coated CMSX-4 while localized attack is evident on the simple aluminide coated CM186LC.

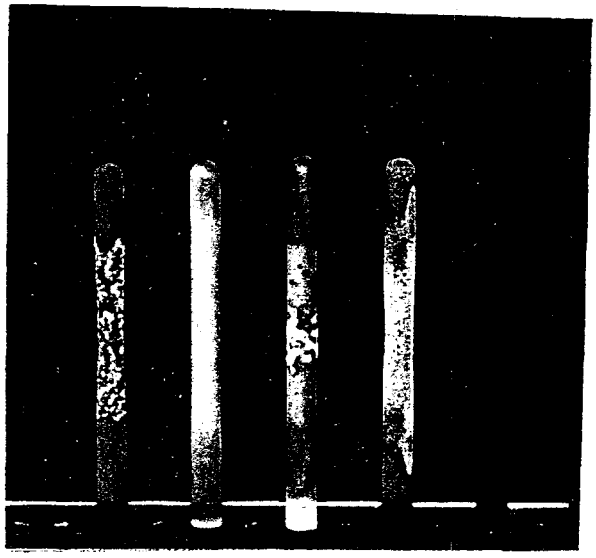

Figure 3.2.12-11. General attack is evident for the bare CMSX-4 (B10), Mar-M247 (B71), and IN 738 (B81). The CMSX-4 + La has a pristine surface condition.

The simple aluminide coated CMSX-4 (S10) exhibited weight loss; the changes occurred at an accelerating rate. The simple aluminide coated CM186LC was the second coated sample to oxidize at an accelerated rate. The PtAl and NiCoCrAlY coated samples did not reach the accelerated oxidation weight changes after 8000 hr. The life estimates beyond the tested 8000 hr listed in Table 3.2.12-VIII were determined by "splicing" the data from the simple aluminides onto the Pt-Al. The estimated life curves to 13,000 hr are shown in Figure 3.2.12-13.

Table 3.2.12-VIII.
Summary of gravimetric results and estimates for bare and coated CMSX-4 and CM186LC.

Sample	Max wt (hr)	Zero wt (hr)	8 mg/cm^2 (hr)	Life ratio to bare (mass)	~10μm loss (hr)	Life ratio to bare (loss)
B10	100	250	1000	1	1000	1
B14	100	180	1200	1.2	--	
N10	2850	6600	*10000*	10	*9500*	9.5
P11	2450	4900	*9200*	9.2	*9400*	9.4
S10	1400	2400	4800	4.8	5500	5.5
S14	900	1400	3300	3.3	3500	3.5
P20	5900	8200	*12700*	12.7	*12500*	12.5
S20	1650	3700	7500	7.5	8000	8.0

Italicized numbers are estimated from the gravimetric data. Duplicate samples were included in the analysis where available.

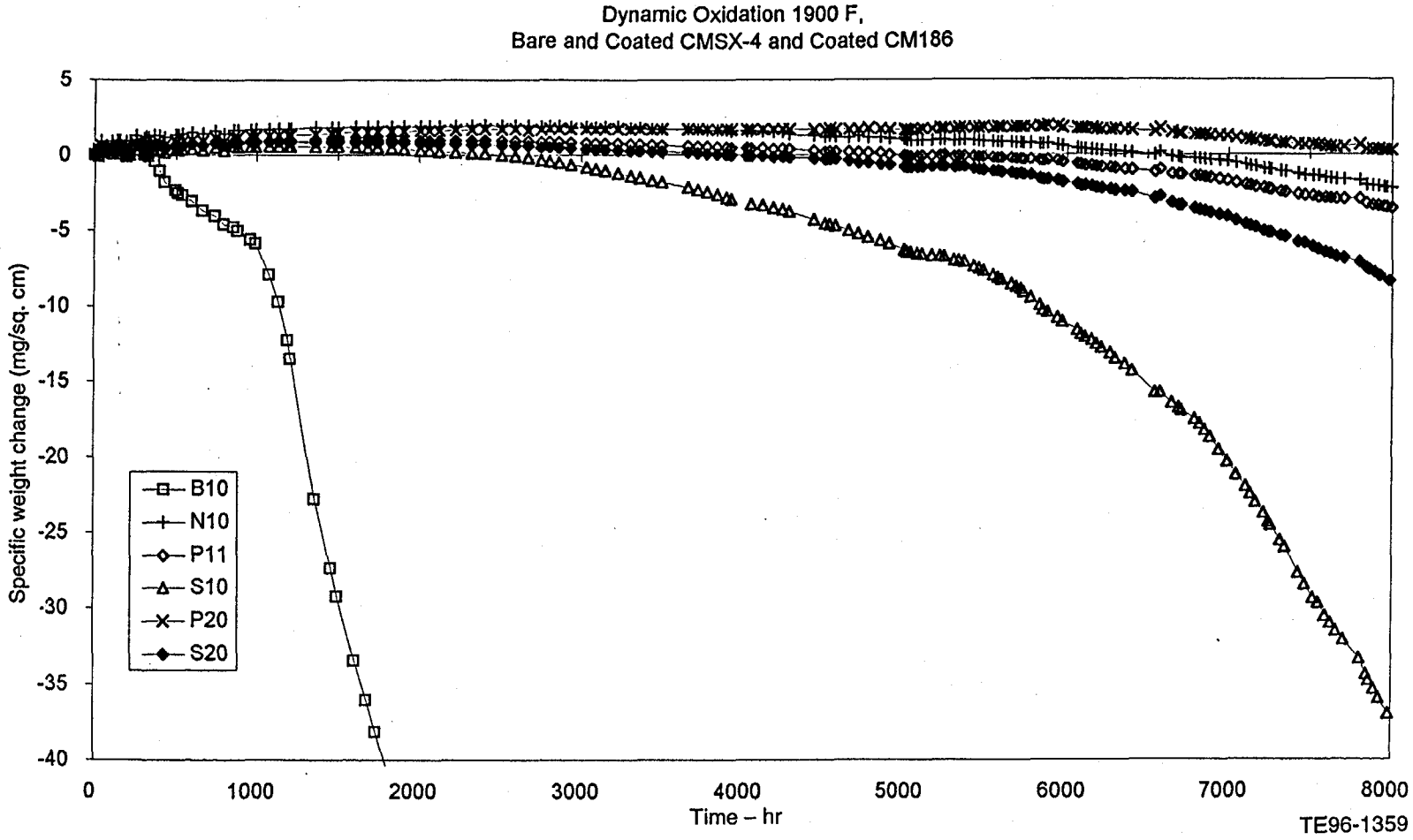

Figure 3.2.12-12. The samples continued the weight change trends established after 5000 hr. CM186LC has the best oxidation resistance of the materials tested.

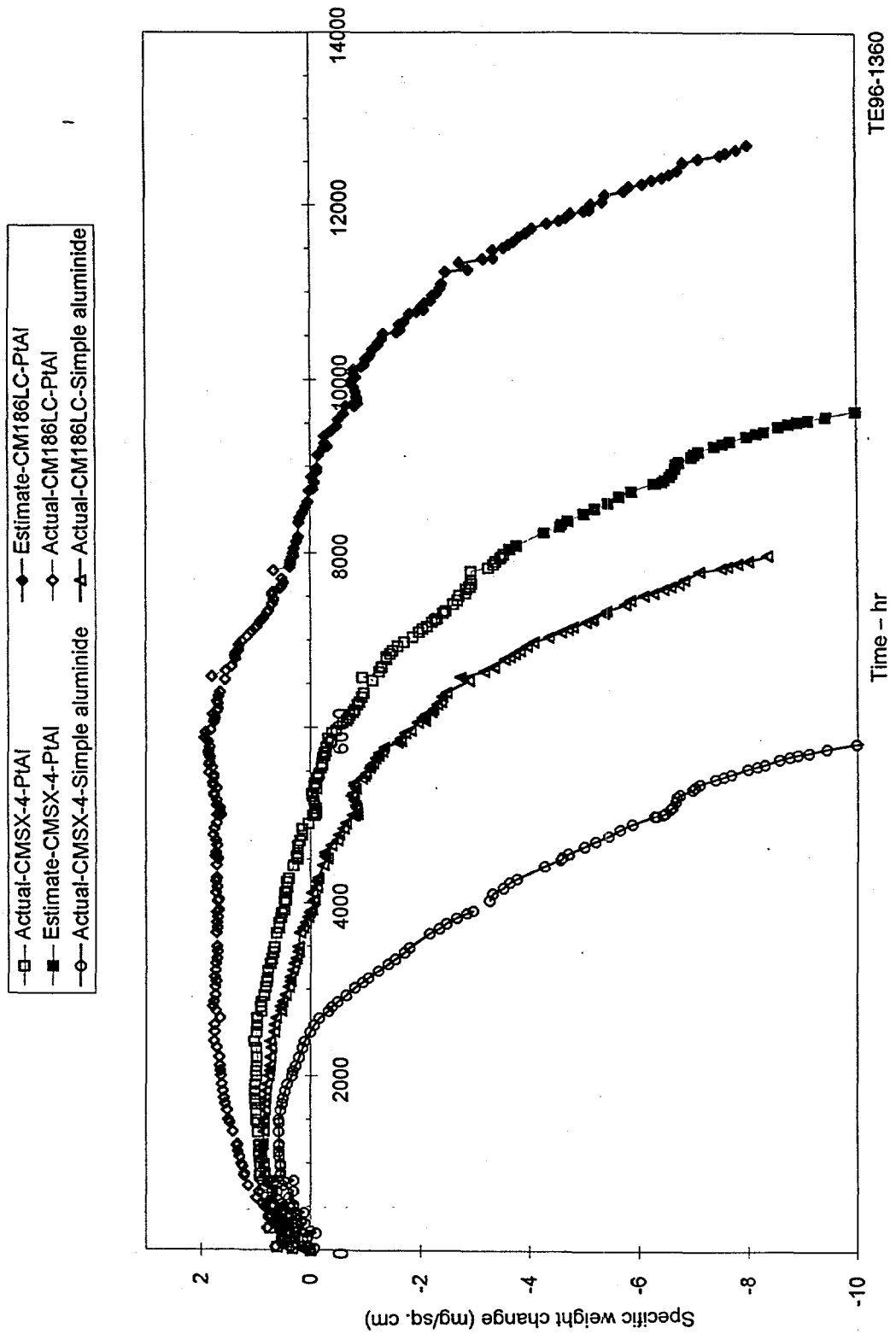

Figure 3.2.12-13. Life estimates reveal that the best obtainable life at 1038°C is approximately half the 30,000 limit.

CMSX-4 + La

The gravimetric results for the bare, simple aluminide, and platinum aluminide coated samples are shown in Figure 3.2.12-14. The oxidation life for the bare CMSX-4 and CMSX-4 + La differ significantly. The bare sample reached a maximum mass gain after approximately 550 hr and a crossover at 1500 hr. This compares to 100 and 250 hr, respectively, for conventional CMSX-4 alloy. It is notable that the CMSX-4 + La alloy with either a simple or platinum aluminide coating has similar oxidation curves. It is not clear why this condition exists and a reasonable explanation is not available at this time. The observed peak oxidation mass change occurred at approximately 1400 hr for both the simple and platinum aluminide samples with crossover occurring at 2700 for the simple aluminide and approximately 4000 hr (estimated from data) for the Pt-Al. These results are in qualitative agreement (within approximately 20%) for the conventional chemistry CMSX-4.

IN 738

The gravimetric data for bare and coated IN 738 are shown in Figure 3.2.12-15 and Table 3.2.12-IX. The bare sample exhibited a significant mass loss almost immediately and reached 8 mg/cm^2 after only 270 hr. The simple aluminide coated sample peaked after 250 hr and crossed over at 1000 hr. Both the Pt-Al and the NiCoCrAlY coated IN 738 alloy did not peak until 2000 hr and both exhibited a smooth weight loss. These results show the importance of a coating for the IN 738 alloy when operating in the 1900°F temperature regime.

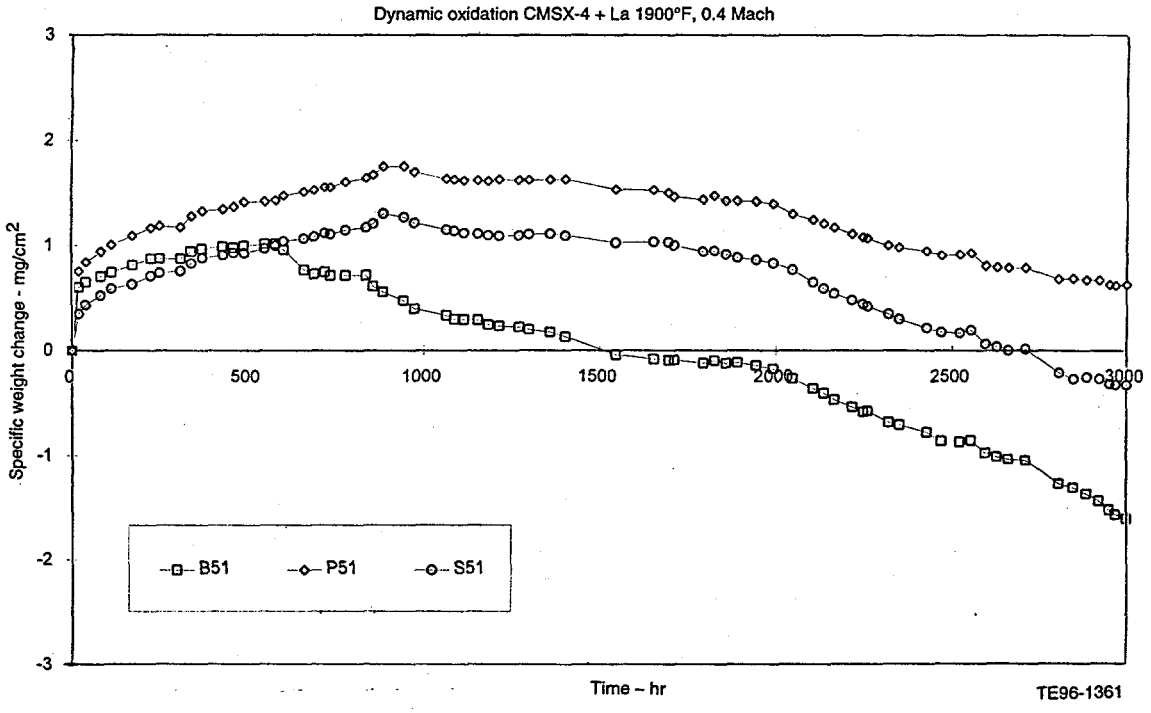

Figure 3.2.12-14. Coated CMSX-4 + La has superior life to bare CMSX-4 + La.

Table 3.2.12-IX.
Summary of gravimetric results and estimates for bare and coated alloys.

Sample	Max wt (hr)	Zero wt (hr)	8 mg/cm^2 (hr)
N31	300	1250	2300
B41	--	<20	80
B42	--	<30	90
N41	>150	>150	
S41	105	135*	135*
S42	90	>150	>150
B71	30	120	1000
B81	20	120	270
N81	2000	>3000	
P82	2000	>3000	
S81	250	1000	>1000
B51	550	1500	>3000
S51	1000	2600	>3000
P51	1500	>3000	>3000

Italicized numbers are estimated from the gravimetric data. Duplicate samples were included in the analysis where available.
*Gross coating spallation occurred; sample S42 was only run 150 hr.

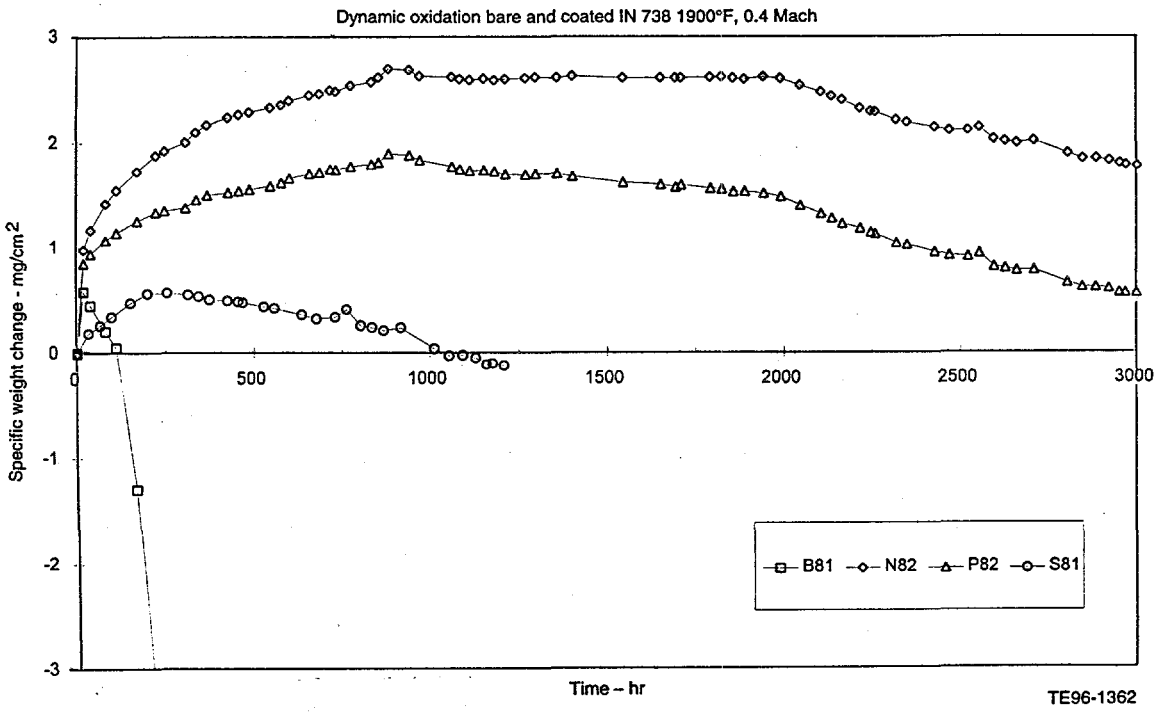

Figure 3.2.12-15. Rapid weight loss is observed for bare IN 738. Simple aluminide coated IN 738 has inferior life to Pt-Al or NiCoCrAlY coated IN 738.

X-40

Figure 3.2.12-16 shows the gravimetric data for the bare and coated X-40 samples. The bare samples exhibit an immediate weight loss, while the coated samples show an initial weight gain. After 105 hr the simple aluminide coated sample experienced a significant loss in the coating. The NiCoCrAlY coated samples both exhibit weight gains to 150 hr while the silicon doped aluminide exhibits a gradual mass loss.

Aluminide Coatings

The gravimetric data for the simple aluminide coatings on CMSX-4, CM186LC, Mar-M247, and IN 738 are shown in Figure 3.2.12-17. This figure clearly shows a significant weight loss difference between the alloys. It is likely that the higher hafnium content in CM186LC is responsible for the improved oxidation resistance since hafnium and other reactive elements have been shown to enhance the oxide scale adherence. The mass change for the simple aluminide coated IN 738 shows the most rapid reduction with a peak mass change after 250 hr and a crossover after approximately 1000 hr.

Pt-Al

The gravimetric data for AEP platinum aluminide coatings on CMSX-4, CMSX-4 + La, CM186LC, and IN 738 are shown in Figure 3.2.12-18. As was demonstrated for the simple aluminide coatings, there is a clear influence of base metal chemistry on the oxidation resistance. The CM186LC has not reached the crossover point after 8000 hr, while the CMSX-4 coated sample reached this point at approximately 5000 hr.

NiCoCrAlY

The gravimetric data for NiCoCrAlY coated CMSX-4 and IN 738 and CoNiCrAlY coated CMSX-3 are shown in Figure 3.2.12-19. These data show superior oxidation resistance of NiCoCrAlY over CoNiCrAlY assuming that one can ignore base metal influences for relatively short exposures (i.e., 1000 hr at 1038°C). Another factor to keep in mind for this comparison is that the NiCoCrAlY was applied by conventional EB-PVD while the CoNiCrAlY was applied by electro-deposition. Within the test duration run (3000 hr), there does not seem to be a dramatic influence of base metal chemistry on the oxidation behavior.

One method of measuring coating life is called surface recession. A relative value for the surface loss can be derived from the mass change data simply by dividing the mass loss by the density of the coating. The coating density was calculated from XEDA line scans that were made on baseline coatings that had been tested previously for ATS in a hot corrosion. The calculated surface loss for all the samples tested is shown in Figure 3.2.12-20; part b of Figure 3.2.12-20 includes an estimate to 13,000 hr.

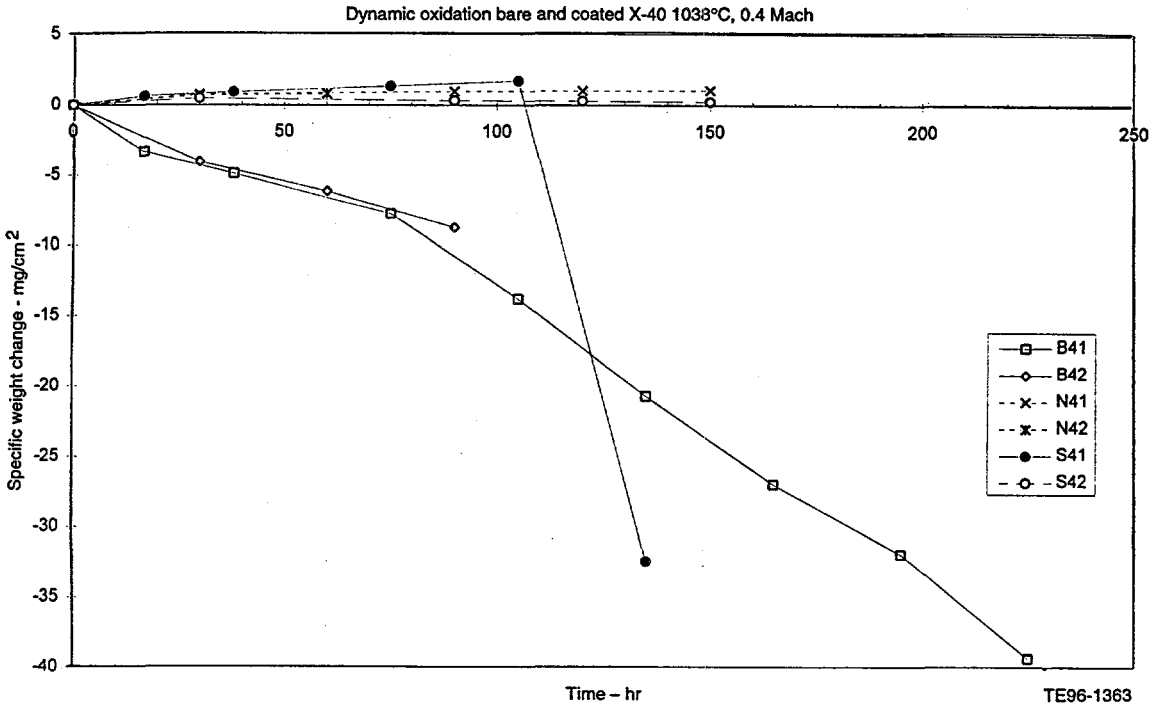

Figure 3.2.12-16. Bare X-40 immediately begins to lose mass while simple aluminide coated X-40 gains mass until coating spallation occurs.

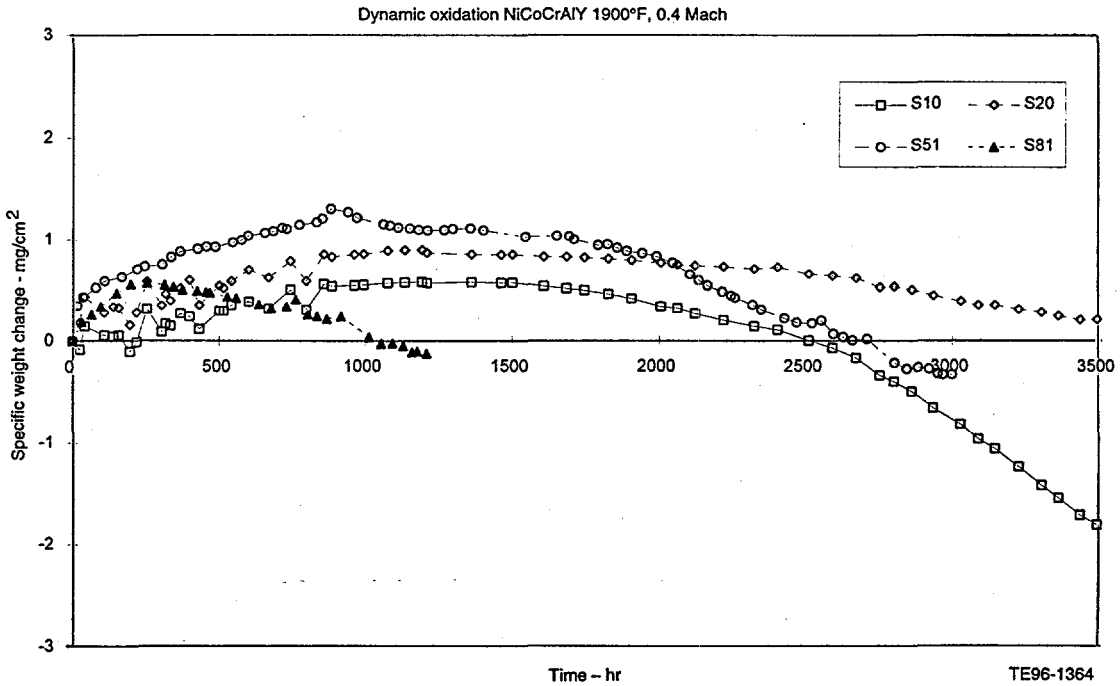

Figure 3.2.12-17. Little benefit is observed for La doping of CMSX-4 when samples are coated with a simple aluminide.

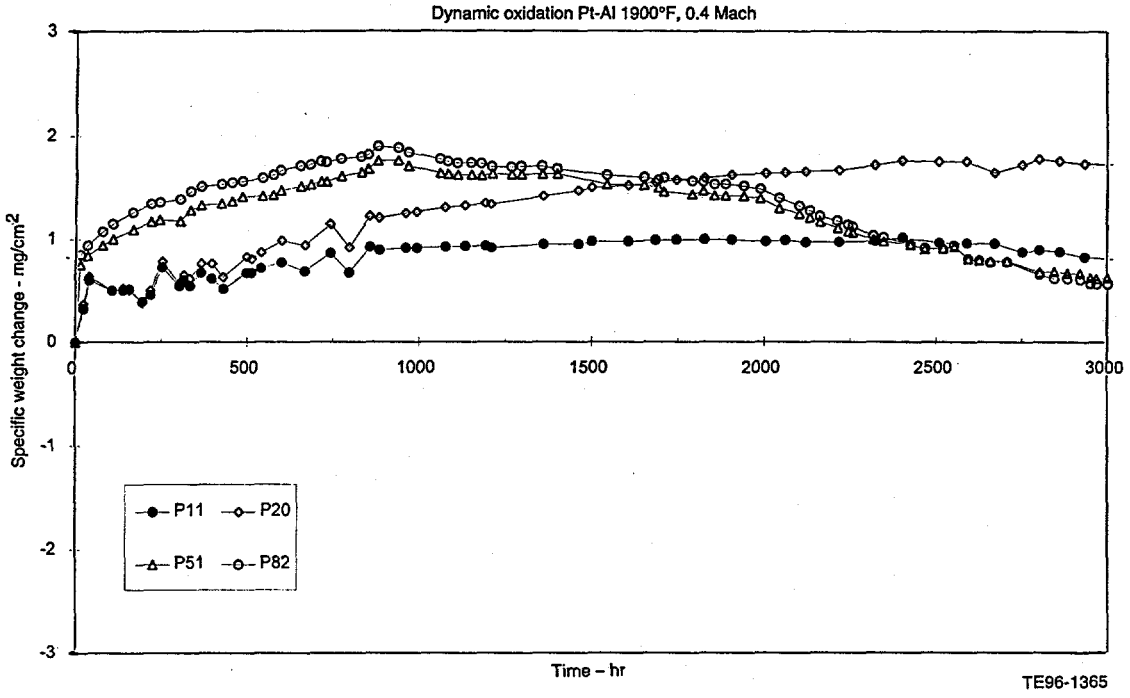

Figure 3.2.12-18. Surprisingly, no substrate effects were observed for Pt-Al on either IN 738 or CMSX-4 + La.

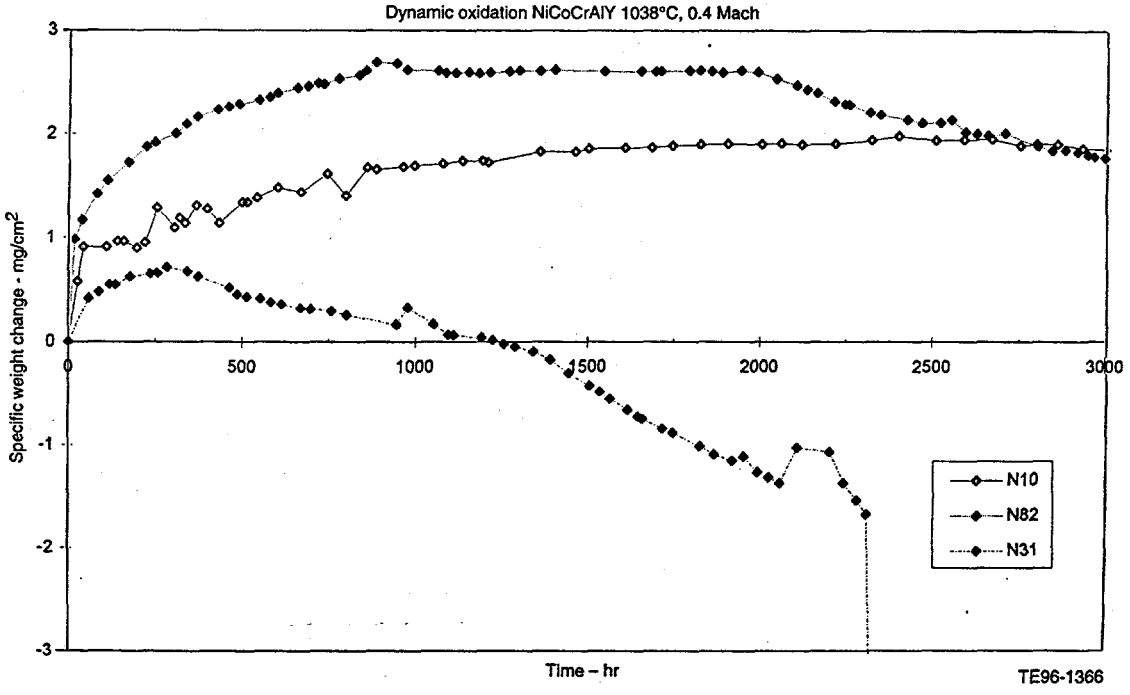

Figure 3.2.12-19. CoNiCrAlY/CMSX-3 (N31) has inferior oxidation life compared to Ni-CoCrAlY coated CMSX-4, IN 738 or CMSX-4 + La.

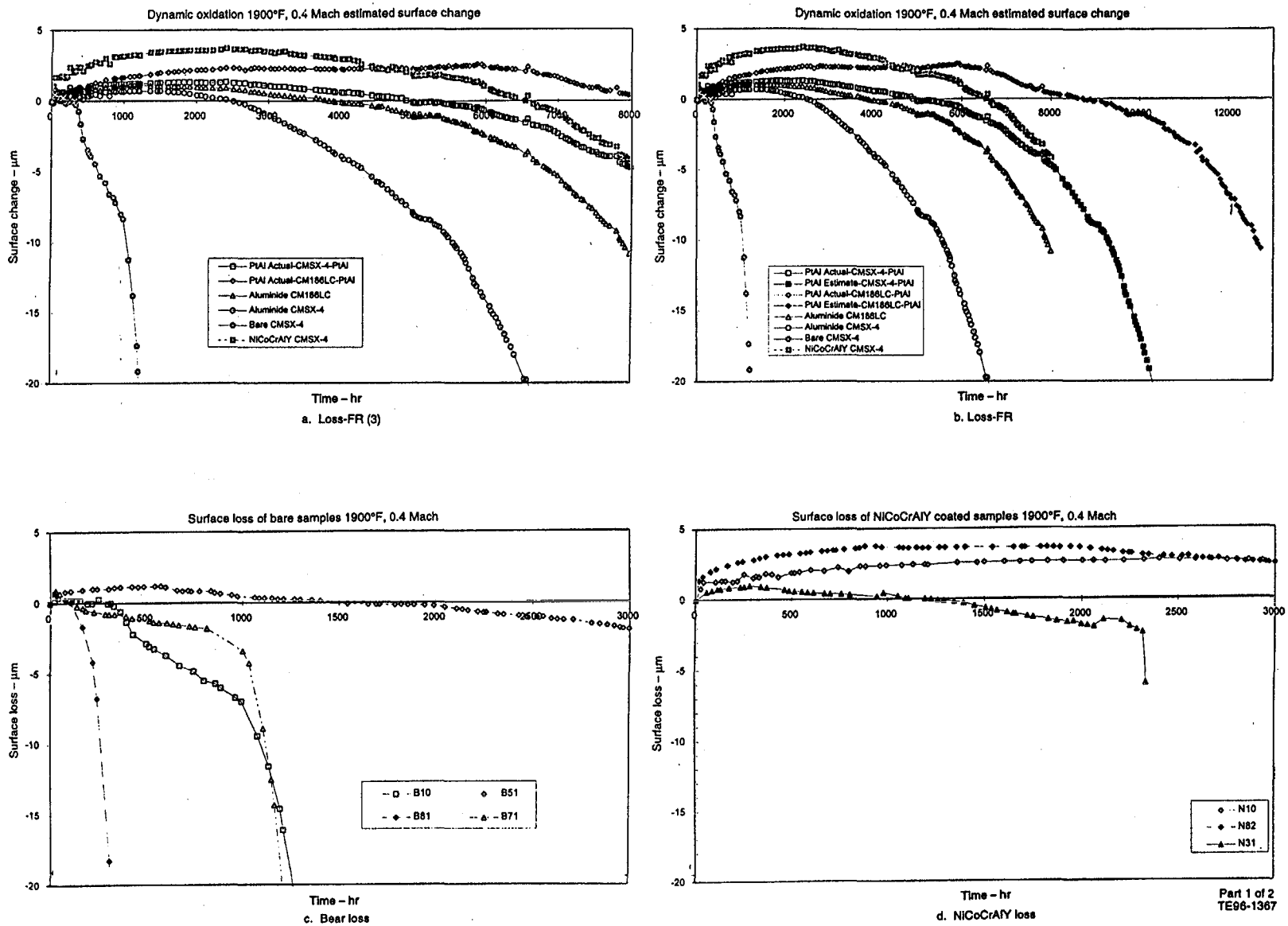

Figure 3.2.12-20. Estimated surface losses agree with the weight change data: (a) long time samples, (b) CMSX-4 + La, (c) IN 738, and (d) bare (part 1 of 2).

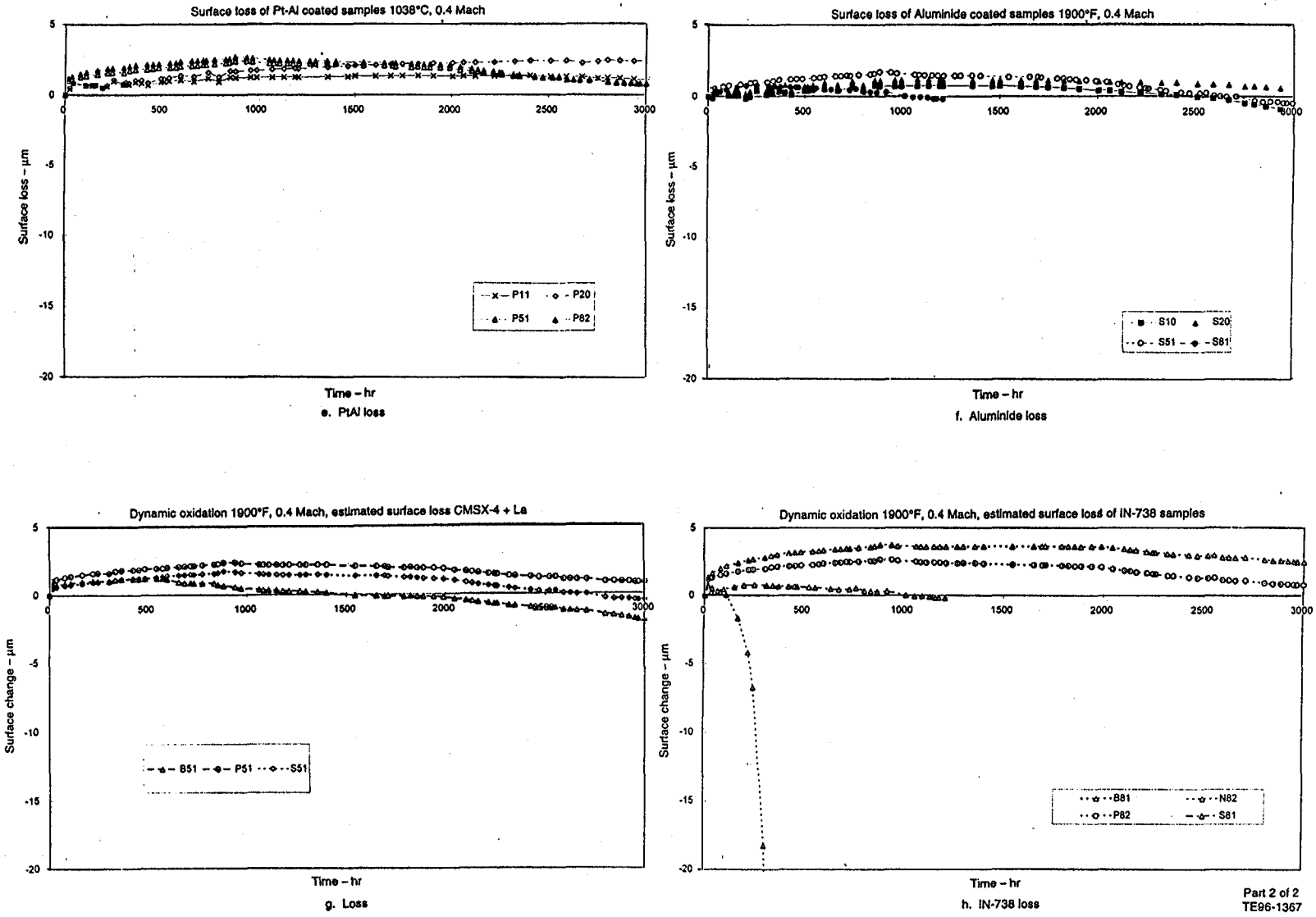

Figure 3.2.12-20. Estimated surface losses agree with the weight change data: (e) PtAl, (f) aluminide, (g) estimated surface, and (h) IN 738 (part 2 of 2).

Metallography

Samples that were exposed for 3500 and 8000 hr are shown in Figure 3.2.12-21. The breakdown of the coating between 3500 and 8000 hr is evident for all of the samples tested. There is a significant interaction depth and associated needle phase presence for all of the coated samples except CMSX-4/AEP aluminide, which has completely consumed the coating and is losing substrate material. Table 3.2.12-X shows the metallographic measurements for the various samples that were tested to 8000 hr.

Summary

The test results indicate a strong influence of the base metal chemistry on the oxidation behavior of both the coated and bare samples. For example, the increased hafnium content in the CM186LC alloy improves the oxidation resistance of both the simple and platinum-aluminide coatings as compared to the CMSX-4 alloy. The first- and second-stage HP turbine blades and vanes will have areas on the airfoil that may approach the 1900°F level. Since the bare alloys have demonstrated they do not have adequate ATS life requirements at 1900°F peak metal temperature, it will be necessary to coat the gas path surfaces of such components to achieve 30,000 hr life.

The test also shows the difference in oxidation life of chromia versus alumina scale former alloys. Alloys such as IN 738, which is a chromia former, do not have the oxidation life necessary to meet 30,000 hr requirements when running at 1900°F. As discussed previously, alloys such as Mar-M247, CM186, and CMSX-4 are alumina formers and consequently are candidates for high temperature applications. Alloys such as IN 738 will be used in later stages of the turbine where metal temperatures are lower in addition to the improved castability of the alloy.

It is recommended that a follow-on test at a higher metal temperature be run to establish the rate of degradation of the alloys with increasing temperatures. Such a test would provide valuable data when assessing the life expectations of selected alloys. Some additional effort to fully characterize the test specimens beyond that included in this report is also recommended.

Table 3.2.12-XI shows the quantitative metallographic data for the samples tested to 3000 hr during the add-on testing.

Figure 3.2.12-22 shows the baseline coating condition for CMSX-4 + La coated with platinum and simple aluminide. There is an obvious precipitation of second phase beneath the simple aluminide coating. This may be due to the extended time at 650-750°C to which the base of the pins is exposed.

Figure 3.2.12-23 shows the sections of the pins exposed to the flame for 3000 hr. There is still some beta phase visible on both the simple and platinum aluminide coated samples. There is an interaction zone of approximately 300 μm.

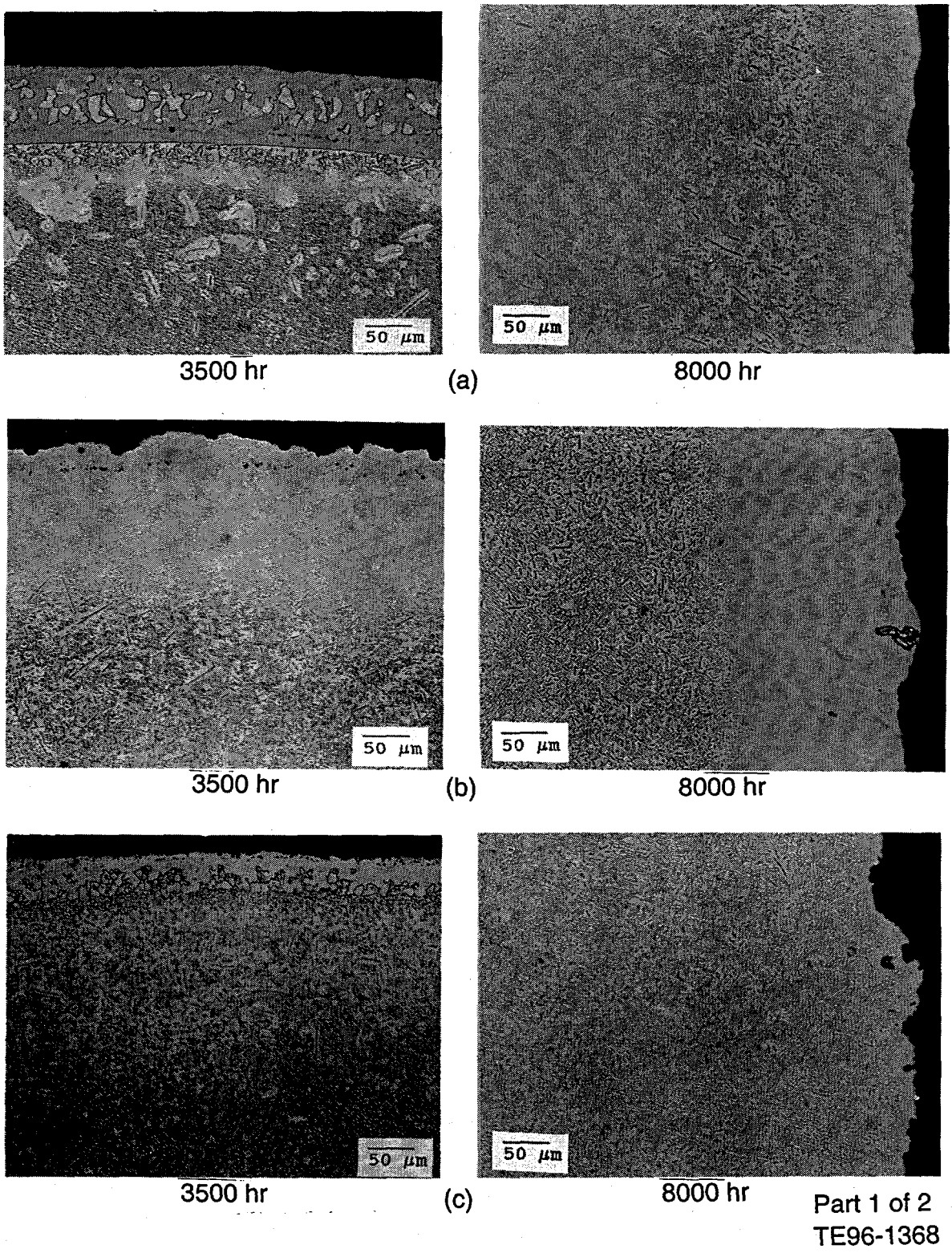

Figure 3.2.12-21. The amount of second phase that has precipitated decreases as the coating is depleted in Al: (a) CMSX-4/NiCoCrAlY, (b) CMSX-4/PtAl, and (c) CMSX-4/aluminide (part 1 of 2).

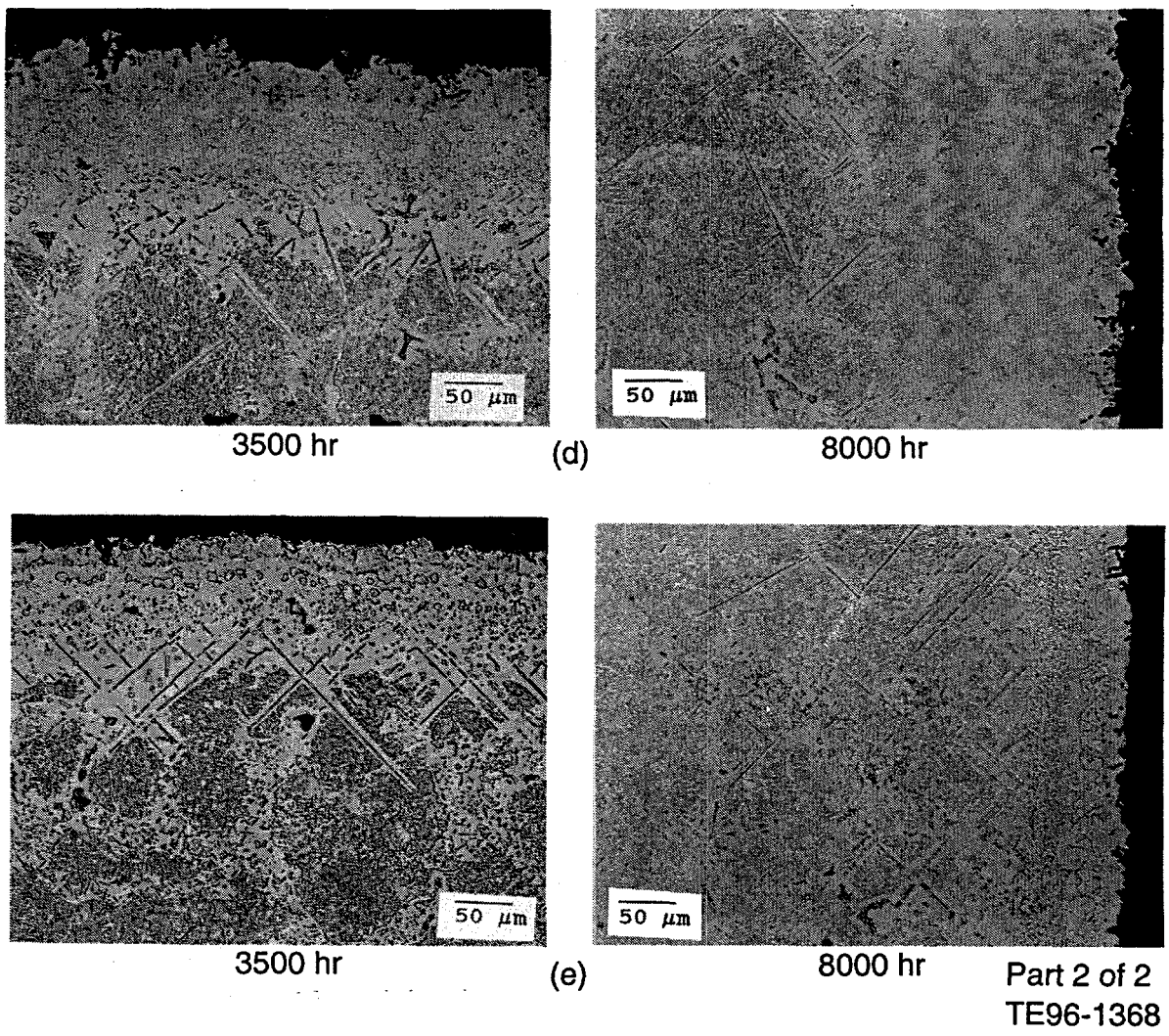

Figure 3.2.12-21. The amount of second phase that has precipitated decreases as the coating is depleted in Al: (d) CM186LC/PtAl, and (e) CM186LC/aluminide (part 2 of 2).

Table 3.2.12-X.
Quantitative metallographic measurements for samples tested to 8000 hr.

		Bare		Coated baseline		Tested				
Sample	Exposure	GPFZ	Pores	Beta	Coating	Beta	Coating	Diffusion	Interaction	Needle
B11	500	37	104							
B12	1000	28	120							
B13	3500	76	140							
B10	5600	26	102							
N11	500				55		59	70	81	
N12	1000				69		63	81	104	152
N13	3500						65	85	125	300
N10	8000				47		67		117	204
P10	500			37	72	50	86		112	167
P12	1000			34	69	48	76		117	194
P13	3500					50	75		150	350
P11	8000			51	58		75		163	613
S11	500			27	53	34	62		114	
S12	1000			20	51	21	33		79	145
S13	3500						50		110	200
S10	8000			29	51		--		37*	
P21	500			37	71	54	91		116	146
P22	1000			35	74	44	89		116	166
P23	3500						50		140	330
P20	8000			40	75				178	277**
S21	500			30	50	32	60		91	
S22	1000			29	54	31	65		89	180
S23	3500						35		75	215
S20	8000			29	53				69	182

*Coating was fully consumed

**Needles were present throughout sample

GPFZ is a gamma prime free zone due to preferential oxidation of aluminum from the surface.

Beta is the Al-rich surface phase of the diffused coatings.

Coating includes the diffusion layer and beta phase.

Interaction layer is a diffusion zone without needle like precipitates but containing globular ones.

Needle is an acircular precipitate, presumably sigma phase.

Table 3.2.12-XI.
Quantitative metallographic measurements for samples tested to 3000 hr.

		Bare		Coated baseline		Tested				
Sample	Exposure	GPFZ	Pores	Beta	Coating	Beta	Coating	Diffusion	Interaction	Needle
B51	3000	10	157							
B71	1245	31	66*							
B81	545	42	40**							
N31	2331				58		42	80	129	186
N82	3000				64		64		80	
P51	3000				75	20	50		208	332
P82	3000				64		57		113	
S81	1208			35	58	20	39		81	
S51	3000			29	55		34		117	204

*Includes internal oxides

**Includes loosely adherent surface oxides

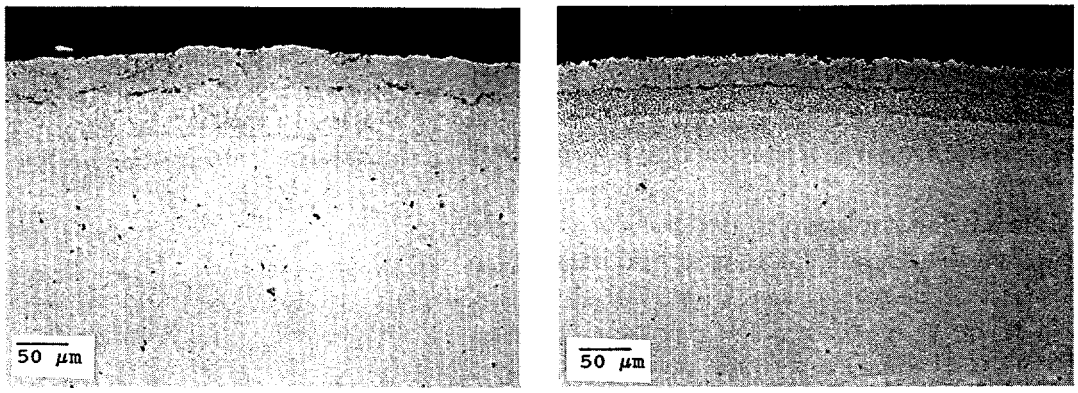

TE96-1369

Figure 3.2.12-22. The PtAl coating on CMSX-4 + La was thicker than the simple aluminide coating.

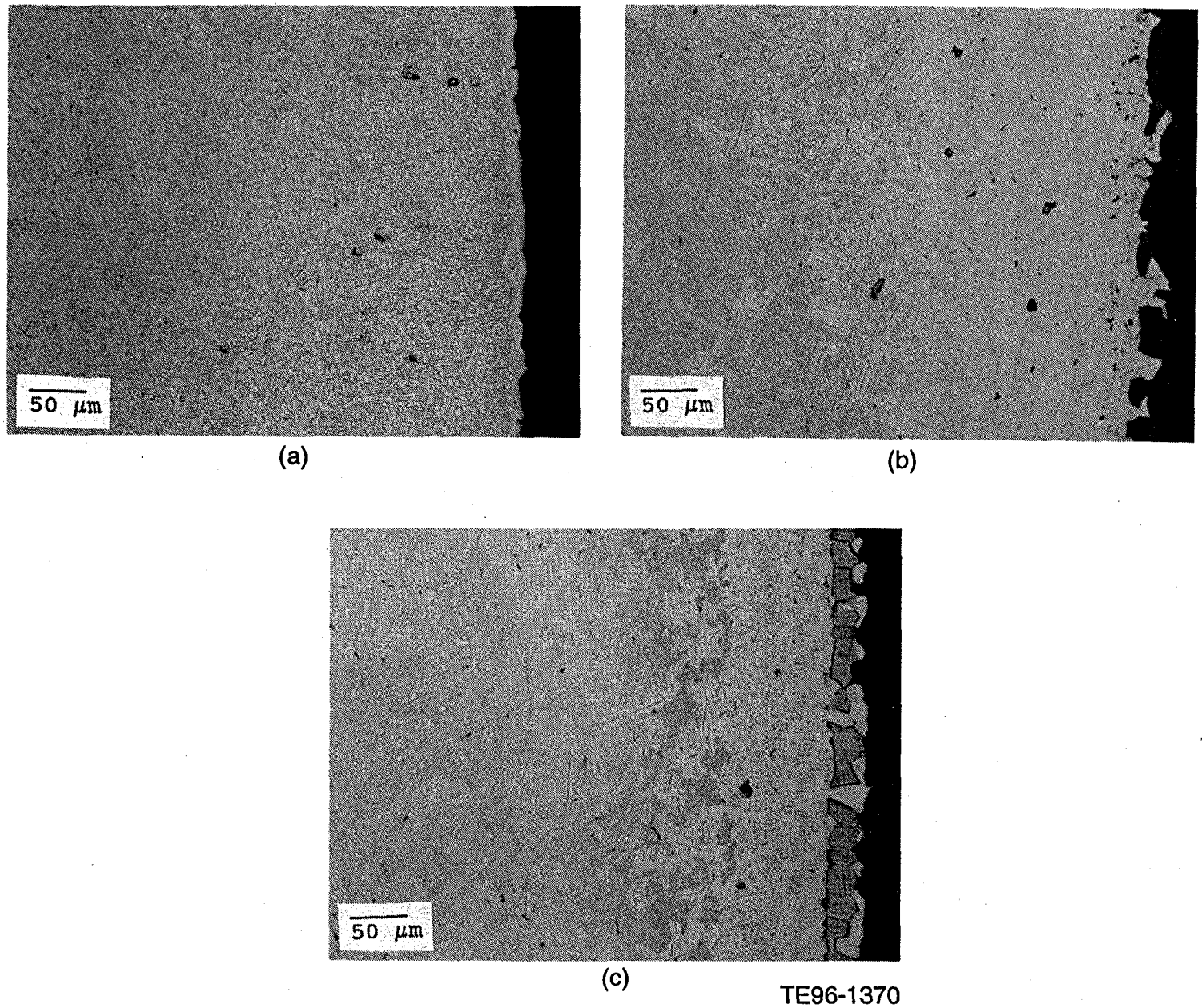

Figure 3.2.12-23. A thin depletion zone is evident for bare CMSX-4 + La (B51) and more substrate interaction is observed for simple aluminide coated CMSX-4 + La than for PtAl coated.

Figure 3.2.12-24 shows the post-test microstructure of the bare samples. There is a voluminous oxide on the IN 738 samples and some internal oxides on the Mar-M247 sample. The CMSX-4 has a gamma prime depletion zone but no internal voids; this result is contrary to previous samples that exhibited internal voids. The CMSX-4 + La sample has a thin gamma prime depletion zone and an adherent oxide film.

Figure 3.2.12-25 shows the baseline and exposed condition of IN 738/NiCoCrAlY. There is a small amount of retained beta phase and some oxide growth into the coating. A gamma prime denuded zone is apparent just beneath the coating. There are also small light gray precipitates throughout the sample.

Figure 3.2.12-26 shows the platinum aluminide coated IN 738. This sample does not exhibit any retained beta phase and has precipitates throughout the sample.

Figure 3.2.12-27 shows the simple aluminide coating on IN 738. A small amount of beta phase is present on the sample and there is a significant amount of coating substrate interaction.

Figure 3.2.12-28 shows that the electroplated CoNiCrAlY on CMSX-3 is not as uniform in microstructure as that deposited conventionally. The coating has been completely removed in one area and there is a gamma prime denuded zone beneath the coating.

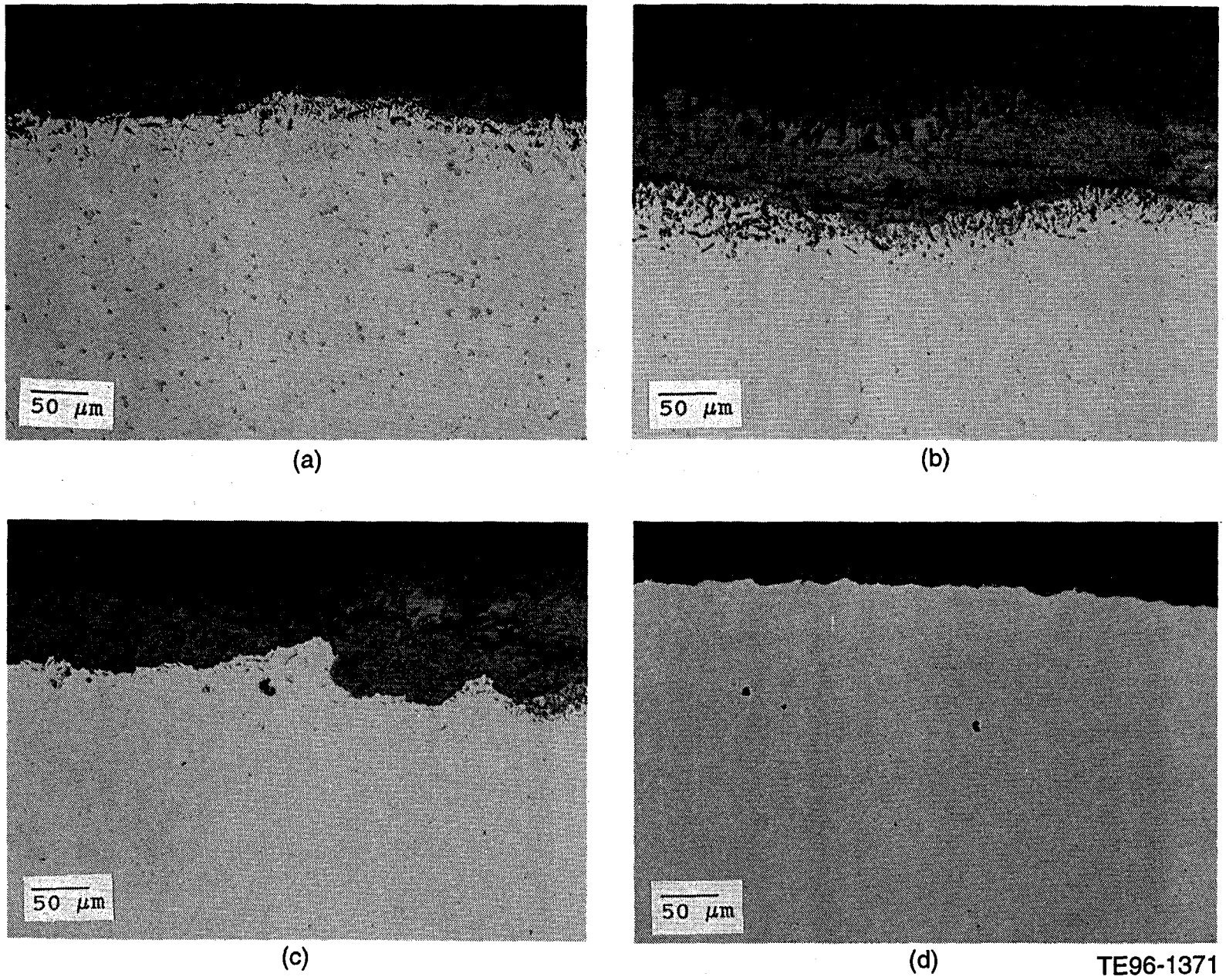

Figure 3.2.12-24. A voluminous oxide is visible on IN 738, while very little oxide is evident for CMSX-4 + La.

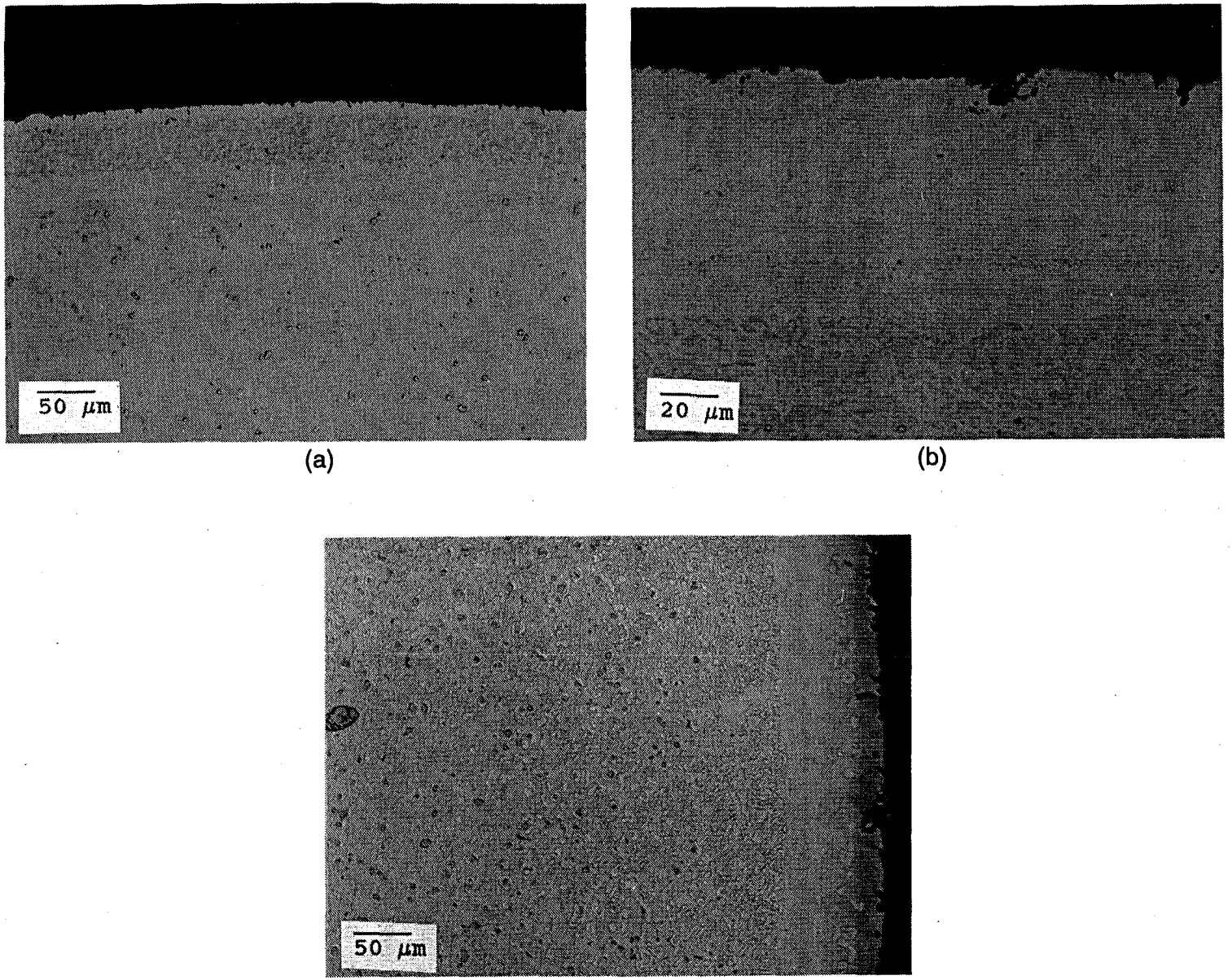

Figure 3.2.12-25. Gray precipitates are visible throughout the NiCoCrAlY coated IN 738 sample and a small denuded zone exists beneath the coating.

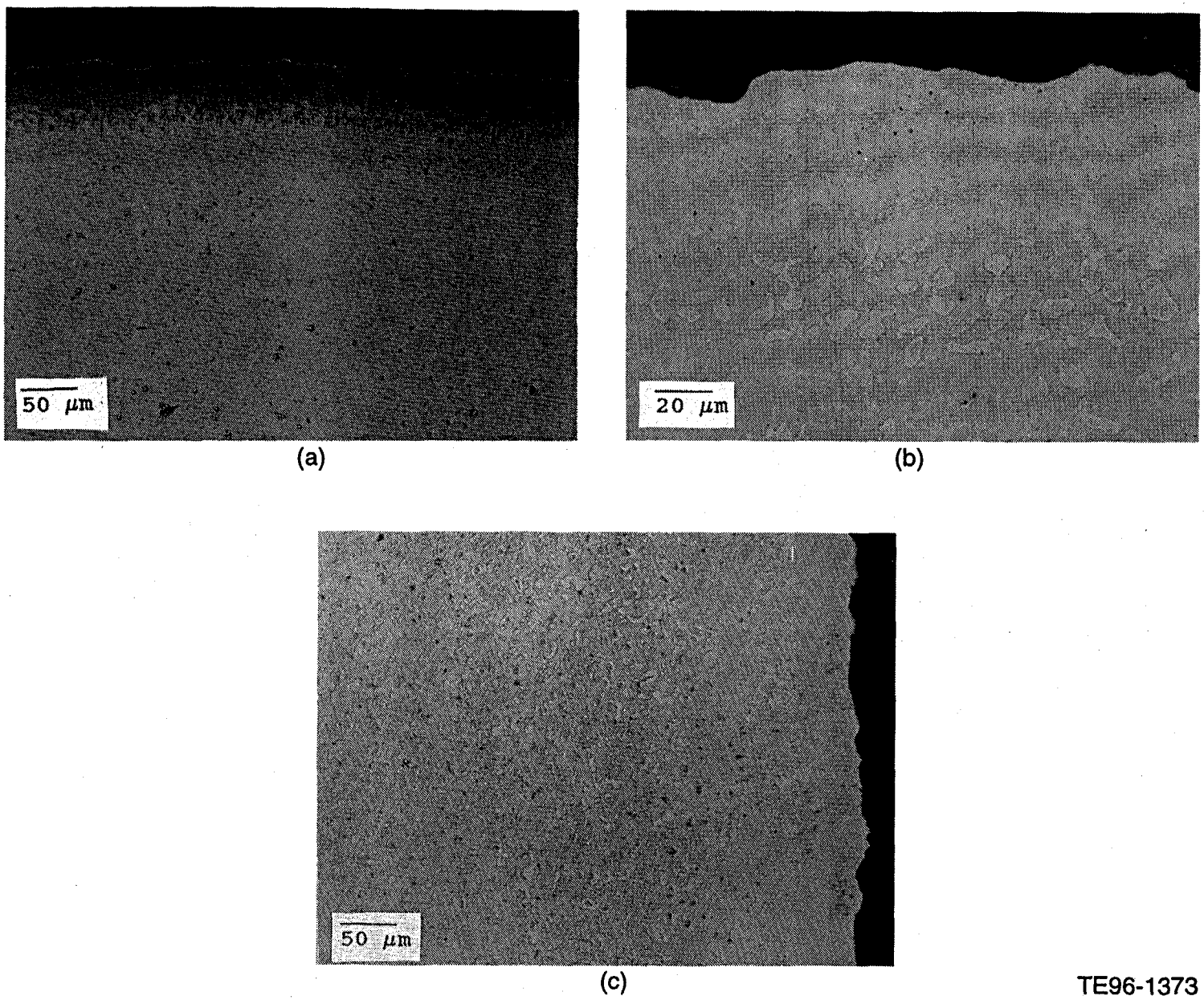

Figure 3.2.12-26. No retained beta phase is visible on PtAl coated IN 738 after exposure for 3000 hr.

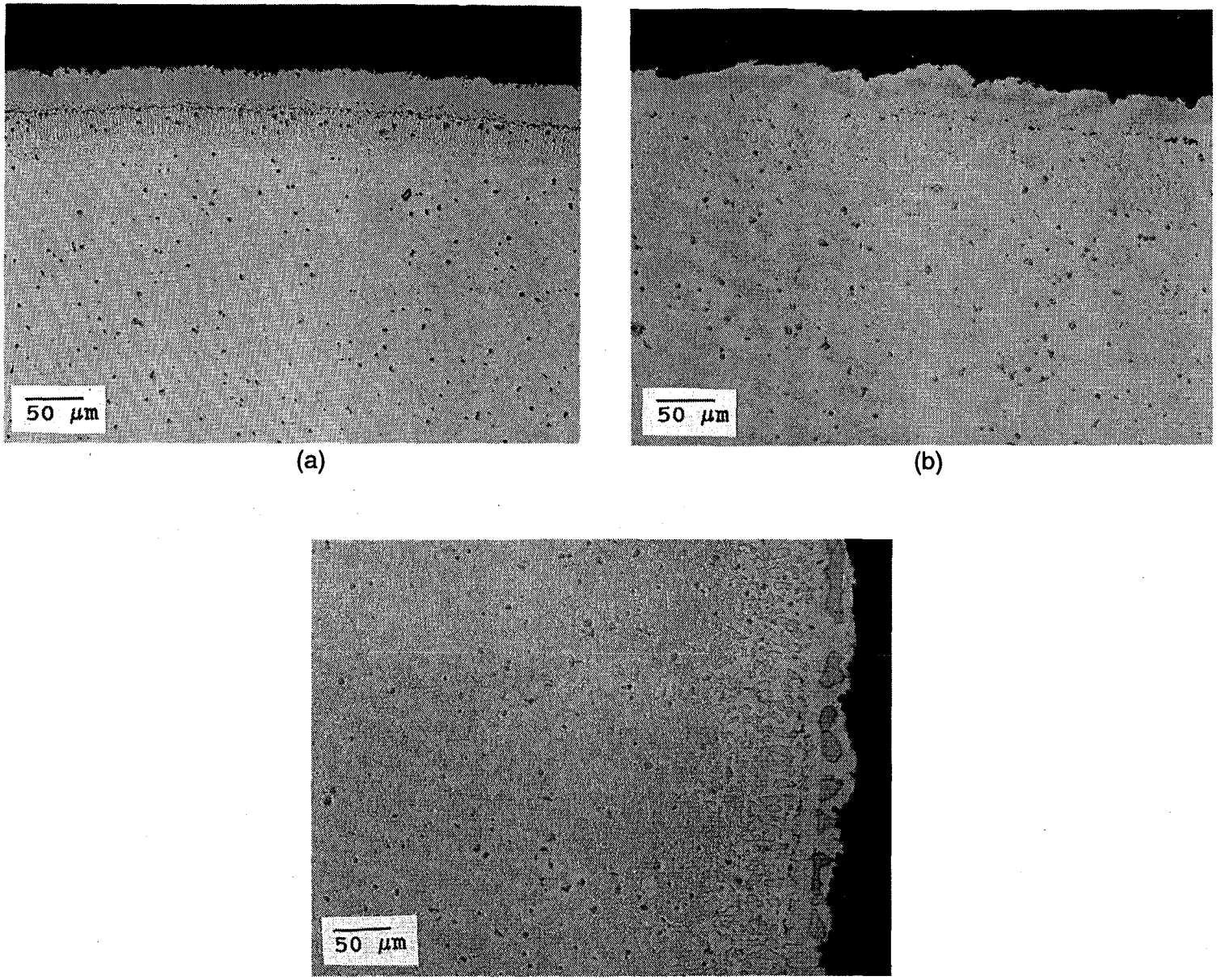

Figure 3.2.12-27. Beta phase is visible and there is a small amount of coating substrate interaction on simple aluminide coated IN 738 exposed for 1208 hr.

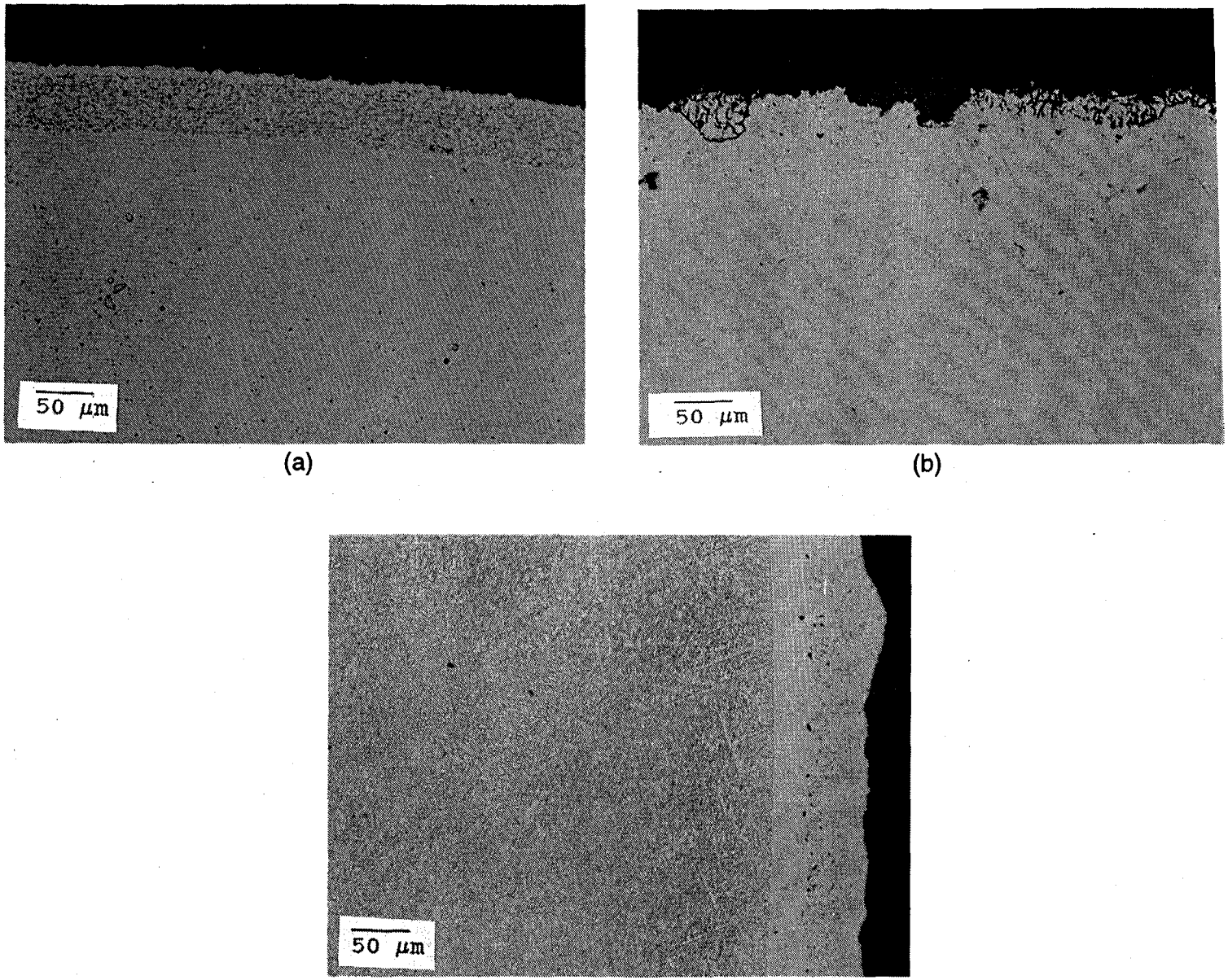

Figure 3.2.12-28. The electroplated CoNiCrAlY on CMSX-3 is not as uniform microstructurally as that deposited conventionally. The coating has been completely removed in one area after a 2330-hr exposure.

3.2.13 Thermal Barrier Coating of Turbine Vane Platforms

Objective

The ATS engine uses a Castcool design to cool the endwalls. Once proposed method to reduce the cooling flow to the endwalls is to apply a thermal barrier coating to the flow-path side of the endwalls. This has the potential to reduce the cooling air flow for improved engine thermal efficiency. A heat transfer study is proposed in this subtask to evaluate this option.

Discussion

Background

The ATS engine was proposed using a Castcool type cooling configuration for the first-stage vane. Castcool has demonstrated excellent cooling effectiveness at high turbine temperatures by using the near transpiration cooling approach. Since the ATS engine will require the maximum possible thermal efficiency, it will be extremely important to minimize cooling air via alternate cooling techniques. One such method is the use of thermal barrier coatings (TBC) to reduce metal temperatures rather than simply expending cooling air to accomplish this task. Vane endwalls have typically not been the focus of most heat transfer work, since the airfoil is the critical element in the vane segment assembly. The ATS engine will employ advanced (silo type) combustor technology to meet emissions goals; the result is a more uniform radial burner profile compared to past can annular combustors. However, the hot spot on the conventional combustor has historically been near the 50% span line, which left the vane endwalls relatively cool. The silo combustor has a much flatter radial profile, which means the vane endwalls, commonly referred to as the platforms, will operate at higher temperatures than in the past. Consequently, a typical solution might be to simply expend more cooling air on the platforms, but this would increase cooling air requirements in an environment where performance and efficiency are critical. The application of the TBC will reduce cooling air requirements by reducing the rate of heat input as it is carried away by the backside cooling. It should be noted that application of TBCs does not mean the elimination of cooling air, but rather a significant reduction compared to the conventional use of cooling air alone. This subtask will address the potential cooling air reductions due to the application of thin (0.010 in. maximum) TBCs. In addition, conventional film cooling coupled with TBCs will also be addressed.

To perform the analysis, some basic operational constraints had to be imposed. The key parameter in the analysis would be the maximum metal temperature that could be tolerated and still meet the general 16,000 hr life requirement for the first-stage vanes. Past experience has shown that 1750°F will permit most high temperature alloys to obtain this life. It is noted that generally the trailing edges of airfoils will experience higher temperatures and show corresponding distress, but 1750°F was judged to be a reasonable temperature for the endwalls to attain the 16,000-hr prior to removal. Consequently, the following analysis uses the 1750°F figure as the goal.

Another physical constraint imposed during the analysis was the use of 0.015 in. diameter for the gas side cooling holes. This is primarily an empirical value required to minimize clogging of the holes during operation. It should be noted that smaller holes would be better from a heat

transfer perspective, but operational considerations must also be imposed to achieve a reliable vane design capable of withstanding typical customer site operation.

Analysis

A heat transfer analysis was requested per TSR AZ.0413-01-800 for the high pressure turbine (HPT) first-stage vane inner and outer endwalls of the Advanced Turbine System (ATS) engine. The ATS engine was proposed using a Castcool HPT first-stage vane doublet from the AE 301X. The first task was to determine a baseline temperature field for the current cooling configuration for ATS cycle conditions. Since the original vane was a Castcool configuration designed for operation at higher temperatures, the second task was to determine the reduction in cooling flow, if any, realized by increasing the endwall gas side metal temperature to the 1750°F maximum temperature limit. The next task was to determine any further decrease in cooling flow due to the application of a thermal barrier coating (TBC) on the endwall. The last concern was the determination of the cooling flow required for a film-cooled endwall with and without a TBC using the ATS cycle conditions.

Method of Analysis

The following features are shared by the Castcool and film-cooled designs and the remaining discussion follows for each design. The Castcool vane doublet is cast from the single crystal alloy, CMSX-4, at the Allison Single Crystal Operation facility. The film-cooled endwall has the same configuration less the Castcool features (spar holes, etch, and coversheet holes) with rows of angled holes added.

The gas side boundary conditions are based on mass averaged conditions from the aerodynamic data bank. Inner and outer endwalls utilize streamline 1 and 11, respectively. At each axial location, the aero data are mass averaged in the circumferential direction resulting in a mass averaged velocity, temperature, and pressure.

Thermal Barrier Coating

The thermal barrier coating is a 8% yttria stabilized zirconia. Application of the TBC system requires that a compliant layer be put down between the base metal and the TBC topcoat. This intermediate layer, known as a bondcoat when used with TBC, can be either a metallic overlay or aluminide coating. Although both are used in the industry, Allison has most of its bondcoat experience with metallic coatings. This system will employ a 0.005 in. thick bond coat of NiCoCrAlY and a 0.010 in. topcoat of ceramic $Y_2O_3ZrO_2$.

Castcool Endwall

The Castcool inner and outer endwalls of the vane doublet were analyzed using an Allison in-house heat transfer program called EWALLOPT. EWALLOPT is based on another Allison program called LAMILOP3 which analyzes Lamilloy configurations for heat transfer, stress, and life requirements and can be operated to analyze a current design or optimize a design for development work. In general, EWALLOPT examines multiple micromodels where hole diameters and spacings, etch patterns, and depth and sheet thickness are input to define the wall geometry. Coolant supply conditions are input and the gas side conditions used for the heat transfer analysis are the mass averaged gas properties from the included aero data bank. If de-

sired, the local static gas pressure is used to size holes at any location to maintain the blowing rate determined from the mass averaged conditions.

The gas side heat transfer coefficients are determined from an integral technique that uses the mass averaged gas side properties. The integral technique is formulated for a transpiration (ideal, complete surface coverage for the blowing) cooled wall with the blowing term in the formulation reduced by a factor to account for the discrete hole locations (blowing) of Castcool configurations. The factor has been correlated with available Lamilloy data. EWALLOPT was operated in the mode (impinge option) that breaks the internal cooling effectiveness into parts (i.e., separate correlations for backface cooling and for cooling in the etch) to solve for the wall temperatures.

In contrast, EWALLOPT can be operated using the older Lamilloy correlation for the internal cooling effectiveness by removing the key word impinge. A schematic of the coversheet hole locations with respect to the vanes on the doublet and the extent of the underlying etch (dashed line) is given in Figure 3.2.13-1 for the outer endwall (the inner endwall is similar). The axial location of the micromodels used is also shown in Figure 3.2.13-1.

Film-Cooled Endwall

A two-dimensional finite element model was made to analyze the outer endwall of the vane doublet for the film cooling scheme. The model uses four-noded quadrilateral elements with model width of arbitrary thickness in the circumferential direction less than the distance between two adjacent vanes. As such, the heat transfer model will be influenced by the film cooling hole diameter and spacing, but not the total number of film holes (i.e., flow per unit width). The mass averaged path is defined by an axial location and turning angle that was determined from the mass averaged velocity data (this path is not a streamline, but is similar in most cases). The length coordinate of the finite element model follows the surface length of the mass averaged path (i.e., the endwall was sliced along the mass averaged path and not alongthe engine axis). By doing this, the model better reflects the gas side conditions that drive the heat transfer. The model mesh and axial location of film cooling holes are shown in Figure 3.2.13-2. The mass averaged path is shown on the endwall in Figure 3.2.13-3.

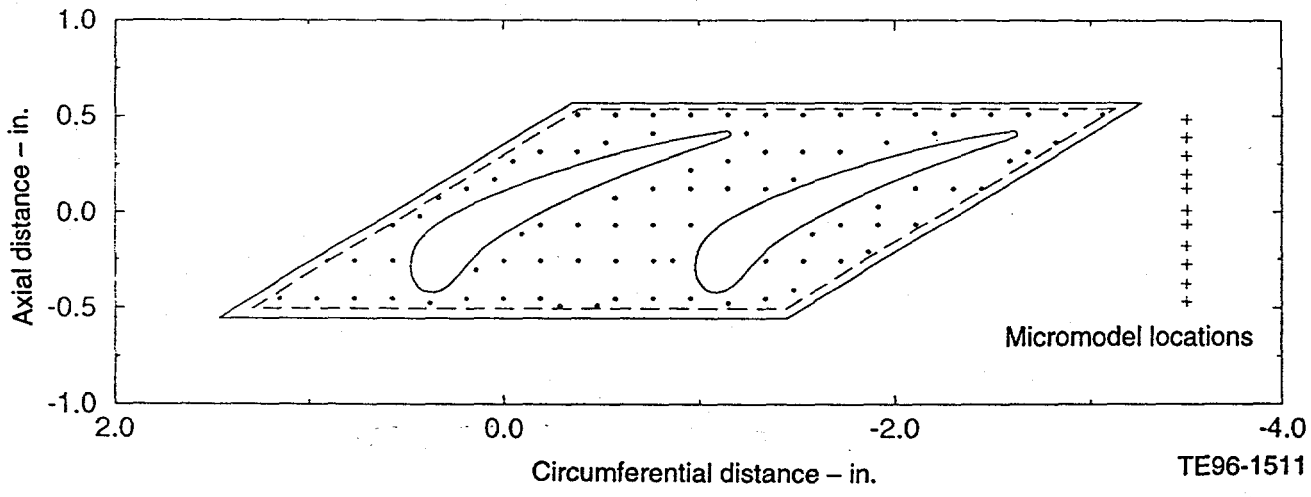

Figure 3.2.13-1. Schematic of gas side cooling exit holes (coversheet holes), vane locations, extent of the internal Castcool etch and axial locations of the micromodels used in the analysis of the outer endwall for the ATS first-stage HP vane doublet.

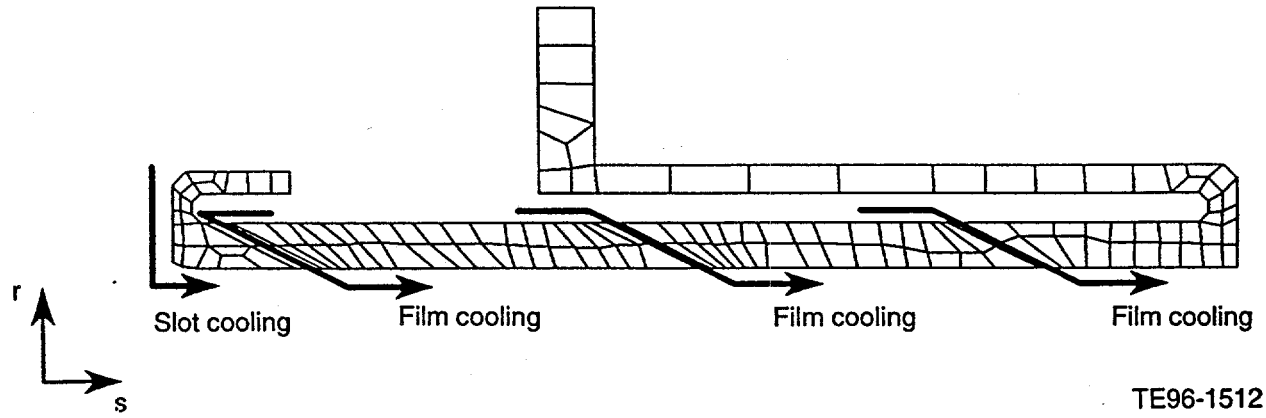

Figure 3.2.13-2. Geometry and finite element model for the film-cooled version of the outer endwall for the ATS first-stage HP vane doublet.

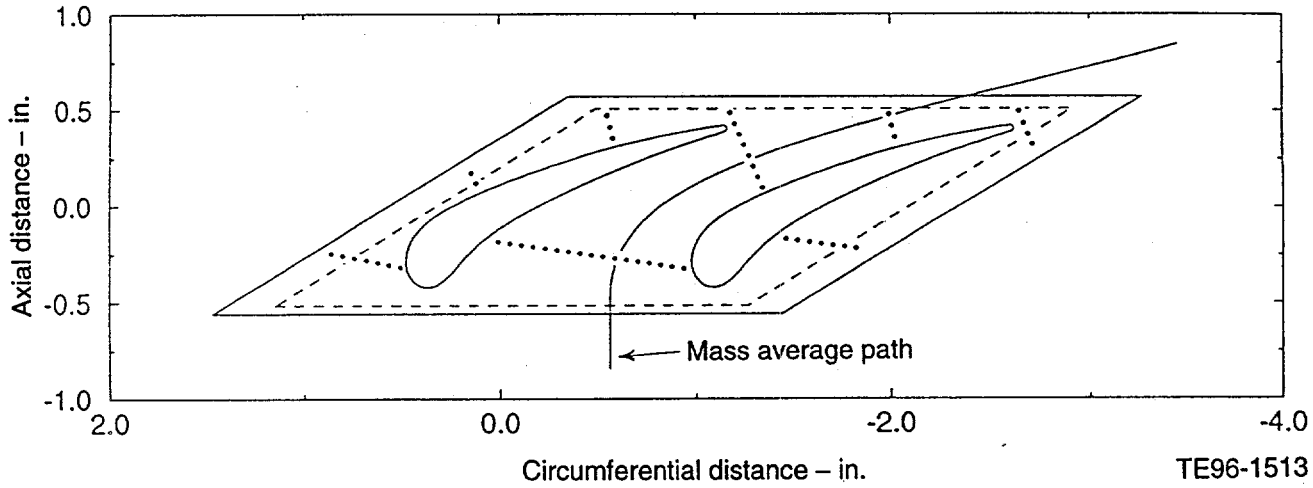

Figure 3.2.13-3. Schematic of film cooling holes, vane locations, and extent of internal coolant supply plenum of the outer endwall for the ATS first-stage HP vane doublet.

The boundary conditions are applied to the finite element model. The gas side heat transfer coefficients are determined from mass averaged gas conditions using an integral code. These heat transfer coefficients are increased by 20% due to the blowing of the film holes per the data for an accelerating boundary layer flow.

The adiabatic wall temperature is a function of the film cooling hole locations, hole angle, and coolant and gas conditions. Using L'Ecuyers film cooling program, the adiabatic wall temperatures with film effects were determined for multiple hole rows by superposition. The slot film cooling at the leading edge of the endwall was modeled, and this was approximated in the film cooling input as a row of holes to account for the effect of this leakage flow at the film holes. The film effectiveness for the slot could not be matched exactly by a row of film holes, but was approximated very well, which saved the need for additional work to account for the leading edge slot flow in the hole film cooling adiabatic wall temperature results. The coolant side of the endwall and film holes was modeled as channels to determine the coolant temperature rise.

The channel exit temperatures were used as input for the film cooling program to get the gas side adiabatic wall temperatures to be input as the gas temperature for the finite element

model. Because of the interdependence between the coolant temperature rise and adiabatic wall temperature, iteration was required.

The coolant side boundary conditions were based on the film hole flows. Except near the entrance to the film holes, the convection coefficient was based on an average flat plate correlation with the length restarted at each row of holes since the boundary layer is being removed out the film holes. Near the entrance to the holes, the correlation was used with modified correlation coefficients based on Lamilloy data. The axial length this heat transfer coefficient was applied to was equal to the hole spacing. The leading and trailing faces and the plenum side of the radial hanger are modeled as a flat plate using the cooling flows of 0.277%, 0.09% (of engine flow) and the total film flow, respectively. The region around the W clip was arbitrarily assigned a convection coefficient of 5 Btu/(hr-ft^2-°F) due to the leakage flow around the clip. The coolant supply cavity has a stagnant region at the downstream end of the cavity. This region was arbitrarily assigned a low convection coefficient of 10 Btu/(hr-ft^2-°F). The coolant temperature for this region was based on a channel with a flow rate equal to 1/100 of the film cooling row upstream to simulate the weak interaction with the row of film holes.

Results

This study has shown that the addition of a TBC topcoat can reduce the cooling air requirements. This minimum hole size causes the endwalls to be overcooled on the Castcool design, which minimizes the potential cooling flow reduction due to the addition of TBC. The film-cooled approach permits 30+% reduction in cooling air to meet the 1750°F metal temperature criterion. This can be attributed to the fact that the non-TBC version has hot spots that require significantly increased cooling air to meet temperature. This investigation shows that Castcool is very effective, but at lower firing temperatures, its ability to reach maximum efficiency is compromised due to the 0.015 physical hole size limitation. Conversely, film cooling benefits greatly from the addition of the TBC due to its lower thermal effectiveness. This study shows that film cooling/TBC system may be a viable cost effective way to cool turbine hardware at lower cost.

A further study of the cooling requirements at the actual operating points in the Phase 3 ATS design is recommended along with cost figures. Costs should include not only component manufacturing cost but also life cycle cost for the engine during operation since the Castcool design will be operating at a lower temperature due to the overcooled condition. Consequently, it may be possible for a more expensive Castcool design to last longer and thus lower the owning and operating cost. This trade study is recommended as part of the work scope for the Phase 3 design work.

Note that the cooling flows alone can be somewhat misleading since the Castcool has the additional criterion of a maximum hole spacing to hole diameter ratio of 12.5 (both designs limit the minimum gas side hole diameter to 0.015 in.). Since the minimum hole size and maximum hole spacing are being used in the Castcool design, the endwall is overcooled (gas side metal temperature below the maximum allowable).

Castcool Endwall

To baseline the study, the current configuration was analyzed under ATS conditions, and the results are given in Figure 3.2.13-4 for both the inner and outer endwall. The axial distance is referenced to the stacking axis (i.e., location 0,0 in Figure 3.2.13-1). The cooling flow for the

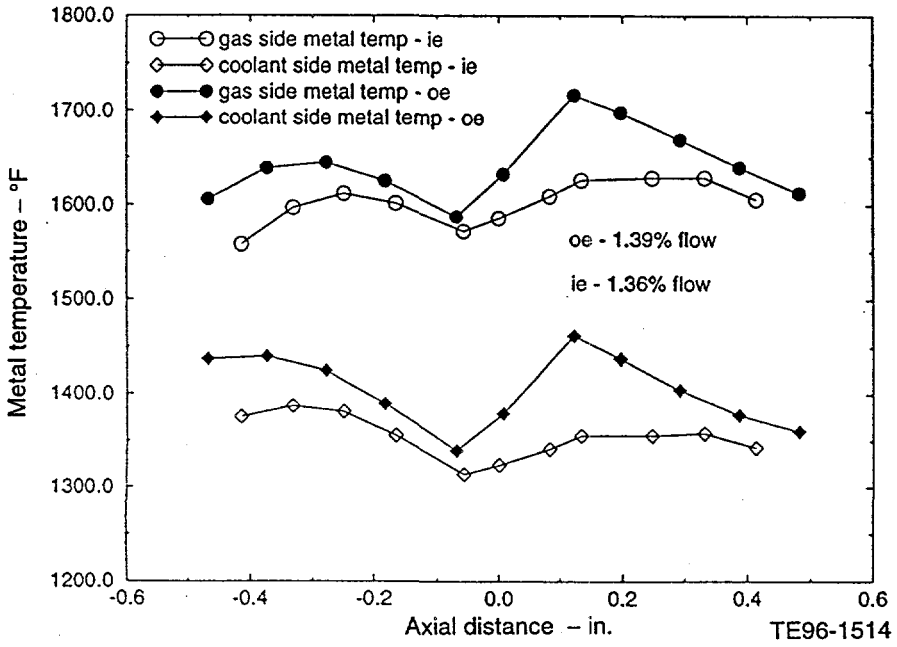

Figure 3.2.13-4. Distribution of the gas and coolant side metal temperature for the Castcool design with the current configuration AE 301X hole sizes.

inner endwalls, 1.36 and 1.39% respectively, is given as a percent of engine flow. The endwall is overcooled and some reduction in cooling flow can be realized by reducing the hole diameters and raising the wall temperature to the 1750°F maximum allowable. This was done with the additional criteria of a 0.015 in. minimum coversheet hole diameter and a maximum hole spacing to hole diameter ratio of about 12.5. Note, the axial spacing of the micromodels is smaller than the hole spacing. This does not improve the modeling of the Castcool geometry, but better correlates with the variation in gas side conditions. The micromodel size is based on the area enclosing four pedestals, but since there is no thermal connection between the micromodels, overlapping the models does not affect the analysis.

The resulting metal temperature distribution is shown in Figure 3.2.13-5 for the case of reducing the coversheet hole diameter (0.015 in. minimum) to raise the gas side metal temperature to the allowable (inner and outer cooling flows are 1.06% and 1.15% of engine flow, respectively). At the trailing edge, the endwall remains overcooled.

Addition of a 0.015 in. TBC (Figure 3.2.13-6) reduces the coolant flow slightly (inner and outer cooling flows are 0.98% and 1.05% of engine flow, respectively). The hole sizes could only be reduced a small amount over the first 75% of the endwall before meeting the hole size minimum. As such, the entire endwall is overcooled. The metal temperature decreases downstream since the blowing rate increases (e.g., for a uniform hole size, the gas side static pressure decreases axially down the endwall and the blowing rate is proportional to the pressure difference across the wall).

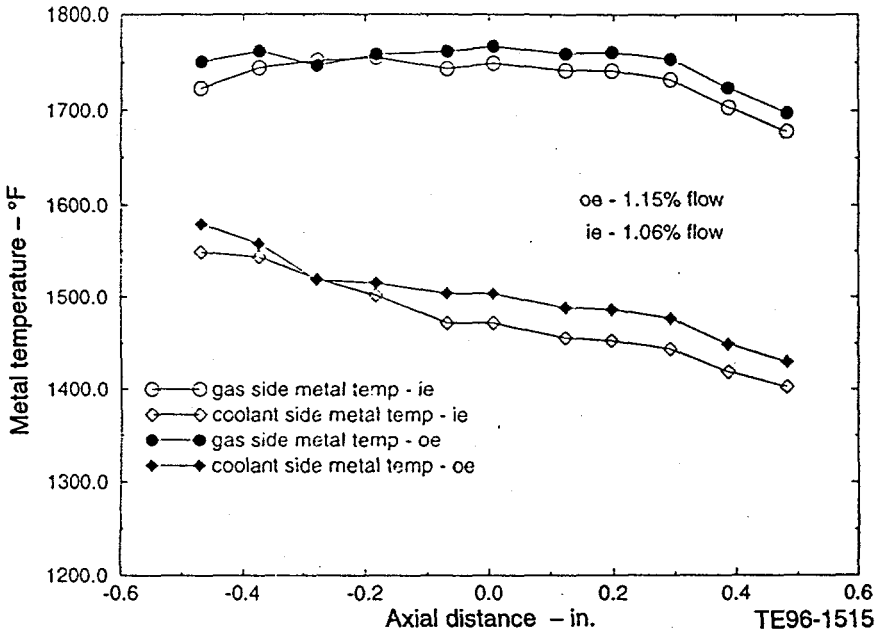

Figure 3.2.13-5. Distribution of the gas and coolant side metal temperature for the Castcool design with a 0.015 in. minimum coversheet hole size.

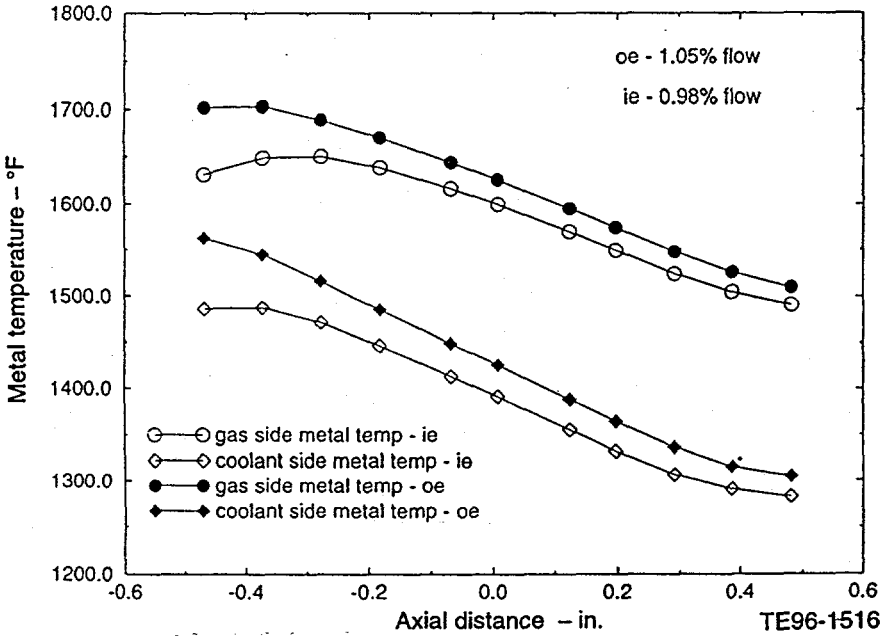

Figure 3.2.13-6. Distribution of the gas and coolant side metal temperature for the Castcool design with a 0.015 in. minimum coversheet hole size and a 0.015 in. TBC.

Film-Cooled Endwall

The wall temperature distribution for the film-cooled design is shown in Figure 3.2.13-7 for the outer endwall with and without TBC (with and without TBC cooling flows are 1.04% and 1.55% of engine flow, respectively). The axial variation in maximum and minimum metal temperature without and with TBC are about 175°F and 225°F, respectively, downstream of the first row of holes. This results from the larger coolant side convection near the entrance to and in the film holes as compared to in between the rows of holes. This is contrasted with the Castcool endwall (Figure 3.2.13-6), which does not show large localized gradients that can contribute to LCF problems. There is some gradient between the holes for Castcool geometries (which is not present in Figure 3.2.13-6 because the micromodels are not connected with axial heat conduction in the wall), but it is smaller since the holes are much closer together.

The total number of holes given in Table 3.2.14-III was determined with a 0.050 in. border around the perimeter of the endwall where no holes were allowed. The temperature field for the film-cooled design without TBC is given in Figure 3.2.13-8 (the temperature field is similar with TBC applied).

In summary, the addition of a TBC topcoat has the potential to reduce the cooling air requirements as noted in vane locations, extent of the internal Castcool etch, and axial locations of the micromodels used in the analysis of the outer endwall for the ATS first-stage HP vane doublet.

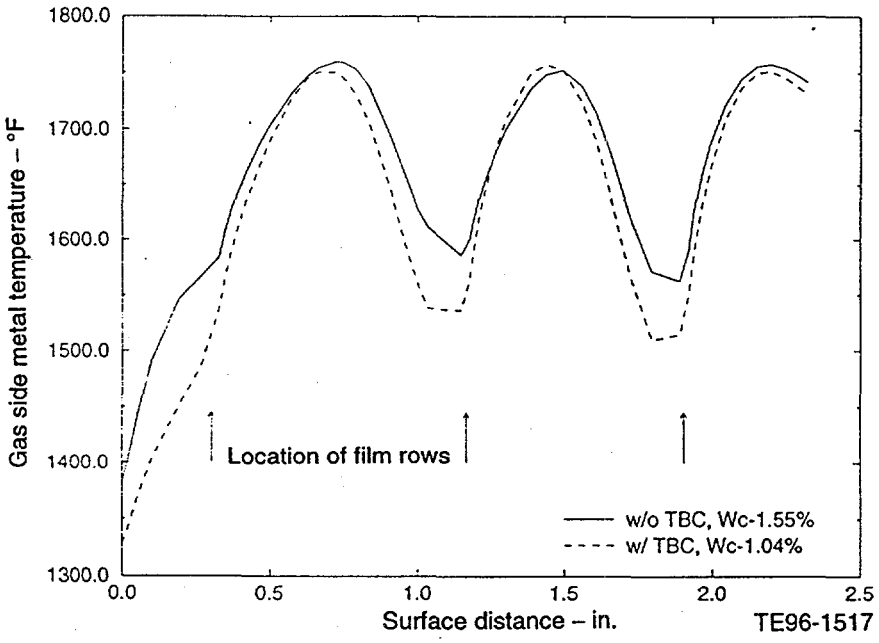

Figure 3.2.13-7. Comparison of the gas side metal temperature distribution for the outer endwall with and without TBC.

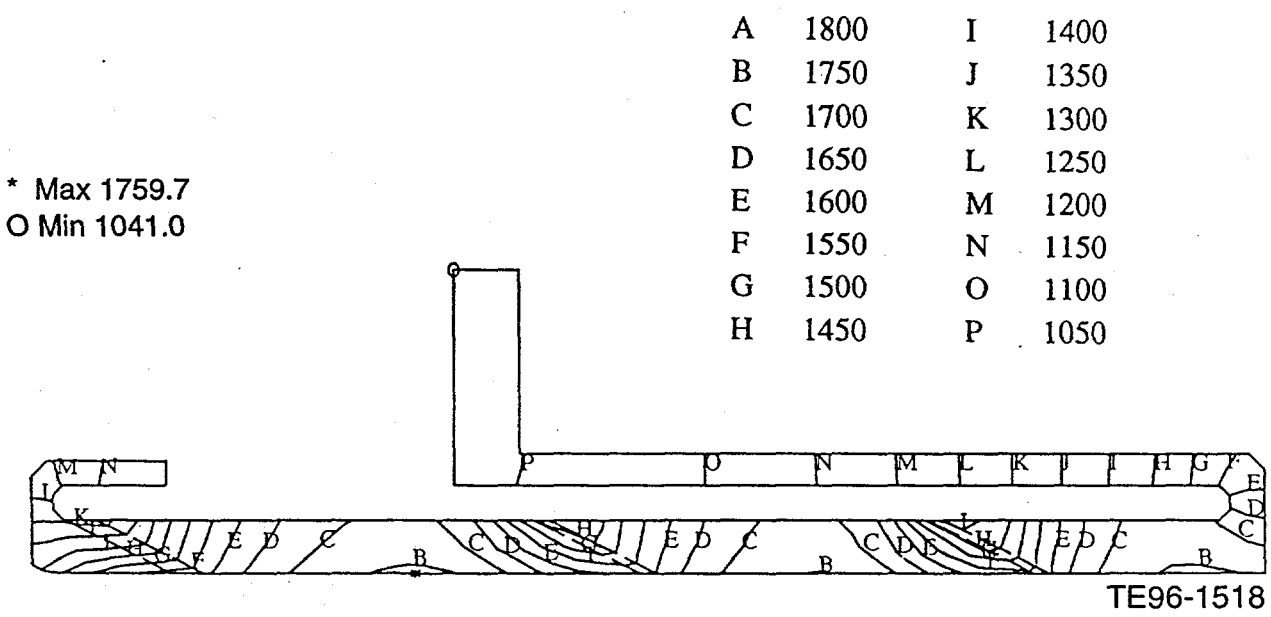

Figure 3.2.13-8. Temperature field of the outer endwall for the film cooled design without TBC.

3.2.14 Design Validation

Objective

The design validation process at Allison requires the creation of a Design Requirements document and a Design Criteria document followed by a series three of design reviews. The first review, the Conceptual Design Review, occurs after the requirements and criteria are published and the General Arrangement drawing is available. The second review is the Preliminary Design Review, which is held after the initial design layout drawings and procurement specifications are completed. The details of design, the test plan, and the schedule are the subjects of this review. The Critical Design Review is held after sufficient development testing has been completed to assess the readiness of the engine for qualification testing or field evaluation. This subtask was intended to cover the creation of the two design documents and the Conceptual Design Review.

Discussion

Section 3.2.8 of this report covers the work done under subtask 6.08 that led to the reconfiguring of Allison's ATS engine. To effectively define the design requirements for the engine, it is desirable to know, in general terms, the configuration of the engine. Therefore, the development of the specific design requirements was delayed until the completion of subtask 6.08 in its redirected form. These requirements have now been written and published as Engineering Design Specification EDS 3334.

According to Allison Engineering Procedures, the Design Criteria document is to be developed from the Design Requirements. Since the requirements were completed late in the Phase 2 Extension contract period, it was decided that the criteria should be developed under the Phase 3A contract. This activity is under way, and will be completed by the time this report is submitted.

The Conceptual Design Review has also been delayed because of the reconfiguration of the engine. This review is now scheduled to occur in October 1996. This will allow time for the completion of the Design Criteria, the General Arrangement drawing, and the Engine Model Specification, all of which are required for the Conceptual Design Review.

Results

The Design Requirements document will be completed by the time this report is submitted. The creation of the Design Criteria and the Conceptual Design Review have been rescheduled to occur early in Phase 3A.

4.0 TASK 8.01 - CASTCOOL TECHNOLOGY DEMONSTRATION

Task 8.01 - Castcool®* Technology Demonstration was designed to build upon Phase 2 programs in the following five key technology areas:

- Castcool blade fabrication
- Castcool HP turbine design analysis
- demonstration of coating Castcool airfoils with platinum-aluminide (Pt-Al)
- development of a film-riding face seal
- Castcool blade abrasive tip development

Each of these tasks provided input, consisting of either assets, processes, or data, for the Gas Generator Testing planned under ATS Phase 3 in August 1996. A discussion of each of these tasks' objectives and accomplishments is provided in the following paragraphs.

4.1 CASTCOOL BLADE FABRICATION

Objectives

Castcool turbine technology is a critical technology needed for the DOE's ATS program. Castcool is a manufacturing process that enables the casting of holes and intricate patterns in high temperature capable single crystal materials. Allison is using the Castcool process to manufacture turbine airfoils that use highly effective cooling schemes, such as Lamilloy®*, in a cost effective manner to improve engine thermal efficiency.

Allison has been developing a Castcool blade that is directly applicable to the ATS turbine. Under an ATS Phase 2 task, Allison continued to refine the fabrication process initially developed under IR&D and cast a number of blades and improved yield by 60% from the start of the effort. However, the fabrication process cannot be validated by making a small quantity of airfoils. A large enough sample needs to be made to verify the yield and overall quality of parts. This subtask was established to build upon the previous efforts and cast an additional number of engine quality blades and complete all detailed inspections of these castings. This includes visual inspections, ultrasound (for wall thickness), borescopes, X-ray (to examine internal features and deviations), chemistry analysis, metallography, water flow, and airflow tests. These data will be compared with the design intent and previous castings to validate the current process and identify potential process refinements required to assure production readiness for ATS applications. As a side benefit, this task will fabricate blades that can be used for other subtasks and for engine testing.

Accomplishments

Good quality blades were finished and fully inspected under this task. Yield demonstrated continual improvement and surpassed the levels demonstrated in the Phase 2 effort. Significant accomplishment in the area of wax assembly quality resulted from continued effort by Allison's Single Crystal Operations working in conjunction with the assembly vendor.

---

* Registered trademark of Allison Engine Company.

During final inspection of the Castcool blades, cracks were detected along a 45-deg angle near the trailing edge. Detailed X-ray inspection found cracks in 14 of the blades, all in the same location in the pin-fin trailing edge area of the airfoil. A review of the blades found that the cracks developed in the final cleaning of the parts. The blades were cleaned using an ultrasonic method. The power level and frequency of the ultrasonic machine was sufficient to excite a panel mode in the thinnest area of the airfoil wall, resulting in cracking of the airfoils. Because the cracks occurred in the trailing edge pin-fin cooling area, not in the Castcool part of the airfoil, we feel that problem is not inherent to the Castcool blade design. Subsequent airfoil processing using a lower power ultrasonic cleaning process has been successful.

Several airfoils were scrapped for destructive inspection and testing in the diagnosis of this problem. A review of all available data, including design, processing, and the observed failure mode, did not indicate a problem in engine operation; therefore, the remaining blades were cleared for demonstration in the ATS Phase 3 gas generator test. All blades will be inspected after the gas generator test to verify successful engine operation.

4.2 CASTCOOL HP TURBINE DESIGN ANALYSIS

Objectives

In 1994, Allison completed testing of an ATS prototype turbine in the AE 301X turbofan engine under a Phase 2 task. This turbine, which featured Castcool technology first-stage vanes, was successfully tested above the ATS turbine rotor inlet temperature goal. As reported in Phase 2 Annual Report, a significant amount of information and experience was gathered on this turbine from the test program. In 1996, Allison will conduct endurance testing at even higher temperatures in a gas generator under ATS Phase 3. This test will include Castcool first-stage blades fabricated under Task 8.01.01. This subtask was established to evaluate the results of the previous test and analyze the design modifications to the turbine in relation to this planned testing.

Accomplishments

Based on available data from the Phase 2 turbine test, the operational requirements for the Phase 3 test were established. Detailed temperature and pressure data from the HP turbine were used to correlate heat transfer and secondary flow models, providing a baseline for the Phase 3 test analyses.

This task has incorporated lessons learned from the Phase 2 engine demonstration and evaluated design modifications required for the Phase 3 testing. Following updates to the analytical models to reflect known design modifications, a complete structural analysis of the HP turbine rotor, case, and static structure to the Phase 3 gas generator test conditions was completed. All of the components, with the exception of the second-stage blade, were found to meet the design criteria for the Phase 3 test. The second-stage blade average section metal temperature was too high for adequate airfoil life. Additional cooling holes were added to the pressure surface tip region and the trailing edge to reduce the blade metal temperature. Based on the additional blade cooling requirement, a modification was made to the second-stage preswirler.

4.3 DEMONSTRATION OF COATING CASTCOOL AIRFOILS WITH Pt-Al

Objectives

Under a previous ATS Phase 2 task, Allison evaluated several types of coatings for long term oxidation resistance. These results indicate that a platinum-aluminide Allison electrophoretic process (AEP) coating is the best solution for the first-stage Castcool CMSX-4 airfoils. Allison has performed some demonstrations of applying this coating on Lamilloy and Castcool disk samples, but not on actual Castcool airfoils. Under this subtask, Allison is developing and demonstrating the application of the platinum-aluminide AEP coatings on Castcool vanes and blades using existing assets.

Accomplishments

Coating trials of four Castcool vanes and five Castcool blades were completed. Subsequent cold flow testing demonstrated acceptable cooling flow levels in all five Castcool blades. These blades will be demonstrated in the ATS Phase 3 gas generator testing. The Castcool vanes were determined to have excessive cooling flow reduction due to hole blockage. The low-flowing holes were enlarged using a highly localized grit-blast procedure, demonstrated successfully on earlier Allison Lamilloy airfoils. Following a successful cold flow recheck, these assets were also cleared for demonstration in the gas generator. The coated blades will be evaluated as part of the Phase 3 post-test hardware evaluation.

4.4 DEVELOPMENT OF A FILM-RIDING FACE SEAL

Objectives

Film-riding seal technology has the potential to reduce seal leakage below levels demonstrated on brush seals with higher ΔP capability and longer durability due to the noncontacting design, making it an attractive technology for ATS applications. Allison has been developing this technology and has demonstrated these potential benefits on a seal rig. This task will take the "next step" and design, fabricate, and rig test an engine configuration film-riding seal. This seal will replace the current three-stage brush seal at the compressor discharge location on the T406/AE engine compressor. After successful rig testing, this seal will be available for gas generator/engine testing. Allison is subcontracting John Crane Company to fabricate and rig test the seal.

Accomplishments

Fabrication and acceptance testing of two film-riding face seals was completed at John Crane Company with Allison personnel on-site. The seals passed all test points with no problems, with leakage flow rates an order of magnitude less than the existing brush seal design. Final preparations were completed for integration of the seal into the gas generator test hardware. The seal has been assembled in the gas generator for the August 1996 demonstration.

4.5 CASTCOOL BLADE ABRASIVE TIP DEVELOPMENT

Objectives

The Castcool blade design incorporates Lamilloy cooling technology to cool an abrasive tip (for clearance control) with a minimal amount of cooling air. Two fabrication approaches are being evaluated for the blade tip:

1. a Castcool tip with a bonded abrasive tip
2. a machined Lamilloy tip with a double-braze, single crystal plate/abrasive tip

Under our completed ATS Phase 2 Castcool blade fabrication development effort, we successfully cast the Castcool tip on several development pieces. The data taken to date clearly show a negative impact on casting yield with this approach. The need exists, therefore, to develop an alternative approach. This task will develop the process to put abrasive tips on both configurations, demonstrate these processes on a set of blades, compare the finished part yield of both approaches, and provide a recommendation for the ATS program.

Accomplishments

Blade tip bonding was completed during this period. Castcool tips with a bonded abrasive tip have been completed. These tips represent a more traditional approach with one braze joint. Problems were encountered with the dual-braze tip required for the machined blade. The tip was curling in the braze furnace due to thermal fight between the single crystal sheet and the abrasive mat material. A new tip configuration was defined consisting of the abrasive mat material sandwiched between two single crystal sheets. After bonding to the blade, the outer sheet was machined off to the abrasive material. Furnace tests showed no curling of the tips. Machined Lamilloy tips with a double-braze, single crystal plate/abrasive tip have been completed. These blades will be demonstrated in the ATS Phase 3 gas generator test to evaluate the durability of both configurations.

5.0 TASK 8.04 - ATS LOW EMISSION COMBUSTION SYSTEM

5.1 CATALYTIC SYSTEM PILOT/PREBURNER DESIGN AND TEST

System Configuration

Various ATS combustor configurations (silo-type, externally mounted canted can, annular, and canted annular) were evaluated. For the same combustor volume, the silo combustor provides the lowest total surface area and the highest backside convective cooling velocity for the same liner/casing gap. However, a silo combustor would require a large envelope for installation and a large catalyst diameter.

During Phase 2 and Phase 2 Extension, it was thought that an Allison 501-KB7 demonstrator engine would be used to demonstrate the catalyst technology. As a result, an investigation to determine the optimal catalytic combustion configuration was performed. Various pilot, preburner, and premixer locations were analyzed to determine fuel and air splits as well as zone temperatures and equivalence ratios over the operational range of the 501-KB7 engine cycle.

Configuration assessments indicated that a parallel staged fuel injection system may be a good approach (see Figure 5-1). This would involve a multiple module setup similar to the one being used in the Ultra-Low Emissions Gas Turbine Combustion System (9 ppm NOx) program. This would be accomplished by using 19 burner modules in 3 different modes depending on the engine operating conditions. These three modes include flowing air only (no fuel), flowing a fuel/air mixture with an equivalence ratio less than the lean blowout (LBO) limit for the combustor, and flowing a combustible fuel/air mixture. The preheated mixture would then proceed to the catalyst where combustion would be completed.

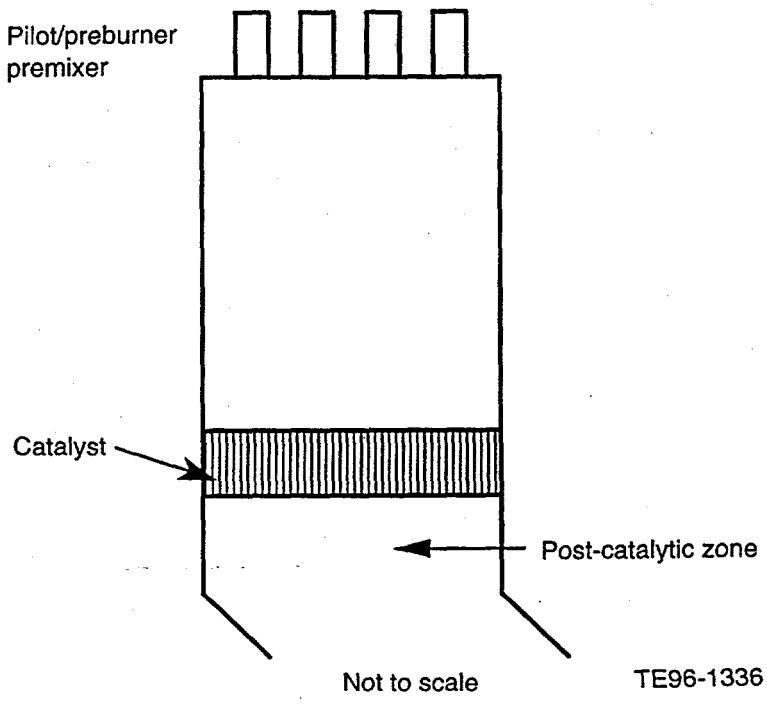

Figure 5-1. Parallel staged fuel injection configuration.

High pressure testing of a parallel staged fuel injection system was performed in the Allison Research Laboratory Facilities. The test involved operating the center lean premixed module (of a group of seven modules) at various equivalence ratios while operating the outer six modules at equivalence ratios below lean blowout. The test indicated there was considerable interaction between the modules such that the minimum overall efficiency was approximately 50%. The pattern factor produced at this efficiency was 0.4. As a result, the parallel staged design will not to considered. The interaction between the modules and the poor temperature distribution made it a less than optimal selection.

During the Phase 2 Extension effort, various series-staged configurations were analyzed. Two series-staged silo combustion systems have been chosen as potential candidates (Figure 5-2). The first system is the "traditional" catalytic combustion system, which includes a pilot/preburner in the first stage, a premixer in the second stage, followed by a catalyst. The high pressure, high temperature ATS cycle allows the consideration of a second system. This system consists of a premixer in the first stage followed by a catalyst and post-homogeneous combustion zone. The pilot and additional premixers are then located farther downstream. This configuration allows for a smaller catalyst as well as keeping the catalyst upstream of the acceleration and part-load combustion. Further analysis and testing under Phase 3 will enable a selection of the ATS combustion system.

5.2 CATALYTIC ELEMENT EVALUATION

Durability Test

In ATS Phase 2, catalyst surface temperatures were shown to be nearly the same in a catalyst designed for an Allison Model 501-KB7 engine as in an ATS catalyst design. Since catalyst

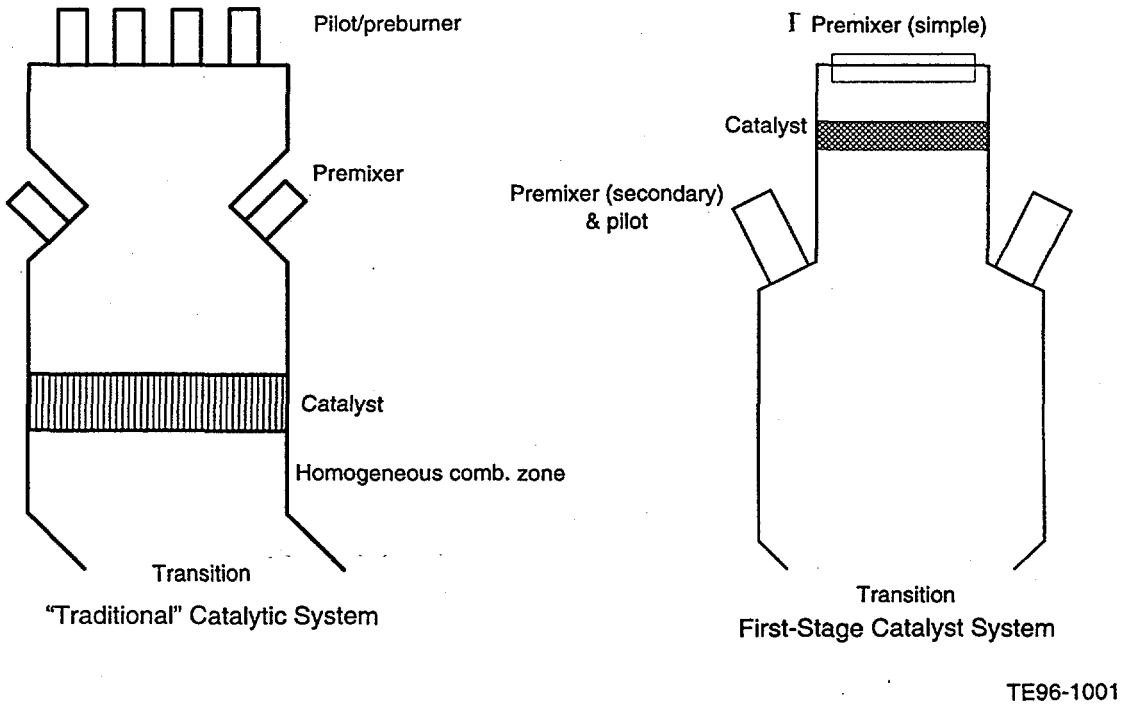

Figure 5-2. Catalytic combustion system configuration.

temperatures would be similar, and pressure of the test facility was limited, we chose to conduct testing at conditions that would be similar to those expected in a 501-KB7.

A catalyst system to work under Allison 501-KB7 full load conditions was designed, built, and tested for 510 hr at steady state. The performance of the catalytic system remained constant for the duration of the test. The emissions for this subscale (two-stage, 2 in. diameter) catalyst system with premixed fuel and preheated air stayed well within specifications at all times: NOx < 0.2 ppm, UHC < 1 ppm, and CO < 2 ppm.

The activity of the catalyst was monitored at intervals by measuring light-off and extinction temperatures. Those measurements show that, after the initial "burn-in" period (approximately 50 hr), catalyst activity remained essentially unchanged for the duration of the run.

Temperatures remained essentially constant through the run. These constant temperatures relate to constant catalyst activity over the duration of the test.

Emissions were monitored with a probe located downstream of the homogeneous combustion zone. The data show no trend of increasing levels of emissions with time.

The performance of the first-stage catalyst was also characterized by measuring the gas temperature rise generated between the inlet and the outlet of the stage as the inlet gas temperature was slowly increased. The activity of the first-stage catalyst was monitored during the durability test at interval of about 100 hr. To run those tests, the reaction was stopped and the combustor was allowed to cool down in flowing air. After setting the fuel flow rate to the desired Tad, the preheat temperature was increased in 5 degree steps. At low inlet gas temperatures, the interstage temperatures overlapped with the curve corresponding to inlet gas temperature, indicating that little or no combustion was taking place. As the preheat temperature approached 340°C, the curve corresponding to interstage gas temperatures recorded after 2 hr of steady state operation rose sharply. This is the light-off point. After the sudden rise, the slope of this curve decreased steadily, reaching a point where it matched the slope of the inlet temperature curve.

The light-off temperature is a function of catalyst activity. As the catalyst ages, the activity decreases and the light-off temperature increases. Curves obtained at times longer than 2 hr seem to overlap, suggesting that after an initial "burn-in" period the activity of the catalyst reaches a steady state.

Contaminant Evaluation

In a study to determine possible common contaminants that would pose a potential problem to catalyst activity, Catalytica found that the major air-borne contaminants appear to be those arising from dust in all locations, and from sea salt in coastal locations. The concentration of the combined oxides of silica and alumina (i.e., dust) range between 4 and 13 parts per billion weight (ppbw) in various California sites. Similarly, the concentration of salt in air ranges from 0.2 to 6.2 ppbw.

Catalytica completed feedstream contaminant testing of a two-stage catalyst reactor. Both salt and dust contamination tests were conducted. For each of the accelerated tests, the salt or dust

contaminant feed rate was adjusted so that a 50-hr test exposed the catalyst to the same total contaminant mass as would 8000 hr of normal operation.

All of the tests were performed at Allison 501-KB7 full power conditions, although at a reduced pressure of 9.4 atm. The dust concentrations ranged from 4 to 13 ppbw. The salt concentrations ranged from 0.032 to 0.160 ppbw (assuming filtering of the previously mentioned salt concentration). For each half of the dust contamination testing, the catalyst was exposed to only once of two separate solutions containing either silica or alumina particles. The salt contamination testing used a saltwater solution.

The results indicate that some degradation of the catalyst may occur even at low exposure levels for both salt and dust.

5.3 AERODYNAMICALLY STABILIZED PREMIXER DEVELOPMENT

Flashback Analysis of RSPN1.2L

Due to the extreme conditions in the ATS cycle, flashback and autoignition are concerns. As a starting point in understanding the parameters involved in determining flashback, extensive testing was done by modifying the RSPN1.2L, which is the standard module for the DOE 9 ppm program. We have significant experience with this RSPN1.2L premixer, and choosing this design for a parametric evaluation would yield the greatest understanding of the variables influential in flashback.

The purpose of a premixer is to uniformly mix fuel and air prior to combustion. As such, a combustible mixture is always present to support a flame. Combustion within the premixer is suppressed by eliminating all ignition sources. The premixer design has a contraction at the discharge of the radial swirler that forms a throat with velocities sufficient to avoid flame propagation into the premixer that would act as an ignition source. In the optimum design, the axial velocity profile at the throat would match with the local fuel-air concentration profile to control upstream flow propagation into the premixer.

In this study, parametric changes were made to the velocity field, mixing efficiency, and fuel-air concentration profile. The impact of these changes was recorded in terms of flashback propensity, NOx formation, pressure drop, and nozzle wall temperature. The following paragraphs briefly describe the modifications and the results. All comparisons will be made to the baseline design.

RSPN1.2LM3 employs a standard module, but blocks the top 4 fuel holes on each tube to lean out the core airflow. This module did achieve better flashback margin, but at the expense of less mixedness, higher NOx, hotter liner walls, and a higher hot flow pressure drop.

RSPN1.2LET uses a standard swirler and fuel injection, but the nozzle contraction is smaller, increasing bulk throat velocity by 56%. Laser Doppler anemometry (LDA) measurements, however, indicated that the throat velocity profile changed to give lower centerline velocities than the standard design. The module flashed back easily, even at lean conditions and high pressure drops. This module also had higher NOx and a very hot nozzle.

RSPN1.2LENT uses a standard swirler and fuel injection, but eliminates the nozzle contraction entirely, with the hope that the velocity profile will flatten, reducing flashback tendency. However, the bulk velocity at the premix cup exit reduced by 44% allowing flashback at all tested conditions.

RSPN1.2LL uses a standard swirler and fuel injection, but the premix cup is lengthened 0.75 in. This modification had no measurable impact on emissions or flashback. Cold flow atmospheric mixing measurements indicate that the mixing profile was unaffected by the increased length.

RSPN1.2LS takes a standard module design and reduces the fuel injection hole diameters to increase fuel pressure drop. Flashback margin appeared unchanged from a standard RSPN1.2L. However, slightly higher NOx, hotter walls and a lower lean blowout indicated an adverse effect on mixing performance.

RSPN1.2LEM4 uses a standard swirler, but employs smaller and fewer fuel orifices than the baseline design. This is in an effort to decrease fuel circuit ACd. The observed higher NOx and greater tendency to flashback can be attributed to the richer centerline fuel concentration at the nozzle throat, as measured by cold flow sampling measurements. A lean center recirculation zone appears to limit NOx emissions more effectively than a perfectly flat mixture fraction profile.

RSPN1.2LEJ is a standard RSPN1.2LE module, but flows an air jet through the pilot fuel port located within the premixer and discharging along the module's centerline. This modification did not have a large impact on NOx or flashback resistance. However, while the module resisted flashbacks at pressure drops greater than 2.7% (same as baseline), the module flashed back again between about 4.5 and 7.5% pressure drop. This anomaly was only observed with this particular module and may be due to changing air splits between the main and pilot jet of air. The actual airflow splits for this module were not determined.

RSPN1.2LLSN uses a standard swirler and fuel injection, but has a shorter nozzle expansion. This module exhibits lower NOx, but similar flashback characteristics to the baseline RSPN1.2L. The liner walls were hotter and needed extra cooling due to the corner recirculation and combustion. This corner combustion may account for the lower NOx, but it is unknown how this zone may be affected by multiple module interactions.

This testing has aided in the understanding of flashback phenomena. The results will be used in future module development in ATS Phase 3.

Atmospheric Mixing and Flashback Measurements for Alternate ATS Module Designs

Methods other than modifying the existing RSPN1.2L were used to develop flashback-resistant ATS modules. Plastic patterns of a premixing module designated as configuration AMP (accelerating mixing passage) were fabricated using the rapid prototype process. Configuration AMP consists of a set of hollow axial swirler vanes that are located upstream of a converging tube. Fuel is delivered to the premixing module through fuel passages within the hollow vanes. The moderate swirl created by the AMP module creates a high degree of flashback resistance.

Two variations of this basic design, AMP1 and AMP2, were fabricated. The difference between AMP1 and AMP2 is that the AMP2 vane leading edges are thicker than those within AMP1. Both of these patterned modules will be tested at Energy Research Consultants (ERC) under atmospheric conditions to evaluate mixing performance.

Mixing tests on configuration AMP1 at ERC revealed a large tangential variation in mixing. This is due to problems with forming consistent fuel passages in the thin leading edges of the vanes. Subsequent modifications to the locations of the fuel delivery holes did not improve the mixing satisfactorily. Since the basic AMP design depends primarily on mixing performance, the AMP1 configuration will not be pursued any further.

Configuration AMP2 was flow tested under atmospheric conditions at ERC. Based on tuft observations, the flow is positive immediately downstream of the hub/centerbody. The mixing profile was optimized to yield a uniform mixture (±11%) across the exit.

Another premixing module design being considered is configuration trspn (tapered radial swirler plus nozzle). The TRSPN module design is a derivative of the RSPN premixer module design being used in the Ultra-Low Emissions Gas Turbine Combustion System (9 ppm NOx) program. The swirl angle of this diverging tapered radial swirler increases as the diameter of the swirler increases. This increases the axial component of velocity at the centerline and increases flashback resistance. The presence of the taper also reduces the premixer volume by about 30%, which reduces the residence time. The TRSPN module provides about 50% less residence time than the RSPN module. This feature is desirable for preventing autoignition within the premixer under ATS cycle conditions. The TRSPN module also has a center pilot and integral fuel passages within the swirler vanes for supplying the main fuel.

Two variations of this basic design, TRSPN1.1 and TRSPN1.2, have been fabricated. The swirl angle of TRSPN1.1 varies from 57 to 63 deg. The swirl angle of TRSPN1.2 varies from 61 to 66 deg. Otherwise, the two designs are identical.

The configuration TRSPN 1.1 premixing module was also tested at ERC. Flashback was observed with the original location of the fuel delivery holes. However, relocating the holes produced a relatively uniform mixing profile with a slightly lean core that was flashback resistant at low pressure drops using either natural gas or a mixture of 75% natural gas and 25% ethane. The ACd of TRSPN1.1 was much higher than that of TRSPN1.2 and the flame position is consistent with all other RSPN designs.

Mixing tests on TRSPN1.2 revealed a uniform profile. Flashback tests with Configuration TRSPN1.2 indicated a problem with high propensity flashback fuel. The core of the mixing profile was further leaned out to increase flashback resistance. This eliminated flashback at 1.5% pressure drop but caused the flame to sit farther inside the throat of the module.

Atmospheric Velocity Measurements

Extensive LDA velocity measurements were made at ERC's atmospheric facility. These measurements were carried out to determine: (i) interaction of swirling flows between adjacent premixers in a parallel stage, (ii) velocity profiles at the premixer/combustor interface, (iii) velocity profiles downstream of the TRSPN module nozzle, (iv) velocity profile at the exit of the nonstabilizing premixer AMP2, and (v) particle size dependency of velocity measurements. The details of these measurements and the findings are presented in the following paragraphs.

Reacting and nonreacting velocity measurements were made on a parallel stage configuration with 3 RSPN1.2L modules. Both sets of measurements showed that a central recirculation zone exists along the centerline of each module. The gas velocity between the modules is high. The swirling flows coalesce into a bulk swirling flow by about 9 in. from the nozzle throat exit.

Velocity at the nozzle throat or the interface between the premixer and the combustor have been made for a couple of premixer designs by providing optical access through 0.25-in. holes drilled in the side of the nozzle. Steps were taken to minimize the impact of this by sealing off the gap between the nozzle and the quartz liner such that the access hole does not provide a leak path. These measurements have provided the first data in this region and have been useful in improving modeling approaches. Further improvements can be expected from the use of the backscatter technique since potentially the need to drill the 0.25-in. holes will be eliminated.

Nonreacting velocity measurements were made downstream of the TRSPN nozzle expansion. The measurements are similar to those obtained with the Green Thumb (DOE 9 ppm) modules with the exception of the shape of the axial velocity profile close to the module at the centerline. The peak negative velocity is not located along the centerline in the recirculation zone but is slightly off-axis. This could be due to the fact that the TRSPN module has a nozzle with a shorter diverging section followed by a sudden expansion. The tangential velocity profiles also show a consistent difference close to the nozzle at the centerline. The peak tangential velocity occurs farther away from the centerline here. At larger distances from the module, both axial and tangential velocity profiles are similar to those obtained with the Green Thumb modules.

ERC attempted velocity measurements on AMP2, the premixer with minimal swirl. They had a lot of difficulties getting any measurements in the region close to the premixer exit. The only satisfactory measurements they could get were away from the region of interest. The AMP2 design incorporates an axial swirler. The central hub is of similar size as the premixer exit. A similar "hole" where no particles are present at the axis of the swirling flow has also been observed with the RSPN type designs.

The inability to maintain particles in the center of the swirling flow of the RSPN type design suggests that the premixer design acts as a particle separator. In the case of the AMP2 hardware, the swirl is minimal and the particles perhaps do not follow the flow and run into the conical converging wall of the module. To confirm this, a particle size dependency of velocity measurements was investigated using a RSPN type design. Two particle sizes were evaluated: 1 micron and 0.3 micron. At the module throat, the smaller particles give a higher velocity. At the exit of the nozzle, the smaller particles give a lower peak velocity. These observations are consistent with the fact that the smaller particles have smaller inertia and can follow the flow better. At the throat, the flow has just been accelerated by the converging section of the nozzle. Smaller particles accelerate faster and hence register a higher velocity (closer to and perhaps lower than the actual velocity). At the exit of the nozzle, the flow has just been decelerated by the diverging section. The larger particles have a higher momentum and maintain their velocities longer and yield higher magnitudes. Unfortunately, very small sized particles cannot be used since the signal drops off very rapidly. Thus the particle size effects should be borne in mind while interpreting velocity measurements from practical hardware.

This testing has aided in the understanding of flashback phenomena and premixer design. The results will be used in future module development in ATS Phase 3.

6.0 TASK 8.07 - CERAMIC VANE DESIGN AND EVALUATION

6.1 EXECUTIVE SUMMARY

This report describes the progress and status of Task 8.7, Ceramic Vane Design and Evaluation, in the DOE/Allison Phase 2 ATS Program. The objective of this task is to demonstrate first-stage ceramic vanes in a commercial industrial turbine. The report describes how the accomplishment of this objective could facilitate the introduction of ceramic airfoils into the second stage of future ATS turbines. Cost, risk, and long-term ceramics stress rupture limitations of current ceramic materials are also discussed that indicate that the second stage is probably the most suitable location to introduce ceramic airfoils into ATS engines.

The design of the ceramic first-stage vanes and metallic mounting hardware for retrofit into an existing Allison 501K turbine is nearly completed. Acceptable ceramic vane fast fracture stresses and probabilities of survival have been calculated for both turbine maximum continuous power and emergency shutdown conditions.

Final design details and dimensions associated with minimizing vane contact loads and differential thermal growths between the ceramic vanes and their metallic mounts are being incorporated into the drawings. The ceramic vanes will be procured, and the metallic mounts will be fabricated upon completion of the drawings.

Introduction

The development of ceramics for gas turbines has been pursued for about 20 years. Much of the work to date has been directed to small automotive gas turbines.* Some recent efforts have been directed to ceramics for industrial turbines. Work is in progress to develop and demonstrate ceramic combustor liners, ceramic first-stage vanes, and ceramic first-stage blades in an industrial turbine.**

A major national effort has been initiated to develop ATS designed for ultra-high efficiencies, environmental superiority, and cost competitiveness compared with current industrial and power plant gas turbine systems.† If metallics are to be used for turbine expander airfoils, advancements in cooling methods and alloys will be needed for the extreme temperatures (rotor inlet temperatures up to 1427°C [2600°F]) necessary to achieve the ultra-high ATS efficiency goals for simple cycle systems. An alternate approach is to develop structural ceramics for ATS turbine vanes and blades, which alleviates cooling requirements.

---

*P. Khandelwal, "Development and Testing of CMC Components for Automotive Gas Turbine Engines," AIAA paper AIAA-91-189, presented at the 27th Joint Propulsion Conference, June 24-26, 1991, Sacramento, CA.
M. W. Rettler, M. L. Easley, and J. R. Smyth, "Ceramic Gas Turbine Technology Development," ASME paper 95-GT-207.

**M. van Roode, W. D. Brentnall, P.R. Norton, and B. D. Edwards, "Ceramic Stationary Gas Turbine Development Program - First Annual Summary," ASME paper 94-GT-313.
M. van Roode, W. D. Brentnall, P.R. Norton, and G. L. Boyd, "Ceramic Stationary Gas Turbine Development Program - Second Annual Summary," ASME paper 95-GT-459.

† U.S. Department of Energy, "Report to Congress - Comprehensive Program Plan for Advanced Turbine Systems," February 1994.

This report describes the progress since initiation (June 1995) in Task 8.7 of the DOE/Allison Phase 2 ATS Program. The objective of this task is to demonstrate ceramic first-stage vanes in an Allison 501 turbine at a commercial site. The potential benefits from use of ceramic airfoils in ATS turbines are discussed along with the significance of this task for introduction of ceramics into Allison ATS engines.

6.2 CERAMICS FOR ATS INDUSTRIAL TURBINES

Benefits

The primary incentive for using ceramics rather than metallics for vanes and blades is improvement in turbine engine cycle efficiency and output that produce economic benefits for the end user of the engine. These improvements in turbine performance for ceramics are due to a reduction in the amount of compressor discharge air that bypasses the combustion process for purposes of cooling the expander components downstream of the first-stage vanes.

Figure 6-1 illustrates the benefits of reducing chargeable cooling air (that air which decreases efficiency) and leakage from a value determined for a 14,700 hp (11 MW) turbine with a rotor inlet temperature of 1427°C (2600°F). Each reduction of 25% in cooling air requirements increases the overall engine efficiency by about 0.80 percentage points and increases the engine output power by more than 900 hp (0.67 MW). Furthermore, the turbine exhaust temperature increases by about 10°C (18°F) for each 25% decrease in chargeable cooling flow to enable slightly higher steam outputs for the turbine operated in a cogeneration plant. As a reference, elimination of first rotor blade cooling would increase the engine efficiency by about 1.2 percentage points, the power output by 1280 hp (0.95 MW), and the turbine exhaust temperature by 14°C (25°F).

Requirements for Ceramic Airfoils

The requirements for ceramic airfoils in industrial turbines are similar to those for the current metallic airfoils. Vane and blade design lifetime requirements are up to 30,000 hr with turbine

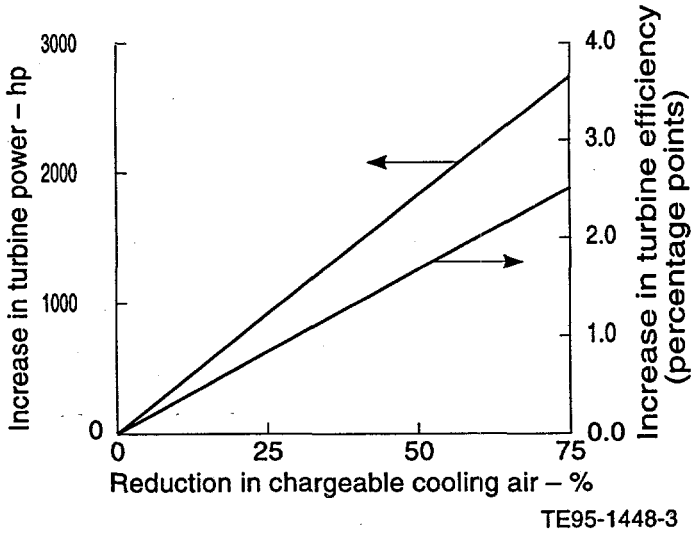

Figure 6-1. Performance improvement for 14,700 hp turbine due to reduction in expander cooling requirements.

operation at maximum continuous power with few shutdowns. In ATS industrial turbines, ceramic airfoils could be exposed to average gas temperatures up to 1427°C (2600°F). Usually the primary source of steady-state stresses in ceramic airfoils would be thermal gradients from the combustor temperature pattern. Additional sources of stress are aerodynamic loads, contact loads, and centrifugal loads (for rotor blades). Periodically, industrial turbines experience unexpected emergency shutdowns due to loss of generator electrical load. Fuel flow to the combustors is immediately terminated to prevent overspinning of the turbine. The thermal shock experienced during emergency shutdown produces the highest expected stresses experienced by ceramic vanes and blades.

Ceramic Capabilities

The capabilities of structural ceramics to meet the ATS industrial turbine requirements just described will now be discussed. A primary issue is ceramic stress rupture lifetimes up to 30,000 hr at the stress and temperature conditions for ATS turbine airfoils. Tests to date of structural ceramics indicate maximum stress and temperature limits less than 210 MPa (30 ksi) and 1315°C (2400°F) for stress lifetime in the 10,000 hr range.

Consequently, cooling would be needed for first-stage ceramic vanes and blades in an ATS turbine with a rotor inlet temperature in excess of 1315°C (2400°F). However, further developments in ceramics processing technology will be needed to produce internal cooling passages, particularly for the thin airfoil trailing edges and the scale of turbines smaller than 15,000 to 20,000 hp. Even if ceramics processing for internal cooling could be developed within the ATS turbine commercialization schedule, ceramic part yields would likely be so low as to significantly increase the cost of ceramic airfoils. Consequently, use of ceramic airfoils at gas temperatures that require cooling could substantially reduce the benefits of ceramics over metallics. Cooling would produce lesser turbine performance improvements at greater turbine cost compared to uncooled ceramics.

Introduction of Ceramic Airfoils into ATS Turbines

The cost and risk considerations suggest introduction of ceramics for ATS turbine airfoils at locations where cooling would be required for metallics but not required for ceramics (i.e., where materials temperatures ≤ 1315°C [2400°F]). The second-stage vanes and blades are components that meet this specification and result in the greatest reduction in chargeable cooling air (and corresponding improvement in turbine performance). Additional advantages of ceramic airfoils in the second stage are a somewhat flattened combustor temperature pattern (resulting in reduced thermal stresses) and reduced risks of foreign object damage (FOD) compared to first stage. The potential for FOD is decreased because any foreign material entering the hot section would tend to be pulverized by the first rotor blades.

Performance and Economics for a Ceramic Second Stage

Introduction of second-stage ceramic vanes and blades into the 14,700 hp (11 MW) ATS turbine described earlier could reduce chargeable cooling by about 24%. This would result in over 850 hp increase in engine power and 0.86 percentage points increase in engine efficiency compared to the all metallic ATS engine. Greater electrical generation revenues are obtained at reduced

fuel cost to result in a $211,000/yr improvement in cash flow for a plant using an ATS turbine with a ceramic second stage compared to a plant using the all metallic ATS turbine.

Since a major driving force for new industrial turbine designs is economic benefit for the end user, there is a significant incentive for use of ceramics in future industrial turbines. However, any increased production cost of a new turbine design using ceramics is important and, if excessive, can counterbalance the benefits of ceramics. Consequently, eventual ceramic production costs have been an important consideration in the ceramic vane design work that will be described later.

Conditions of ATS Turbine Second Vanes Versus 501 Turbine First Vanes

Advantages of introduction of ceramic airfoils in the ATS turbine second stage have been discussed. Now the temperature and stress environments for the second-stage vanes of an ATS turbine with a rotor inlet temperature of 1427°C (2600°F) will be compared to the environments in the current production Allison 501K turbine with a turbine inlet temperature in the vicinity of 1100°C (2000°F). Ceramic performance in these engines depends on peak materials temperatures and stresses, which are greatly affected by the combustor temperature patterns.

Smaller combustor pattern factors result in lower peak temperatures and lower peak stresses (due to smaller thermal gradients). The Allison ATS turbine design utilizes an off-board combustor that can produce a smaller combustor pattern factor than the on-board 501K turbine combustor cans. Furthermore, the ATS combustor pattern is somewhat flattened through the first stage. Consequently, the ATS turbine second vanes are expected to experience a somewhat lower peak gas temperature in addition to somewhat less severe thermal gradients and resulting stresses than 501K turbine first vanes. Emergency shutdown thermal shocks are also expected to be somewhat less severe in the ATS engine than in the 501 turbine because of a higher temperature of compressor discharge air flowing over the vanes after the fuel is shut off.

The previous discussions indicate that second-stage ATS turbine ceramic vanes should experience a comparable, and somewhat less severe, materials environment than first-stage ceramic vanes in a 501K turbine. Consequently, operation of ceramic first vanes in a 501K turbine would provide a reasonable test of the same material for second-stage vanes in an ATS turbine with a much higher inlet temperature. The remainder of this report discusses the efforts of Task 8.7 with the objective of demonstrating first-stage ceramic vanes in a 501K turbine. This task is based on work started in an Allison internally funded project for a novel ceramic vane mounting arrangement.

6.3 APPROACH

This task consists of several activities:

- design of first-stage ceramic vanes and mounting hardware
- ceramic vane procurement and mount fabrication
- thermal shock proof tests of the ceramic vanes
- proof test of the vanes and mounting hardware in an engine
- demonstration of the ceramic vanes and mounting hardware in a long-term Allison 501K turbine run at a commercial site

Design/Analyses of Ceramic Vanes and Mounting Hardware

Ceramic vanes and mounting hardware will be specified and designed for retrofit into an Allison 501K turbine. For that engine, the first-stage vanes are exposed to an average combustor outlet temperature up to the vicinity of 1100°C (2000°F) with hot spots several hundred degrees higher. The intended vane life is 30,000 hr, comparable to the current design life of metallic vanes.

Computerized heat transfer and stress analyses will be used to evaluate an initial design and refine it, as needed. Ceramic properties of the vendor materials will be used in the analyses.

A probabilistic design methodology has been developed by Allison that addresses the statistical nature of a ceramic's strength distribution and the reliability requirement for the component in service. The engine operating environment will be input to the finite element modeling of the component to analytically assess the fast fracture reliability and probability of survival. Both steady-state and transient (startup and shut down) thermal and mechanical loads for engine operation will be considered in design analyses.

The results of the design and analyses activities will be used to specify the ceramic vane configuration to ceramic vendors. These activities will also be used to produce mounting hardware drawings for fabrication or procurement.

Procurement of Ceramic Vanes

The ceramics suppliers will be involved in the definition of vane and mount designs. Limiting the cost of ceramic components to about the same cost as the metallic components they replace can result in economic benefits to the end user of the turbine. The purpose of interaction with the ceramics suppliers is to assure that the vane design is engineered not only for long life but also for acceptable production costs. Procurement of the ceramic vanes will be based on the specifications and drawings resulting from the iterative design, analyses, and supplier interactions.

Thermal Shock Proof Tests

Thermal shock due to turbine emergency shutdown is expected to produce the highest stresses experienced by the ceramic vanes. These thermal stresses result from the differential temperature between the vane thicker leading edges and thin trailing edges. Proof tests representing vane differential temperatures and resulting stresses during emergency shutdown will be conducted for the ceramic vanes that will later operate in engine tests. Each vane will be visually inspected and analyzed by nondestructive techniques (e.g., using fluorescent penetrant) after the thermal shock proof tests.

Vane/Mount Proof Test in Engine

A full set of first-stage ceramic vanes and their mounting hardware will be operated in a 501K turbine at Allison. The purpose is a proof test of both ceramic vanes and metallic mounting components in an operating test engine prior to installation at a commercial site. The test will verify that the metallic mounting hardware does not transmit excessive contact stresses or ex-

cessive mechanical loads to the ceramic vanes due to distortions caused by the combustor temperature patterns. The test will probably consist of a normal startup of the turbine, operation for up to 50 hr at load, and a normal shutdown.

Ceramic Vane Field Demonstration

Since the field demonstration depends on a final agreement with the end user, the following test plans are preliminary.

Vanes that had been screened in the thermal shock proof test and the engine proof test will be installed with mounting hardware in an Allison 501 turbine that has been taken out of commercial service for maintenance.

The turbine will reenter service at its commercial site for up to 8000 hr under its normal operating conditions. The commercial site will most likely be a cogeneration plant, at which operation is essentially continuous at full load, except for unanticipated shutdowns (such as generator trips) and scheduled maintenance (probably 6 month intervals). Inspection frequency for the ceramic vanes and their mounts will depend on the agreement with the end user, since any additional inspection outages result in loss of plant revenues. At the end of the test, ceramic vanes will be removed from the engine and analyzed to assess their condition and expected additional life.

6.4 PROGRESS

Screening Analyses

Since the ceramic vanes will be retrofitted into an existing 501K turbine, it would be desirable to use ceramic airfoil shapes that are the same as for the metallic vanes in that engine. Thermal and stress probability of survival (POS) analyses were conducted for a ceramic first-stage vane with the current 501K vane shape (Figure 6-2) to determine the effects of the relatively thick leading edge on emergency shutdown thermal shock performance. Other design screening thermal, stress, and aerodynamic analyses considered hollow vane construction and alternate airfoil shapes with various trailing edge and maximum thicknesses for more uniform thermal mass along the airfoil chord. Two-dimensional thermal and stress analyses were used and platform effects were not considered for these screening evaluations. Properties of two Si_3N_4 ceramics and a composite of SiC particulate in an aluminum matrix were used in the analyses. These analyses were conducted prior to incorporation of the ceramic vane efforts into the ATS Phase 2 program but are discussed here for completeness.

Results of Screening Analyses

The calculated POS for all 60 first-stage ceramic vanes exposed to a single emergency shutdown was 98.7% for the best (AS800, Si_3N_4) material and the current 501K turbine airfoil shape. To improve the POS, hollow ceramic vanes with the same airfoil shape were evaluated. The hollow vane would experience lower thermal shock stresses than the solid vane, due to less variation in thermal mass along the chord. Although the hollow design does reduce thermal shock stresses, information from the ceramic suppliers has shown that the vane cost increases for increasing dimensions of the hollow region such that only a small hollow cavity can be produced

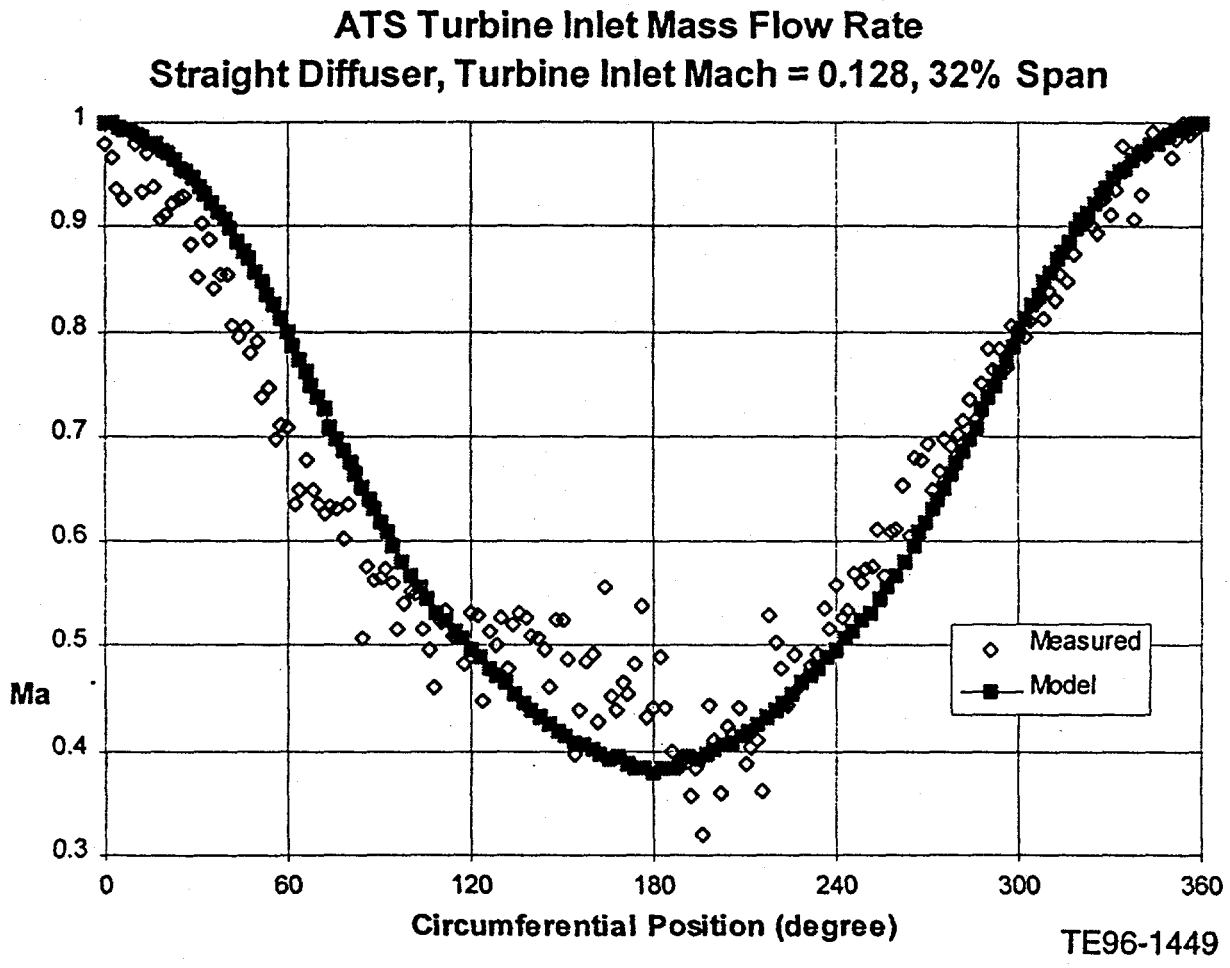

Figure 6-2. First-vane metal airfoil profile for 501K turbine.

for ceramic vanes at a competitive cost in production quantities. Consequently, inadequate thermal shock benefits can be realized for competitively priced hollow vanes (with a small hollow region) of the scale for the 501K turbine.

Another option evaluated to alleviate thermal shock stresses was to increase the vane trailing edge thickness and restagger the first stator airfoils. However, this reduces the minimum flow area of the engine and decreases turbine performance by an unacceptable degree.

Solid vanes with modified airfoil shapes were then evaluated. The trailing edge thickness was not changed from that of the current production engine, but the dimension of the thickest part of the airfoil was reduced. The Allison aerodynamics group designed a new airfoil with a ratio of maximum thickness to trailing edge thickness of 3.6 compared with a value of 6 for the original vane. However, discussion with a ceramics supplier revealed that the thinner airfoil

was beyond the supplier's experience for economical production and process development would be needed to produce that ceramic vane in commercial quantities at a competitive price.

Consequently, a second vane shape with a somewhat thicker nose region was generated by the Allison aerodynamics design group. The shape was reviewed with the prospective ceramic suppliers for the program and was judged to be acceptable for economics of production.

The ratio of maximum thickness to trailing edge thickness of the second redesigned vane is 4.3 compared with 6 for the original 501K turbine first-stage vane. The profiles stacked radially are shown in Figure 6-3 for the second redesigned vane. As for the thinnest vane, this airfoil provides somewhat lower aerodynamic losses than the original 501 turbine vane, which was designed years ago before advances in computer aerodynamic design procedures. Furthermore, the stress levels due to thermal shock for the vane with a thickness ratio of 4.3 are only slightly higher than for the thinnest vane (with a ratio of 3.6). For an Si_3N_4 (AS800) material, the calculated emergency shutdown thermal stress levels in the 4.3 ratio vane are 24% lower than for a vane of the shape currently used in the 501K turbine, and the probability of thermal shock survival of a single emergency shutdown predicted by the POS analysis for the full set of 60 vanes now exceeds 99.9%.

As a result of these vane shape evaluations, the airfoil with a 4.3 thickness ratio (shown in Figure 6-3) was selected as the new baseline design for further 3-D analyses for thermal shock and the steady-state environment in the engine.

Vane Design and 3-D Fast Fracture Analysis

Design Features

Various vane platform and mount design alternatives have been discussed with ceramic suppliers for inputs on design features that affect production costs. An initial design was chosen for 3-D thermal and stress analyses. The ceramic vane is not hard mounted in this design and the contact area at metallic interfaces is minimal. These design features reduce contact stresses and the extent of expensive diamond machining needed for ceramic surfaces in contact with metallic mounts.

Figure 6-4 illustrates the ceramic vane and mount design and the finite element mesh network used for the 3-D ceramic vane analyses. The ceramic vane consists of an airfoil with simple platforms bounding the inner and outer flow passage surfaces. The inner and outer platforms seat in the circumferential grooves of inner and outer metallic mounts.

Stress Conditions

As indicated earlier, the most significant source of vane steady-state stress results from thermal gradients of the combustor temperature pattern. Ten vanes are located at the exit of the transition section from each of six combustors in the 501 turbine. Each vane experiences a different portion of the combustor temperature pattern and each combustor produces a somewhat different pattern. Three bounding temperature patterns were determined for the purpose of thermal and stress analyses from thermocouple data in 501K engine tests. These bounding contours (shown in Figure 6-5) result from radial planar cuts through the measured combustor

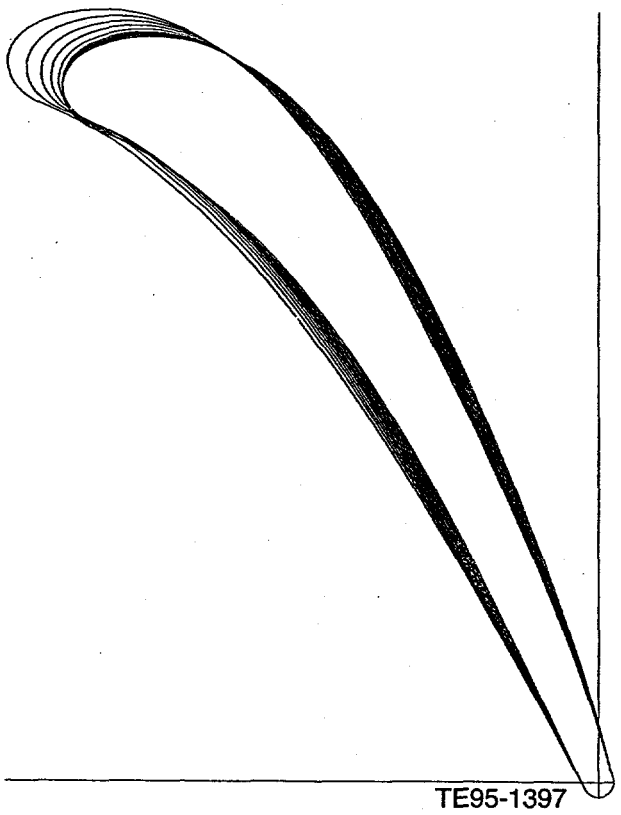

Figure 6-3. Redesigned ceramic vane for improved thermal shock performance.

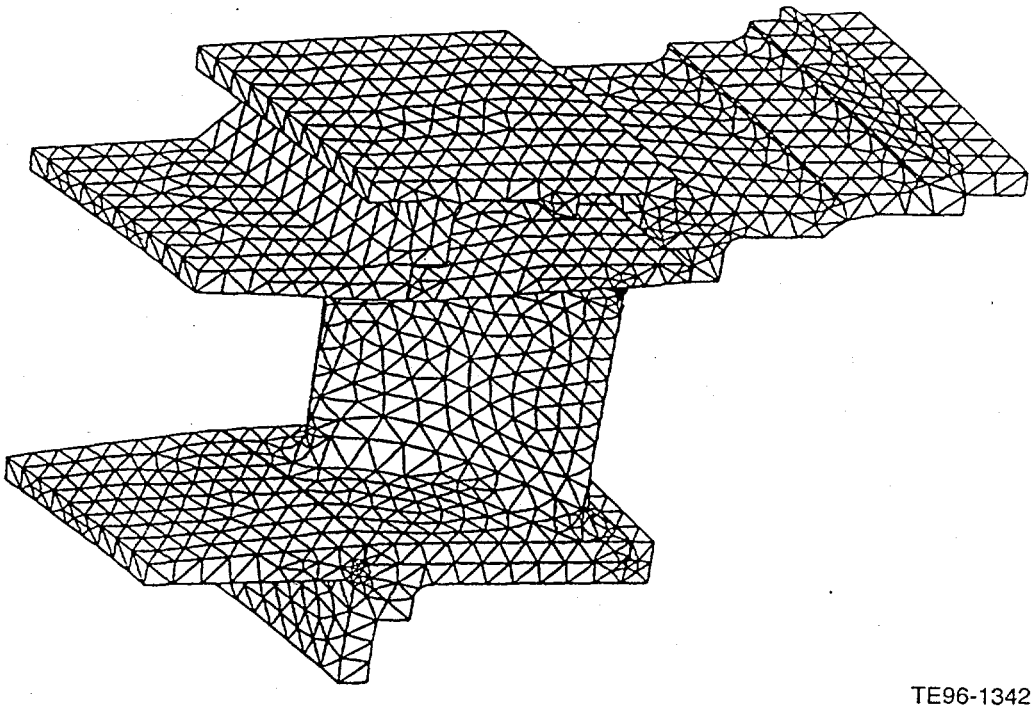

Figure 6-4. Finite element mesh.

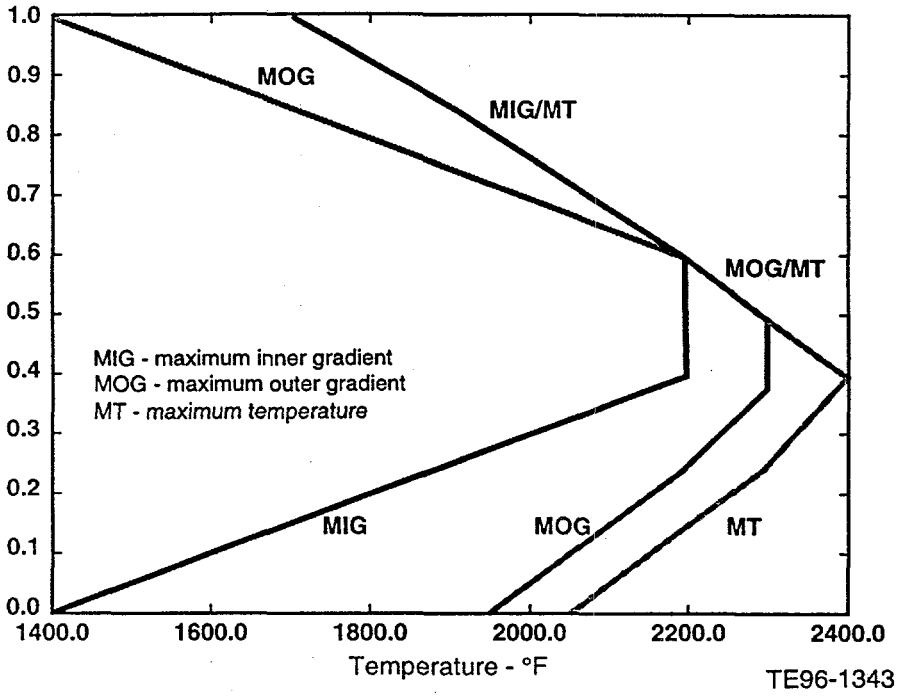

Figure 6-5. Bounding combustor radial patterns.

patterns at locations that produce the maximum inner gradient (MIG), maximum temperature (MT), and maximum outer gradient (MOG). The highest stresses are associated with the most severe gradients and the lowest material strength is associated with the highest temperature.

The most severe stresses in the ceramic vanes result from thermal shock temperature gradients caused by the emergency shutdown. Figure 6-6 shows calculated temperature traces versus time after an emergency shutdown at two locations within the ceramic vane for the bounding combustor pattern with the maximum inner gradient. The two locations within the vane are at about one-half the vane chord and at the trailing edge, both in the midspan plane. Figure 6-6 shows that the thicker midchord region of the airfoil cools at a slower rate than the thin trailing edge during the emergency shutdown.

Figure 6-7 shows that the difference in temperature between the midchord and trailing edge locations reaches a maximum value of about 500°F at about 1 sec after the initiation of emergency shutdown.

3-D Analyses Results

All maximum continuous power and emergency shutdown stress analyses have been completed for the ceramic vanes using the three bounding combustor temperature patterns and the AS800 Si_3N_4 materials properties. Calculated ceramic vane stress levels and probability of survival values have been acceptable for all of these cases. Tables 6-I and 6-II show results of the stress analyses. Maximum stresses in the vane are given for each condition along with the location of maximum stress, the material temperature at that location, and the probability of survival of all 60 vanes considering the statistical nature of the ceramic properties.

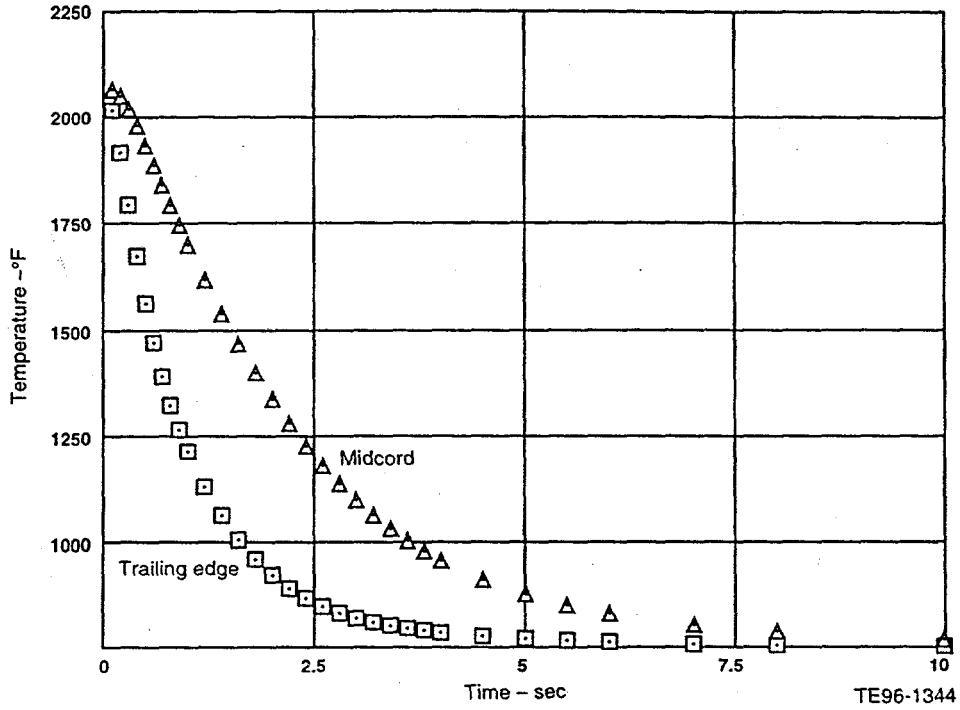

Figure 6-6. Vane temperatures at midchord and trailing edge due to emergency shutdown.

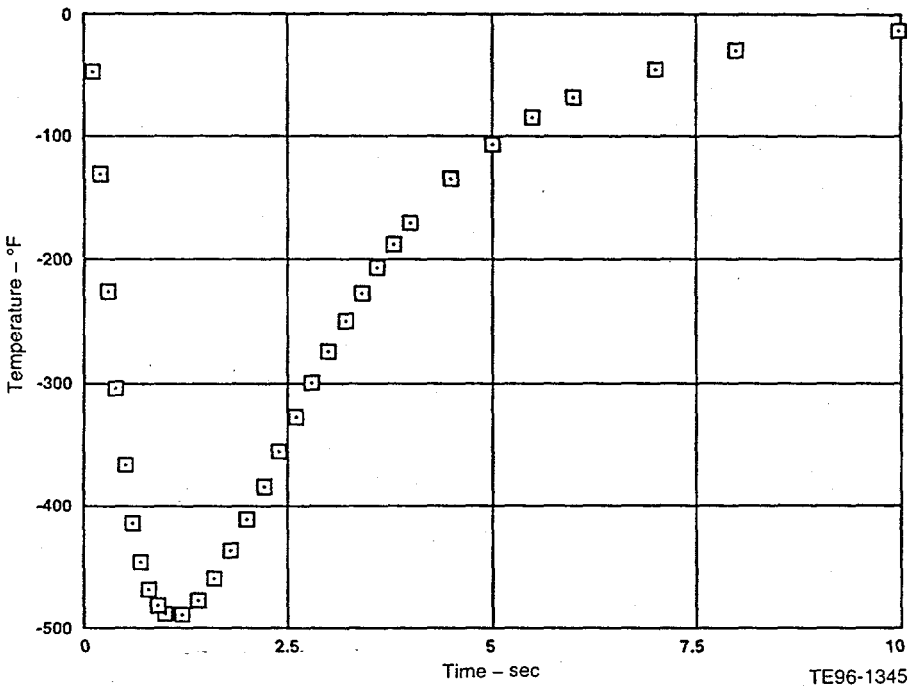

Figure 6-7. Vane temperature differential between trailing edge and midchord due to emergency shutdown.

Table 6-I.
Turbine emergency shutdown.

	Bounding combustor pattern		
	Maximum inner gradient	Maximum temperature	Maximum outer gradient
Max stress (ksi/MPa)	30.2/208	25.4/175	28.9/199
Vane set probability of survival	>0.9999	>0.9999	>0.9999
Temperature at max stress location (°F/°C)	1345/729	1370/743	1350/732
Location	Midspan trailing edge	Midspan trailing edge	Midspan trailing edge

Table 6-II.
Turbine maximum continuous power.

	Bounding combustor pattern		
	Maximum inner gradient	Maximum temperature	Maximum outer gradient
Max stress (ksi/MPa)	24.5/169	17.6/121	21.8/150
Vane set probability of survival	>0.9999	>0.9999	>0.9999
Temperature at max stress location (°F/°C)	2160/1182	2330/1277	2260/1238
Location	Midspan trailing edge	Midspan trailing edge	Midspan trailing edge

Figure 6-8 shows the thermal shock stress contours for the maximum inner gradient bounding combustor temperature pattern at about 0.9 sec after initiation of emergency shutdown. These conditions produce the highest calculated stress (30.2 ksi) of all the conditions evaluated. This stress, as well as maximum stresses for all the transient and steady-state analyses, occurs at the trailing edge of the ceramic vane in the region of midspan. Because the vane is experiencing rapid cooling in the emergency shutdown cases, the material temperature is relatively low. At the location of the highest (30.2 ksi) stress, that materials temperature is calculated as 1345°F. Table 6-I shows that the calculated fast fracture probability of survival exceeds 99.99% for all 60 vanes for this highest stress condition, as well as for all the other emergency shutdown combustor pattern conditions.

Figure 6-9 shows that the highest calculated stress is 24.5 ksi at conditions of maximum continuous power and the maximum inner gradient bounding combustor temperature pattern. Table 6-II indicates that this is the highest steady-state stress calculated in the ceramic vane and that the fast fracture probabilities of survival exceed 99.99% for all steady-state conditions evaluated. The ceramic material temperature is about 2160°F at the trailing edge location of maximum stress. The highest continuous power stress is slightly lower than that (26 ksi) reported by Solar for their ceramic vane stress analyses.

6.5 TASK STATUS

Acceptable fast fracture stresses and probabilities of survival have been calculated for the 501K turbine first-stage ceramic vane design for conditions of maximum continuous power (steady state) and emergency shutdown (transient). Final design and drawing modifications are in

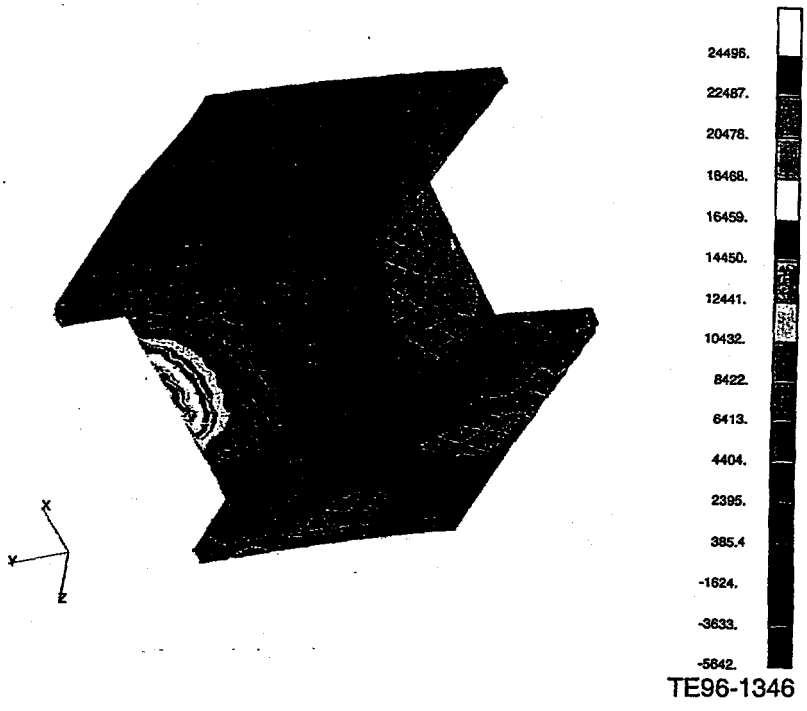

Figure 6-8. Model 501 vane, 0.9 sec after emergency shutdown - MIG condition.

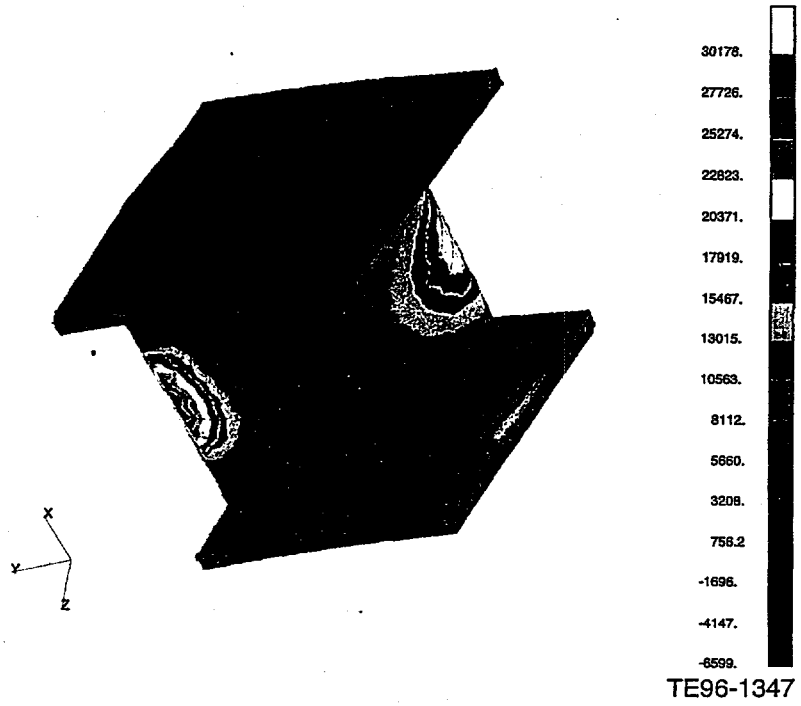

Figure 6-9. Model 501 vane, steady-state - MIG condition.

progress. These include fine tuning of the final design and dimensions of the ceramic vanes and their metallic mounts considering:

- significantly different coefficients of thermal expansion between the ceramics vanes and metal mounts that result in differential thermal growths from cold engine startup to steady-state operating conditions
- desired running clearances between adjacent vanes and between vanes and their mounts considering flow leakages and loads transmitted to the vanes for the range of turbine operating conditions
- constraint of the inner and outer vane support mounts to minimize relative movement and associated contact loads on the ceramic vanes

A two-dimensional axisymmetric thermal analysis has calculated gaps in clearances (e.g., between adjacent vanes, between mount segments, and between ceramic vanes and metallic mounts). Plots of these gaps and clearances were obtained for turbine operating conditions from startup to on load to off load to shutdown. The plots indicate a closing of circumferential gaps between vanes and mount segments immediately after startup to produce the minimum gaps throughout the turbine operating range. This closure of gaps immediately after startup establishes the as-manufactured circumferential dimensions of the vanes and mounts to prevent pinching. It also establishes tolerances on the dimensions of the circumferential restraining pins to prevent their pinching the vanes. The results of the analyses also show that the circumferential restraining pins must be redesigned to prevent rotation of the vanes and closing of the first vane throats as gaps open.

The ceramic vanes will be ordered from ceramic suppliers and fabrication of the metallic mounts will start after completion of the drawings.

7.0 TASK 9.0 - PROGRAM MANAGEMENT

Allison's program management included cost and schedule management and providing technical guidance to individuals performing the tasks consistent with the goals outlined in DOE's Statement of Work. This task included submitting the following reports to DOE in accordance with the contract requirements:

- Monthly reports - by the 20th of each month for activities conducted during the previous month
- Quarterly reports - at the end of each quarter by the end of the following month
- Annual reports - at the completion of one year after the start of the project
- Topical reports - as specified

The monthly reports were submitted in the final form. Other reports were initially submitted as drafts and finalized after DOE/METC's approval.

A presentation on the program management plan was provided to DOE as required by the contract. Allison was notified on August 28, 1995, by Ms. Abbie Layne that the revised Management Plan for the project, submitted to her on August 4, 1995, was approved. This plan was used as the detailed project scope,with schedule and funding identified for each task.

A presentation on industrial ATS was given at the International Gas Turbine Institute, Cogen Turbo `95 in Vienna, Austria on August 24, 1995. Allison's presentation covered a progress report on an industrial ATS program. The overall title of the paper, prepared jointly by Mr. William Parks, Jr., of DOE/EE, and Sy Ali of Allison was "Industrial Advanced Turbines for Sustainable Development and Effective Climate Change." A copy of this paper was sent in July to Ms. Layne, COR on the Allison ATS Phase 2 Extension. Due to the unavailability of Mr. Parks, Allison presented the DOE material prepared by Mr. Parks and then presented the Allison accomplishments on ATS.

Allison personnel made presentations in five technical sessions and one poster session during the Advanced Turbine Systems Annual Program Review Meeting October 17 through 19, 1995. The topics and names of individuals making these presentations are as follows:

- Session 2A - ATS Program Element Overviews
  Allison ATS Program Element Overview - Sy Ali

- Session 2B - ATS Program Technical Reviews
  Allison Engine ATS Program Technical Review - Dale Mukavetz

- Session 4 - University/Industry Consortium Interactions
  Overview of Allison/AGTSR Consortium Interactions - Sy Ali

- Session 5 - ATS Supportive Projects
  DOE/Allison Ceramic Vane Effort - Richard Wenglarz

- Poster Session P29
  Improved Modeling Techniques for Turbomachinery Flow Fields - Ed Hall

- Workshop on Very High Efficiency Fuel Cell/Advanced Turbine Power Cycles
  Allison Engine Company Perspective - Terry Knickerbocker

Two papers, "Ceramics for ATS Industrial Turbines" and "Government/Industry Partnership: A Revolutionary Approach in Global Leadership of Advanced Gas Tubines," were presented at the ASME/IGTI Conference in June 1996.

A semiannual presentation to the DOE/METC Project Manager, Mr. L. Paulson, was provided on December 5, 1995. At that time Allison requested approval to shift certain amounts from one task to another, without increasing the overall cost or changing the project schedule. This request was formally approved by Mr. Paulson in January and implemented in February 1996.

Allison also submitted nonproprietary copies of the following topical reports to DOE/METC:

- Final topical report EDR 17288A - Task 6: ATS System Definition and Analysis
- Final topical report EDR 17253A - Task 8.4: ATS Combustion System

A request was submitted to Mr. Paulson to allow Allison to submit one final report per the revised schedule, at the completion of all tasks except Tasks 5.0 and 8.07. The request also included an extension to complete Task 5.0, and an increased funding approval for Task 5.0 from $40,000 to $100,000, without increasing the cost of the overall contract.

At a Phase 3 program review meeting on June 26, 1996, Mr. Paulson recommended that Allison should submit the current scope of Task 8.7 (ceramic vane design and evaluation) and the funding requirements for the current contract. He advised Allison that the funds obligated would be short of the total contract value. He and Mr. S. Waslo, DOE/EE Program Manager, also asked Allison to provide a scope and cost summary for the continuation of the Ceramic Vane Design and Evaluation (Task 8.07) task in Phase 3. This information is being prepared and will be submitted to Mr. Waslo in July per the request.

Tasks 5.0 and 8.07 will continue until the end of March, 1997. Therefore, program management task will also continue. The overall program is within budget and on revised schedule.